British Geological Survey
Engineering Geology and Geophysics Group

Technical Report WN/95/37

Methods for the recognition of geological weakness zones and other surface discontinuities caused by underground mining in Carboniferous terrain

Final Report. Part 2: Figures

D Beamish, R C Flint, P G Greenwood, P D Jackson
P I Meldrum, R J Peart, M G Raines and C Williams

The **Final Report** comprises the volumes - **Part 1: Text**
Part 2: Figures

Biblographic Reference :

Beamish, D, Flint R C, Greenwood, P G, Jackson, P D Meldrum, P I, Peart, R J, Raines, M G, Williams, C Methods for the recognition of geological weakness zones and other surface discontinuites caused by underground mining in Carboniferous terrain.
British geological Survey, Technical Report, WN/95/37

Research funded in part by the Commission of the European Communities European Coal and Steel Community.
EC Contract No. 7220/AF/136

British Geological Survey, Keyworth, Nottingham, NG12 5GG

List of Figures

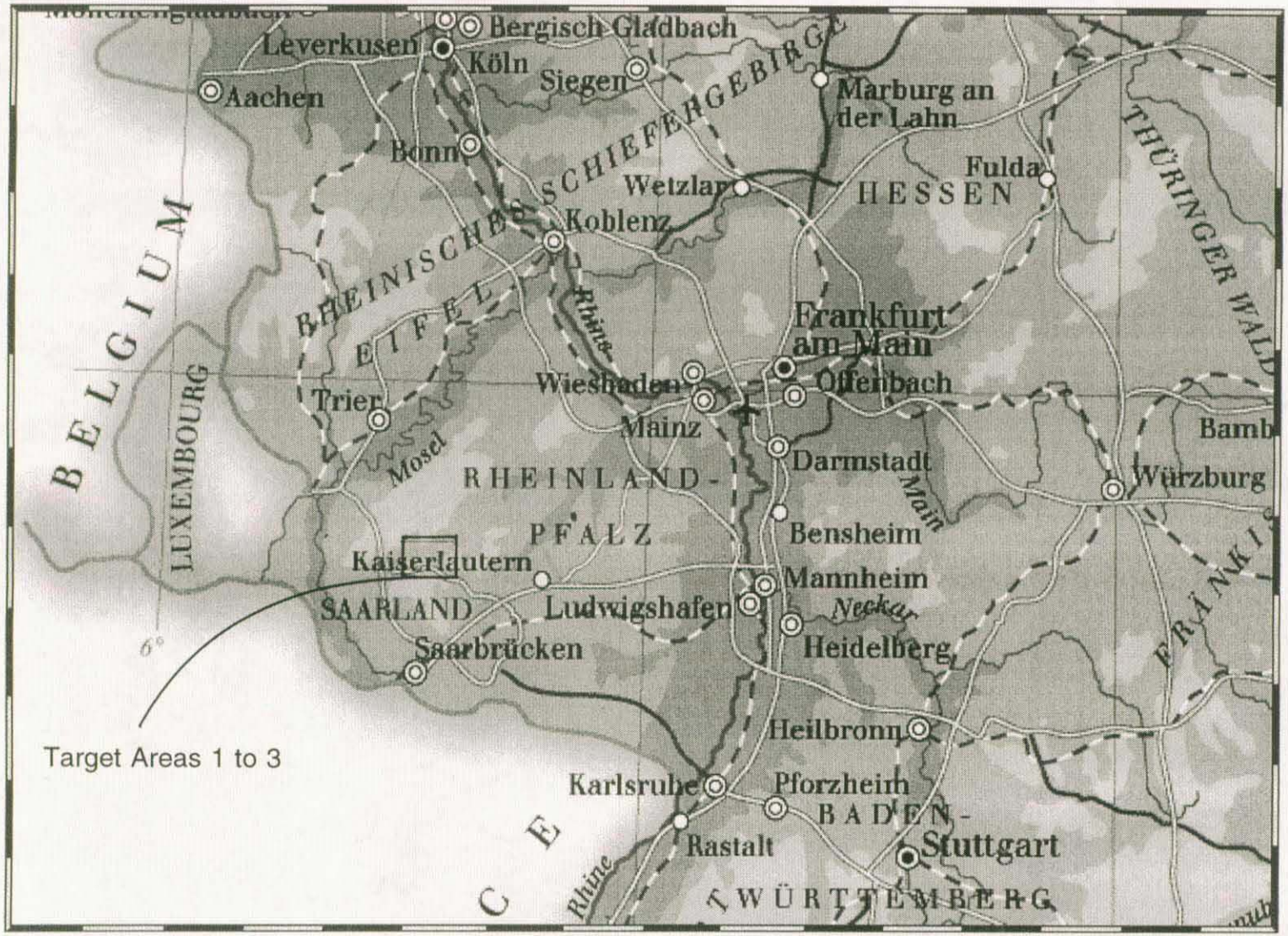

After Dorling Kindersley Multimedia (1995)

Figure 1a. Location map for Saarland.

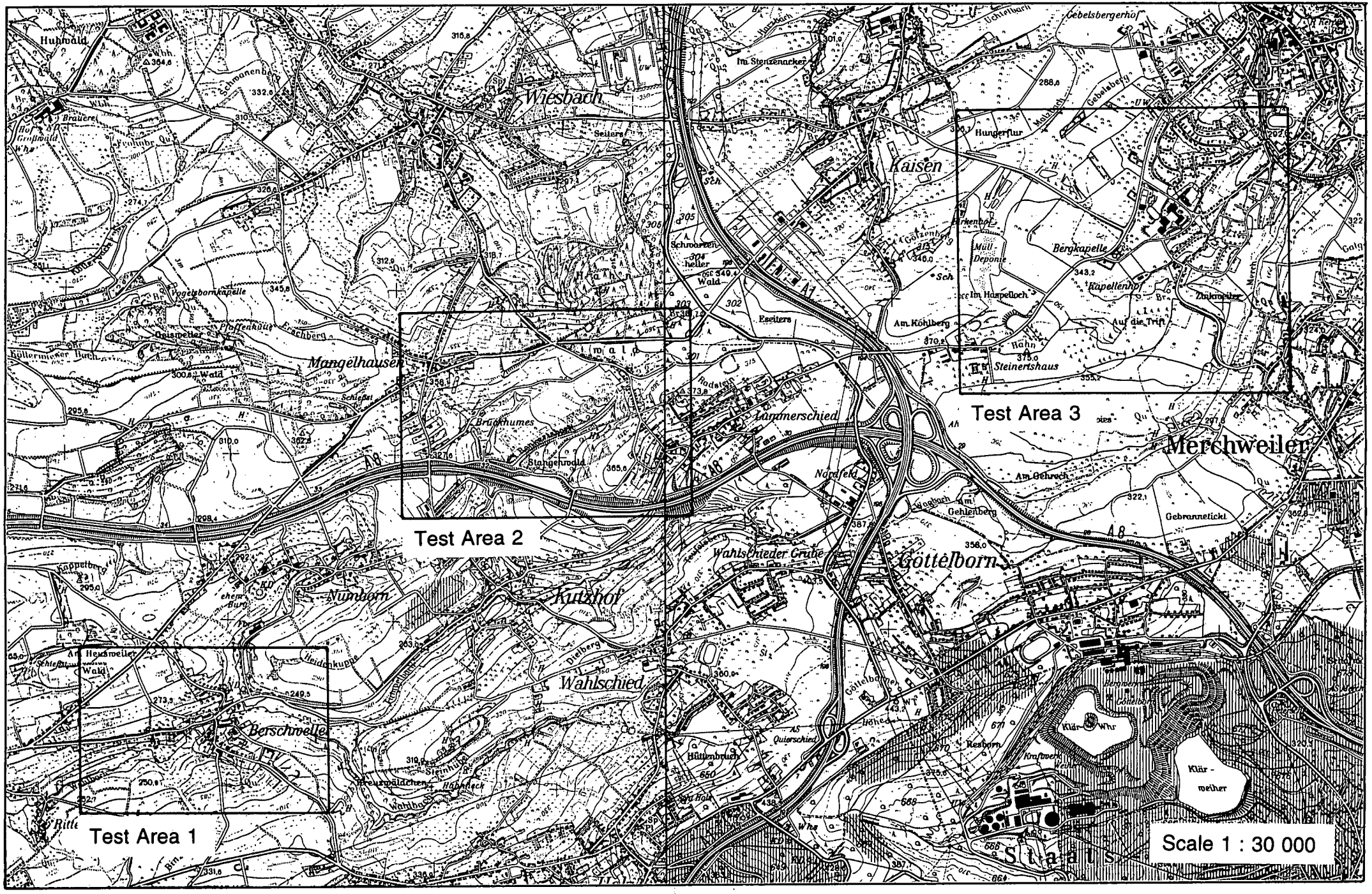

Figure 1b. Location map for Target Areas 1 to 3.

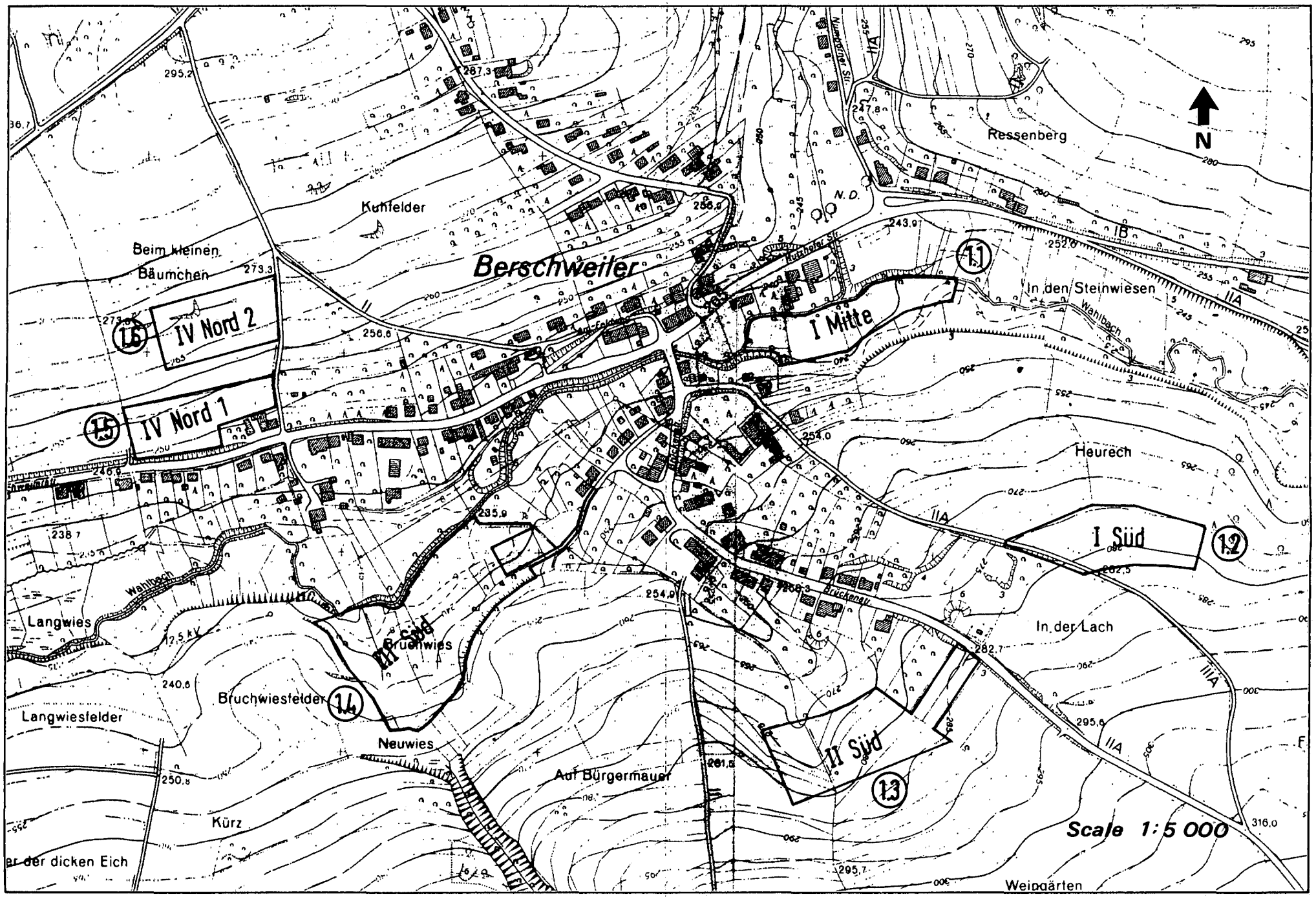

Figure 2. Location map for Test Sites 1.1 to 1.6.

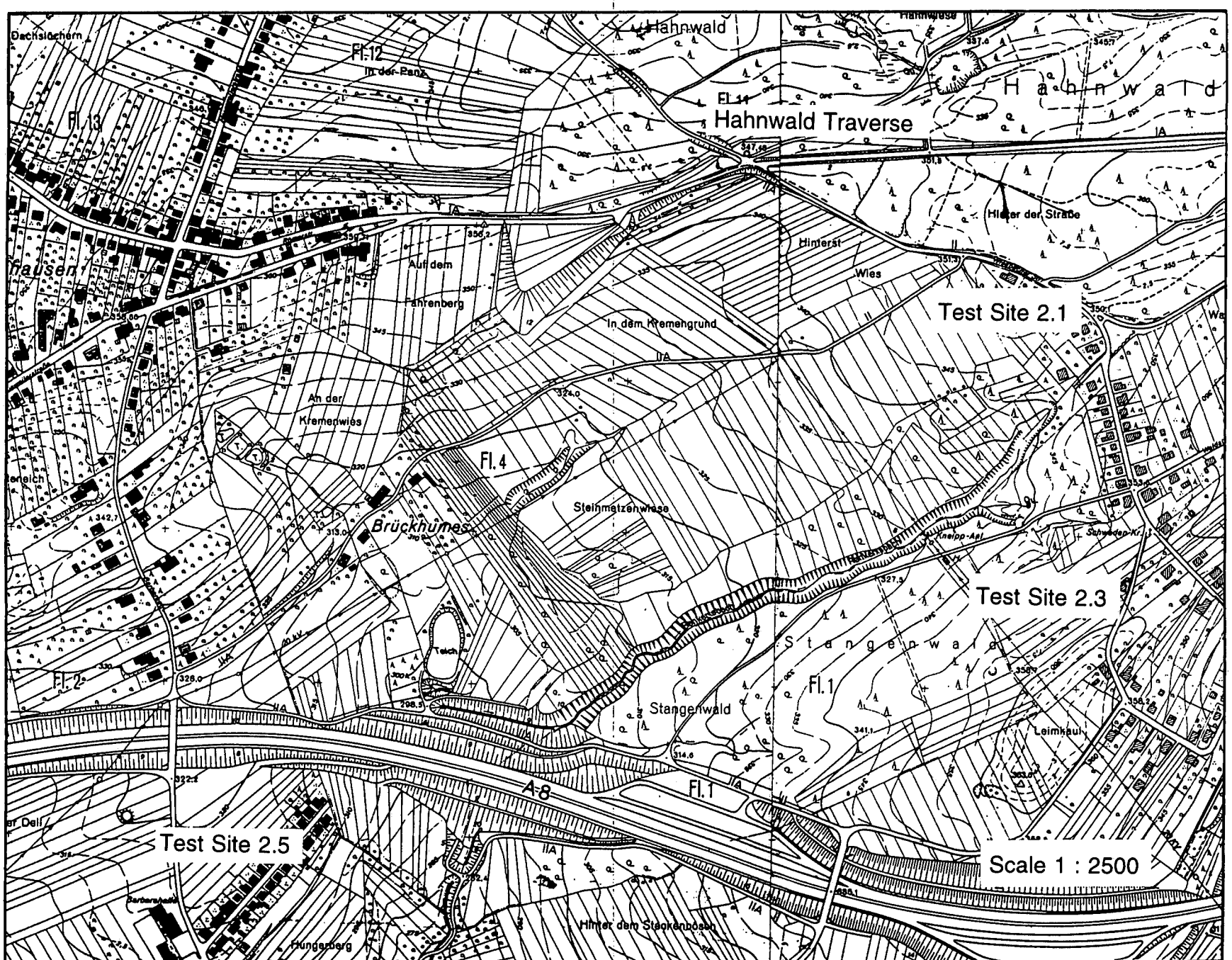

Figure 3. Location map for Test Sites 2.1 to 2.5.

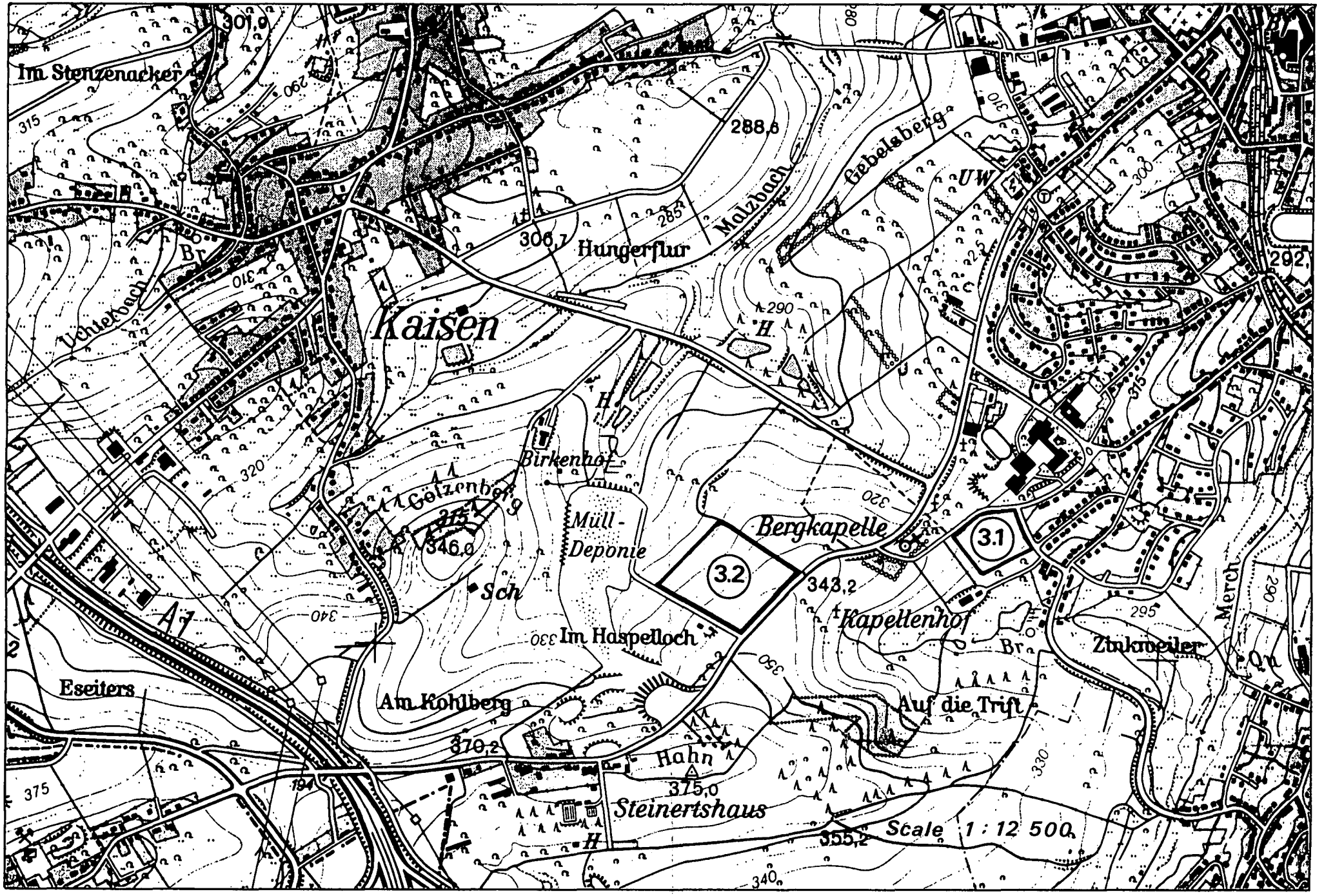

Figure 4. Location map for Test Sites 3.1 to 3.2 and 3.2 (Ext).

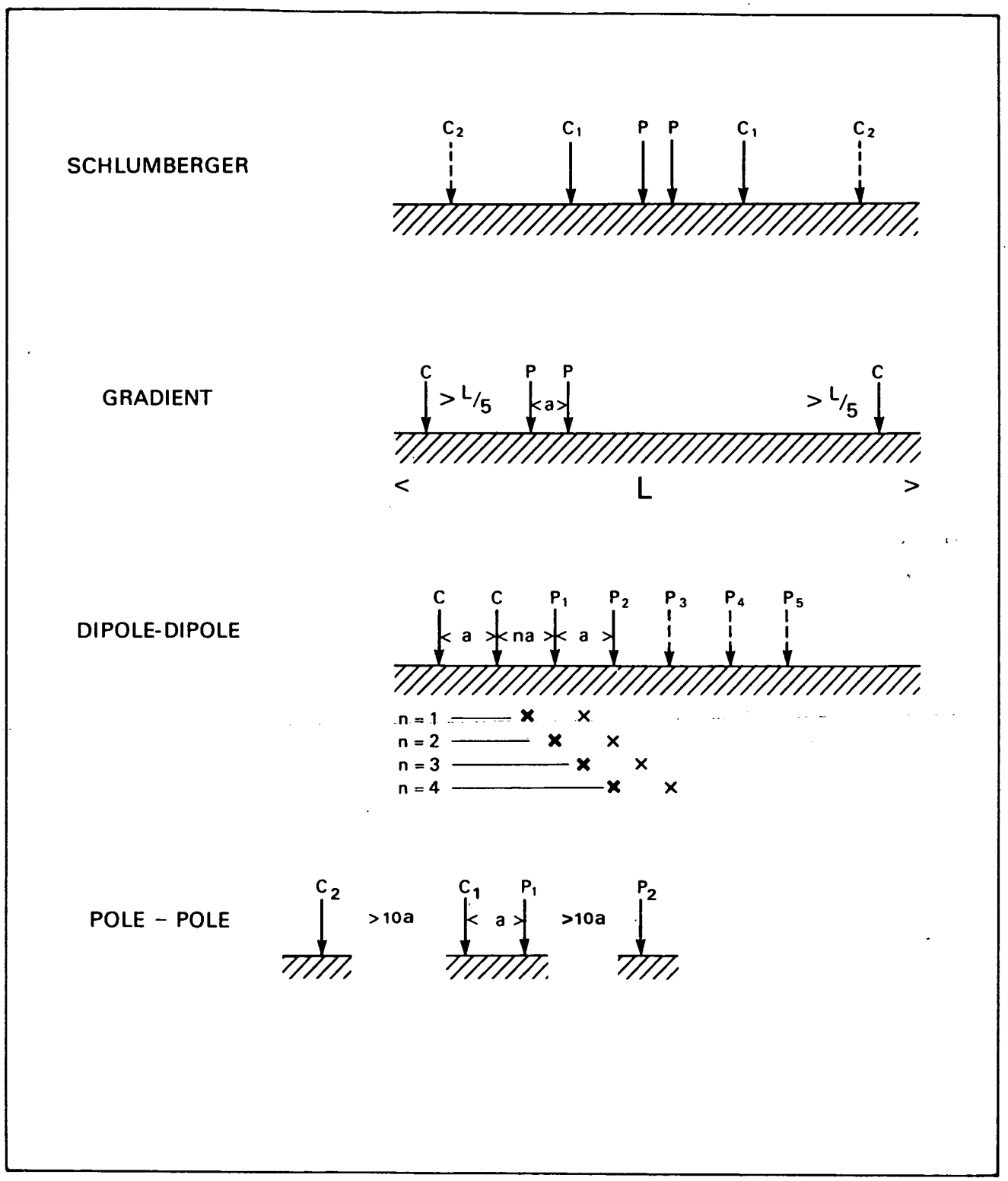

Figure 1 *res.* Electrode arrays used for the resistivity surveys.

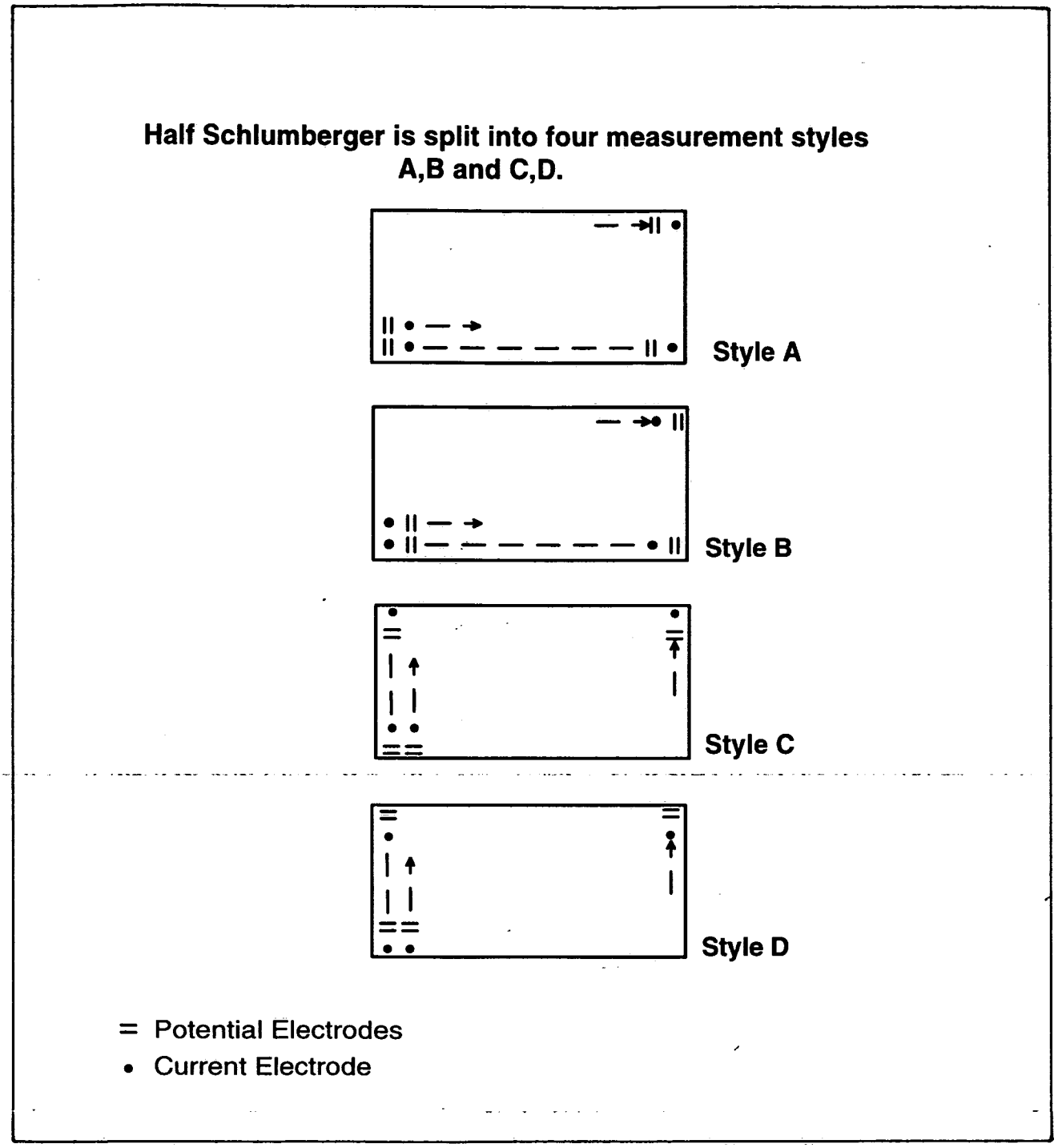

Figure 2 *rsc*. The 2D electrode grid used for RESCAN surveys, and the definition of the 'half Schlumberger' mapping technique.

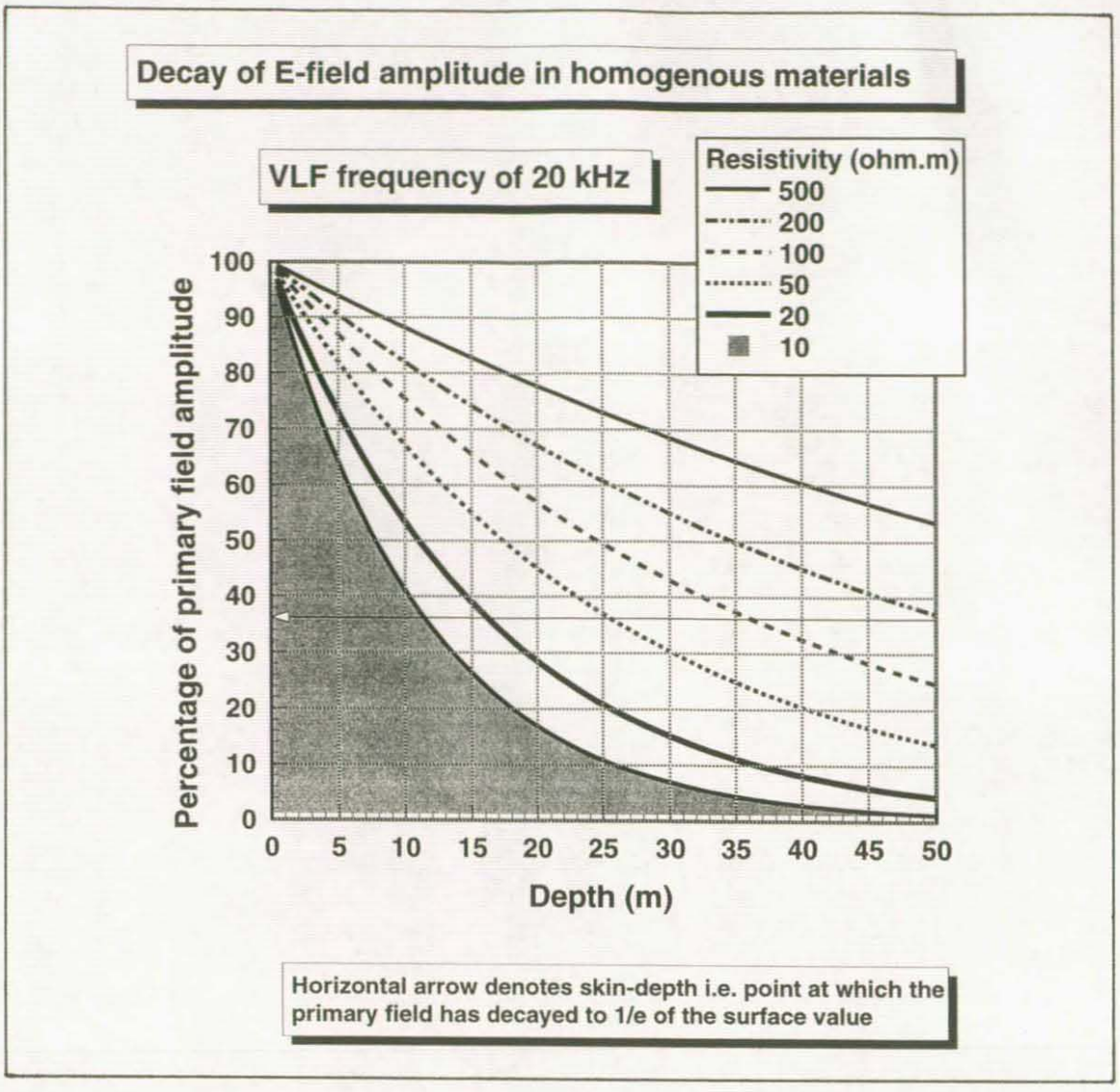

Figure 1 *vlf*. Depth of investigation of VLF EM fields.

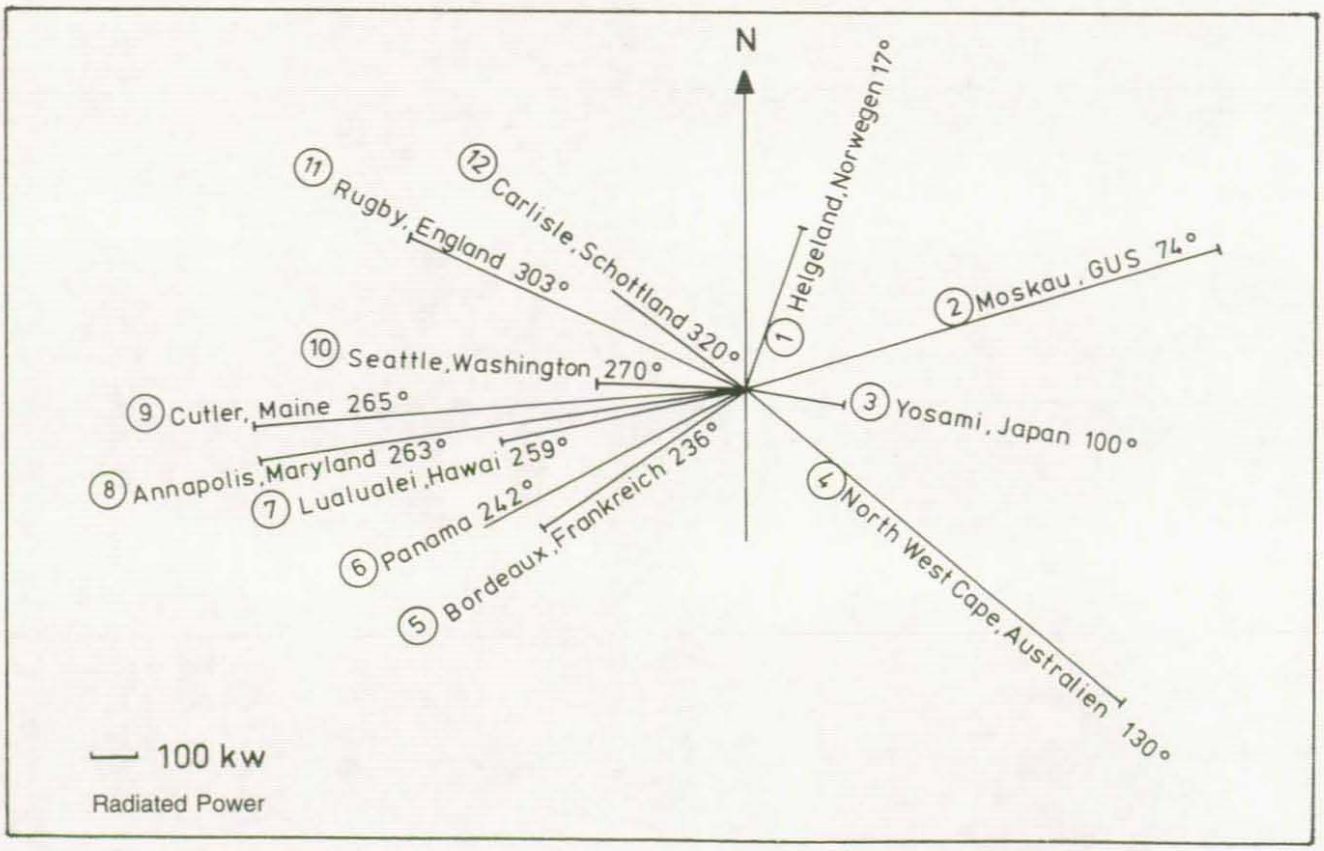

Figure 2 *vlf*. Azimuths of VLF transmitters relative to Test Areas 1, 2, and 3.

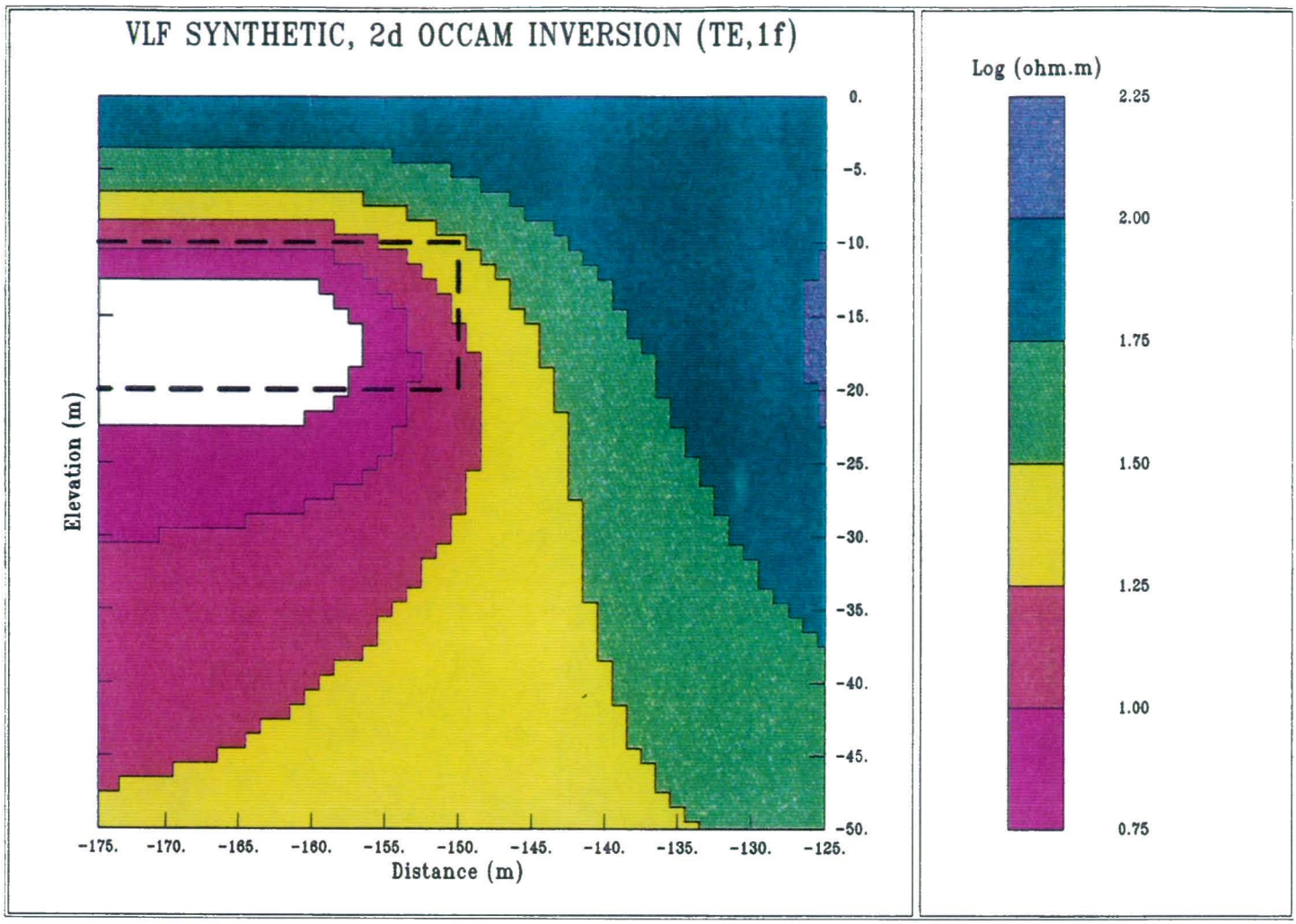

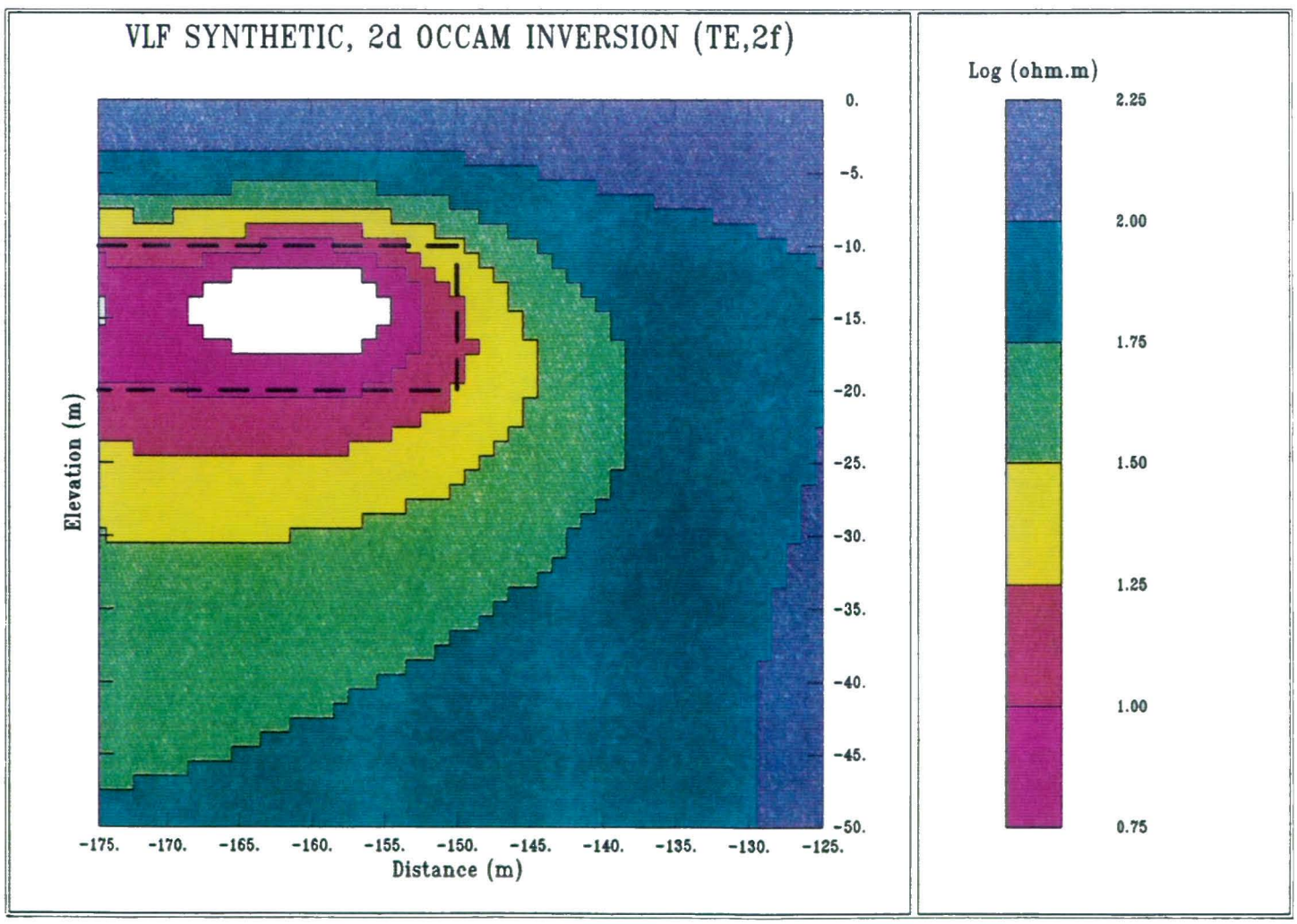

Figure 3 *vlf*. Synthetic VLF model for non-dipping target.

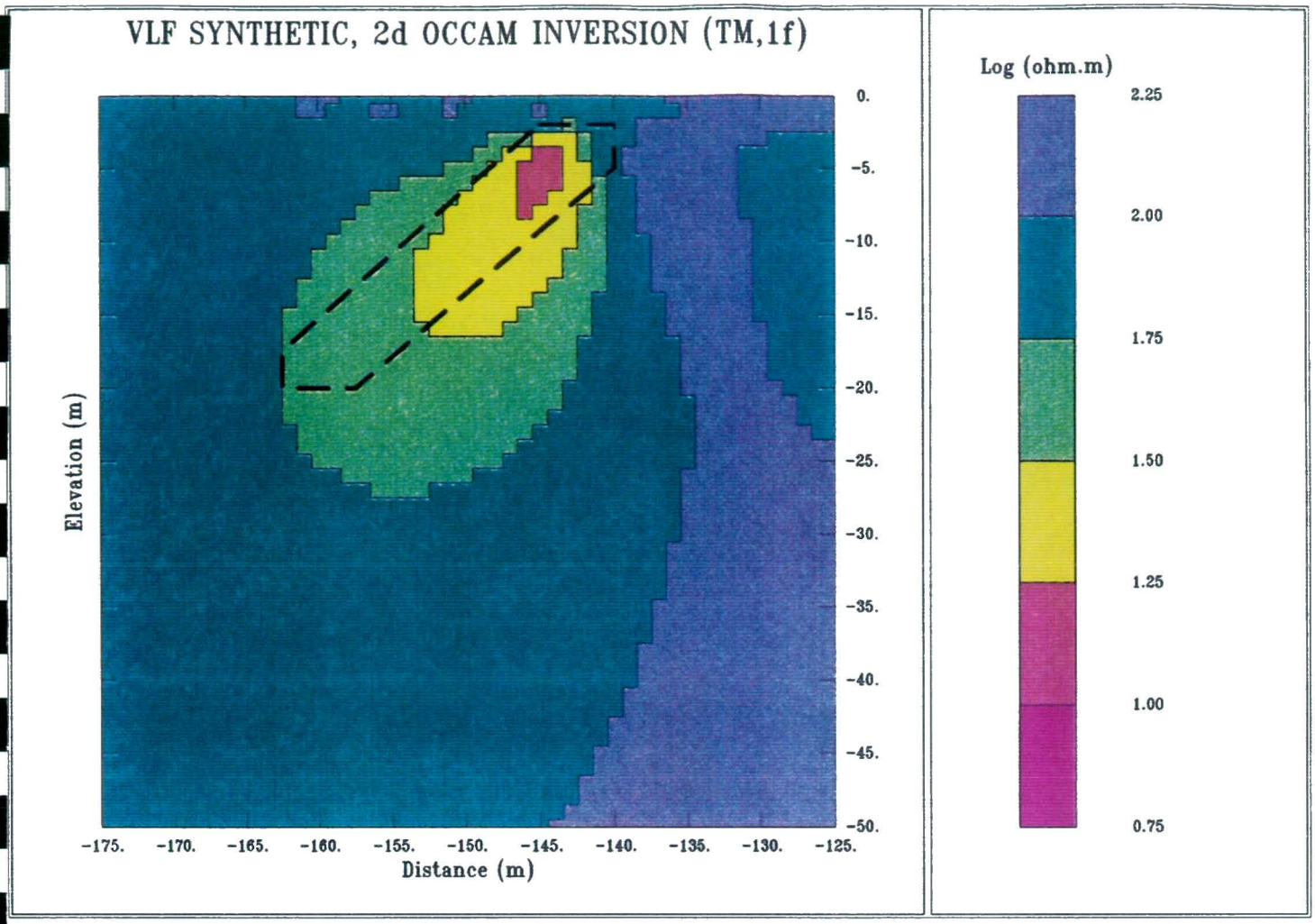

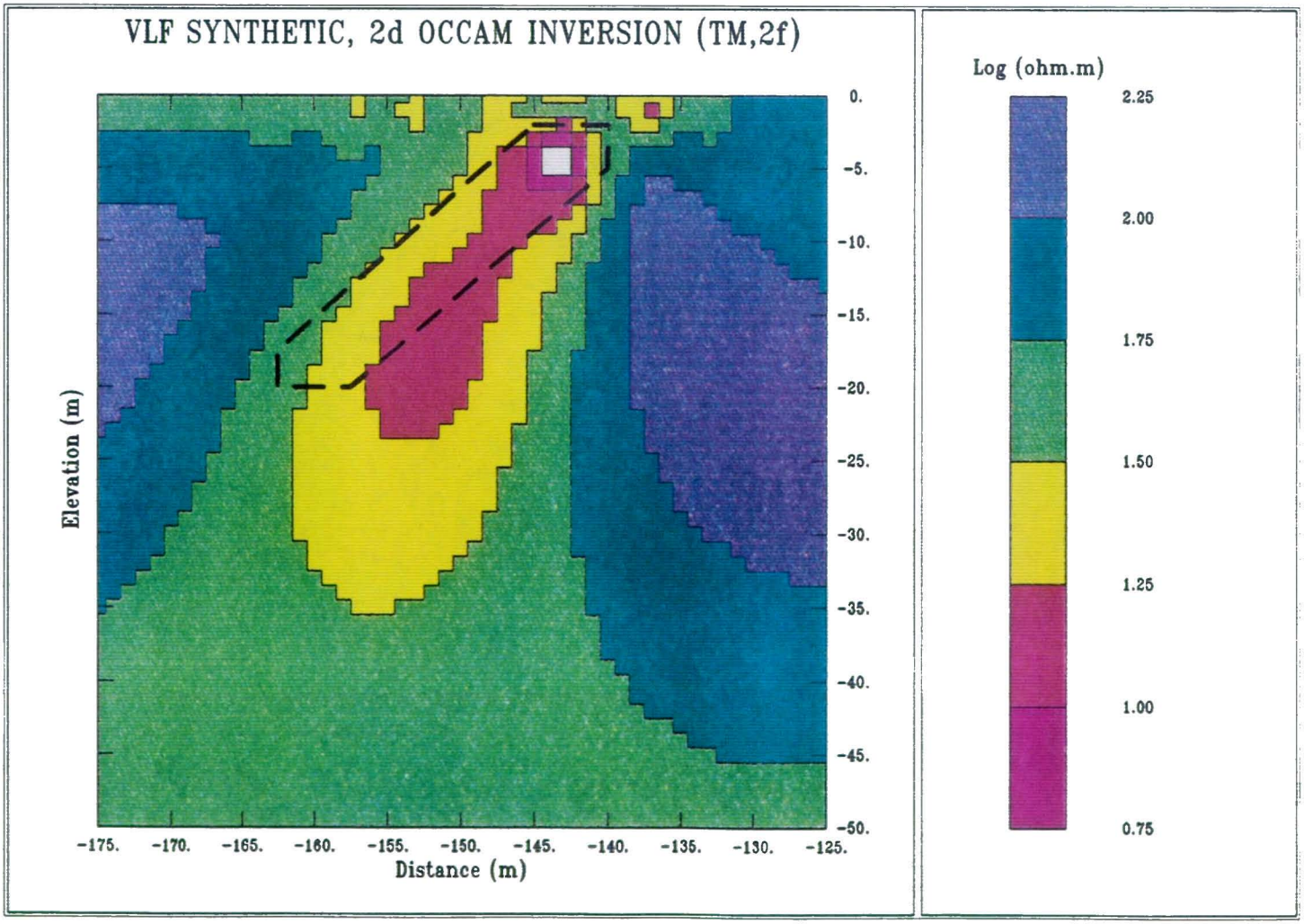

Figure 4 *vlf*. Synthetic VLF model for dipping target.

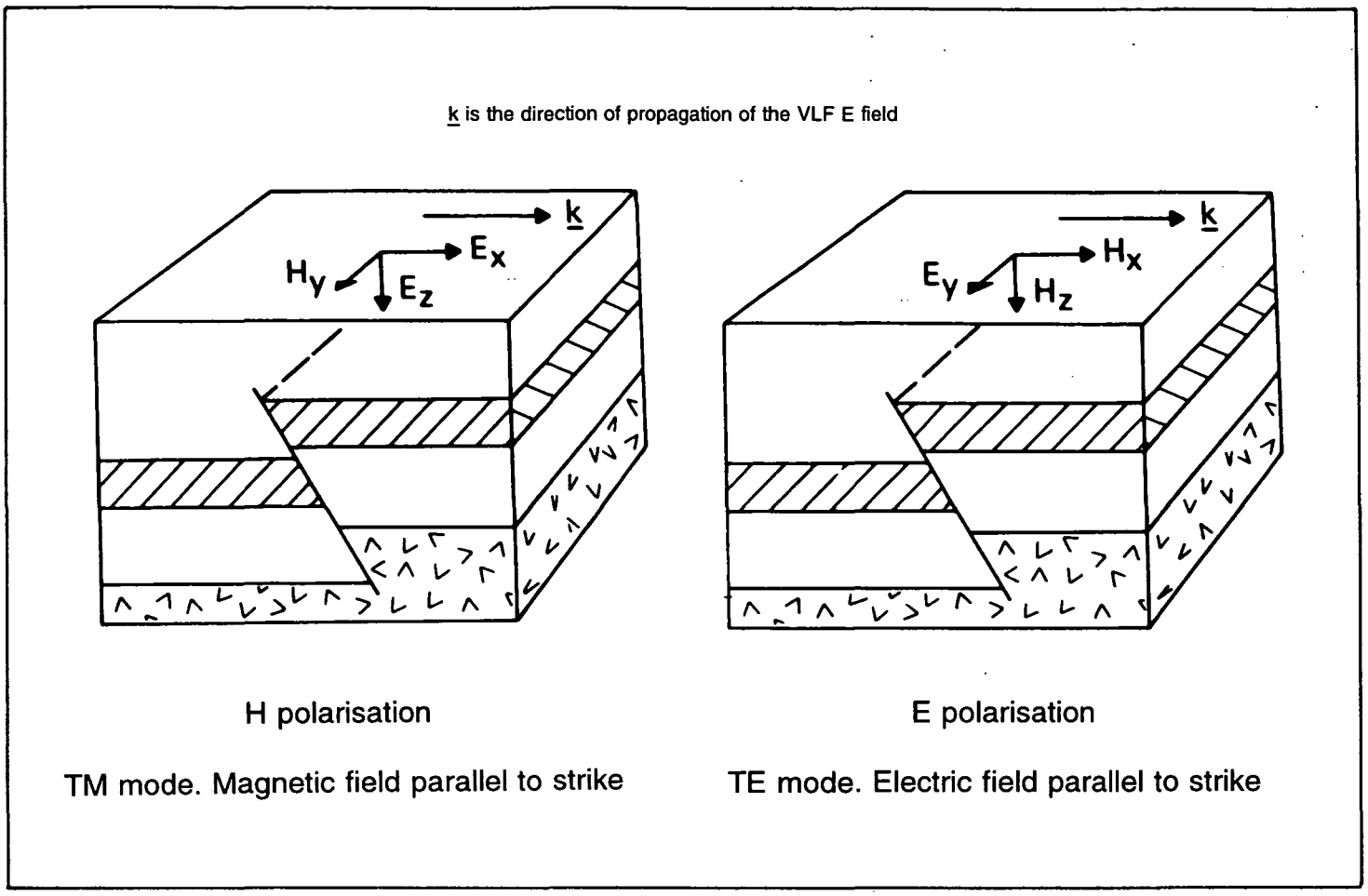

Figure 5 *vlf*. Principal components of the VLF field.

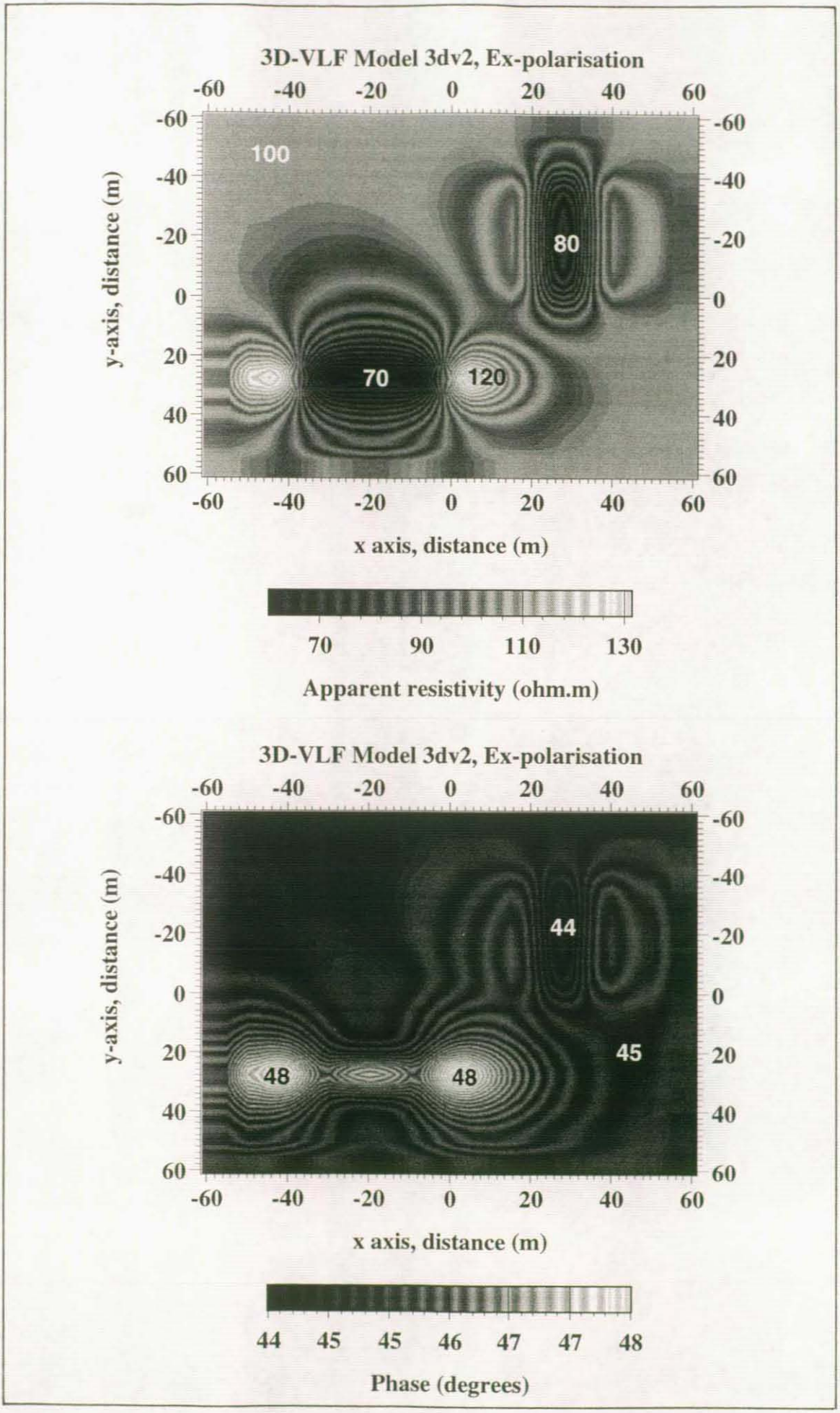

Figure 6 *vlf*. VLF modelling. Model 1: apparent resistivity and phase.

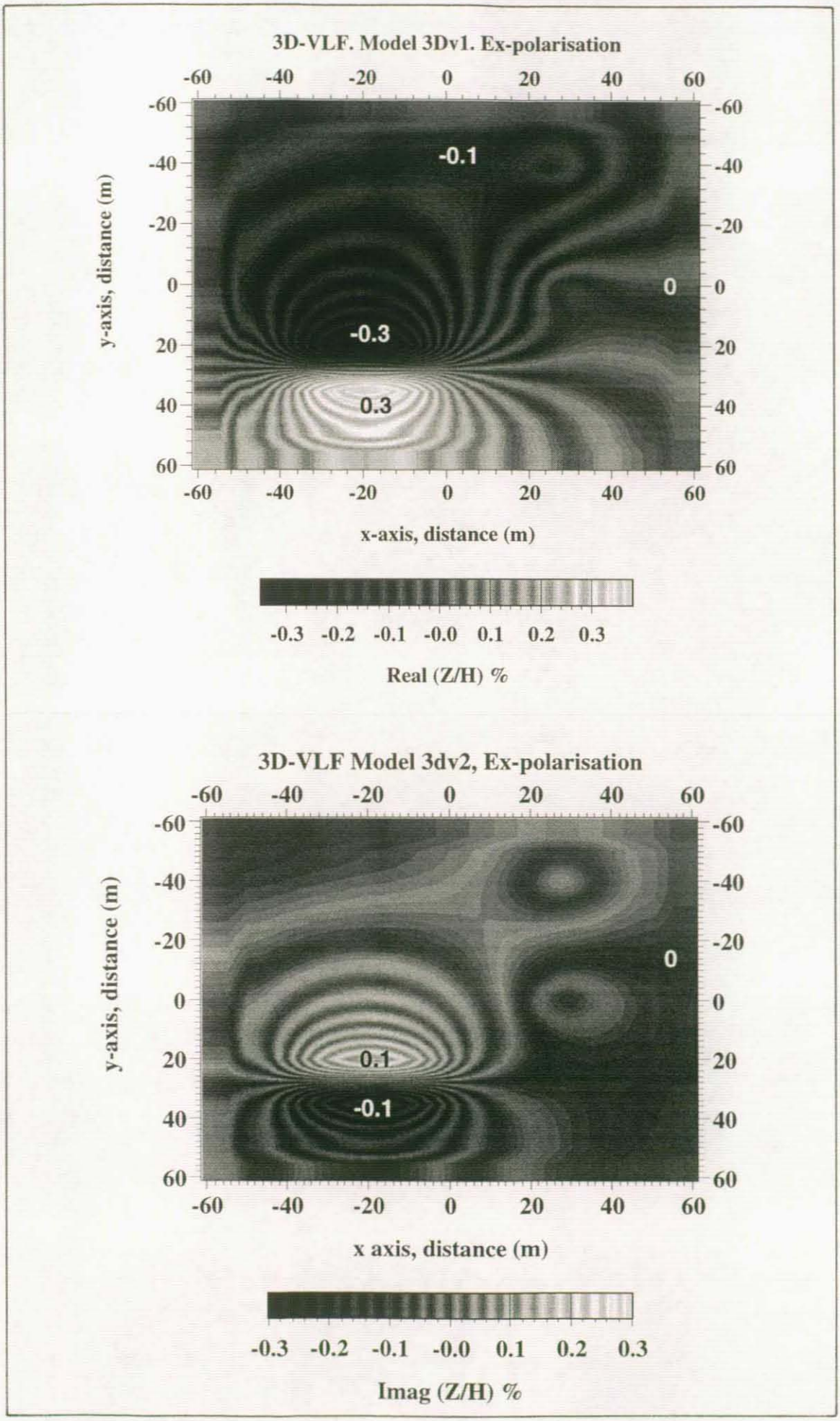

Figure 7 *vlf*. VLF modelling. Model 1: Z field ratios.

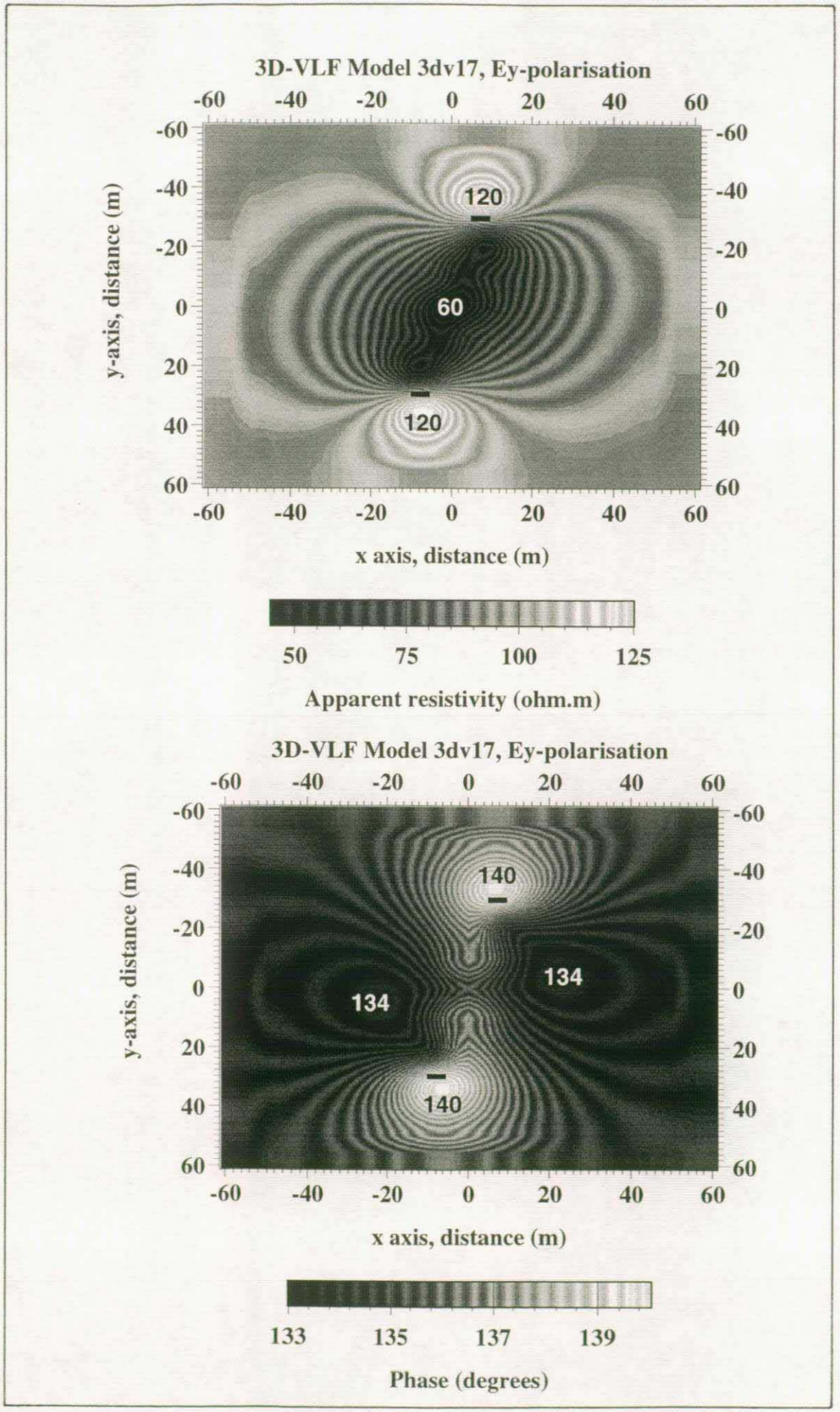

Figure 8 *vlf*. VLF modelling. Model 2: apparent resistivity and phase, E_y polarisation.

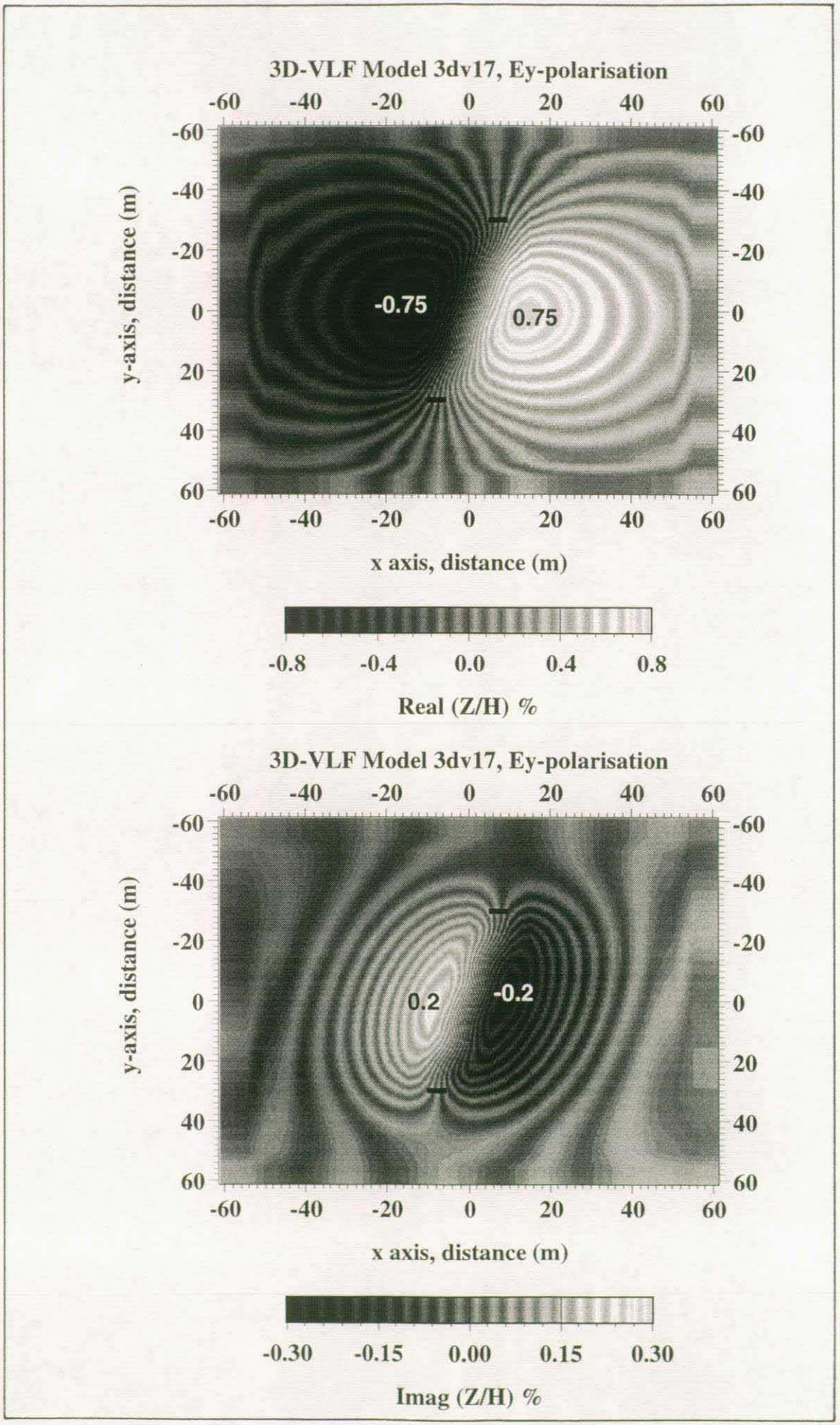

Figure 9 *vlf.* VLF modelling. Model 2: Z field ratios, E_y polarisation.

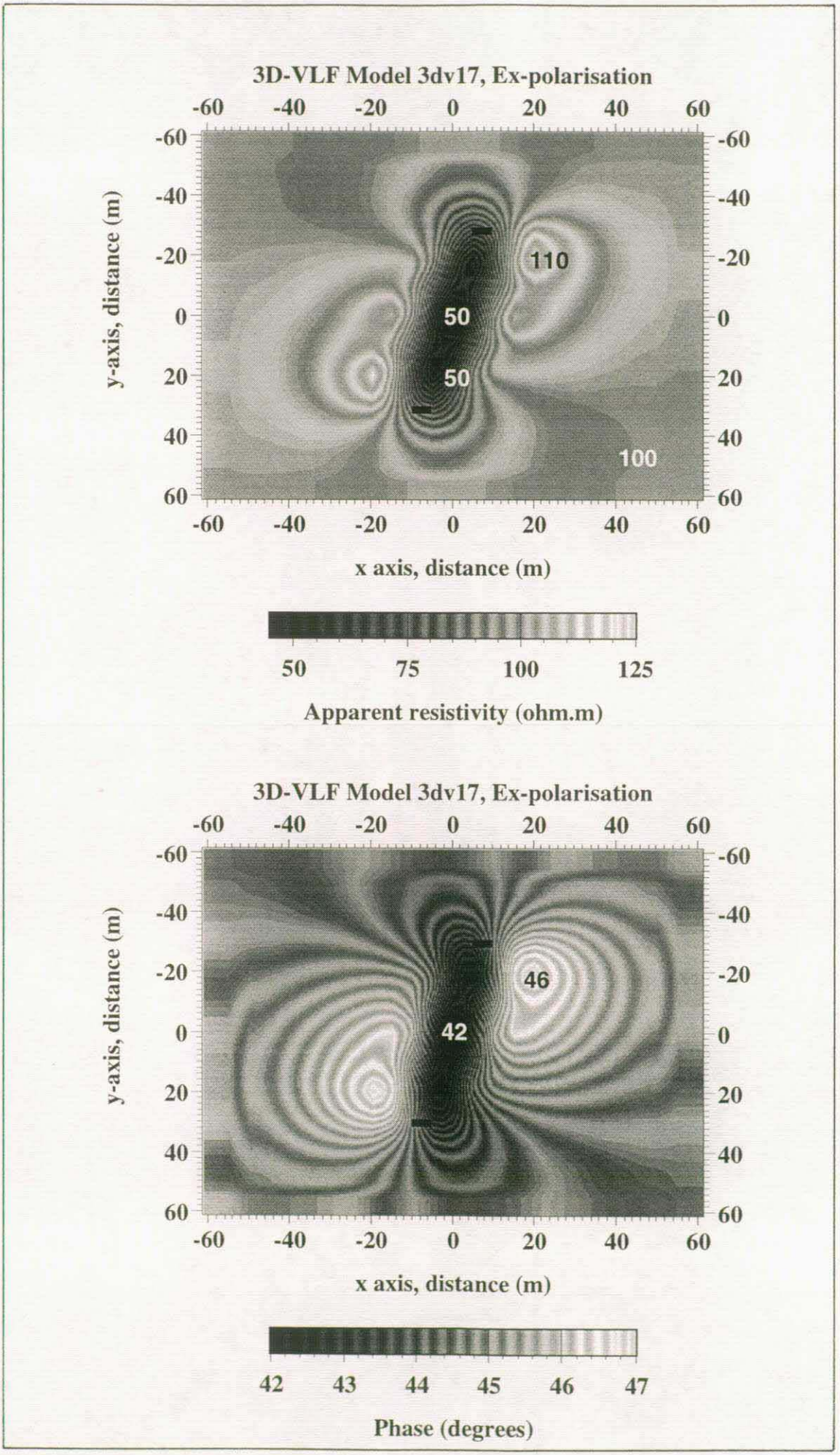

Figure 10 *vlf*. VLF modelling. Model 2: apparent resistivity and phase, E_x polarisation.

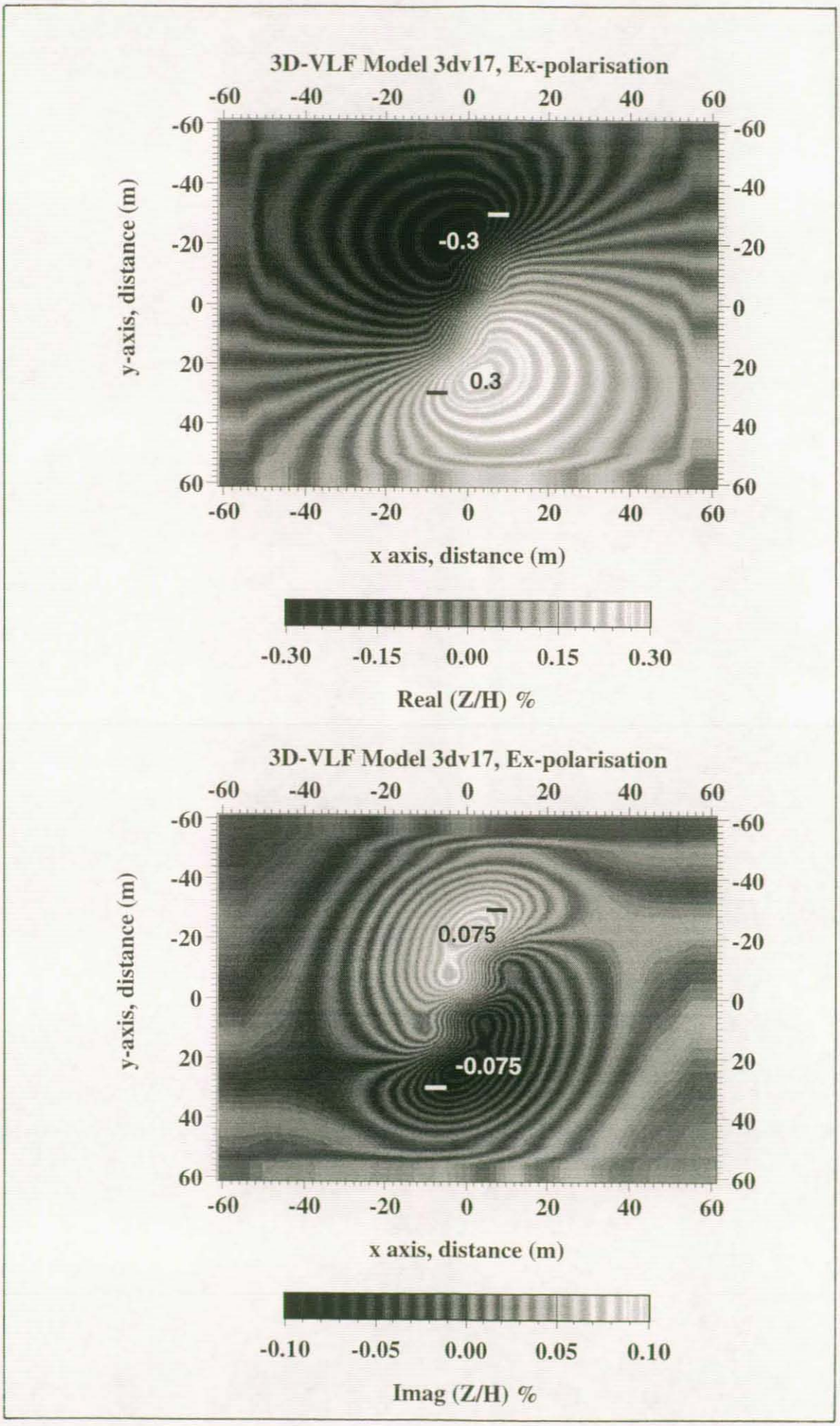

Figure 11 *vlf*. VLF modelling. Model 3: Z field ratios, E_x polarisation.

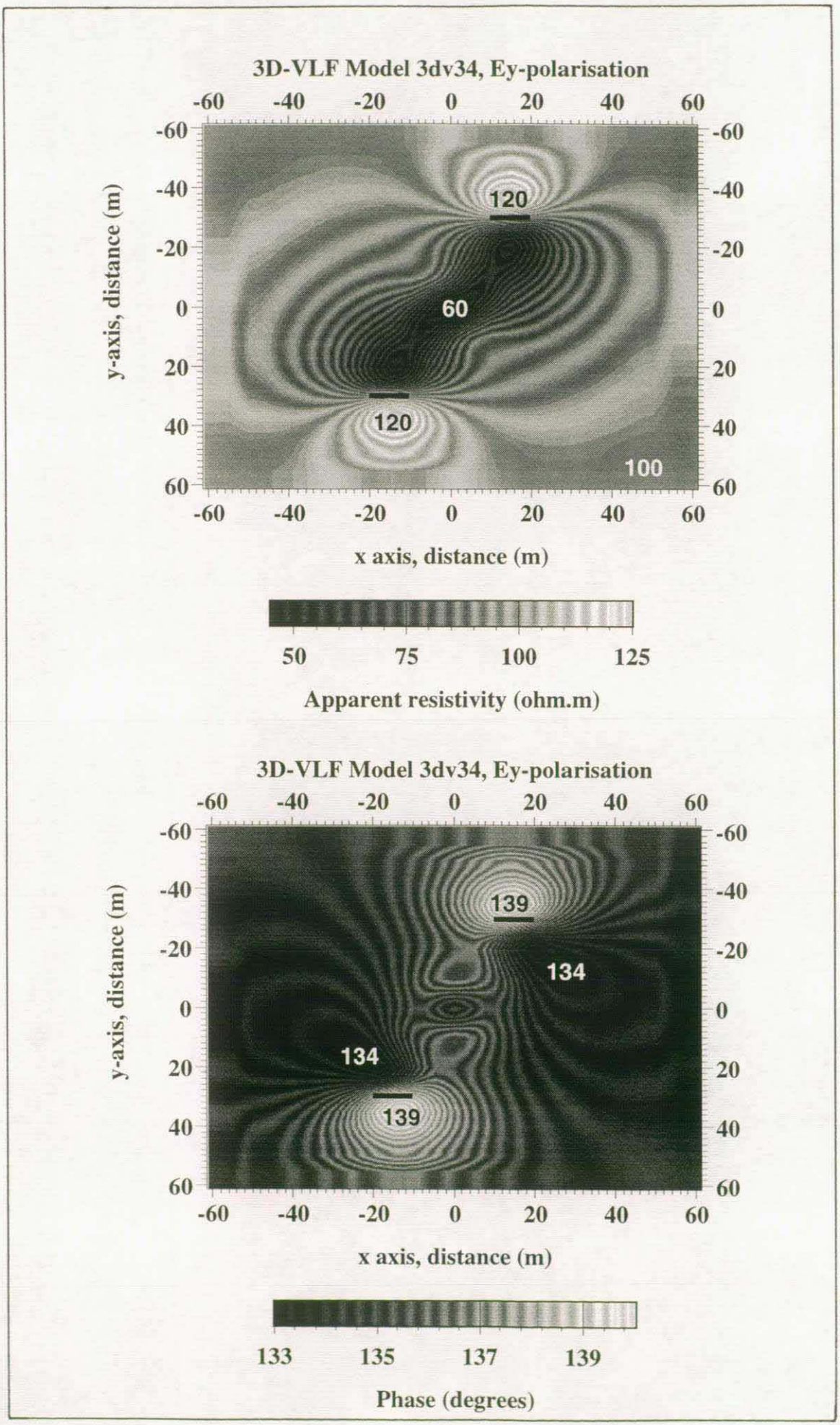

Figure 12 *vlf*. VLF modelling. Model 3: apparent resistivity and phase, E_y polarisation.

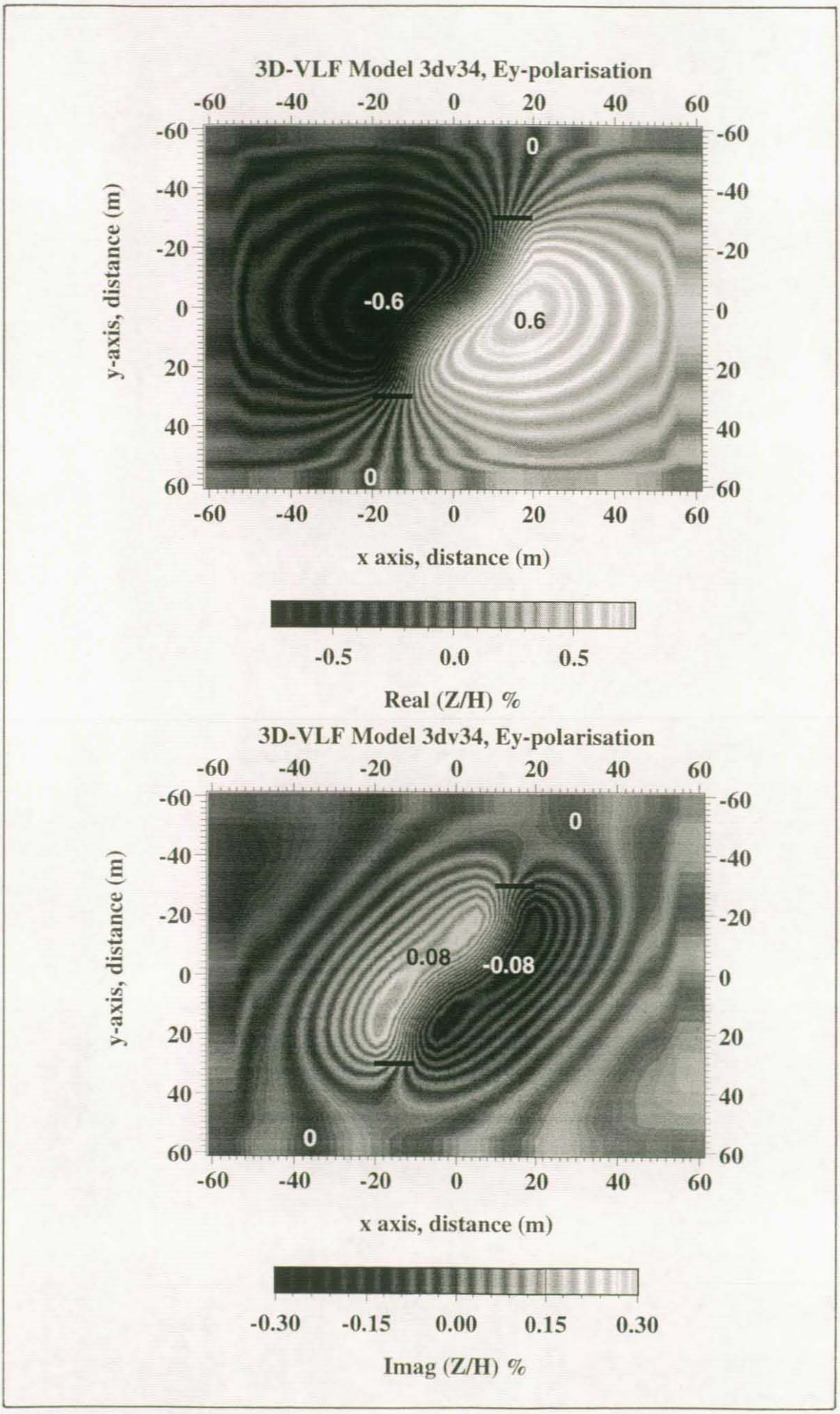

Figure 13 *vlf.* VLF modelling. Model 3: Z field ratios, E_y polarisation.

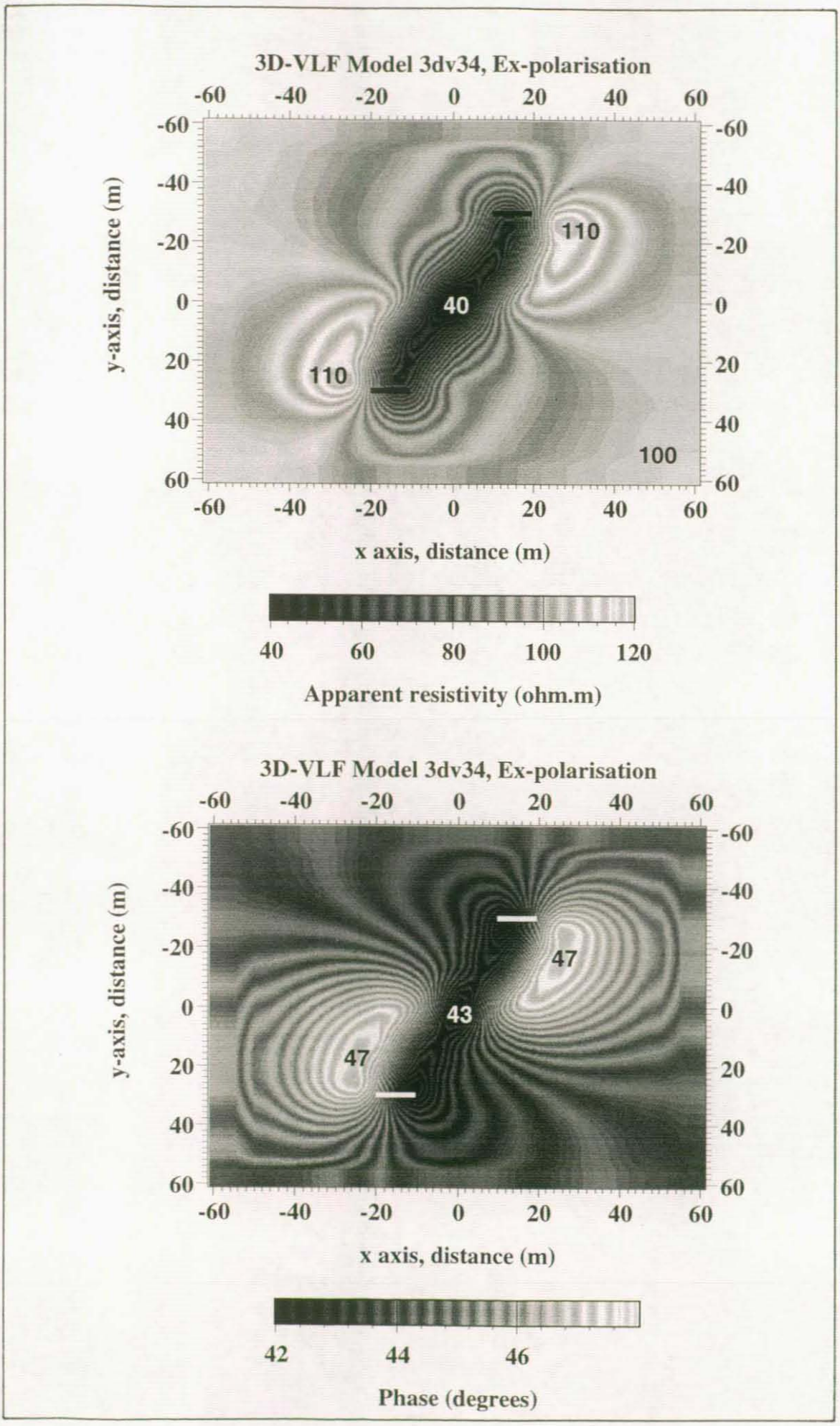

Figure 14 *vlf*. VLF modelling. Model 3: apparent resistivity and phase, E_x polarisation.

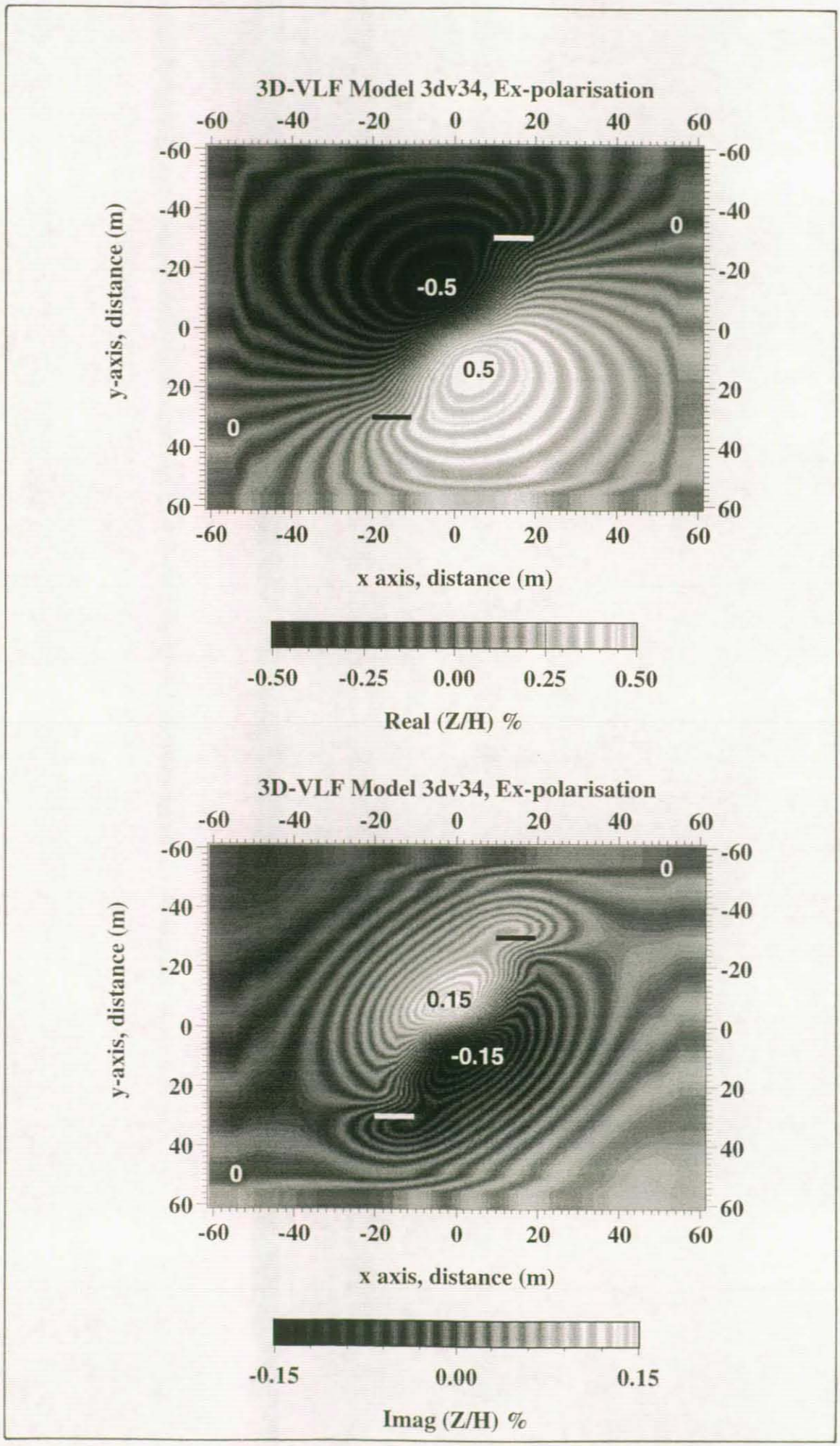

Figure 15 *vlf*. VLF modelling. Model 3: Z field ratios, E_x polarisation.

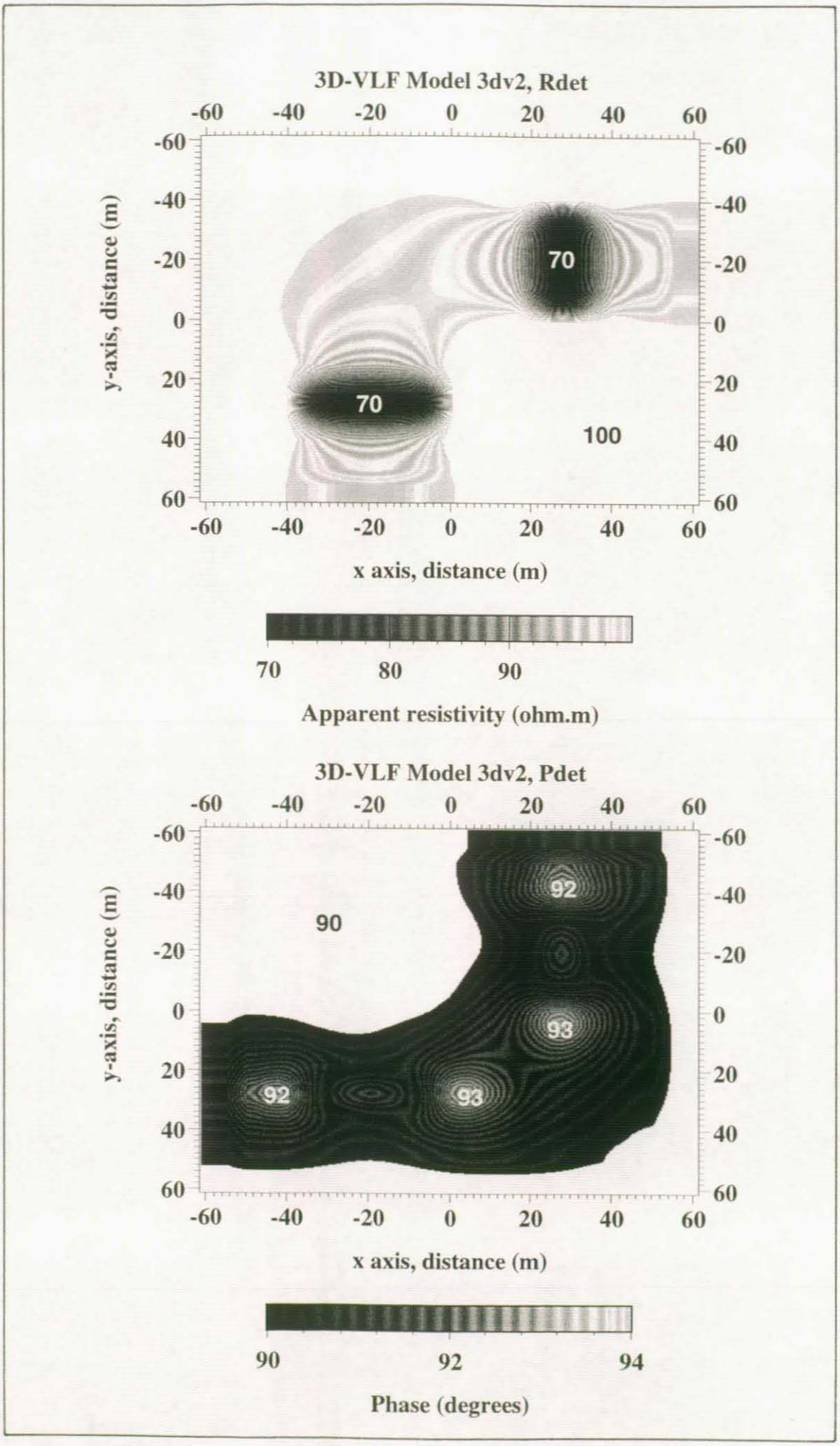

Figure 16 *vlf*. VLF modelling. Model 1: use of rotational invariants.

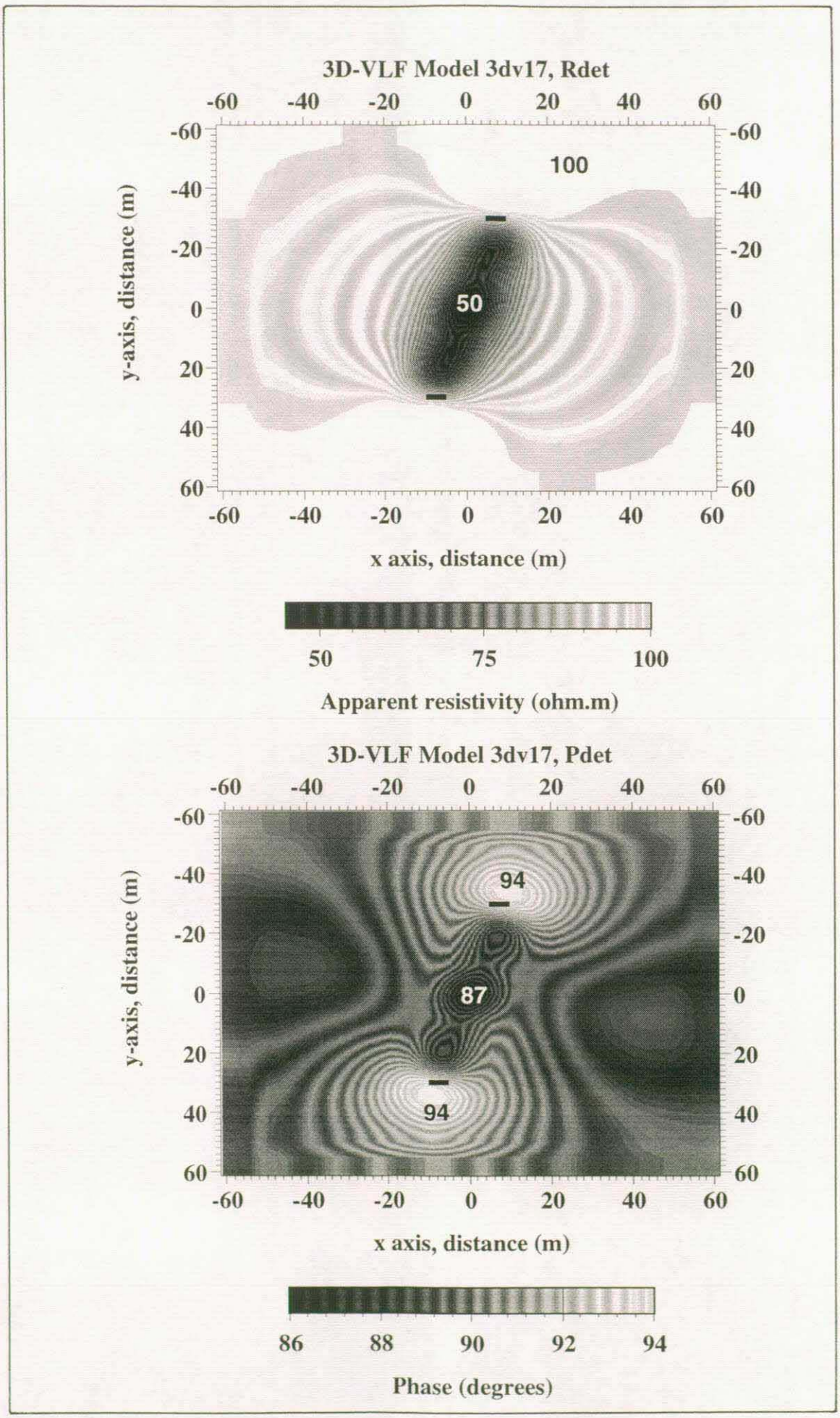

Figure 17 *vlf*. VLF modelling. Model 2: use of rotational invariants.

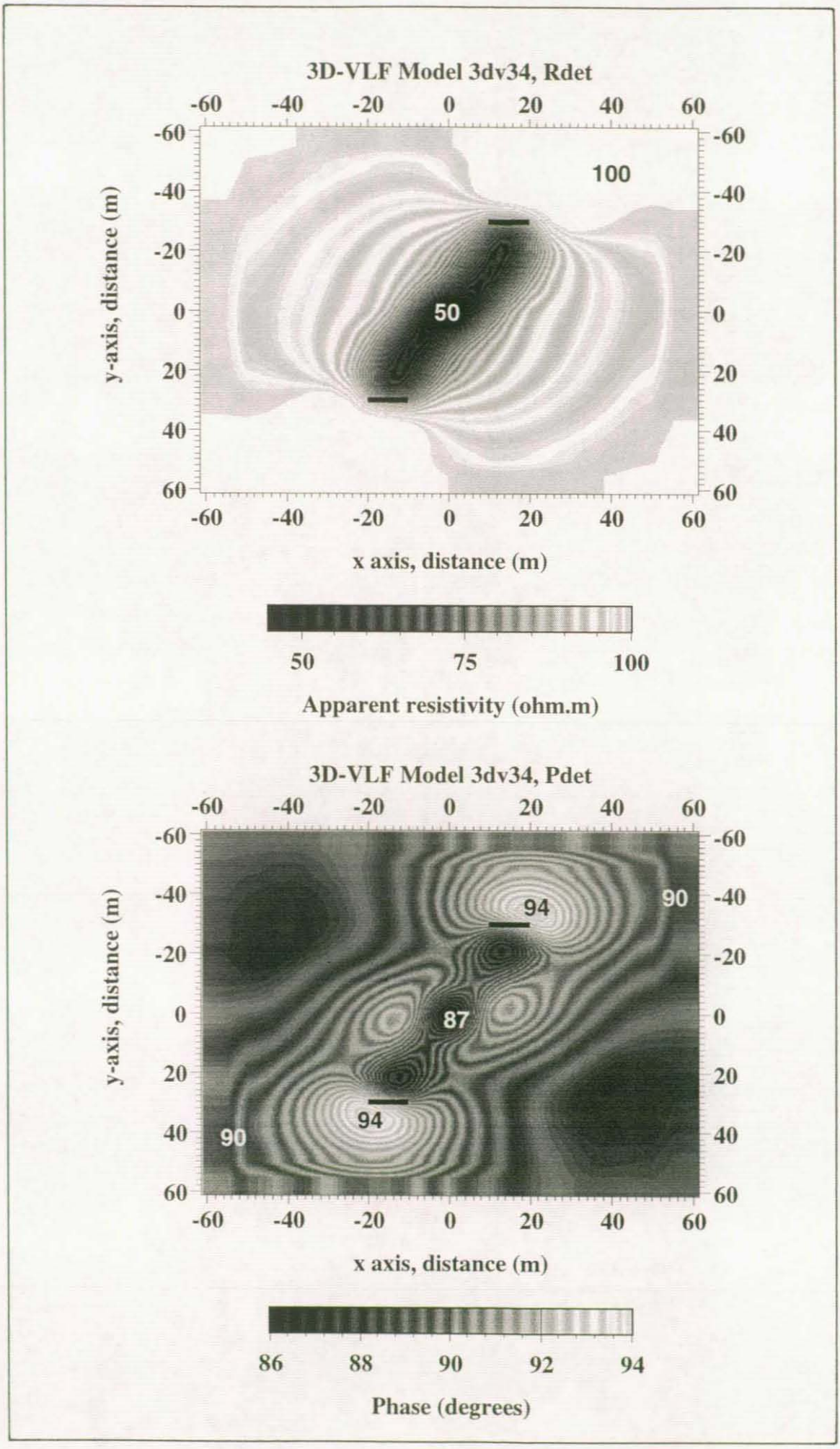

Figure 18 *vlf*. VLF modelling. Model 3: use of rotational invariants.

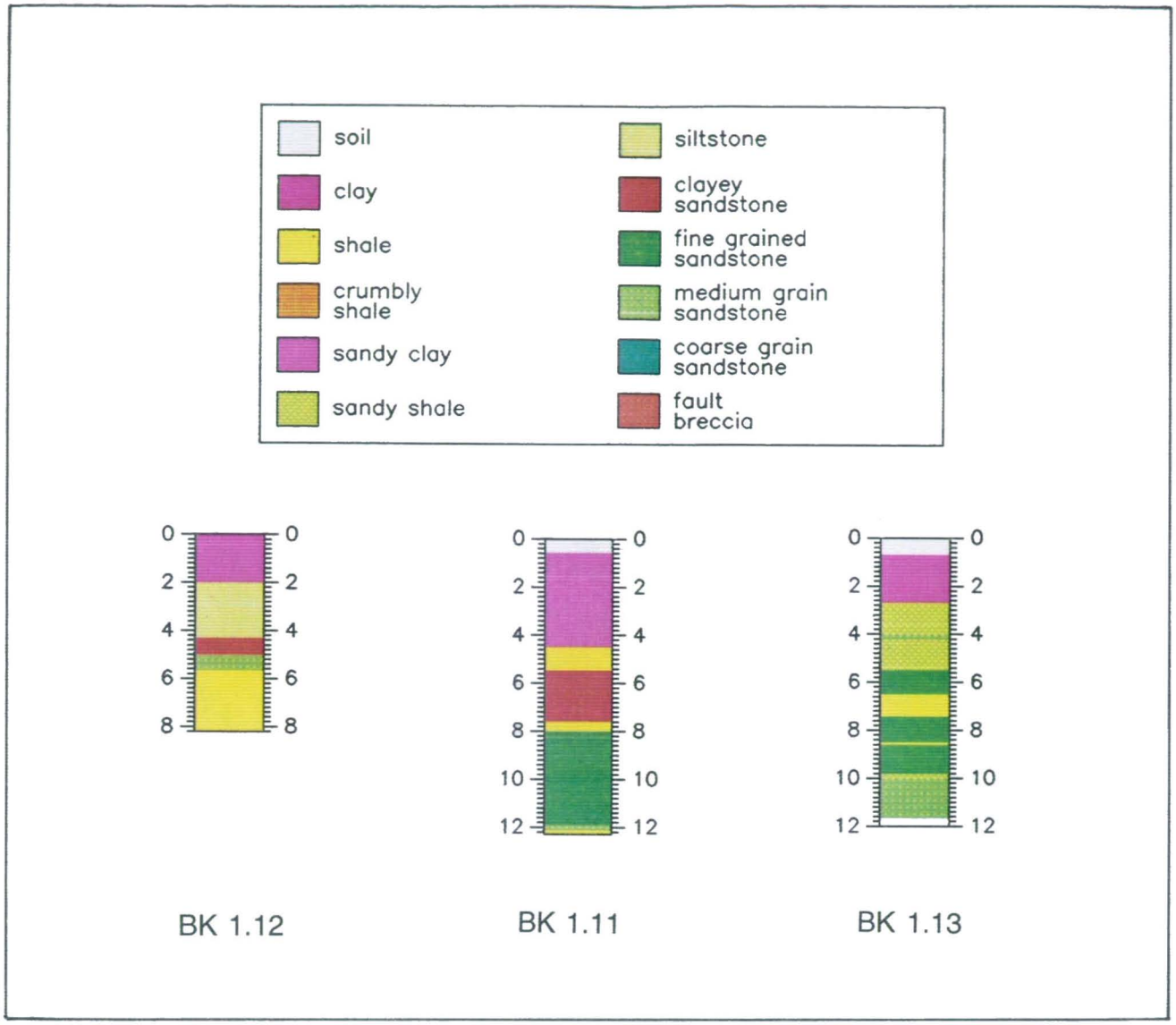

Figure 6. Test Site 1.1. Geological section: boreholes BK1.11, BK1.12, and BK1.13.

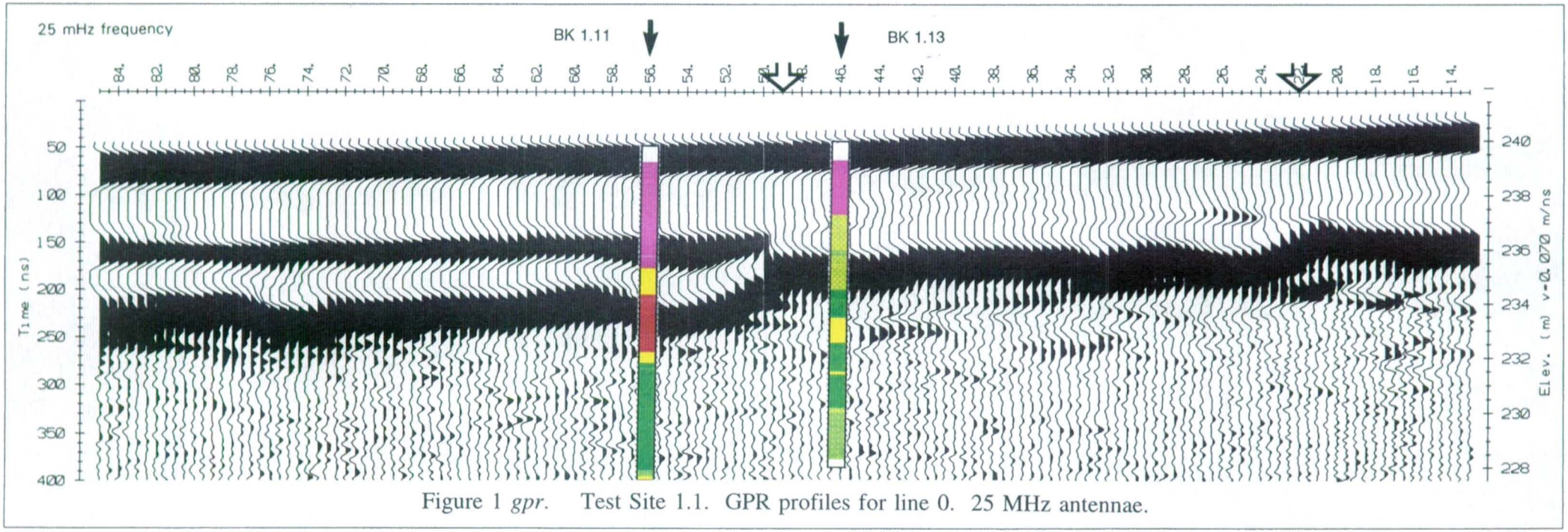

Figure 1 *gpr*. Test Site 1.1. GPR profiles for line 0. 25 MHz antennae.

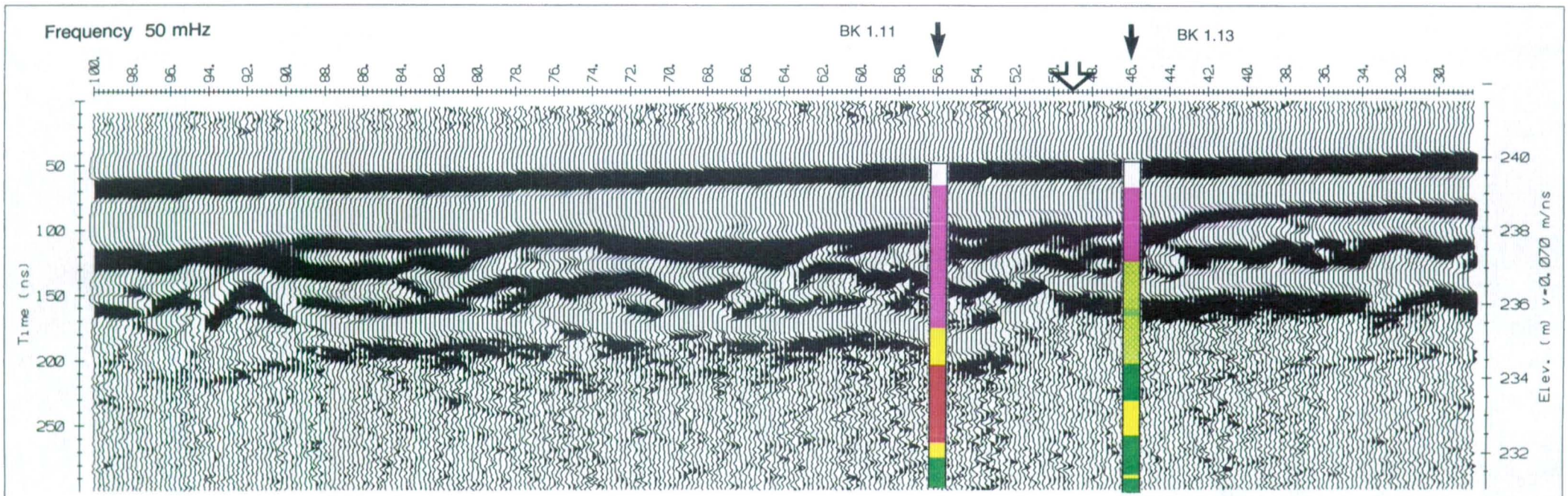

Figure 2 *gpr*. Test Site 1.1. GPR profiles for line 0. 50 MHz antennae.

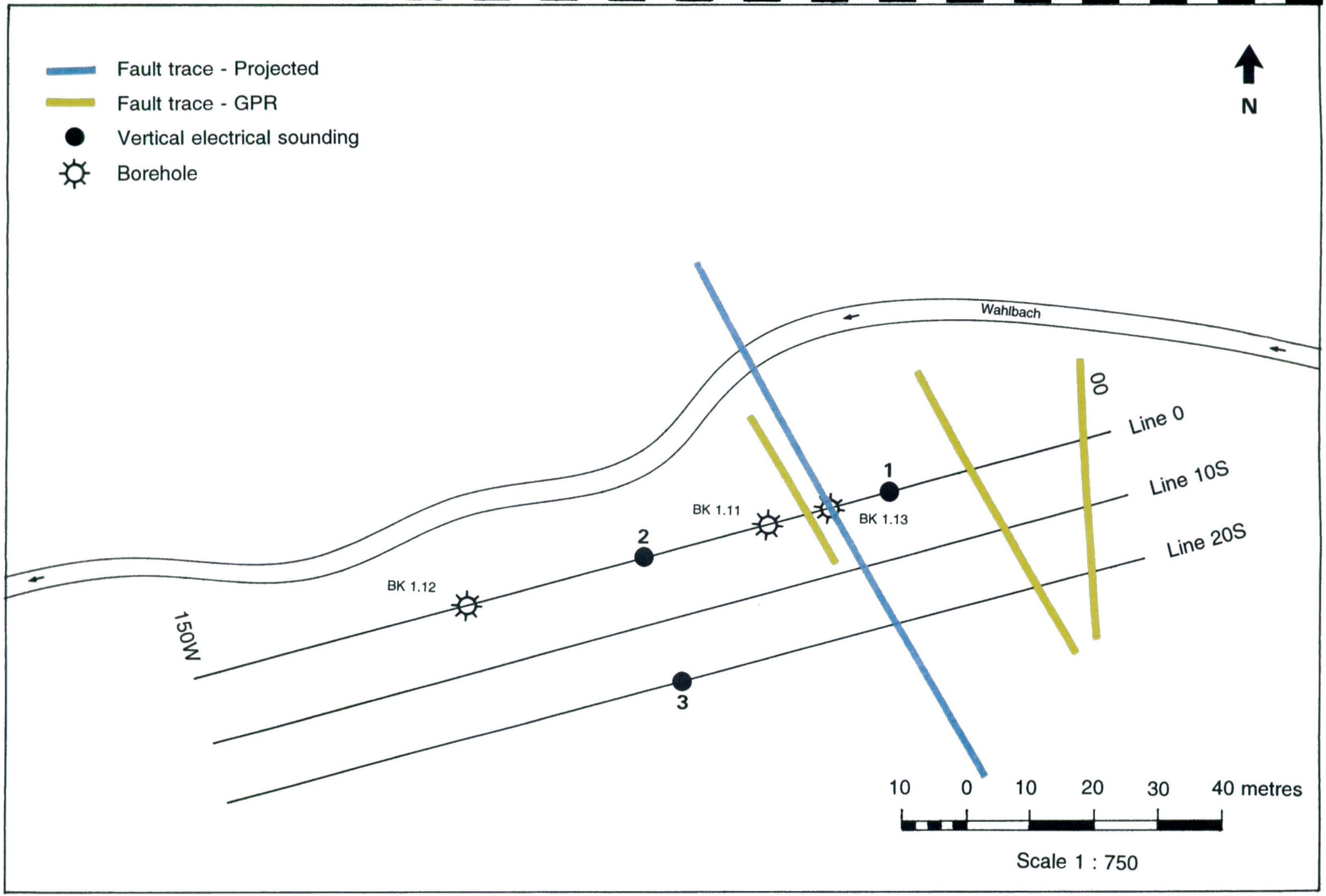

Figure 5. Test Site 1.1. Geophysical grid, borehole locations, and interpretation.

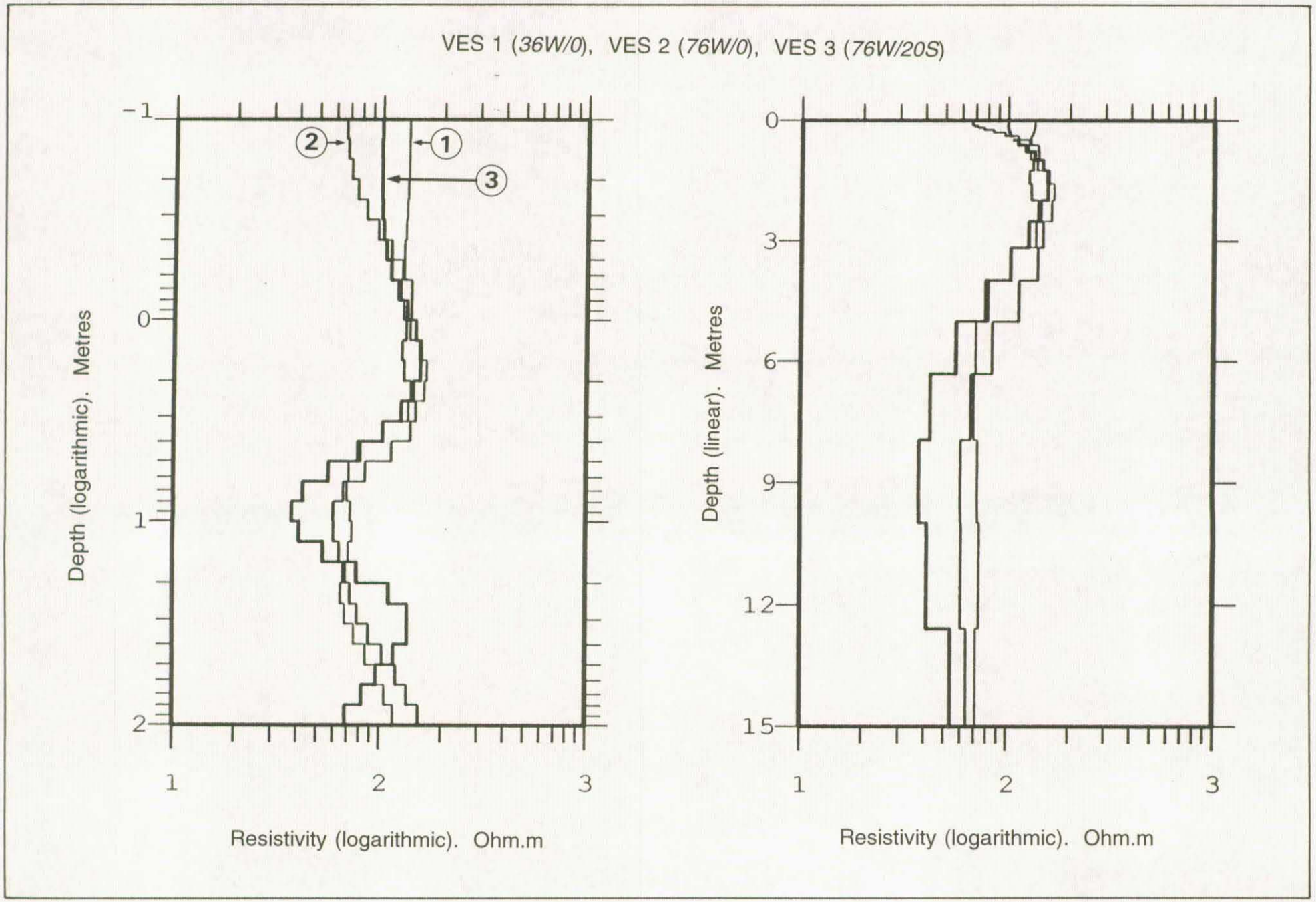

Figure 2 *res.* Test Site 1.1. Interpretation of VES 1, 2, and 3.

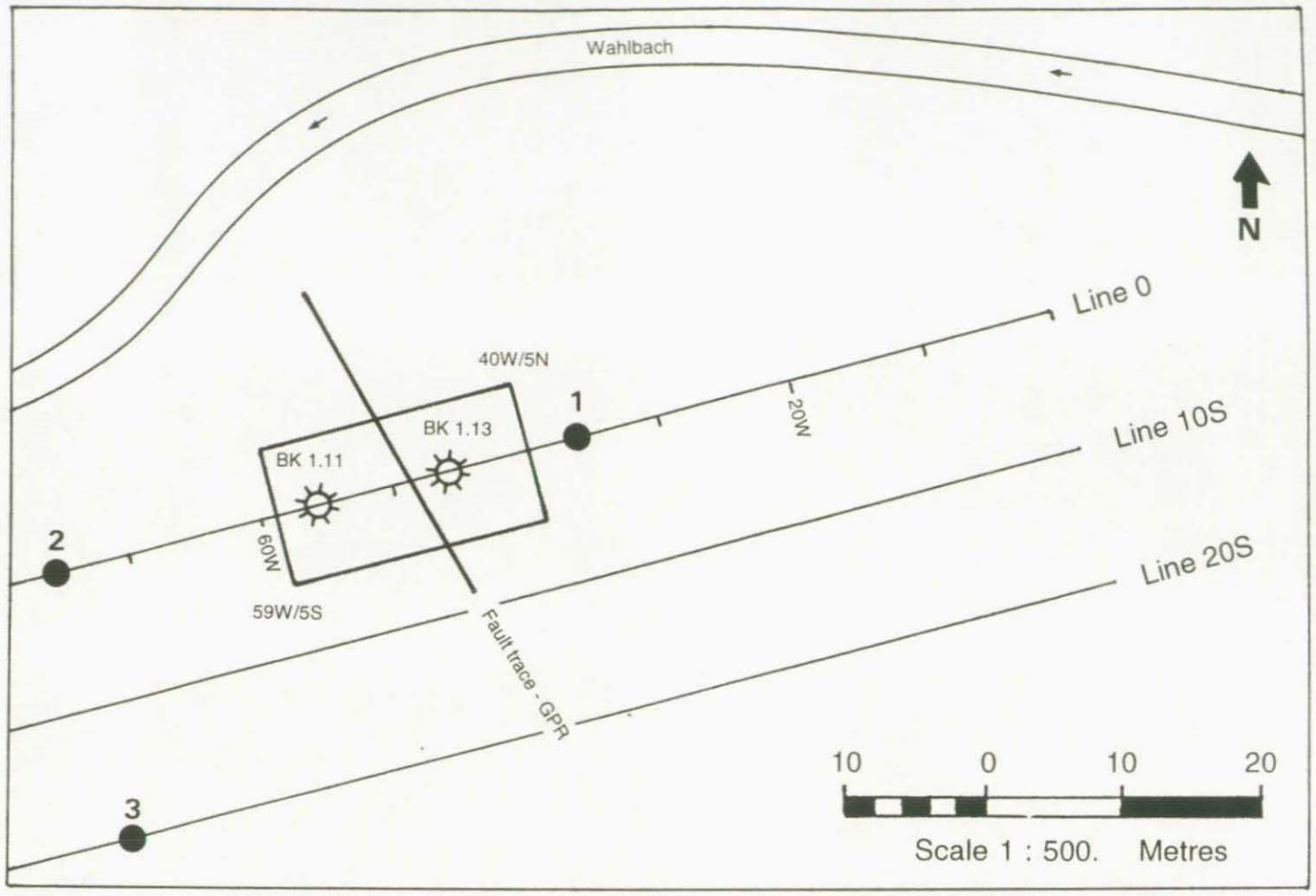

Figure 9 *rsc*. Test Site 1.1. Plan (partial) of site showing location of RESCAN survey grid.

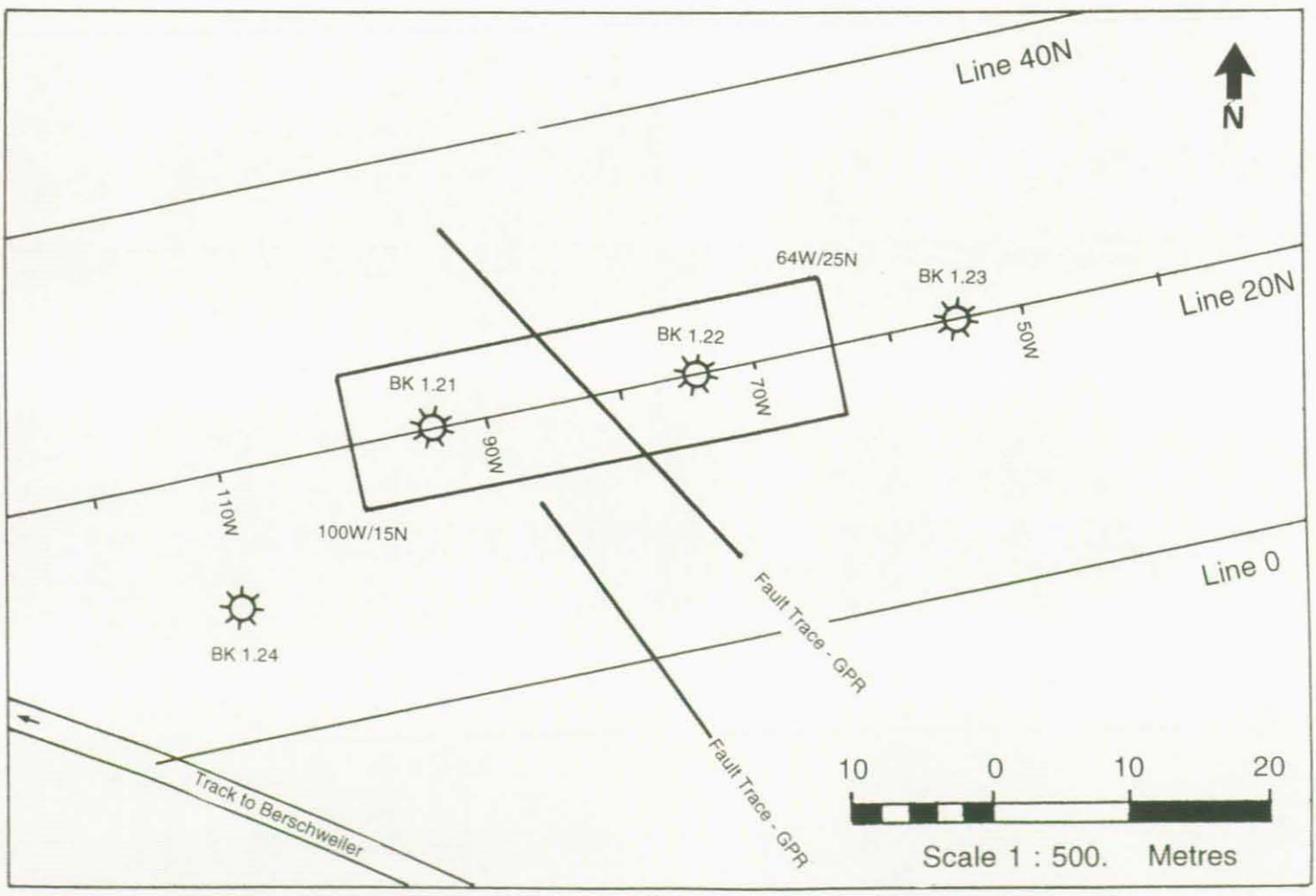

Figure 29 *rsc*. Test Site 1.2. Plan (partial) of site showing location of RESCAN grid.

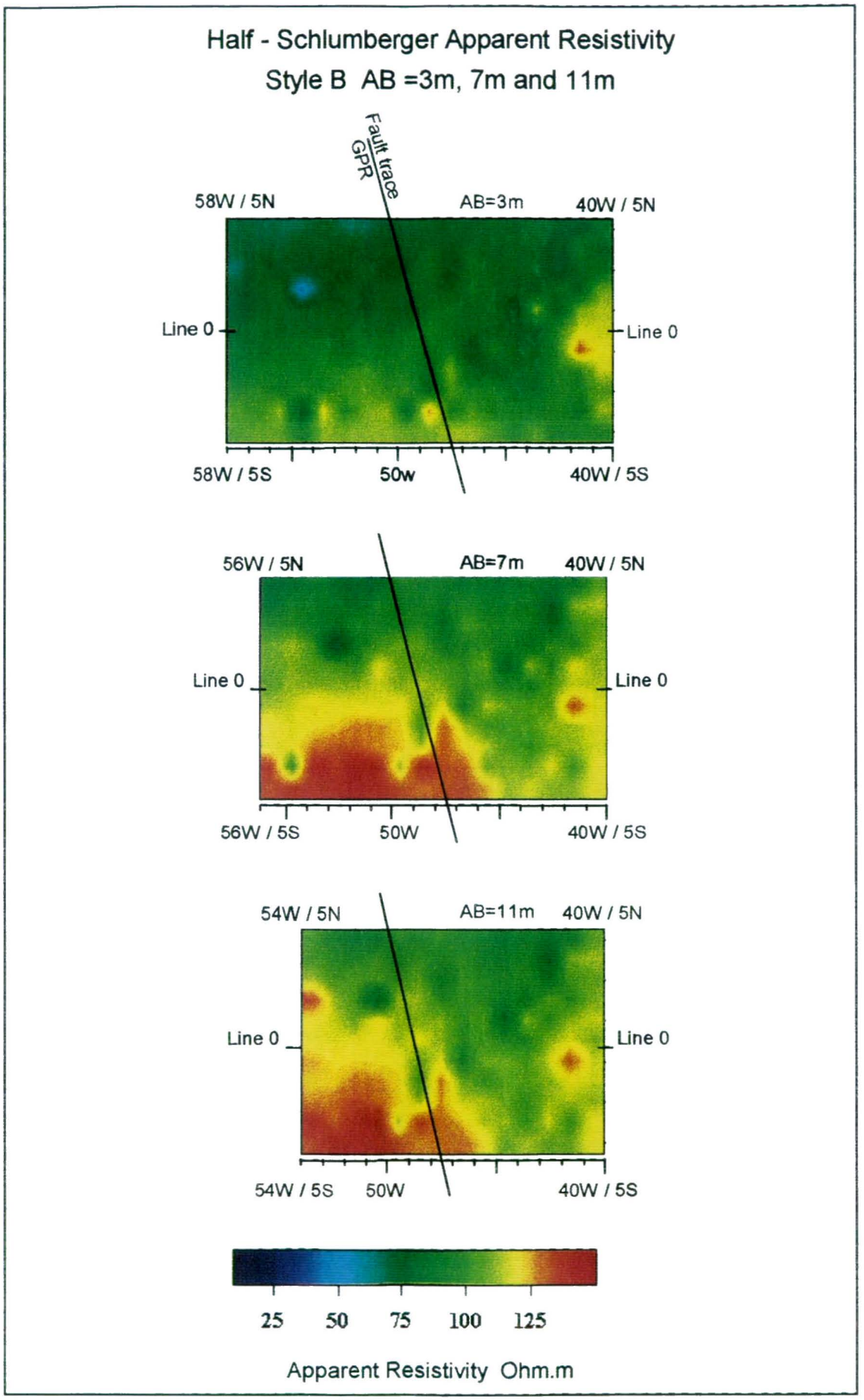

Figure 10 *rsc*. Test Site 1.1. Apparent resistivity data, showing projected position of the fault.

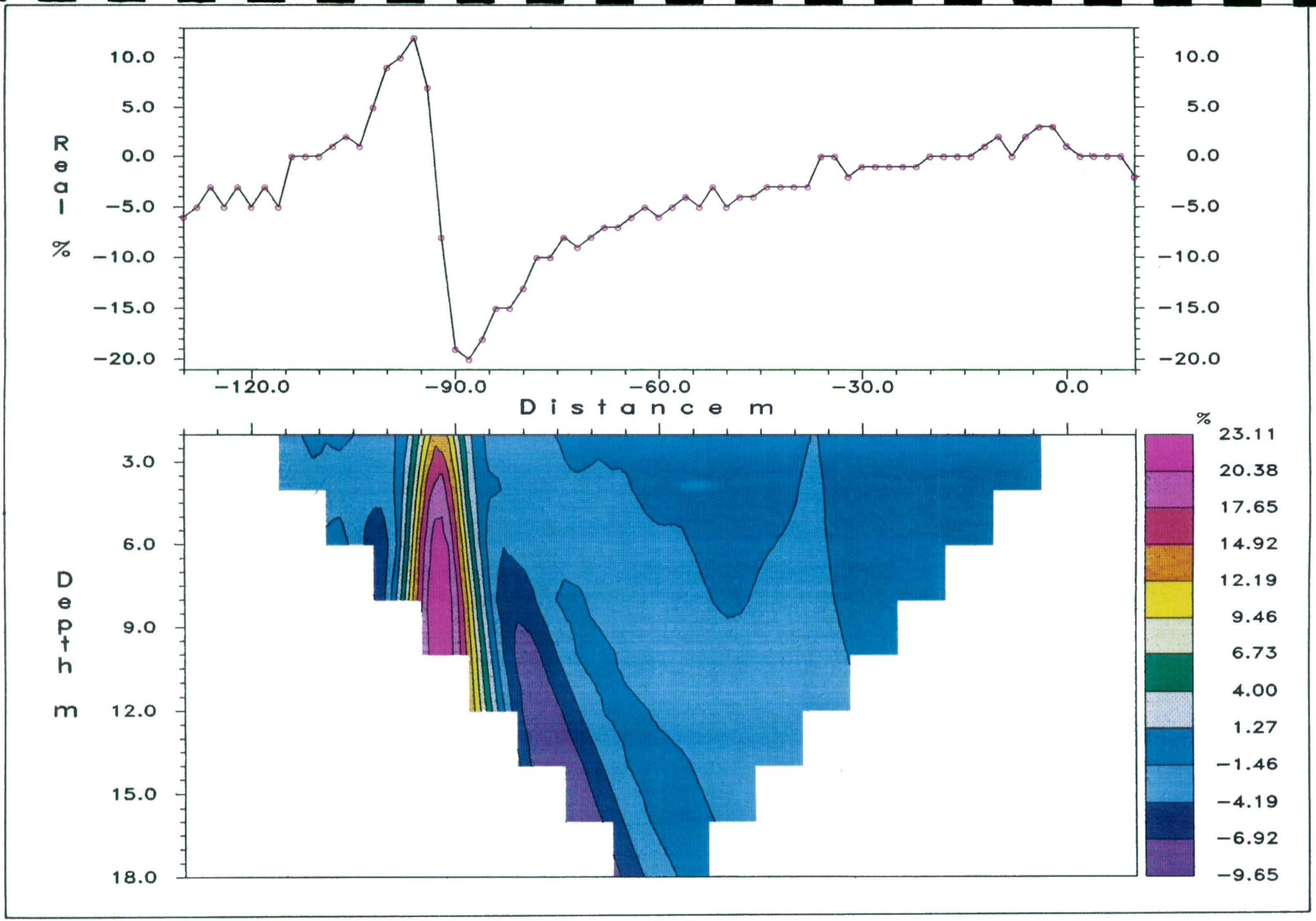

Figure 19 *vlf*. Test Site 1.1. Line 10S. Karous-Hjelt filtering of VLF M-field response over cultural feature.

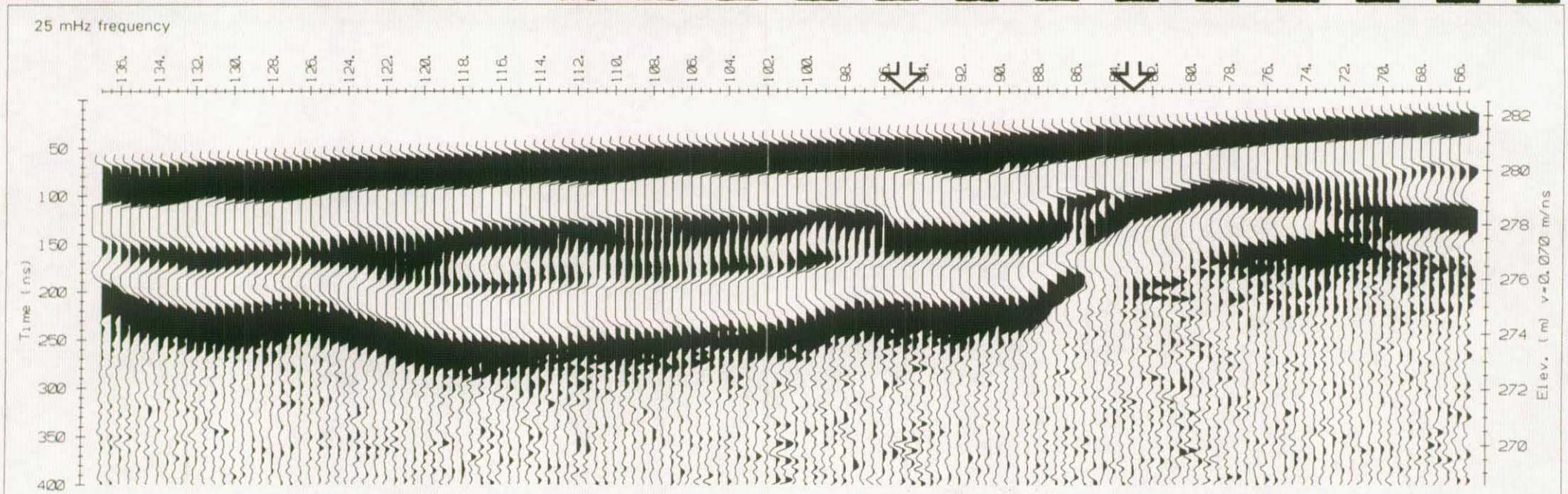

Figure 3 *gpr*. Test Site 1.2. GPR profiles for line 20S. 25 MHz antennae.

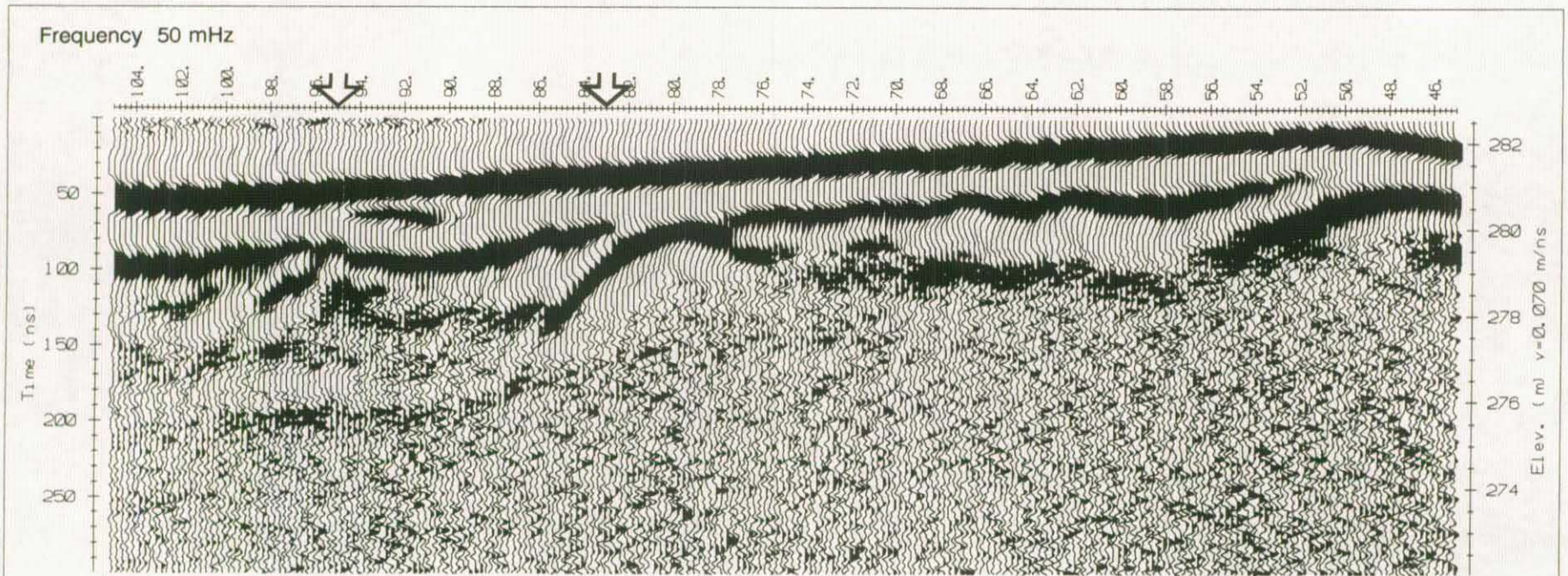

Figure 4 *gpr*. Test Site 1.2. GPR profiles for line 20S. 50 MHz antennae.

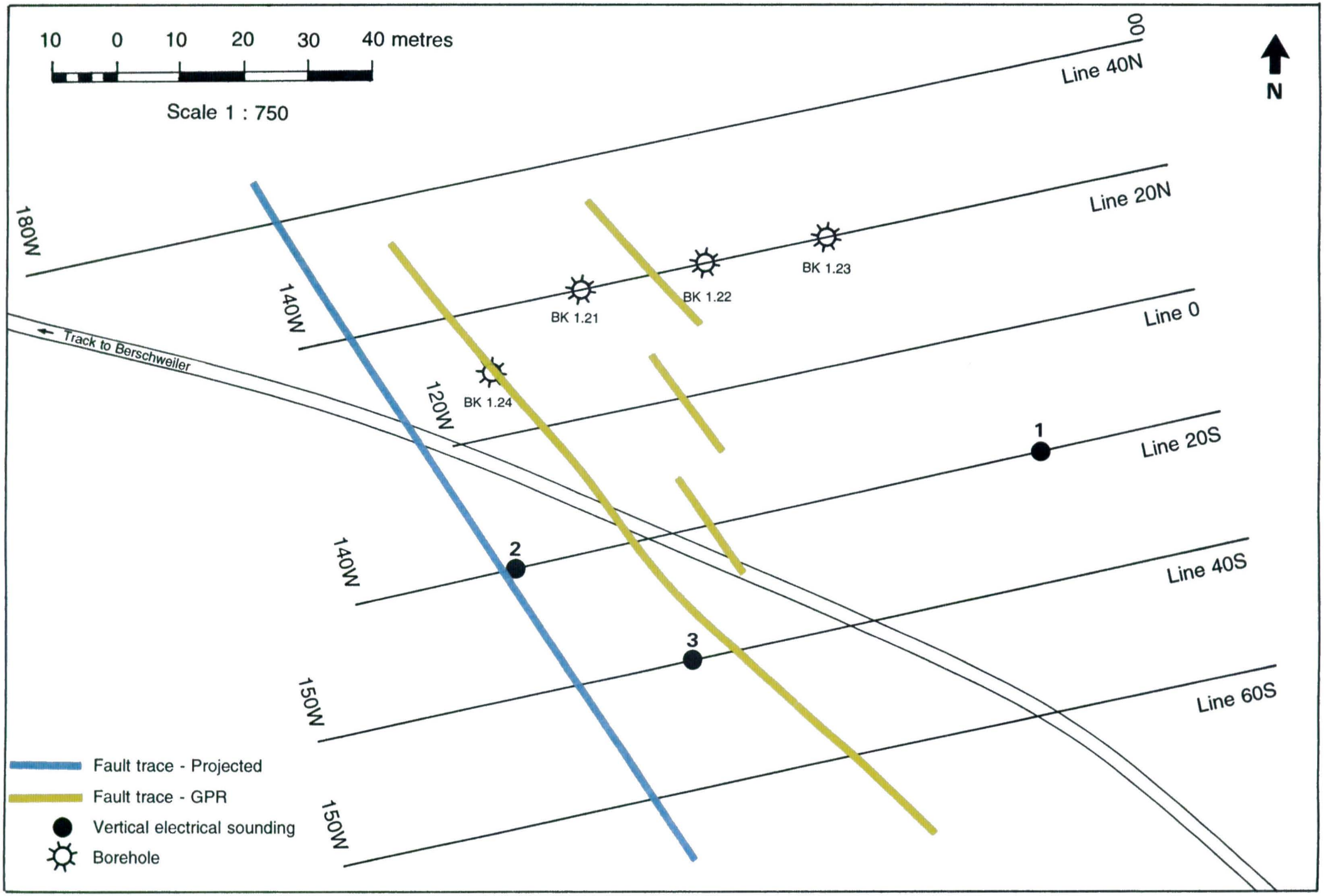

Figure 7. Test Site 1.2. Geophysical grid, borehole locations, and interpretation.

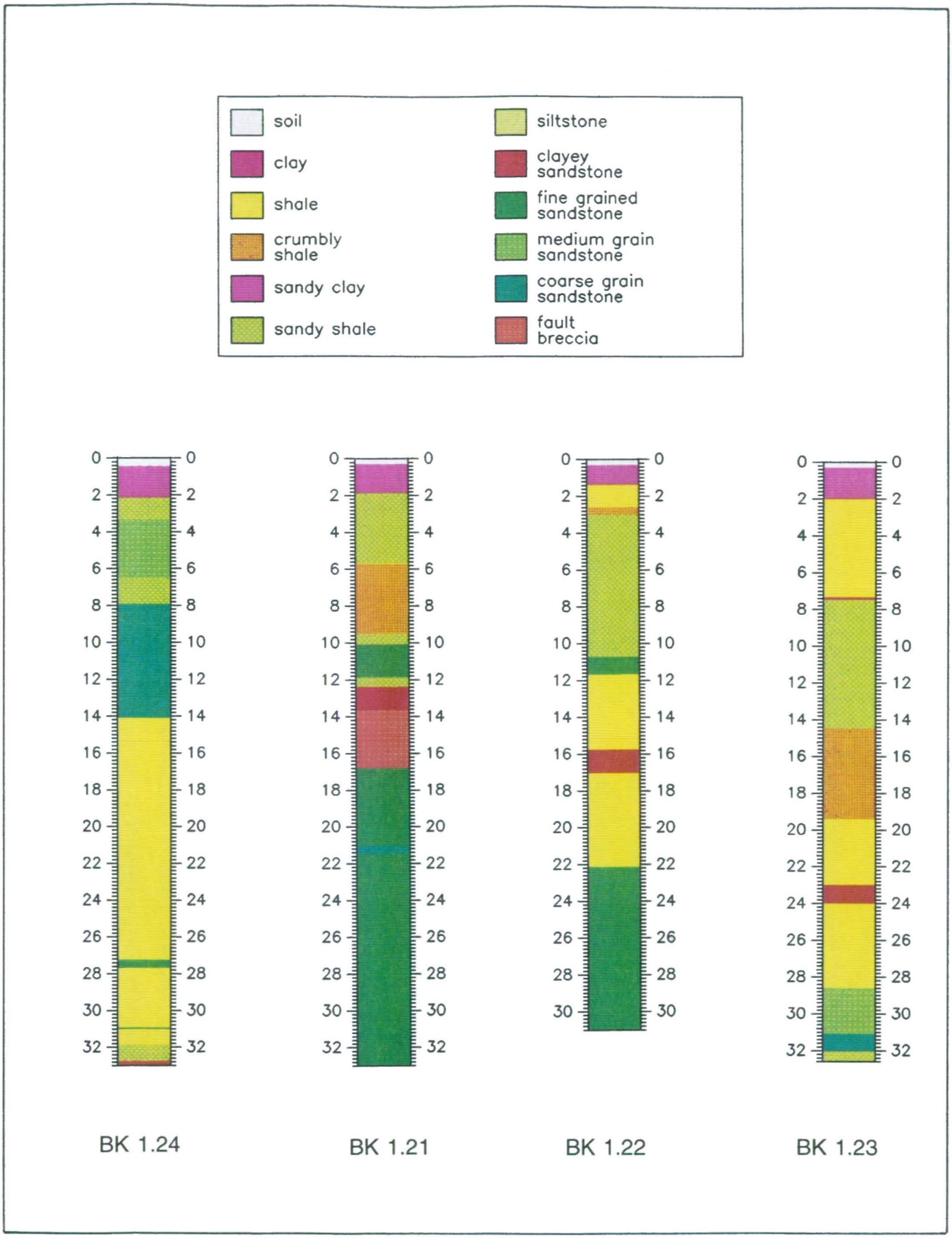

Figure 8. Test Site 1.2. Geological section: boreholes BK1.21, BK1.22, BK1.23 and BK1.24.

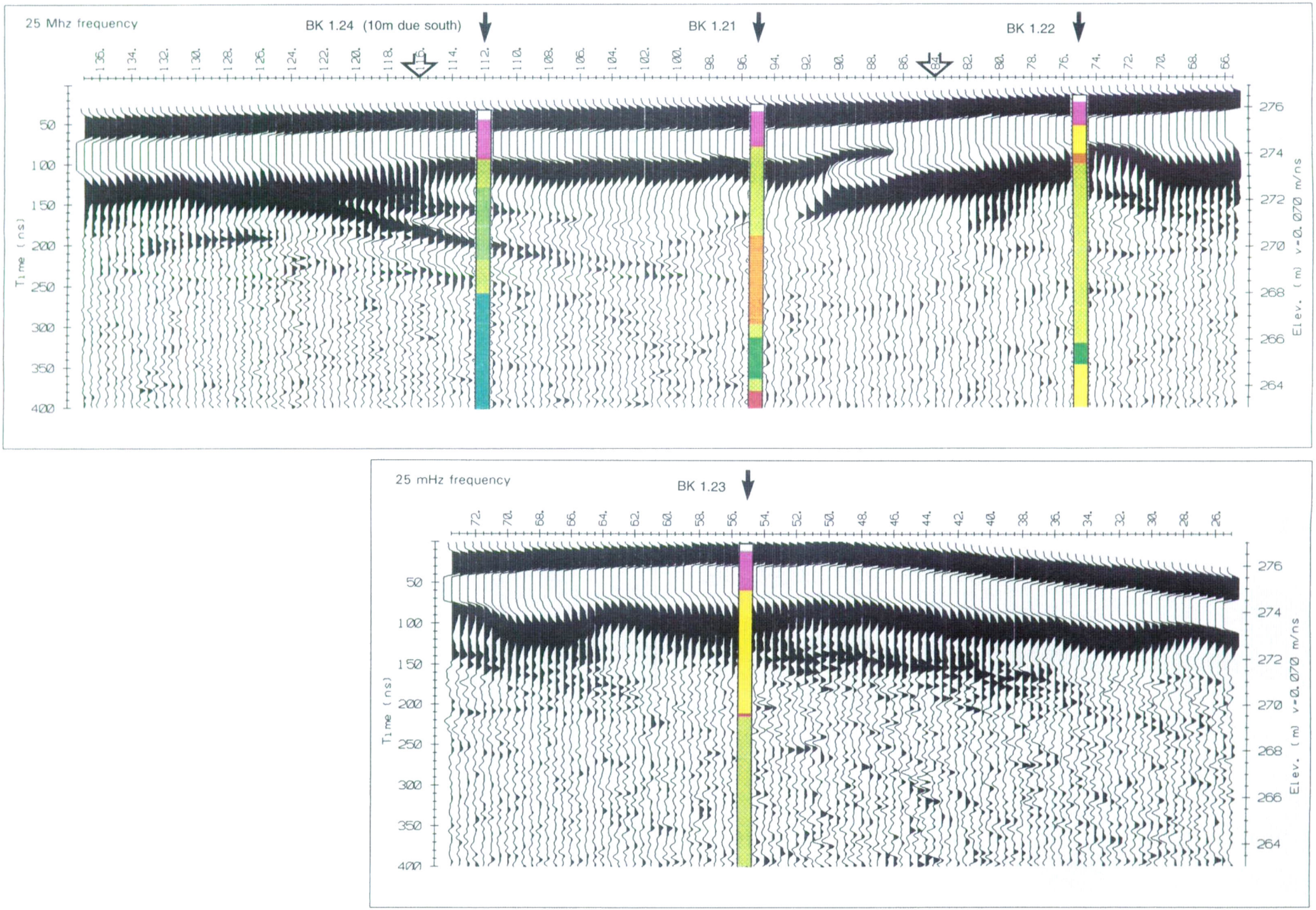

Figure 5 *gpr*. Test Site 1.2. GPR profiles for line 20N. 25 MHz antennae.

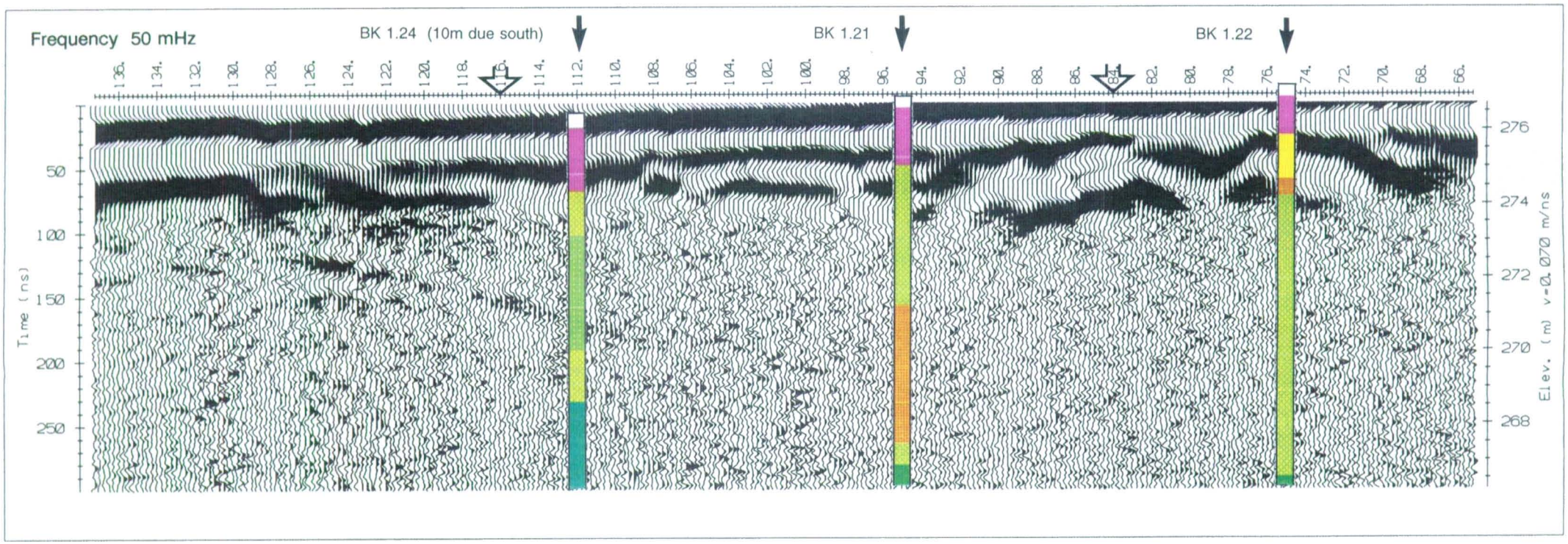

Figure 6 *gpr*. Test Site 1.2. GPR profiles for line 20N. 50 MHz antennae.

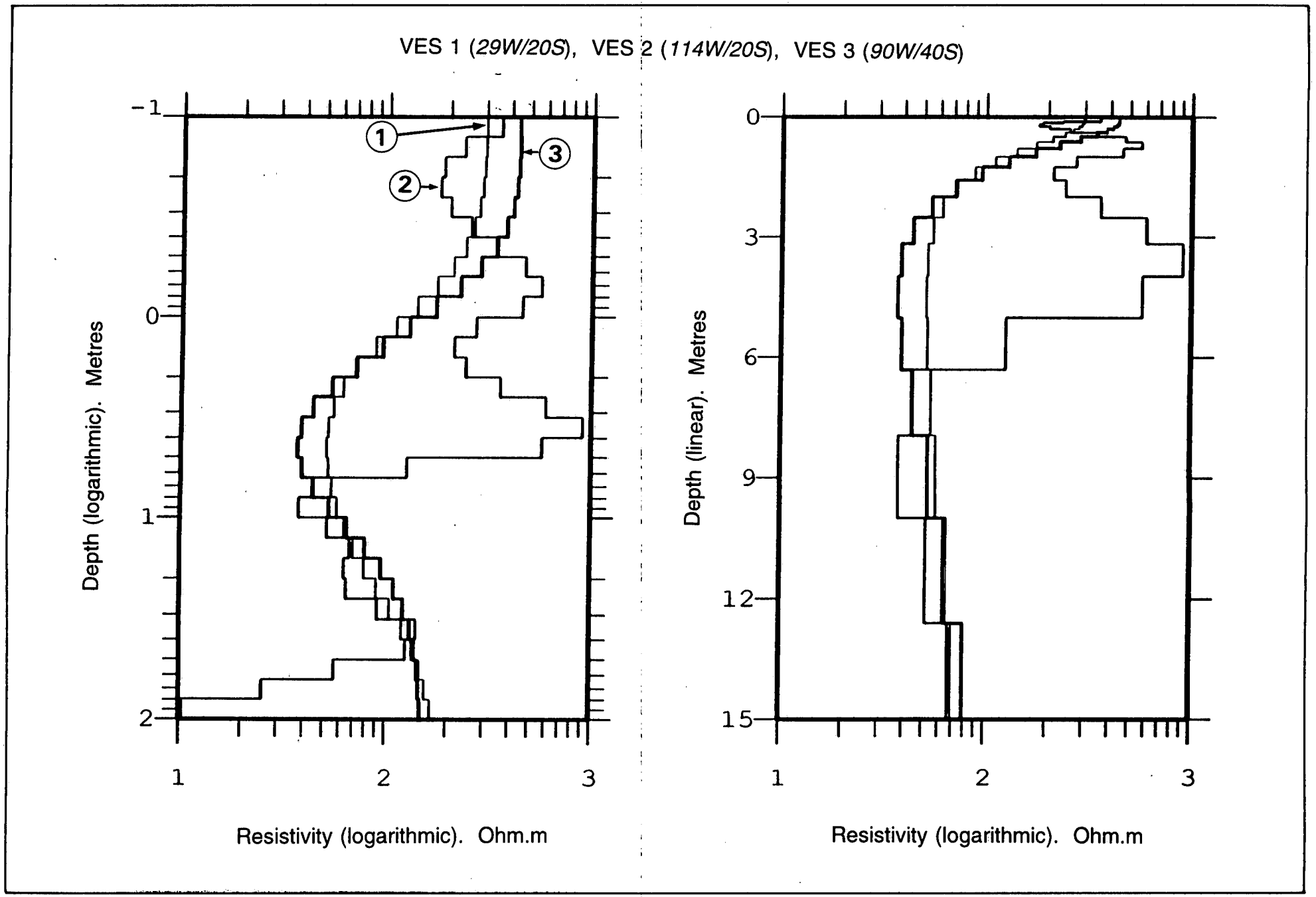

Figure 3 *res.* Test Site 1.2. Interpretation of VES 1, 2, and 3.

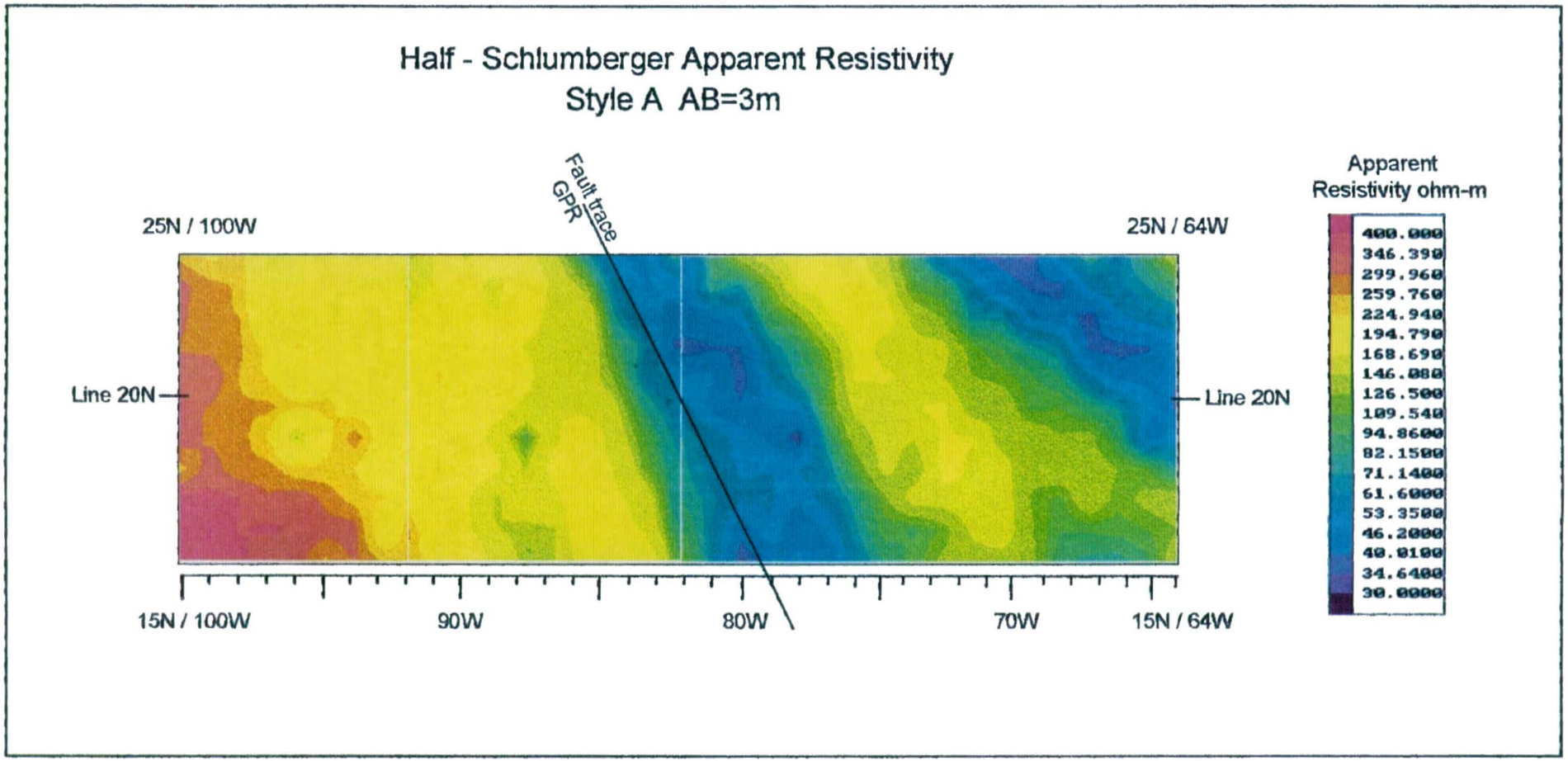

Figure 7 *rsc*. Test Site 1.2. RESCAN apparent resistivity maps for three overlapping sections.

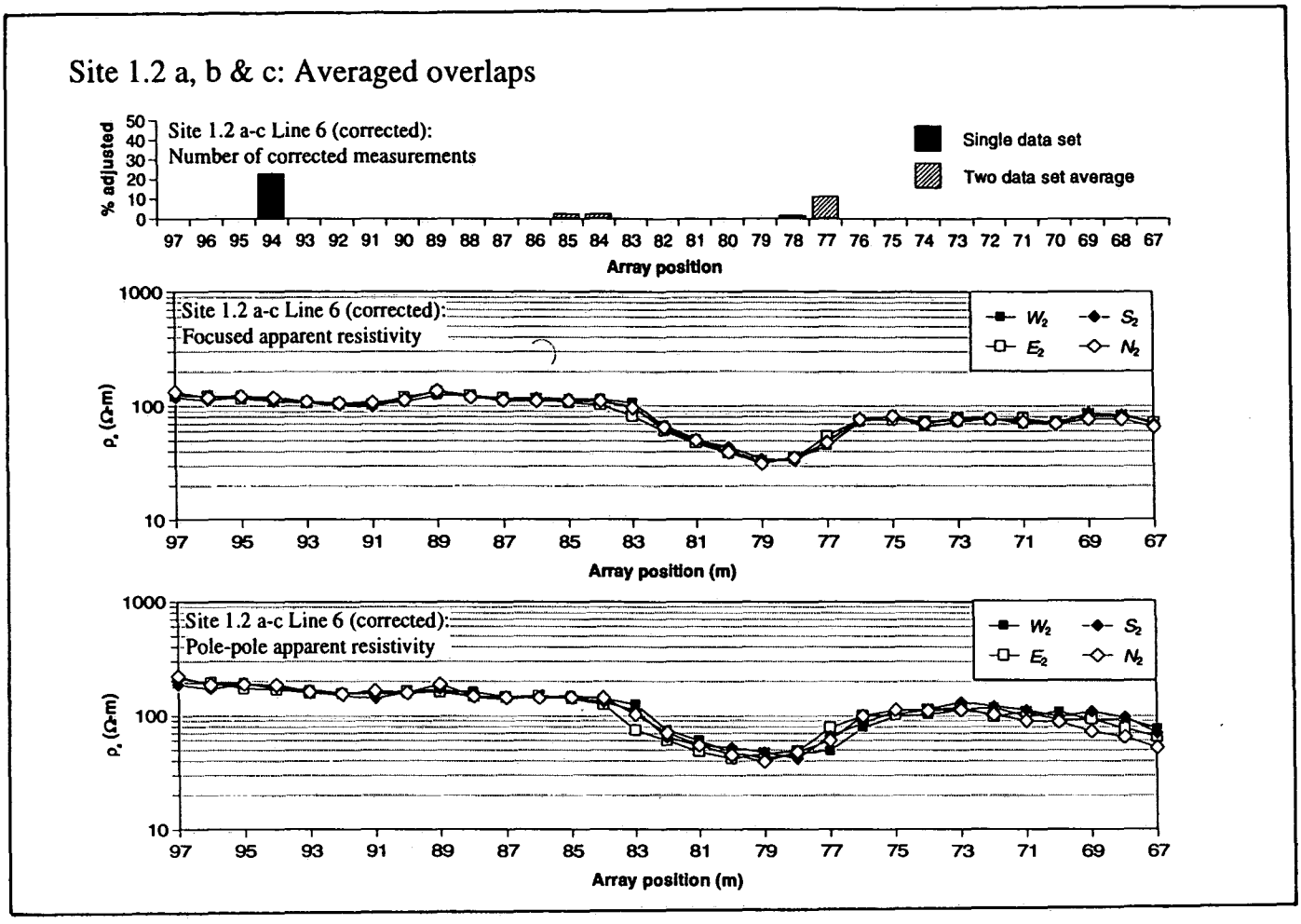

Figure 27 *rsc*. Test Site 1.2. Grids a, b, and c. Apparent resistivity traverse.

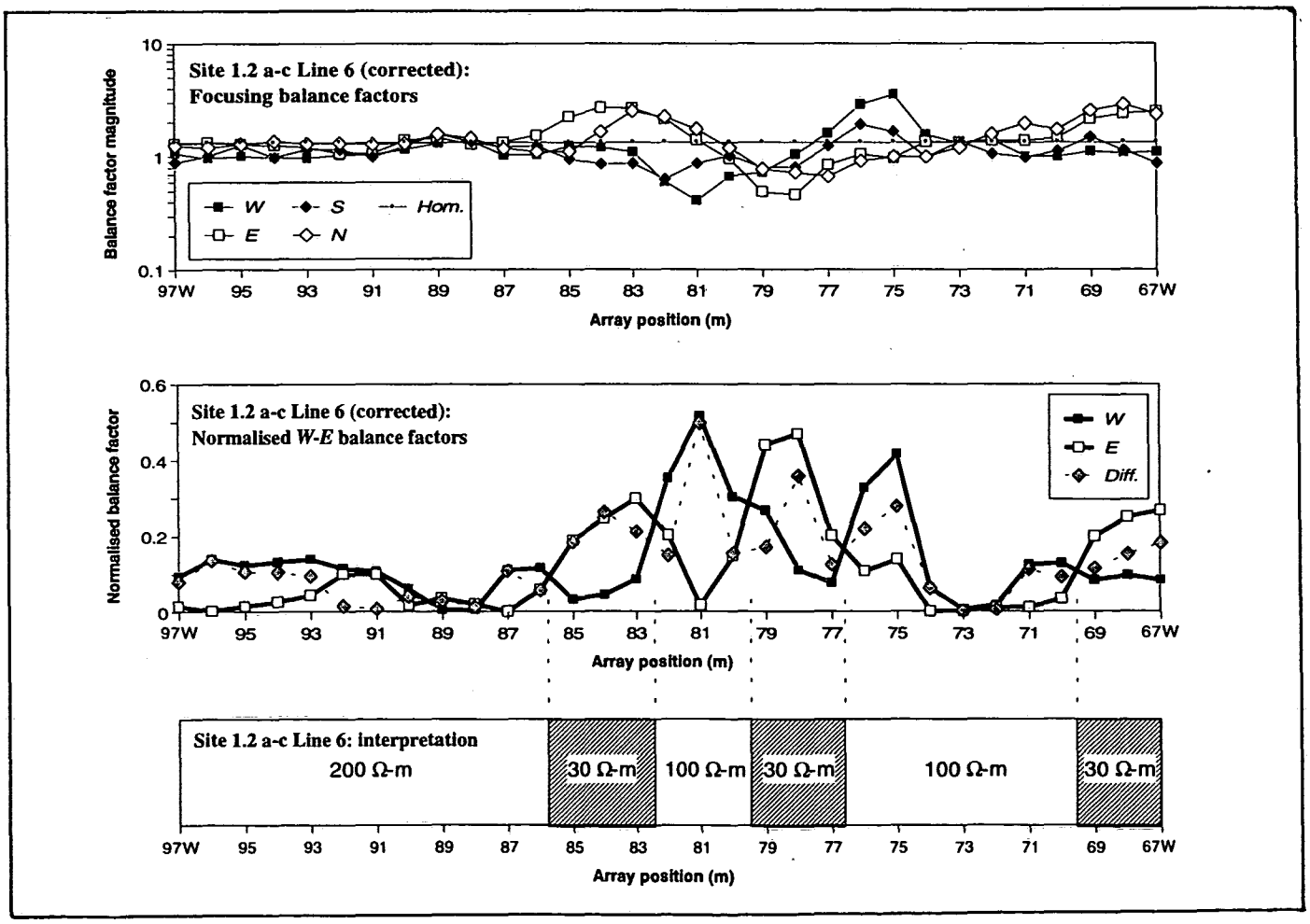

Figure 28 *rsc*. Test Site 1.2. Grids a, b, and c. Focussing balance factors.

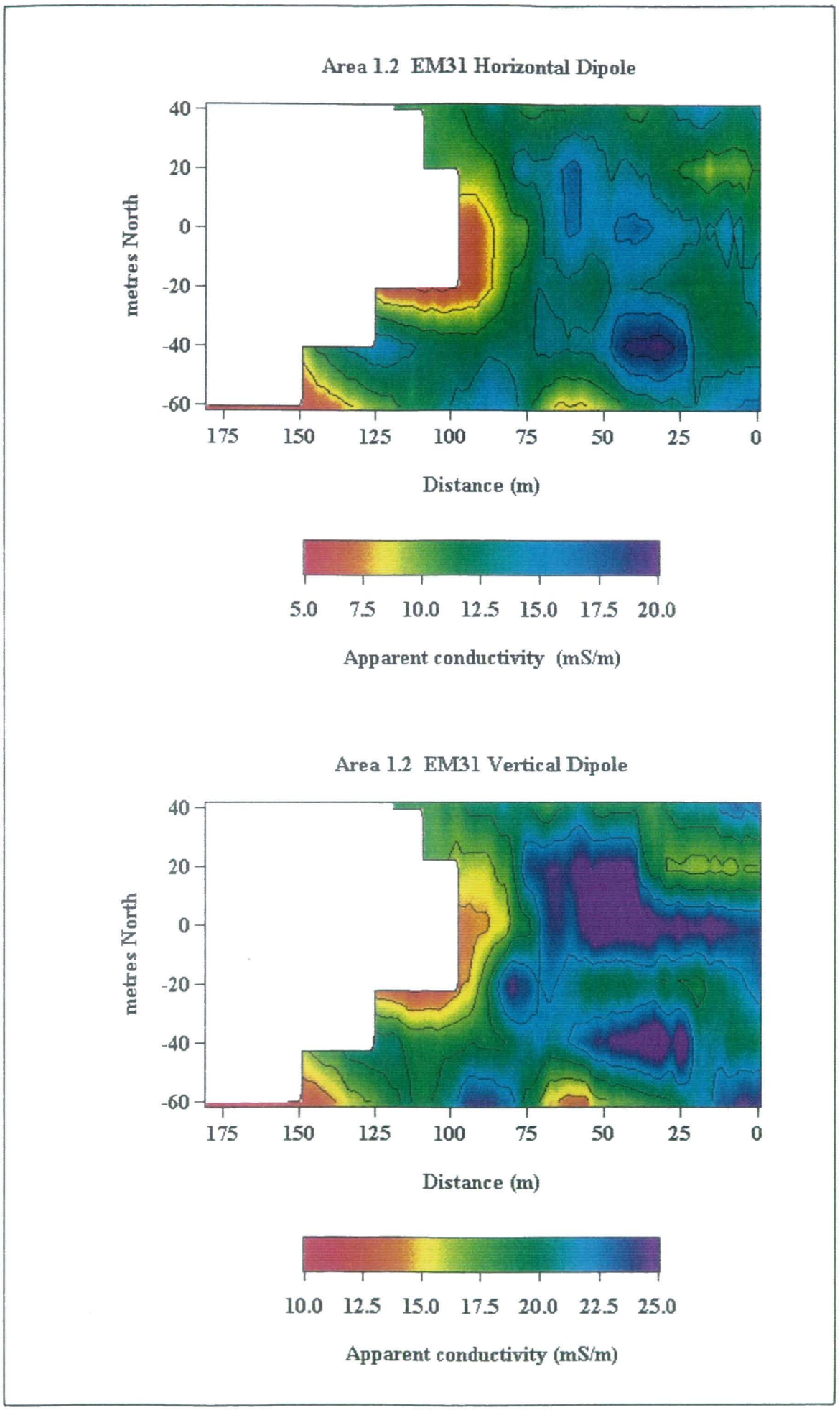

Figure 1 *em*. Test Site 1.2. Horizontal and vertical dipole conductivity contours.

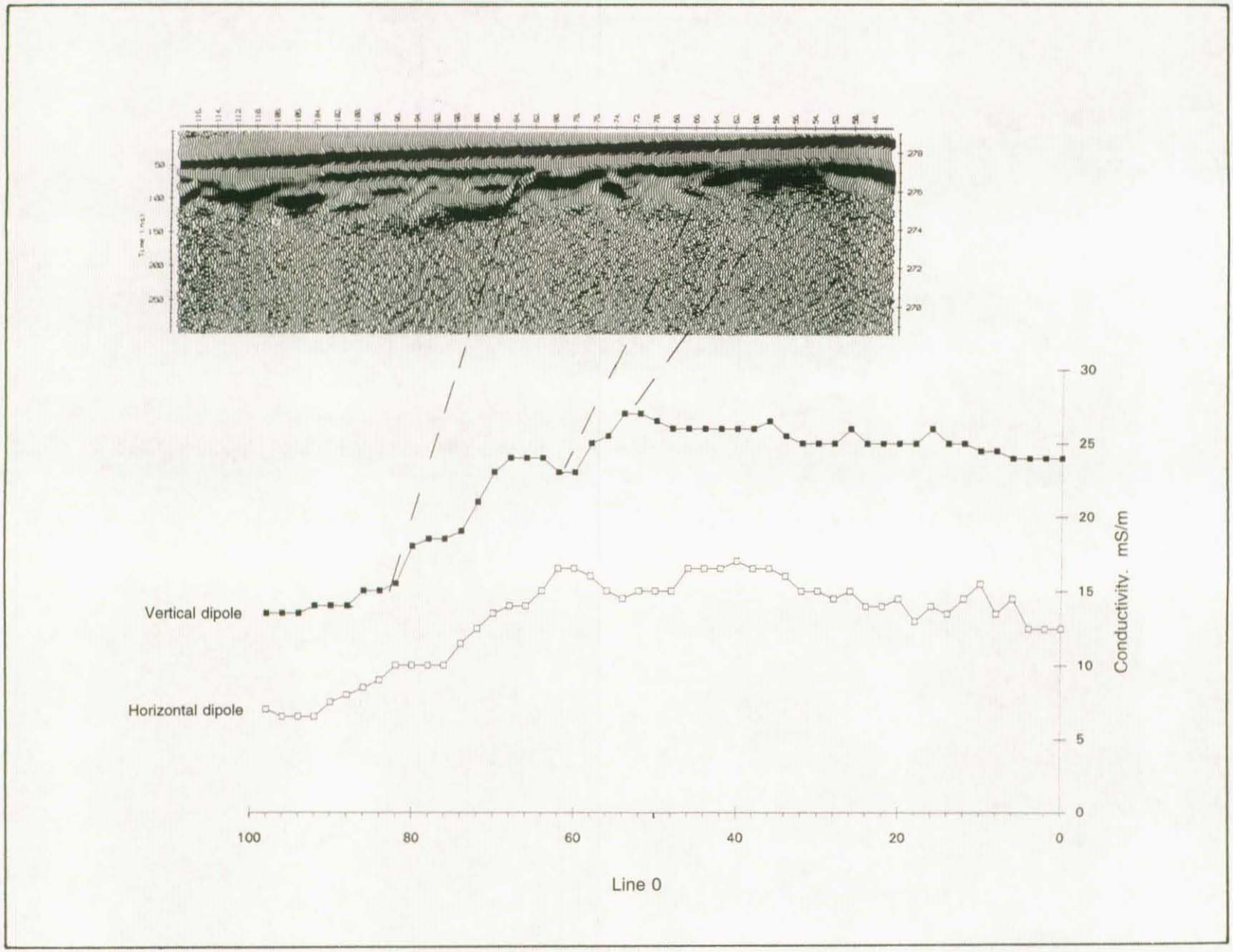

Figure 2 *em*. Test site 1.2. Composite horizontal and vertical dipole conductivity and GPR section for line 0.

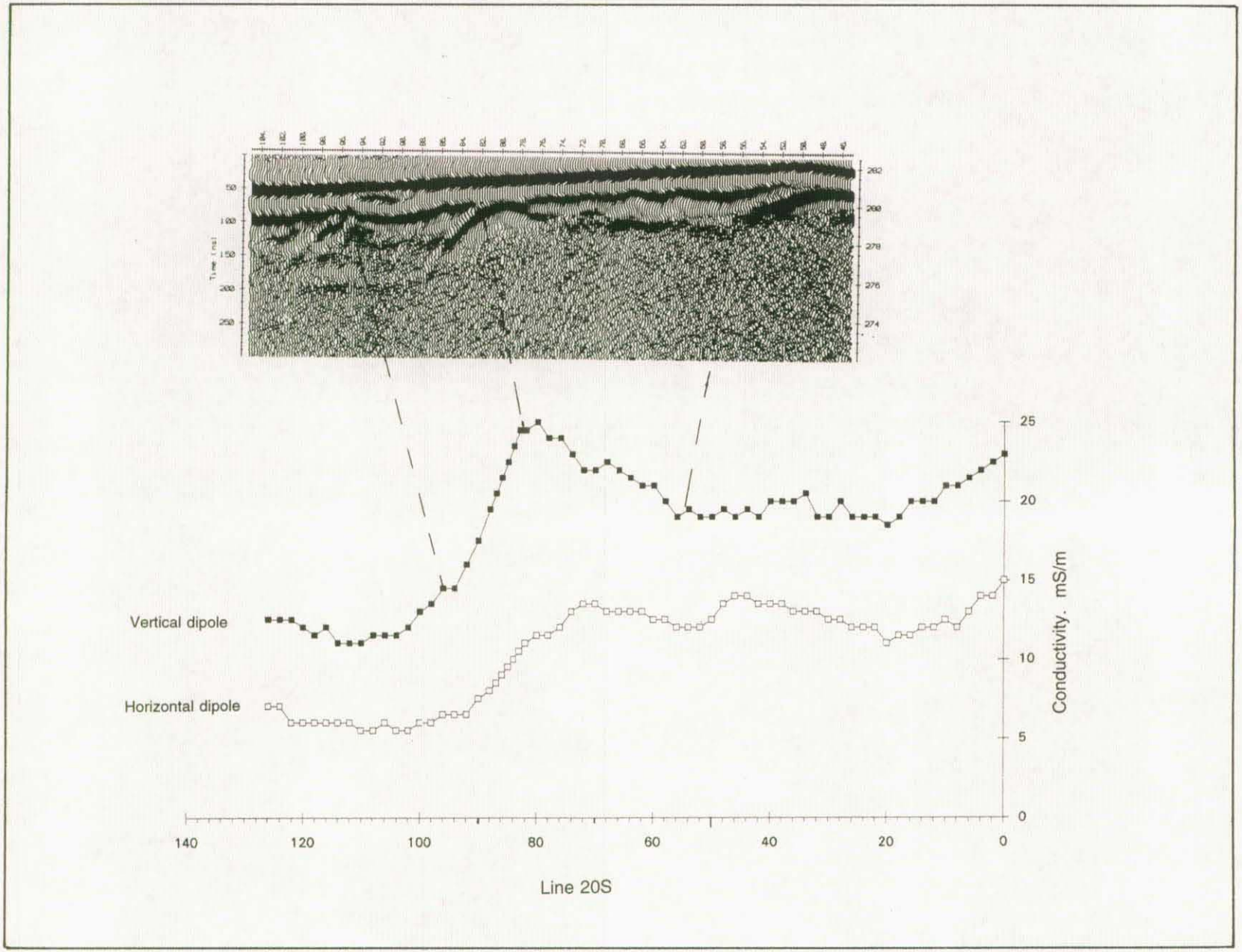

Figure 3 *em*. Test Site 1.2. Composite horizontal and vertical dipole conductivity and GPR section for line 20S.

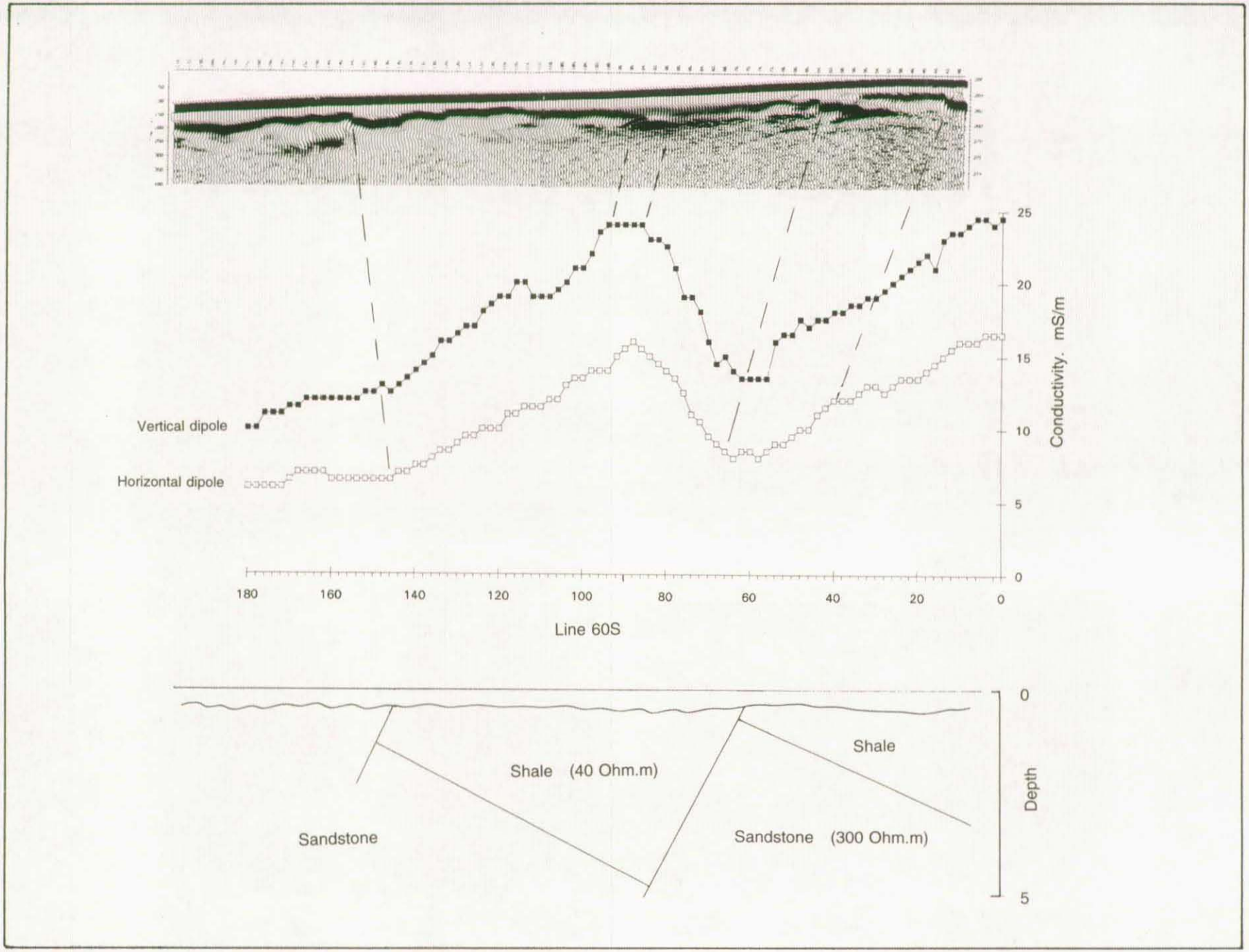

Figure 4 *em*. Test Site 1.2. Composite horizontal and vertical dipole conductivity and GPR section for line 60S and possible geological section.

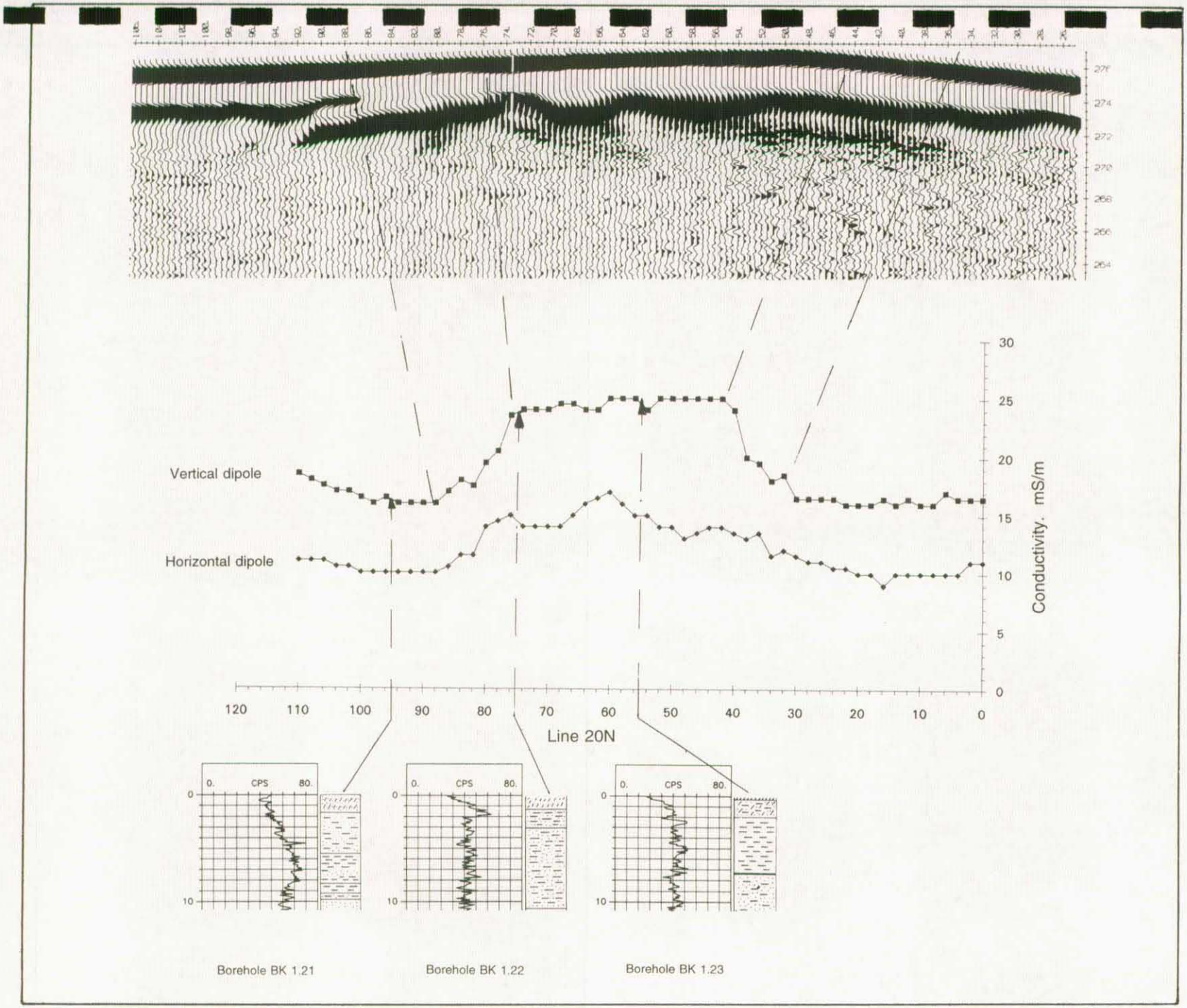

Figure 5 *em*. Test Site 1.2. Composite horizontal and vertical dipole conductivity and GPR section for line 20N and proven geology.

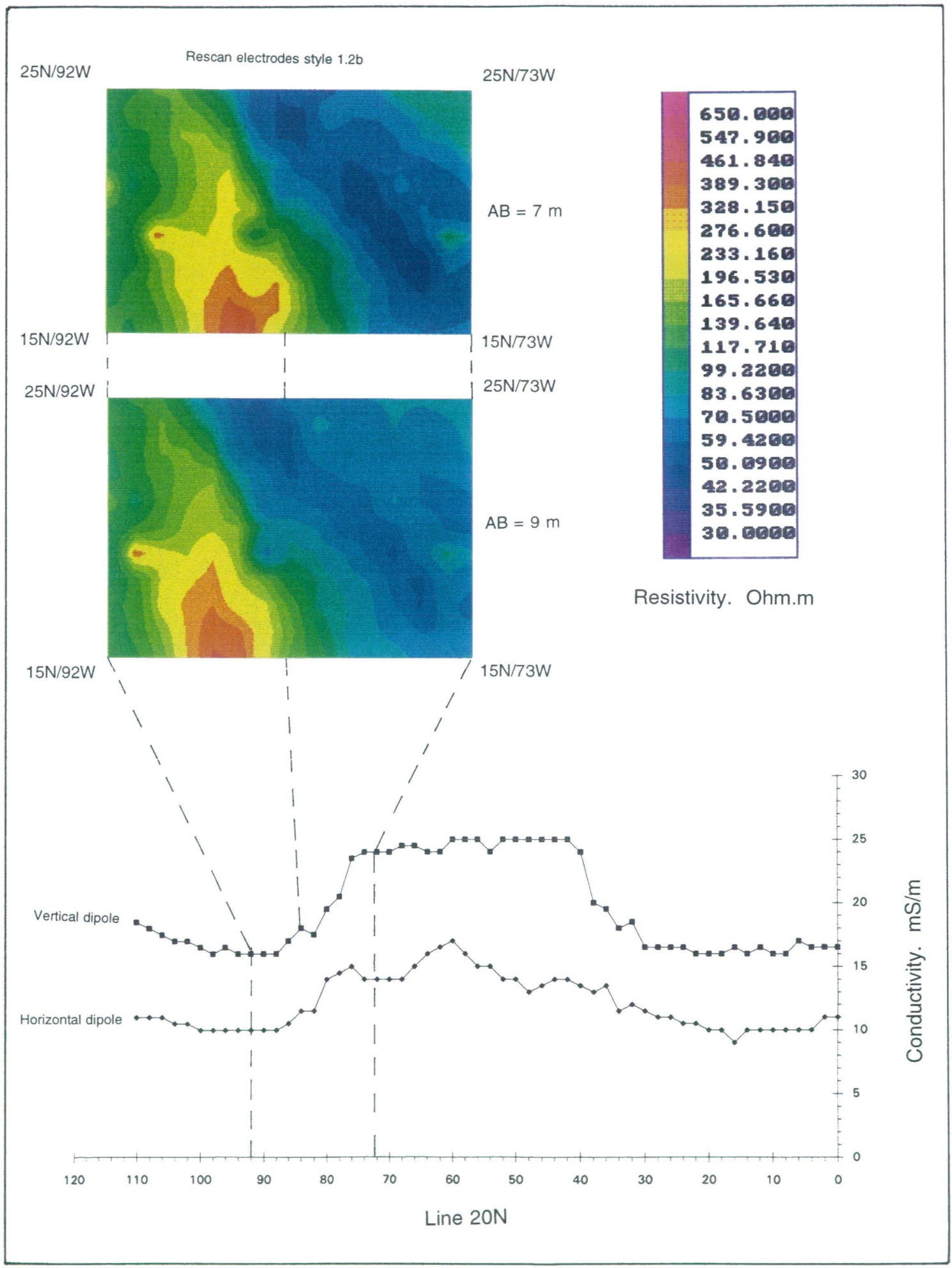

Figure 6 *em*. Test Site 1.2. Composite of conductivity profiles and Rescan images of part of line 20N.

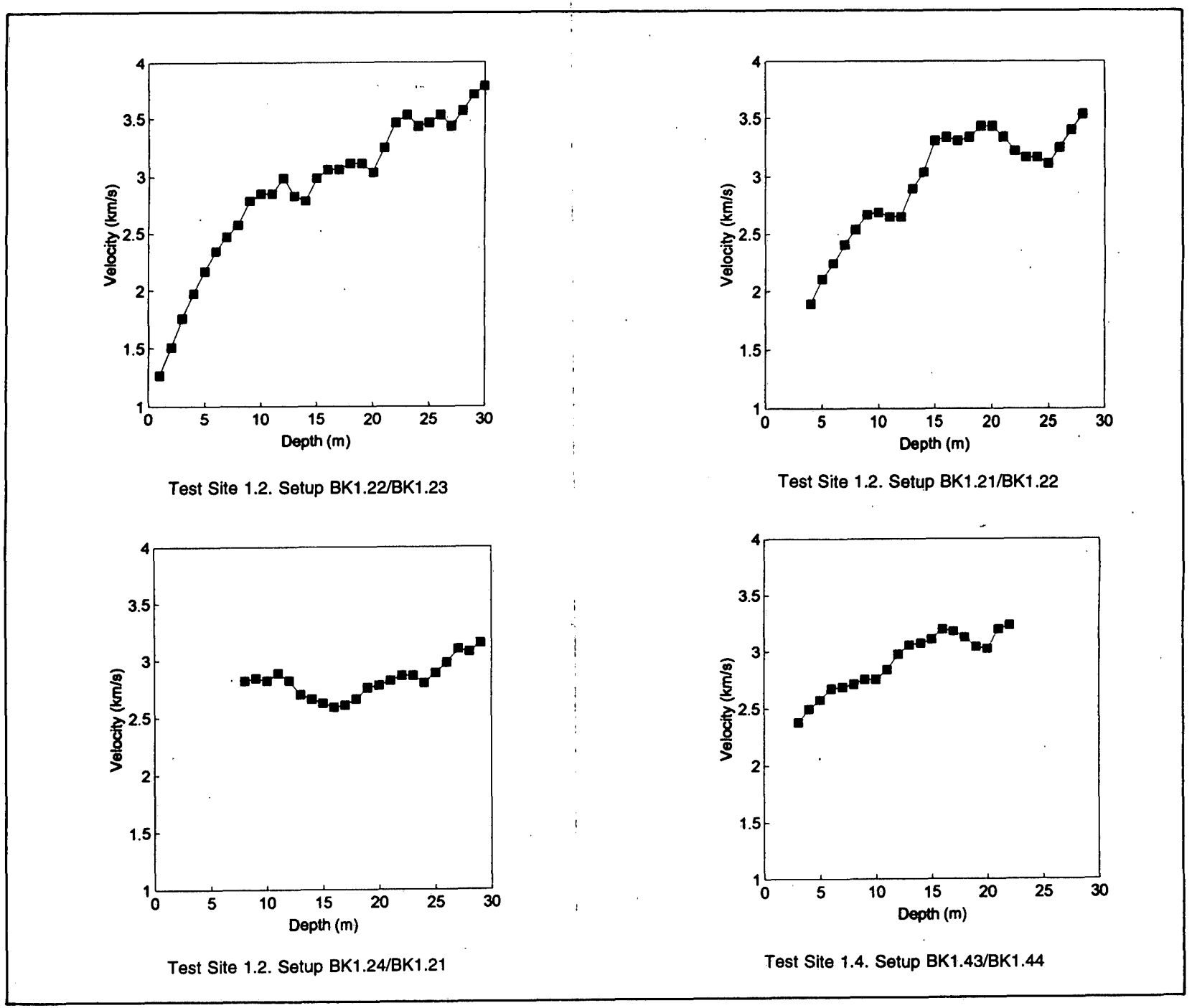

Figure 1 *sei.* Test Sites 1.2 and 1.4. Plots of horizontal velocity versus depth.

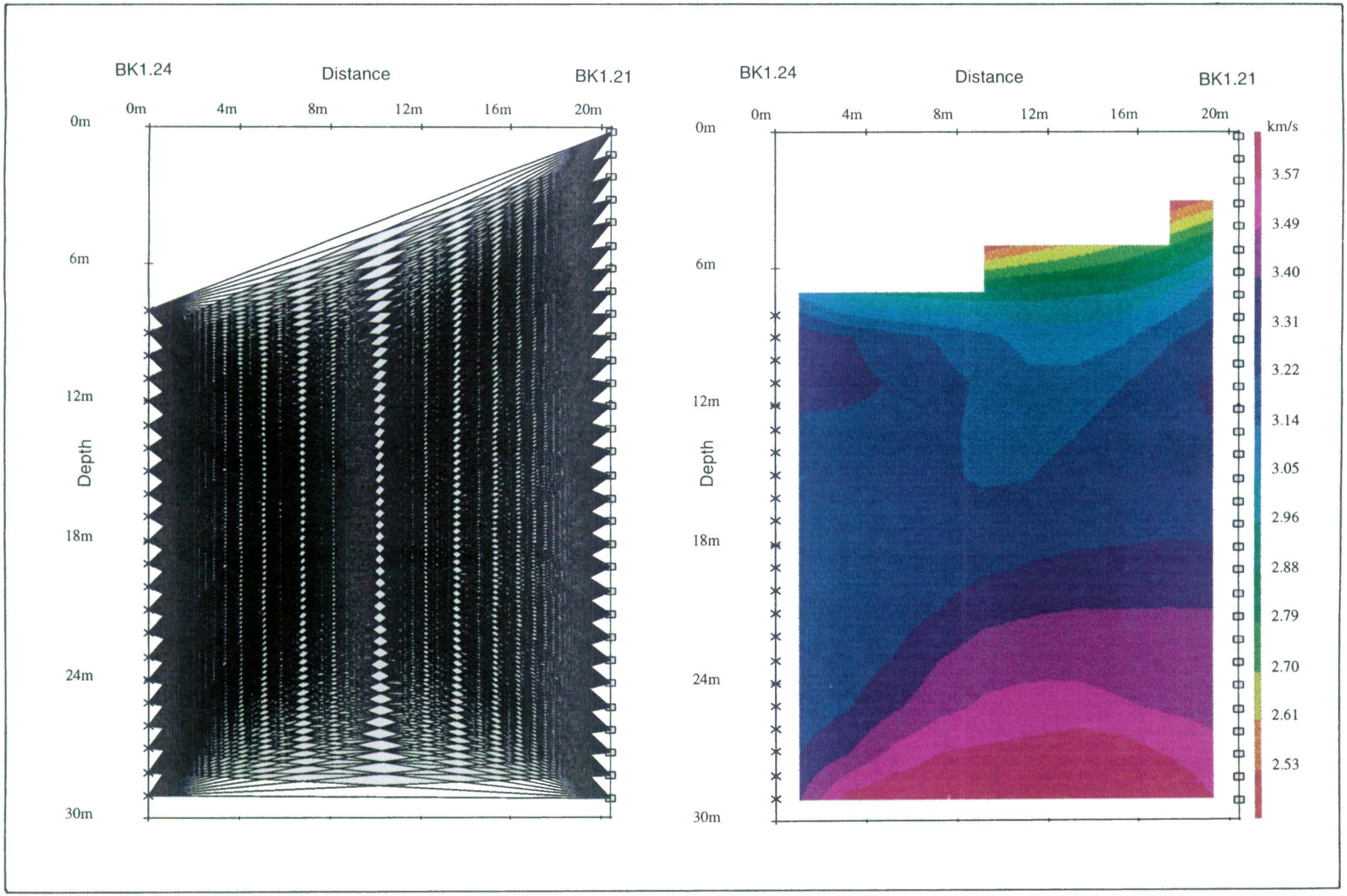

Figure 2a, 2b *sei.* Test Site 1.2. Setup BK1.24/1.21. Hydrophone data. (a) Raypath coverage. (b) Straight ray, 10% anistropy correction.

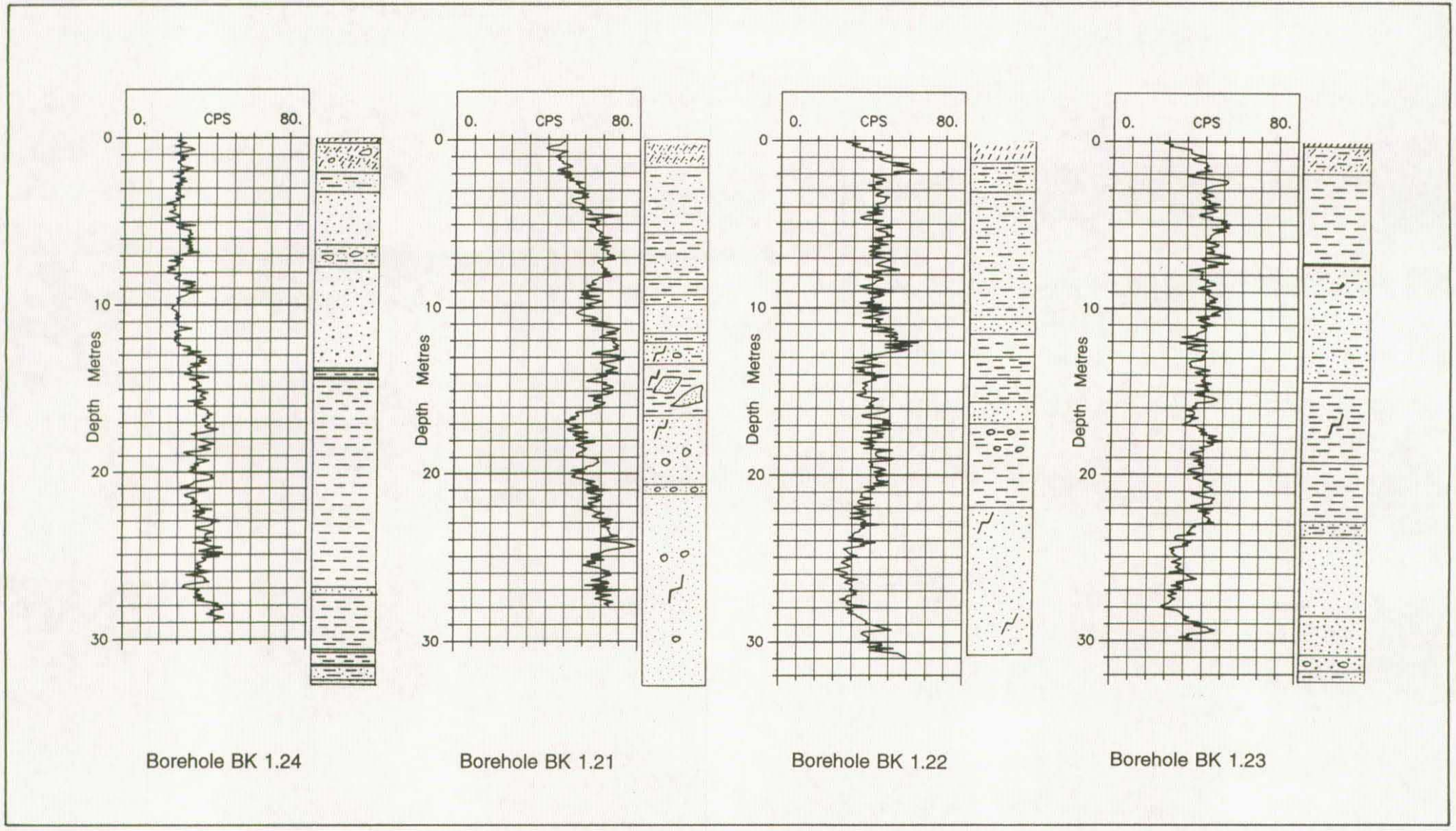

Figure 1 *gam*. Test Site 1.2. Natural gamma logs for boreholes BK1.21 to BK1.24.

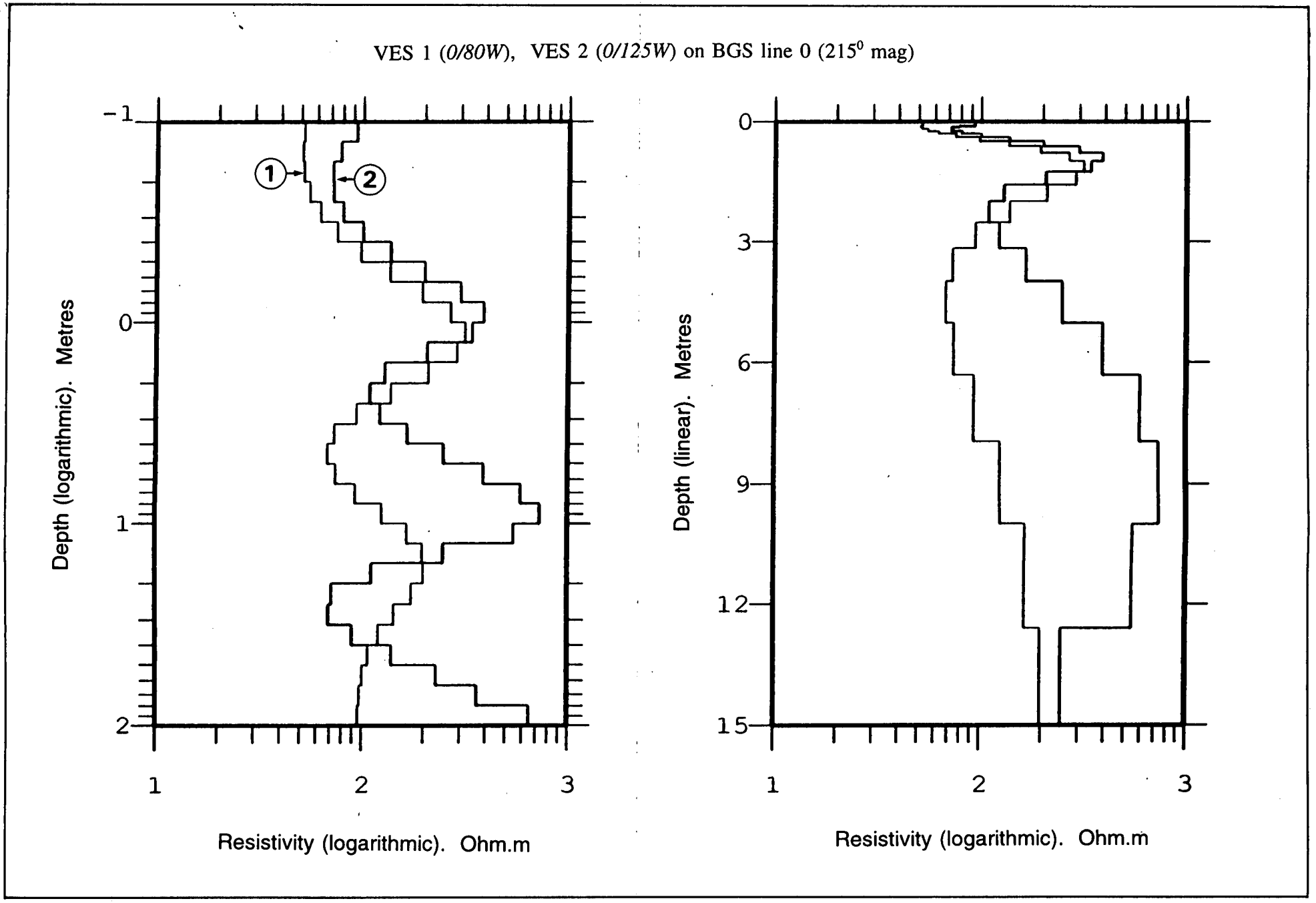

Figure 4 *res.* Test Site 1.3. Interpretation of VES 1, and 2.

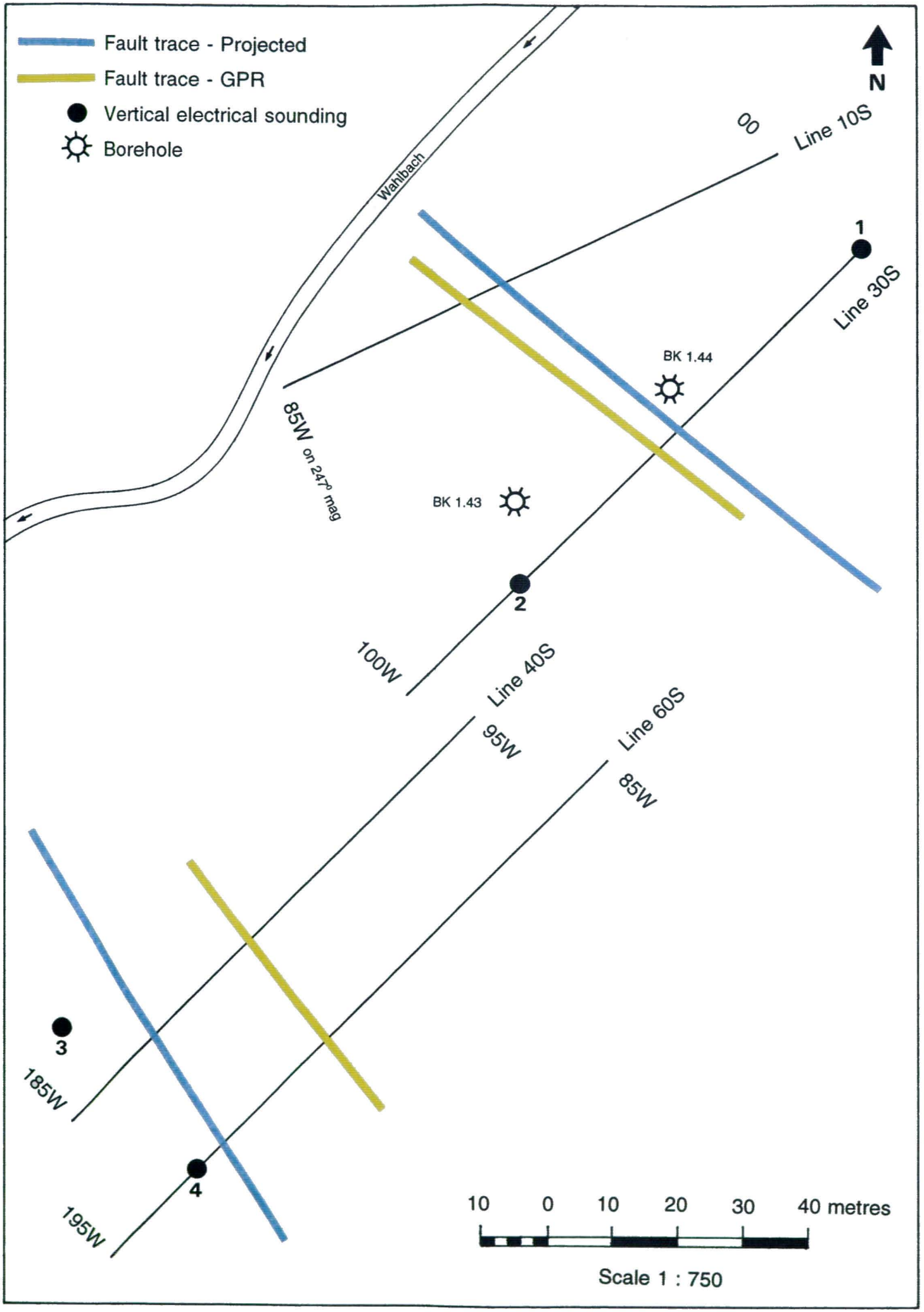

Figure 9. Test Site 1.4. Geophysical grid, borehole locations, and interpretation.

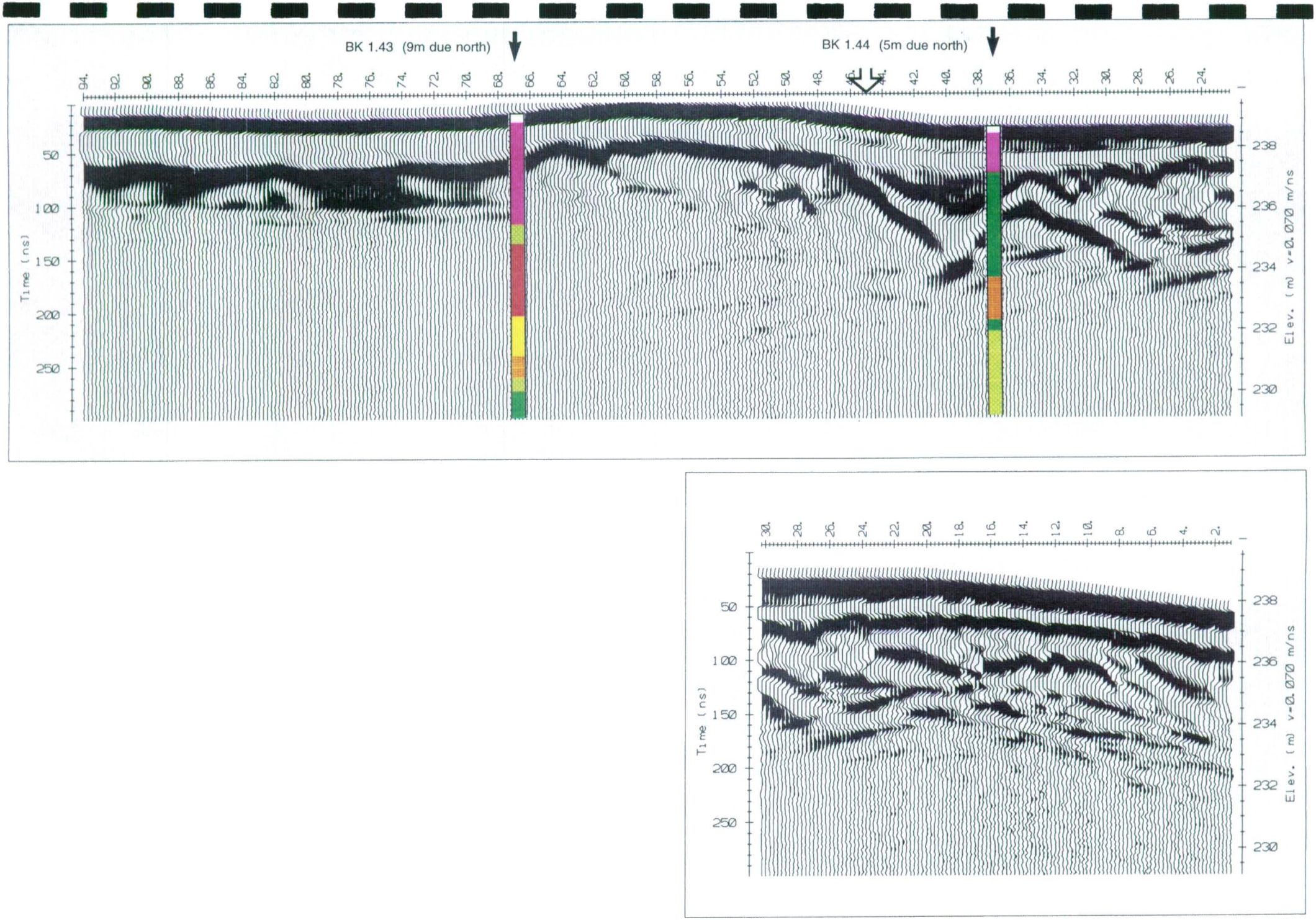

Figure 7 *gpr*. Test Site 1.4. GPR profile for line 30S. 50 MHz antennae.

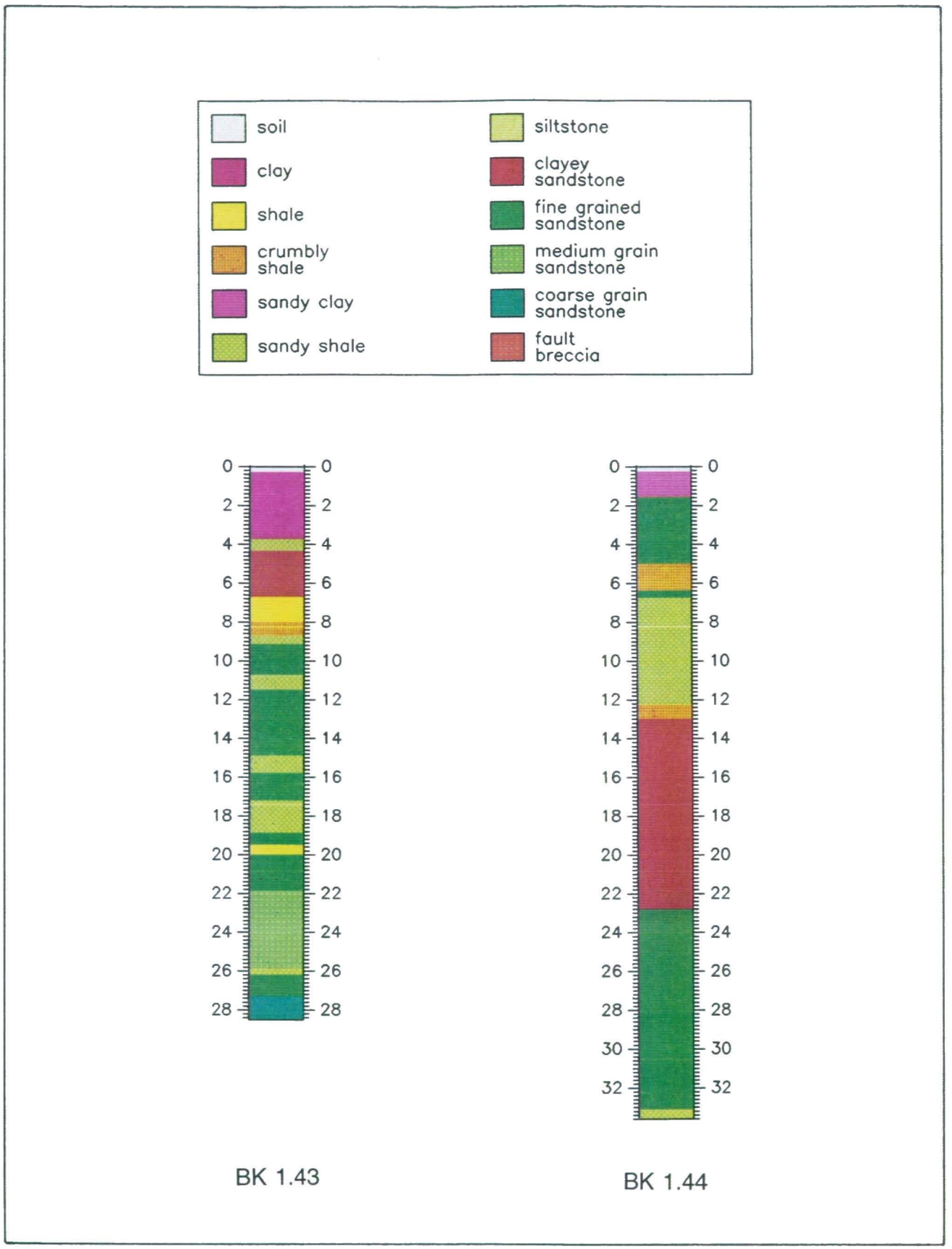

Figure 10. Test Site 1.4. Geological section: boreholes BK1.43, BK1.44

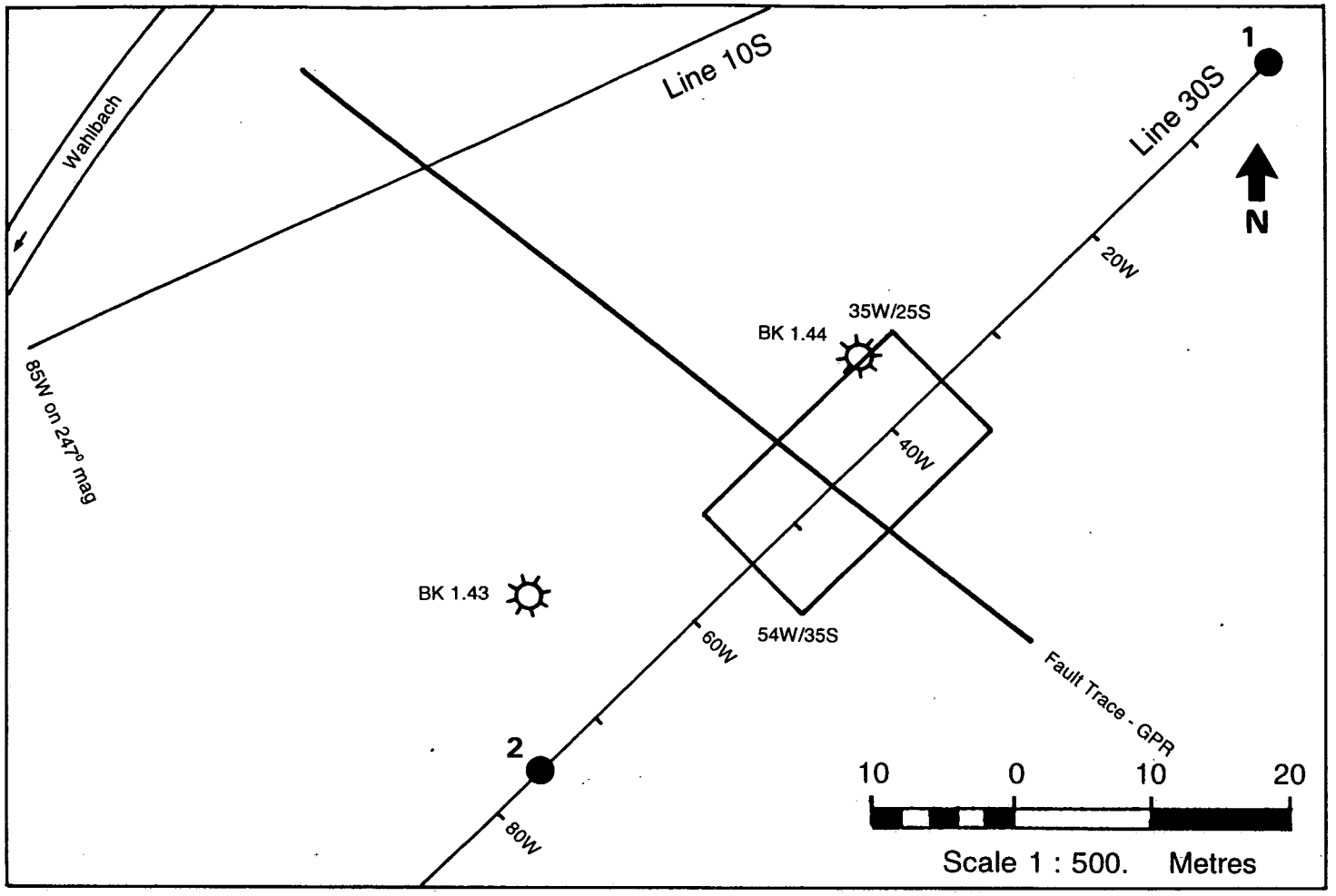

Figure 30 *rsc*. Test Site 1.4. Plan (partial) of site showing location of RESCAN grid.

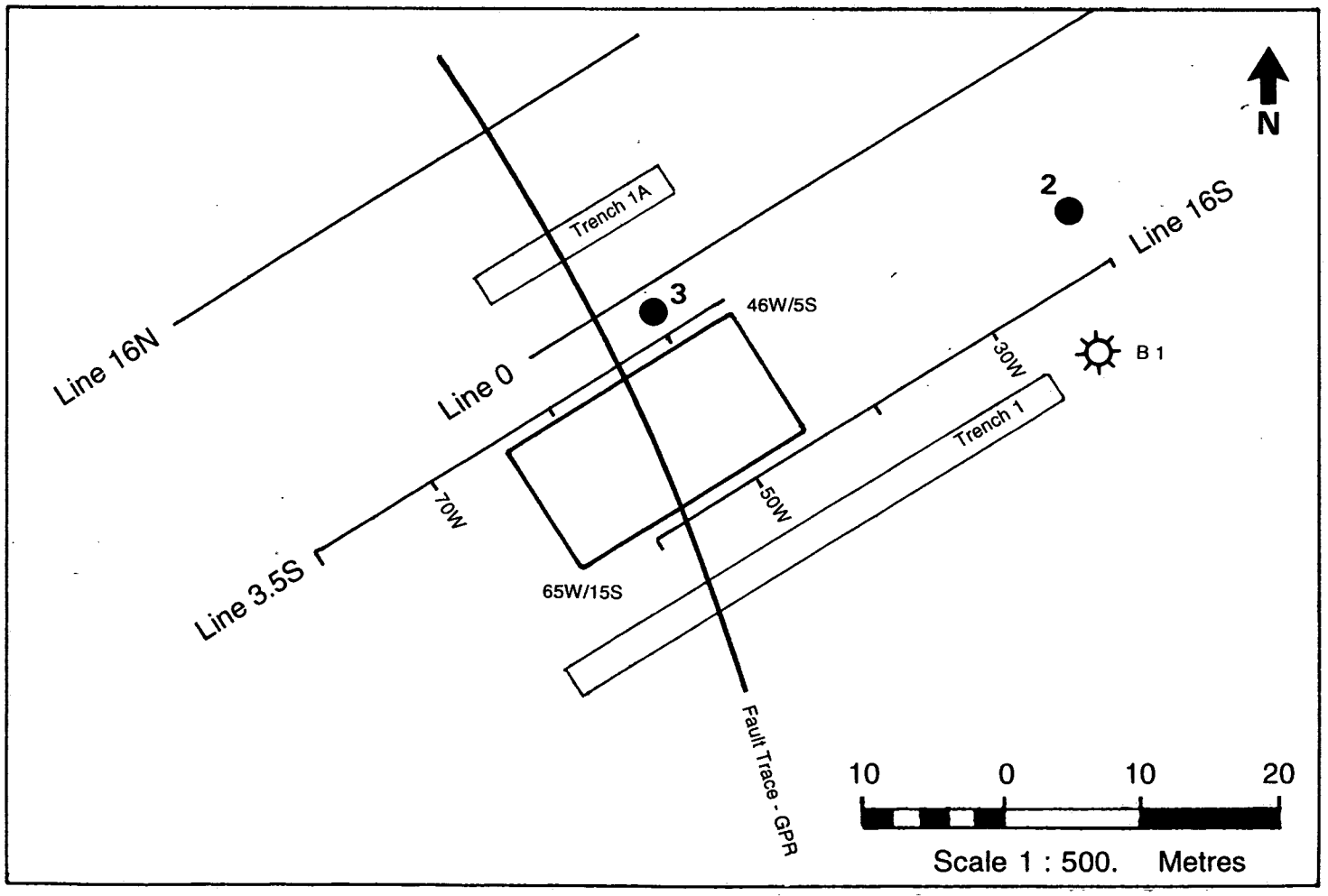

Figure 31 *rsc*. Test Site 2.1. Plan (partial) of site showing location of RESCAN grid.

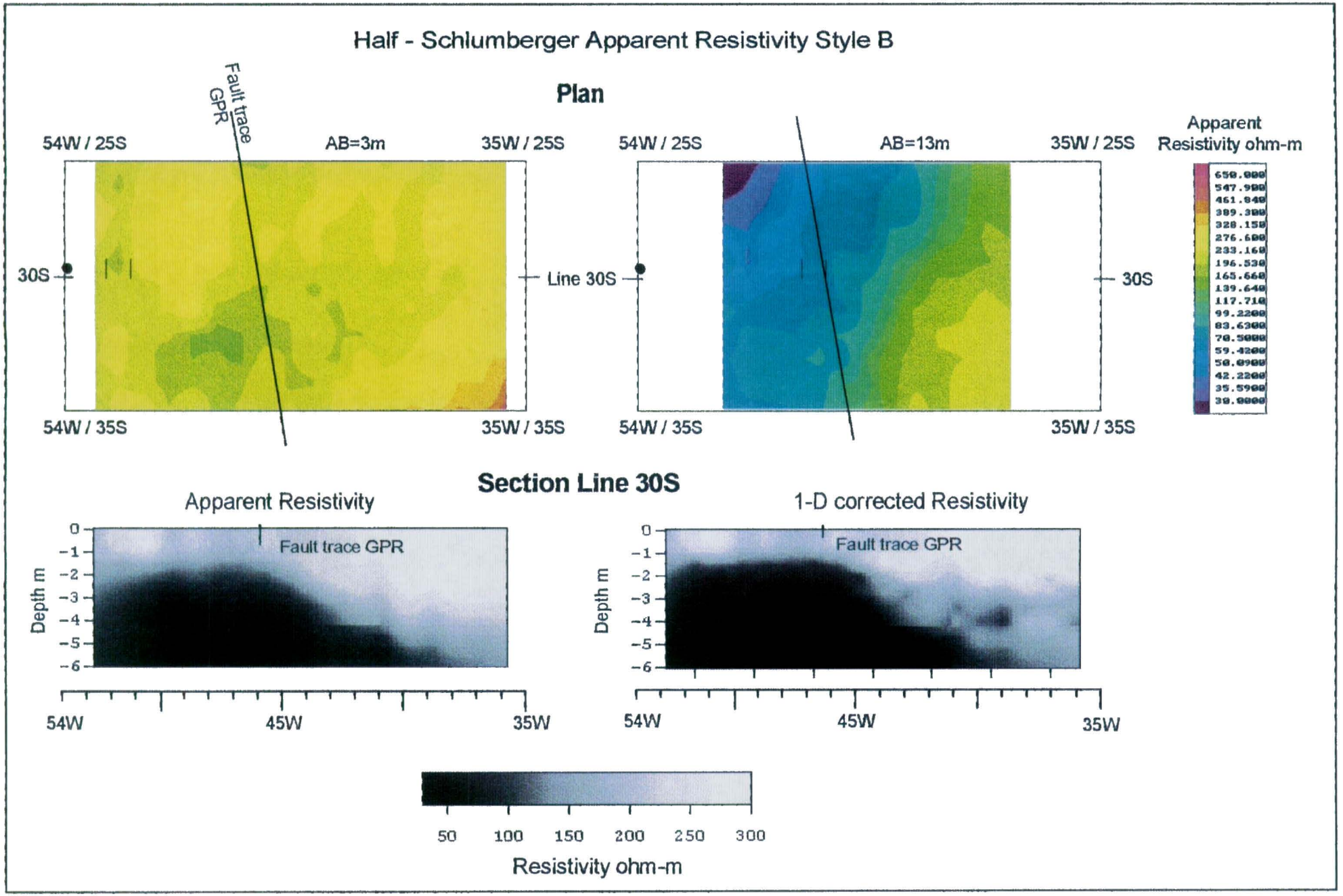

Figure 8 *rsc*. Test Site 1.4. Resistivity imaging using pole-dipole 'half Schlumberger' measurements made under computer control. Pseudo and 1D corrected XZ sections show different responses over a fault identified by GPR.

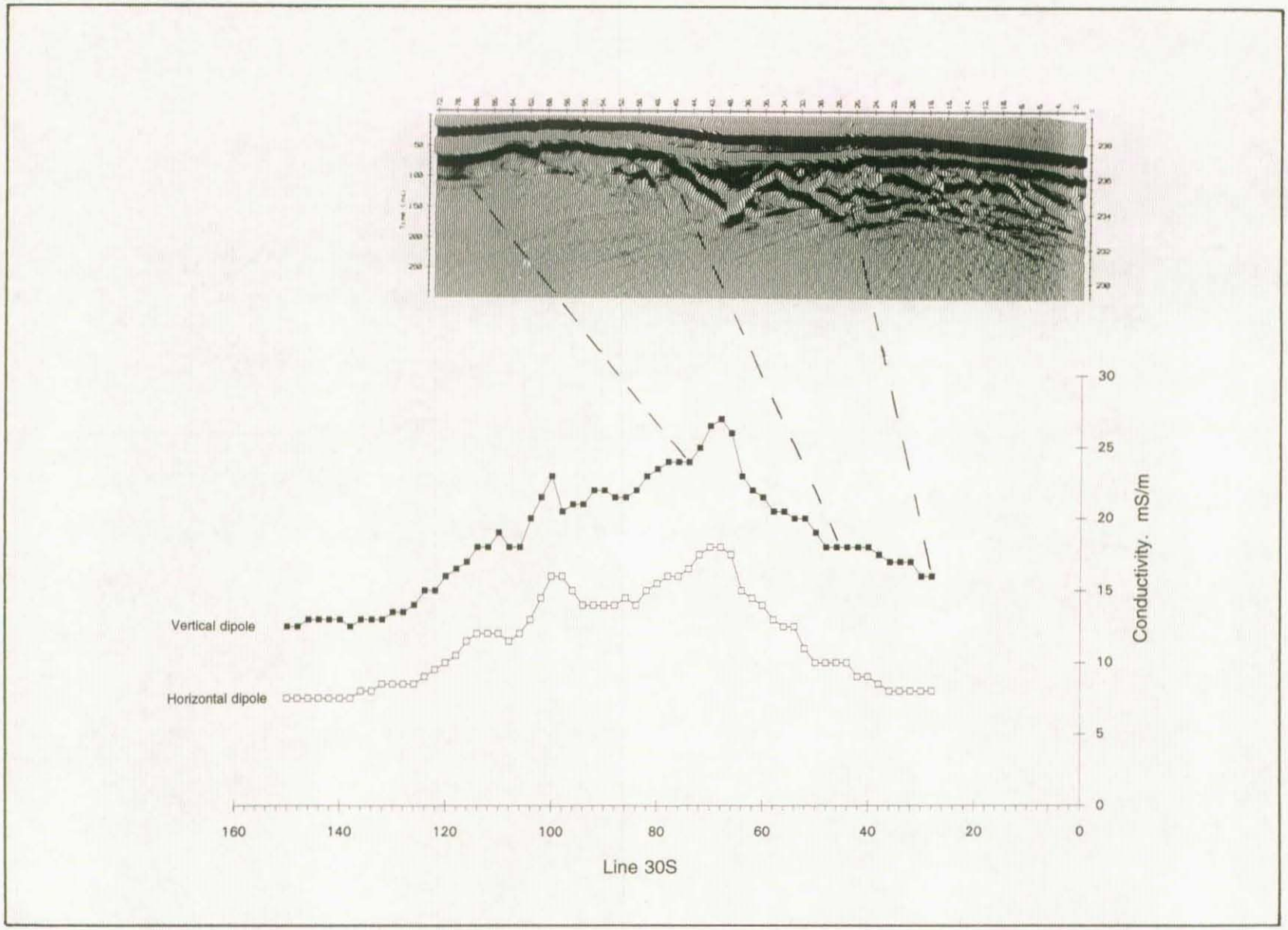

Figure 7 *em*. Test Site 1.4. Composite horizontal and vertical dipole conductivity and GPR section for line 30S.

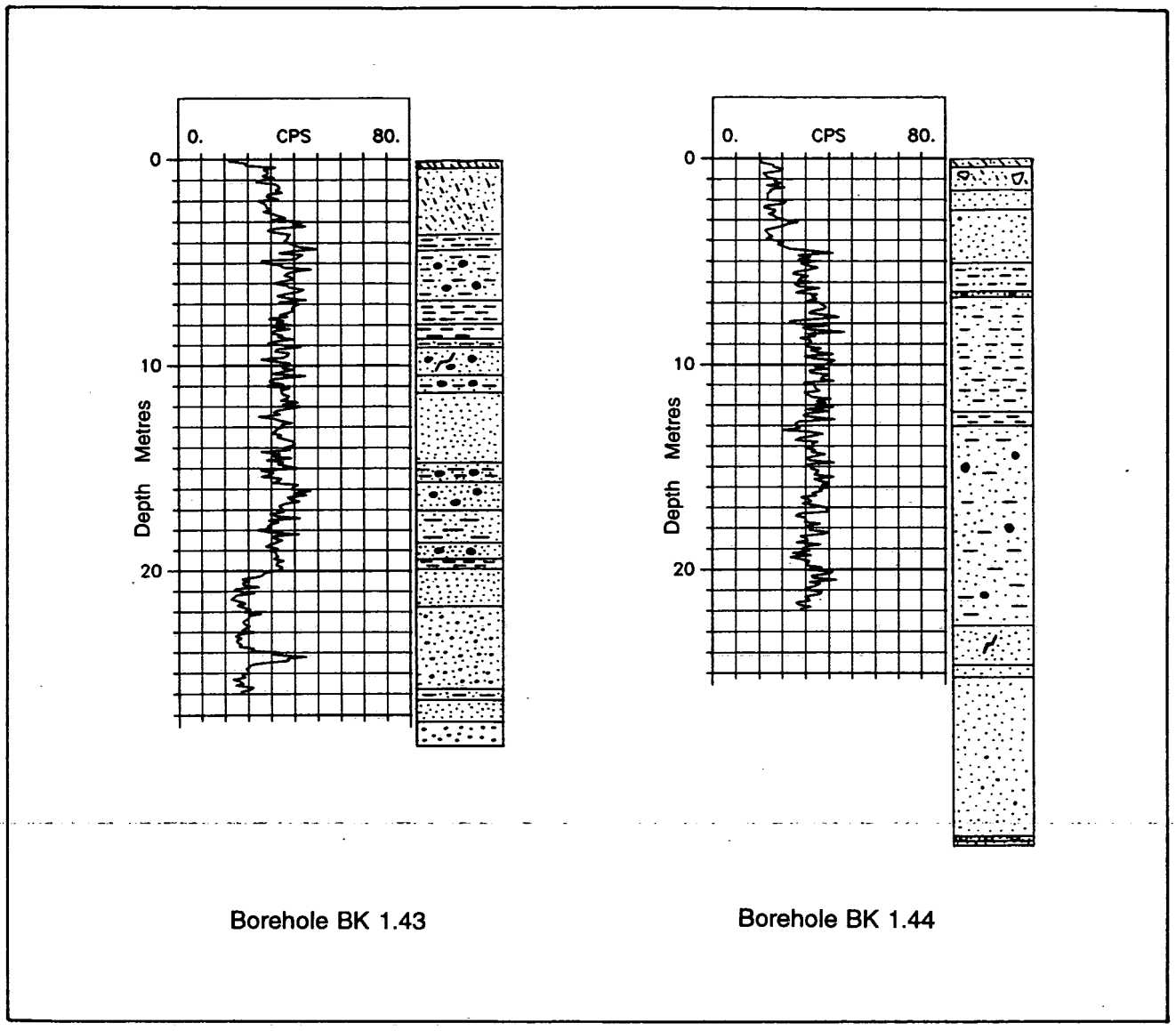

Figure 2 *gam*. Test Site 1.4. Natural gamma logs for boreholes BK1.43 to BK1.44.

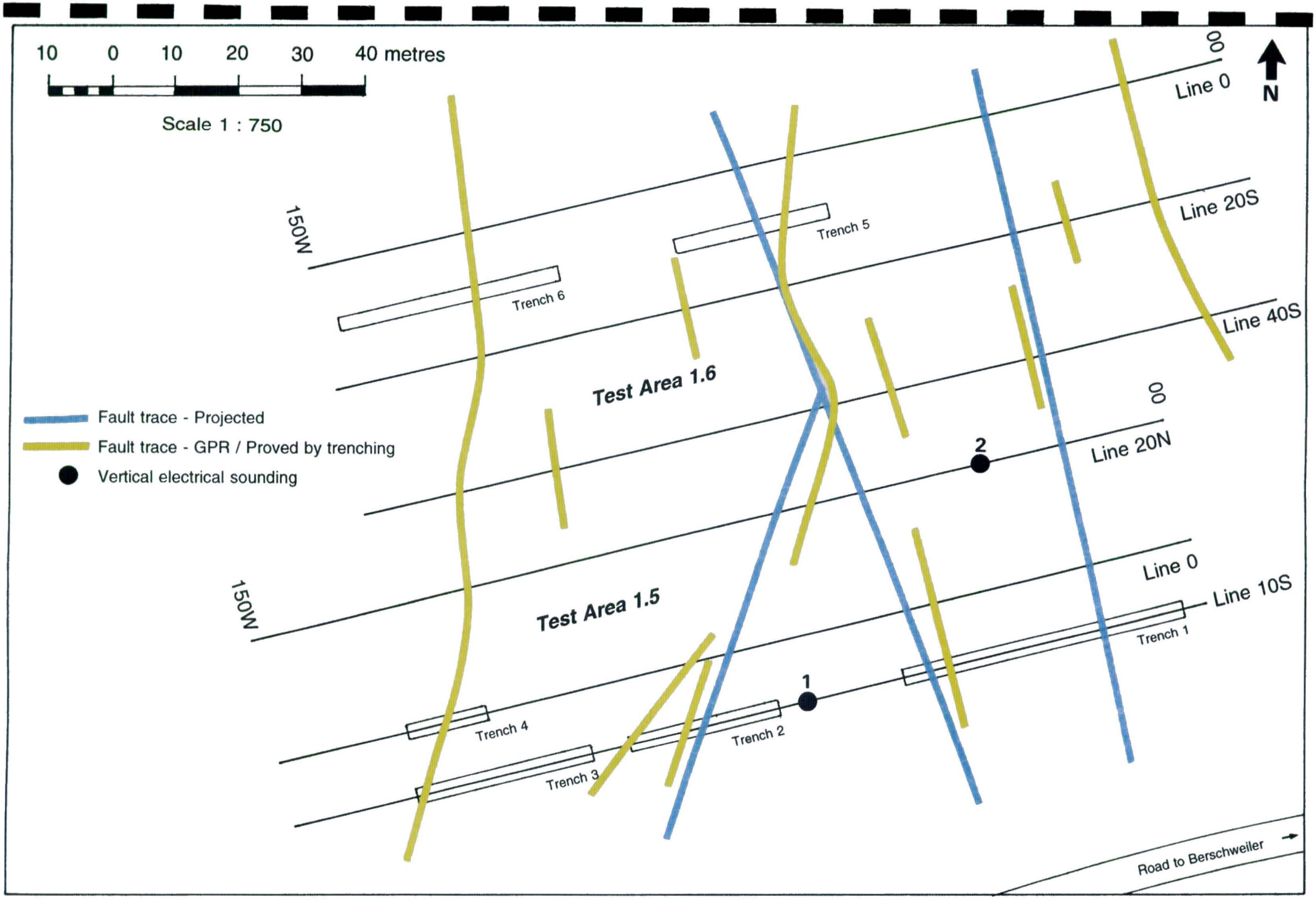

Figure 11. Test Sites 1.5 and 1.6. Geophysical grid, trench locations, and interpretation.

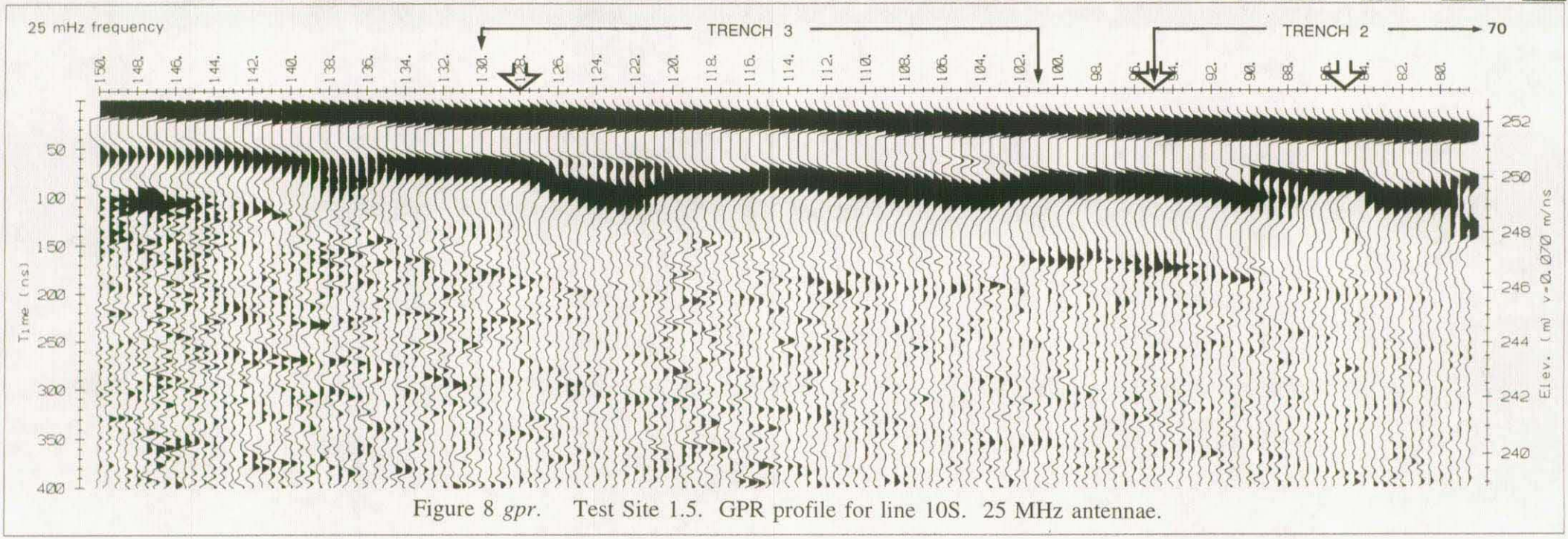

Figure 8 *gpr*. Test Site 1.5. GPR profile for line 10S. 25 MHz antennae.

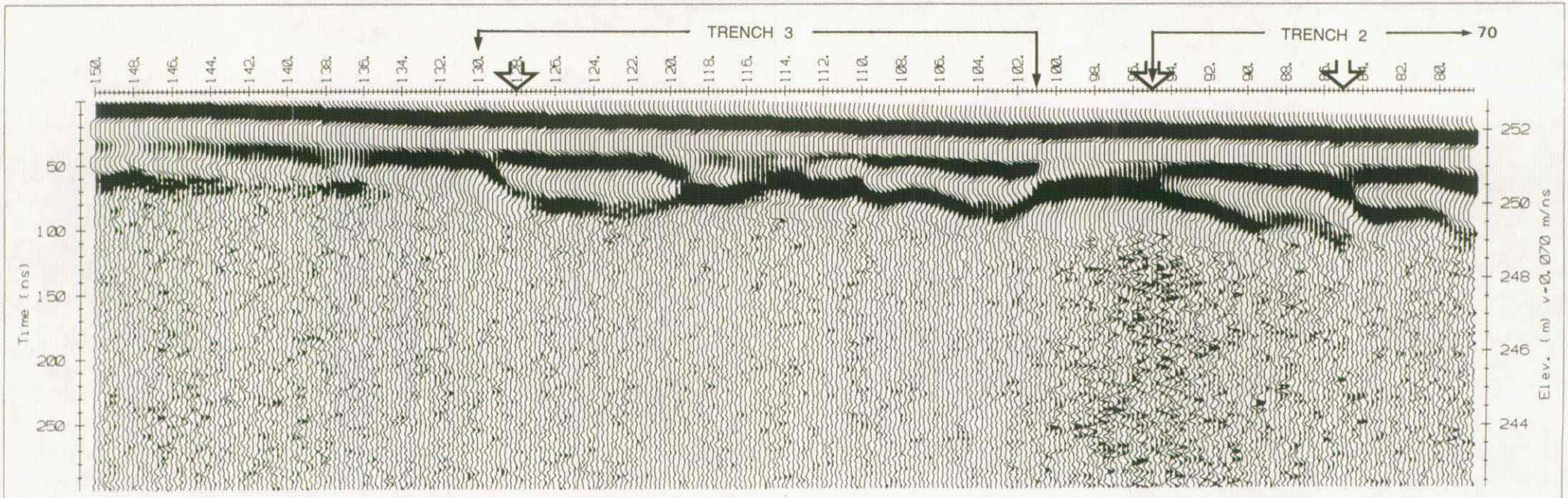

Figure 9 *gpr*. Test Site 1.5. GPR profile for line 10S. 50 MHz antennae.

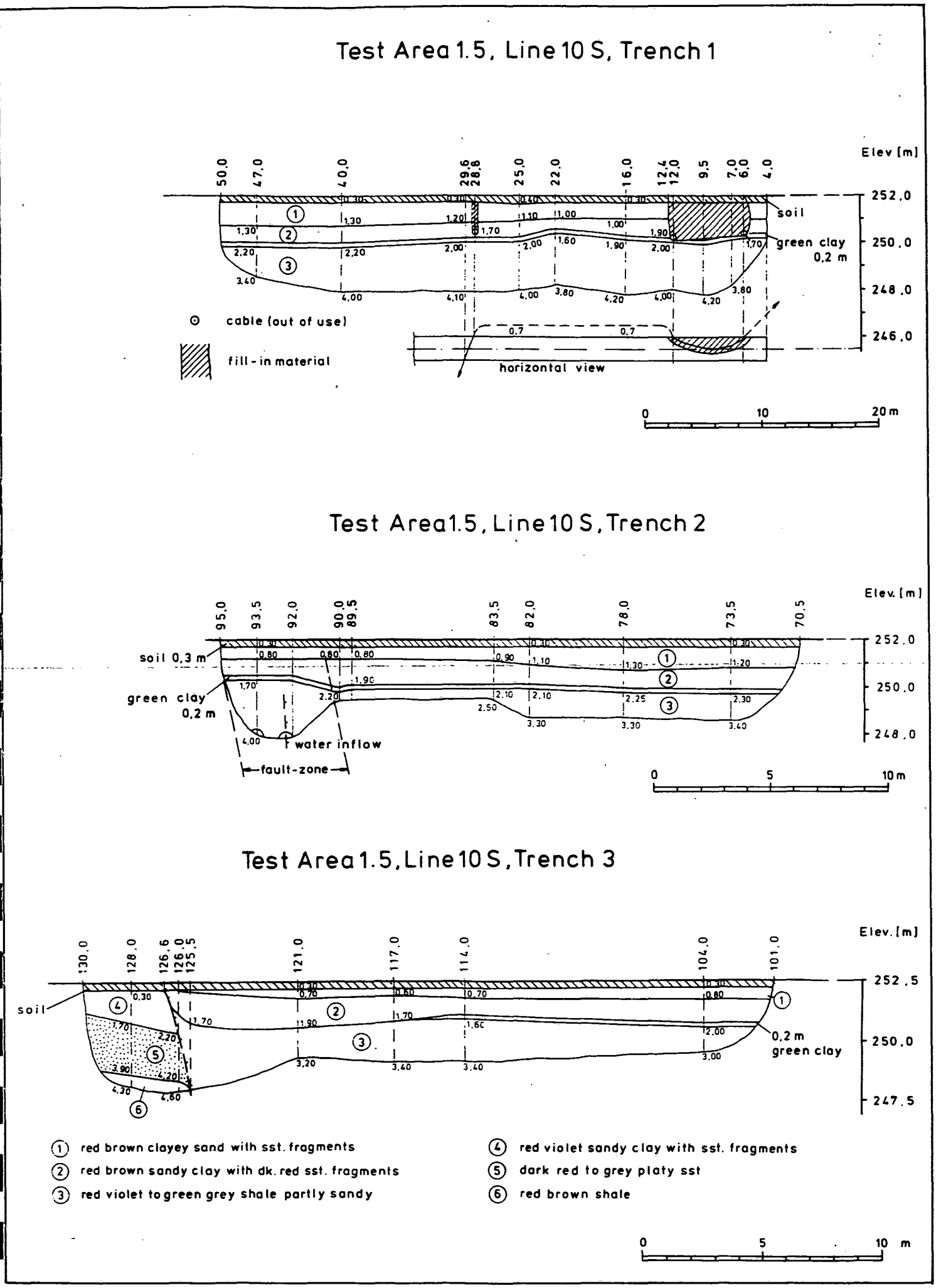

Figure 12. Test Site 1.5. Trenches 1, 2, and 3, line 10S.

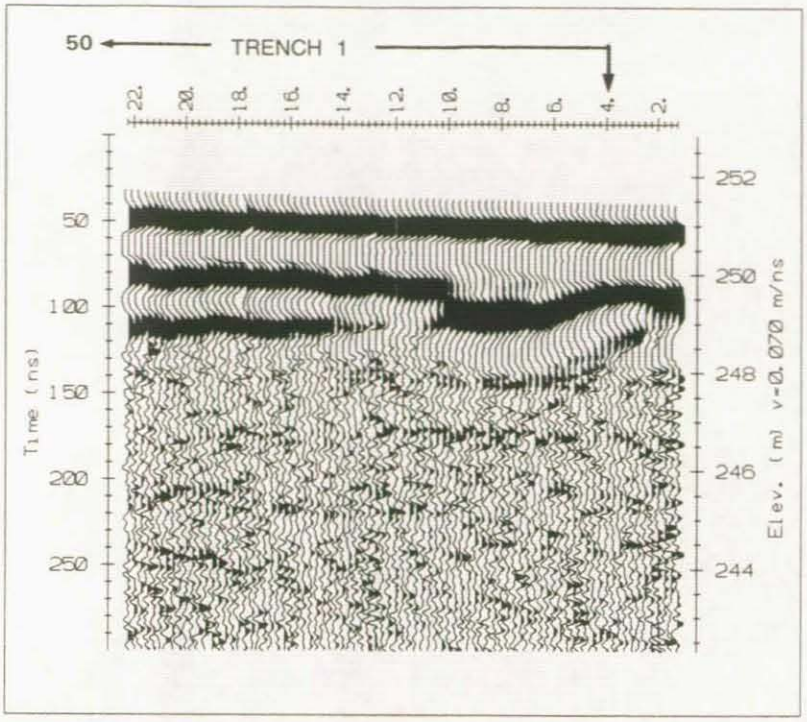

Figure 10 *gpr*. Test Site 1.5. GPR profile for line 10S (eastern end). 50 MHz antennae.

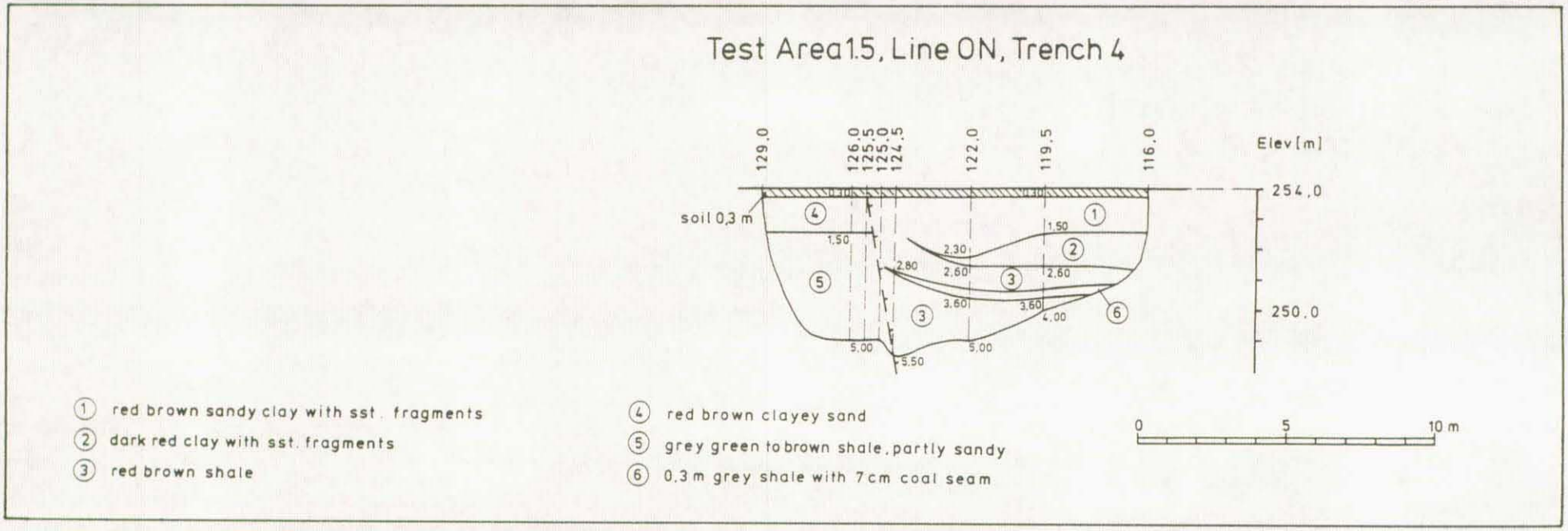

Figure 13. Test Site 1.5. Trench 4, line 0.

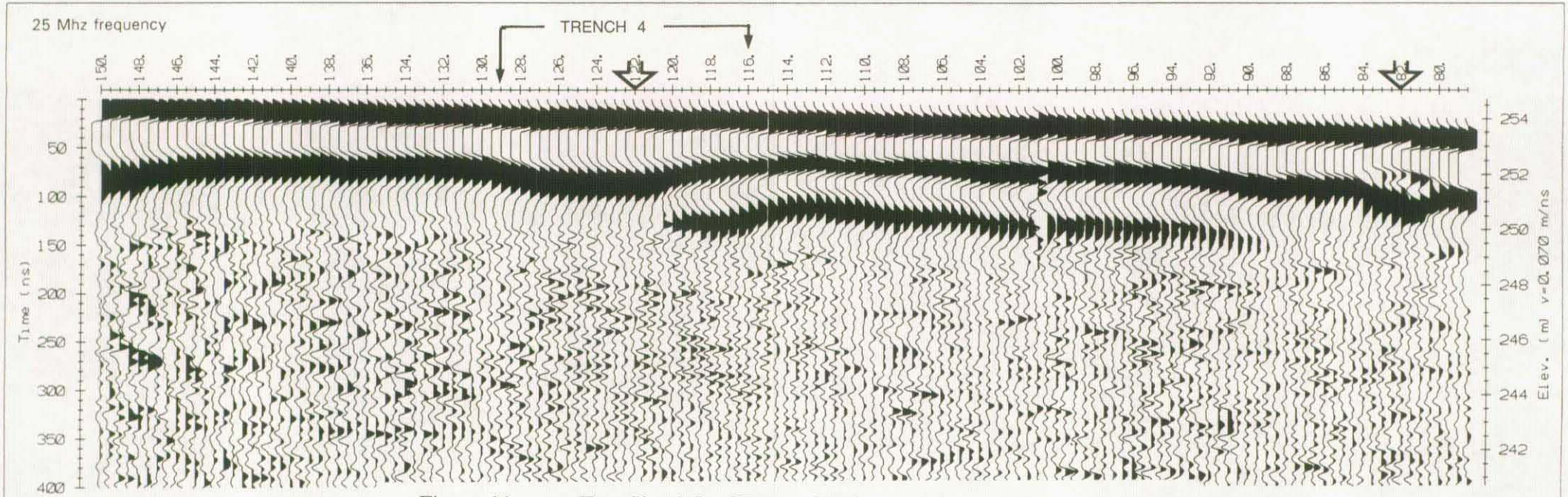

Figure 11 *gpr*. Test Site 1.5. GPR profile for line 0. 25 MHz antennae.

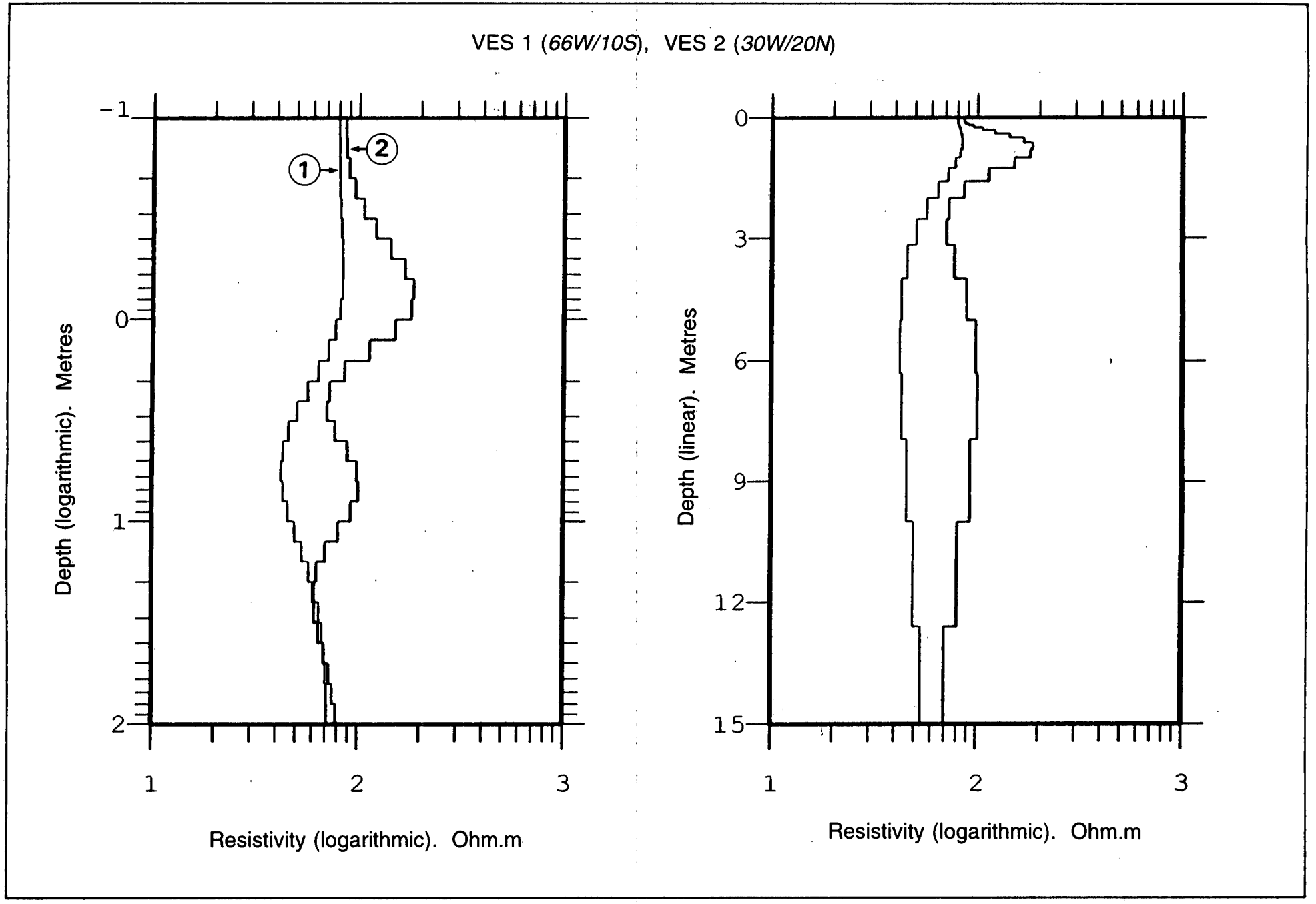

Figure 5 *res.* Test Site 1.5. Interpretation of VES 1, and 2.

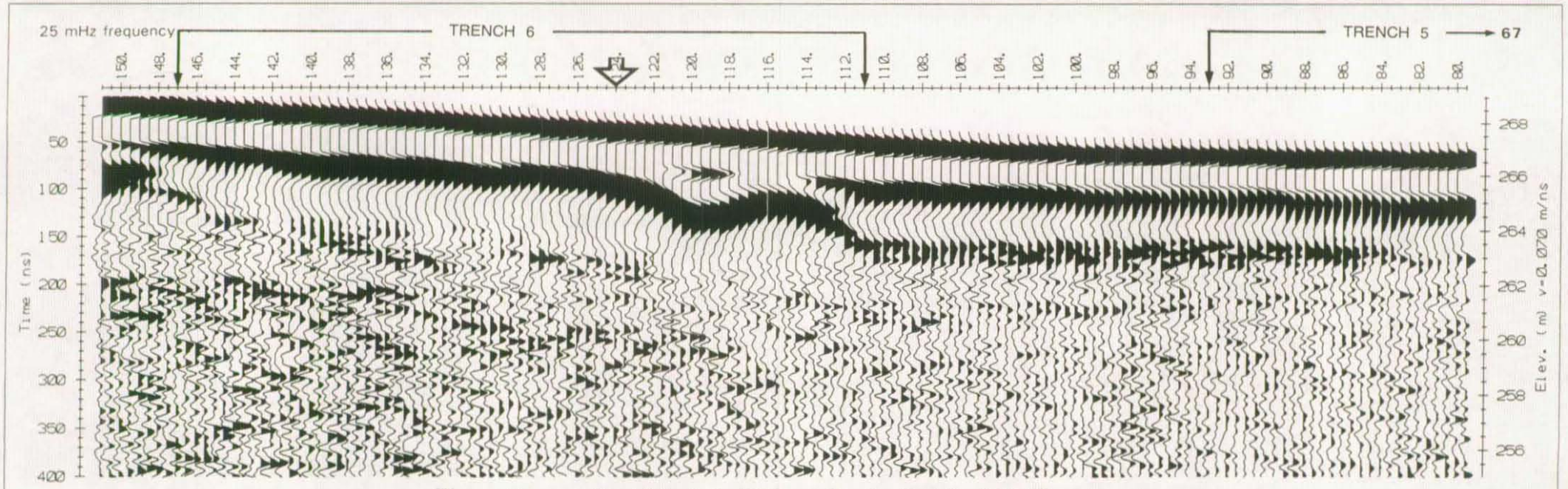

Figure 12 *gpr*. Test Site 1.6. GPR profile for line 0. 25 MHz antennae.

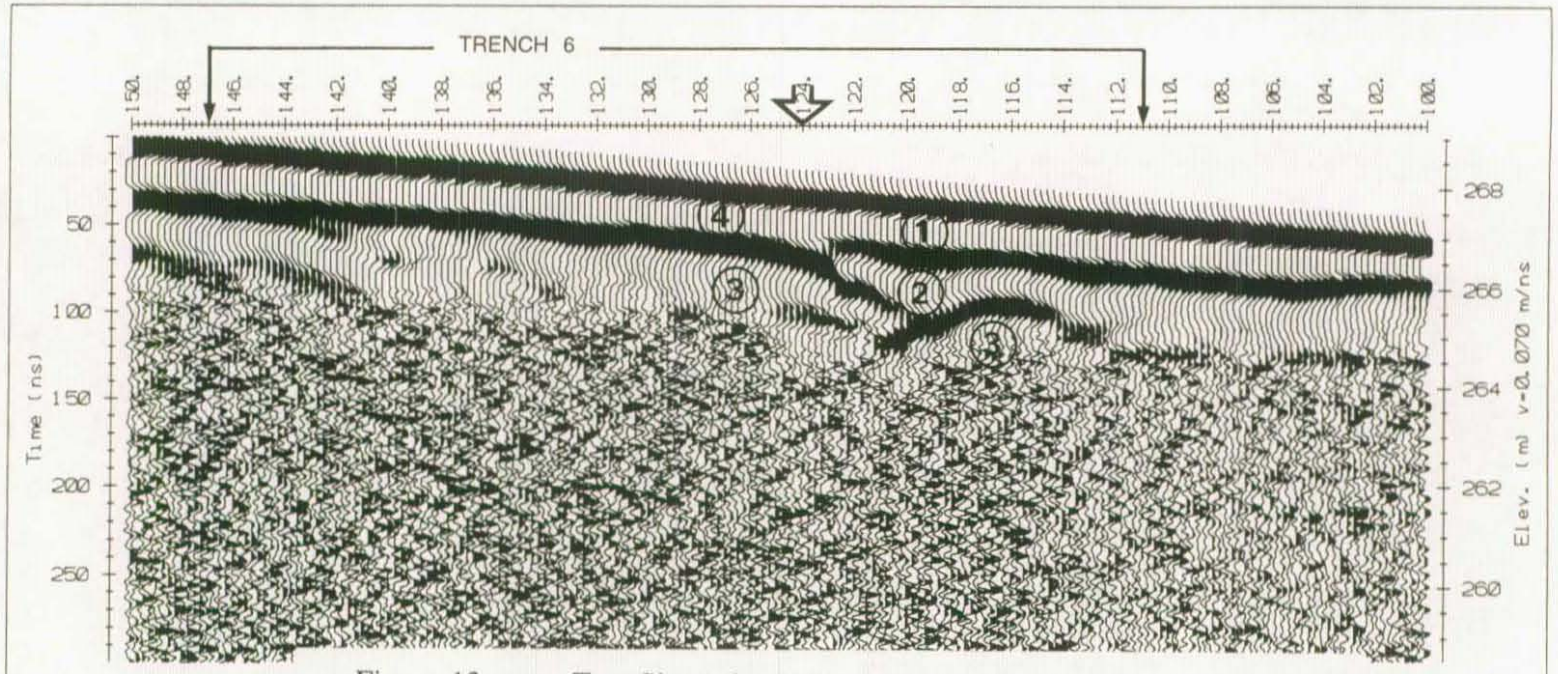

Figure 13 *gpr*. Test Site 1.6. GPR profile for line 0. 50 MHz antennae.

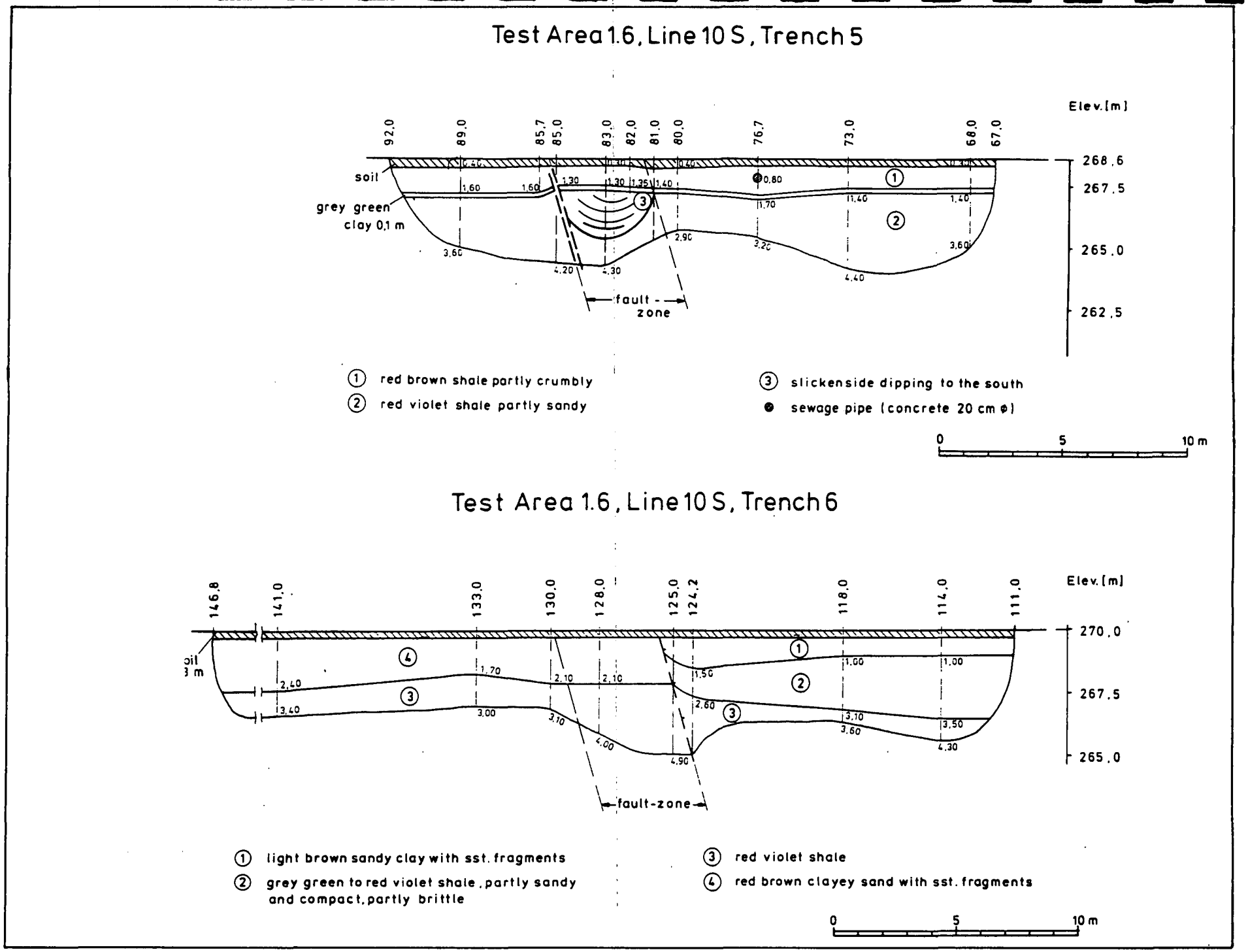

Figure 14. Test Site 1.6. Trenches 5 and 6, line 10S.

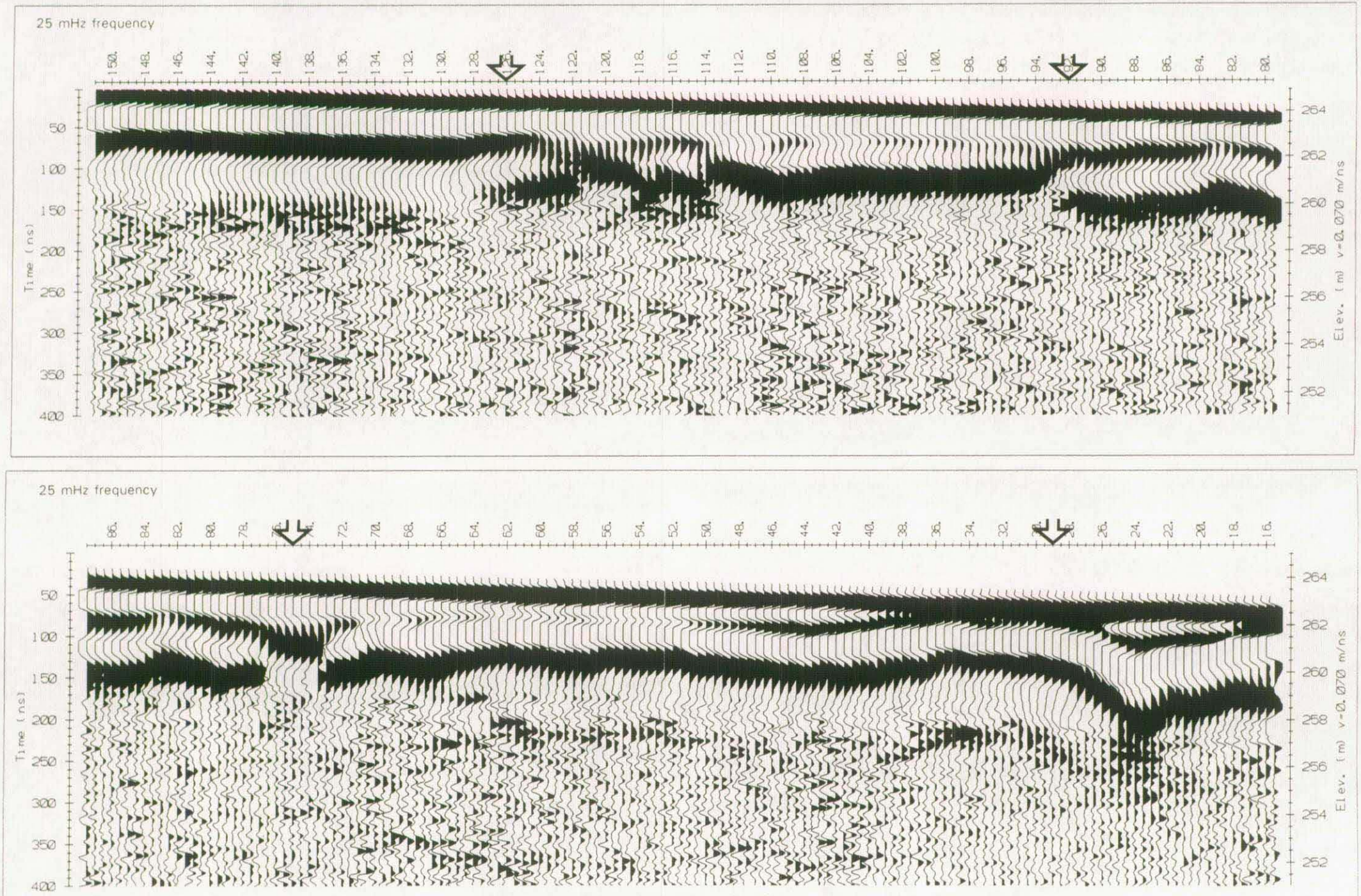

Figure 14 *gpr*. Test Site 1.6. GPR profile for line 20S. 25 MHz antennae.

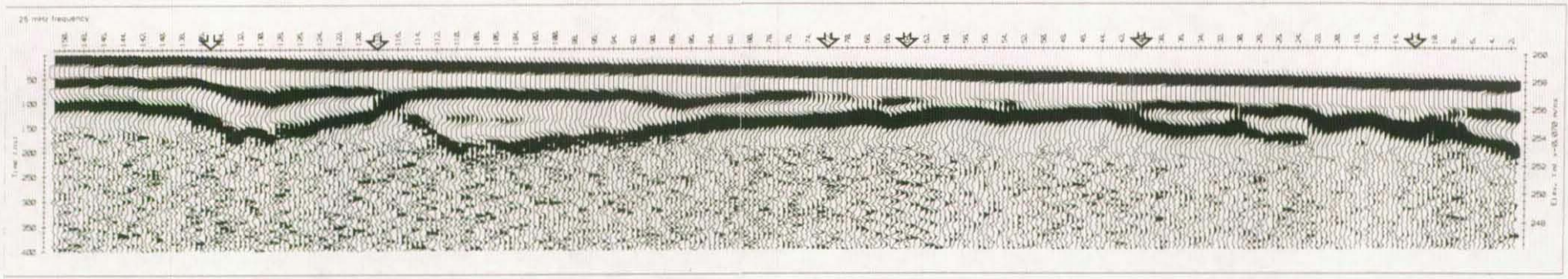

Line 40S (Test Site 1.6)

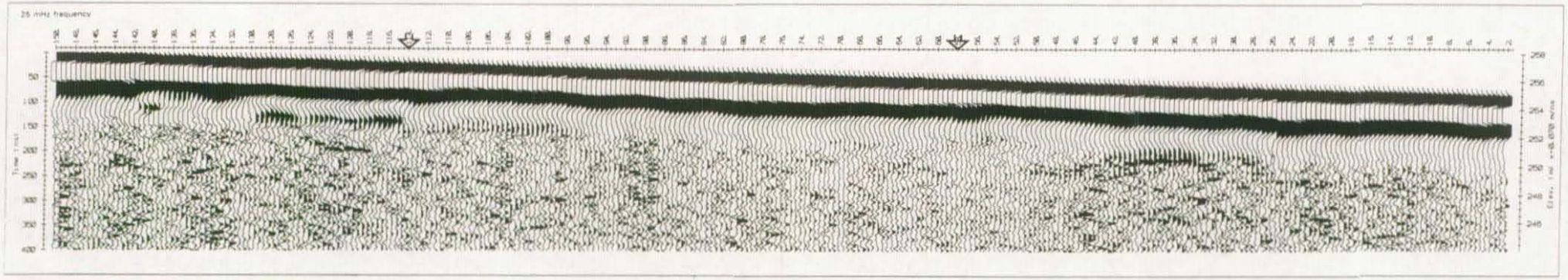

Line 20N (Test Site 1.5)

Figure 15 *gpr*. Test Site 1.6. GPR profile for line 40S and line 20N (Test Site 1.5). 25 MHZ antennae.

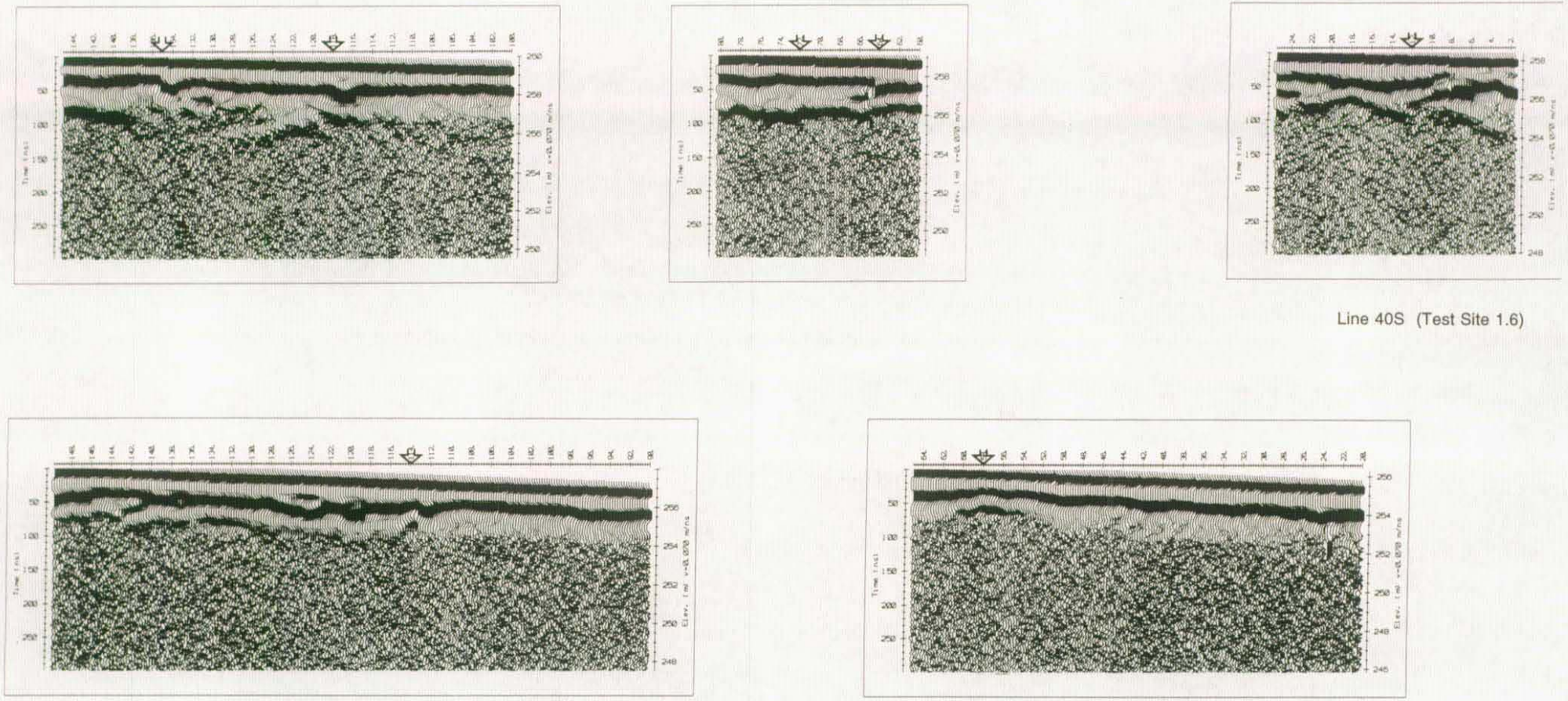

Line 40S (Test Site 1.6)

Line 20N (Test Site 1.5)

Figure 16 *gpr*. Test Site 1.6. GPR profile for line 40S and line 20N (Test Site 1.5). 50 MHZ antennae.

Figure 15. Test Site 2.1. Geophysical grid, trench and borehole locations, and interpretation. May 1992 survey.

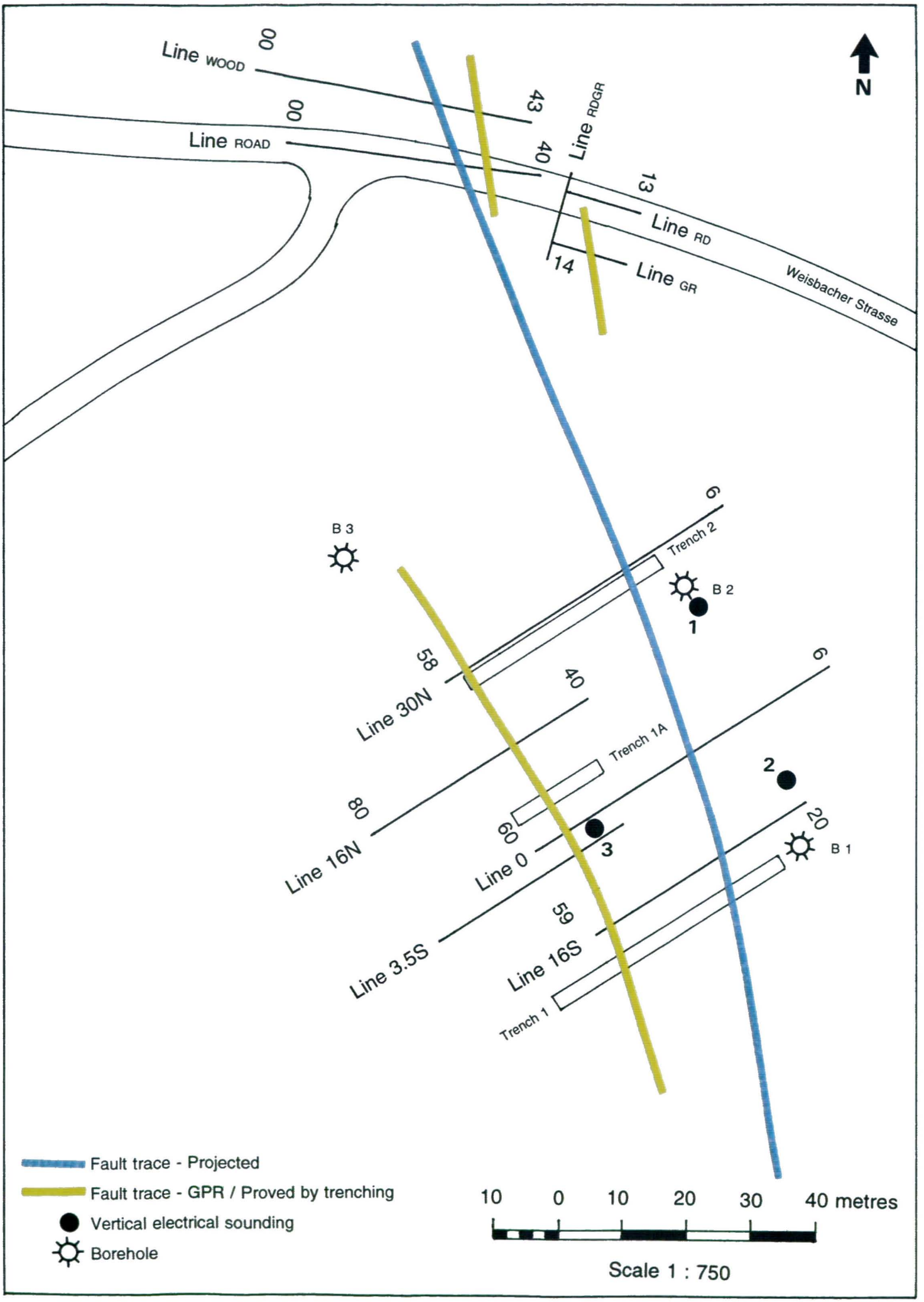

Figure 16. Test Site 2.1. Geophysical grid, trench and borehole locations, and interpretation. December 1992 survey.

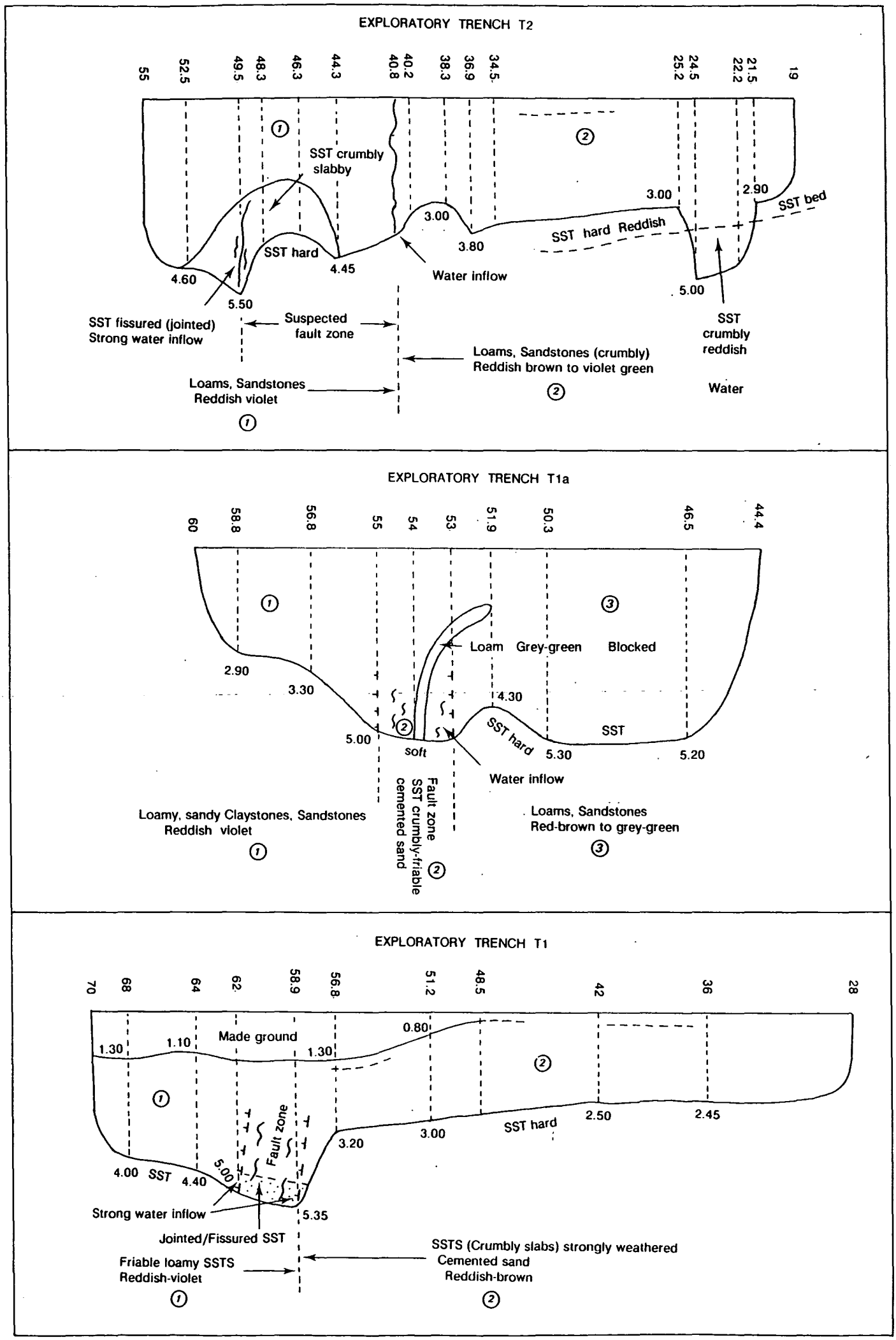

Figure 17. Test Site 2.1. Exploratory trenches T1, T1a, and T2.

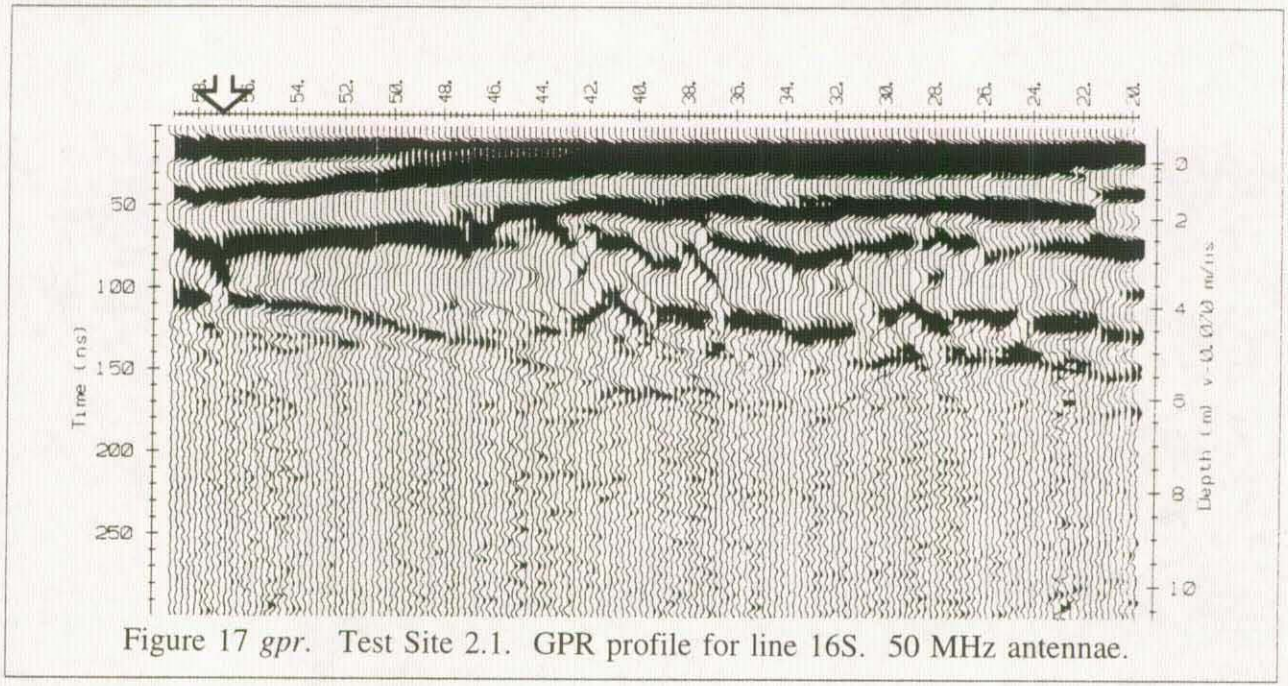

Figure 17 *gpr*. Test Site 2.1. GPR profile for line 16S. 50 MHz antennae.

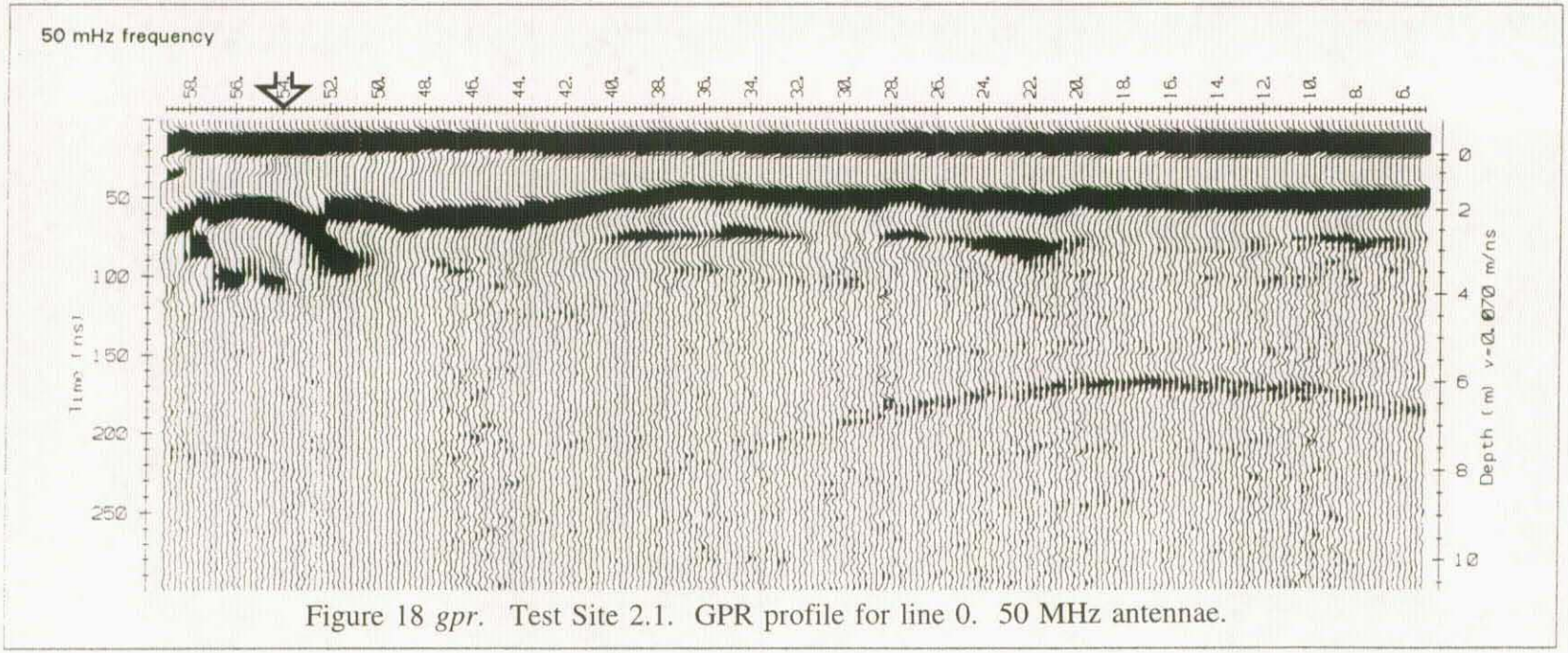

Figure 18 *gpr*. Test Site 2.1. GPR profile for line 0. 50 MHz antennae.

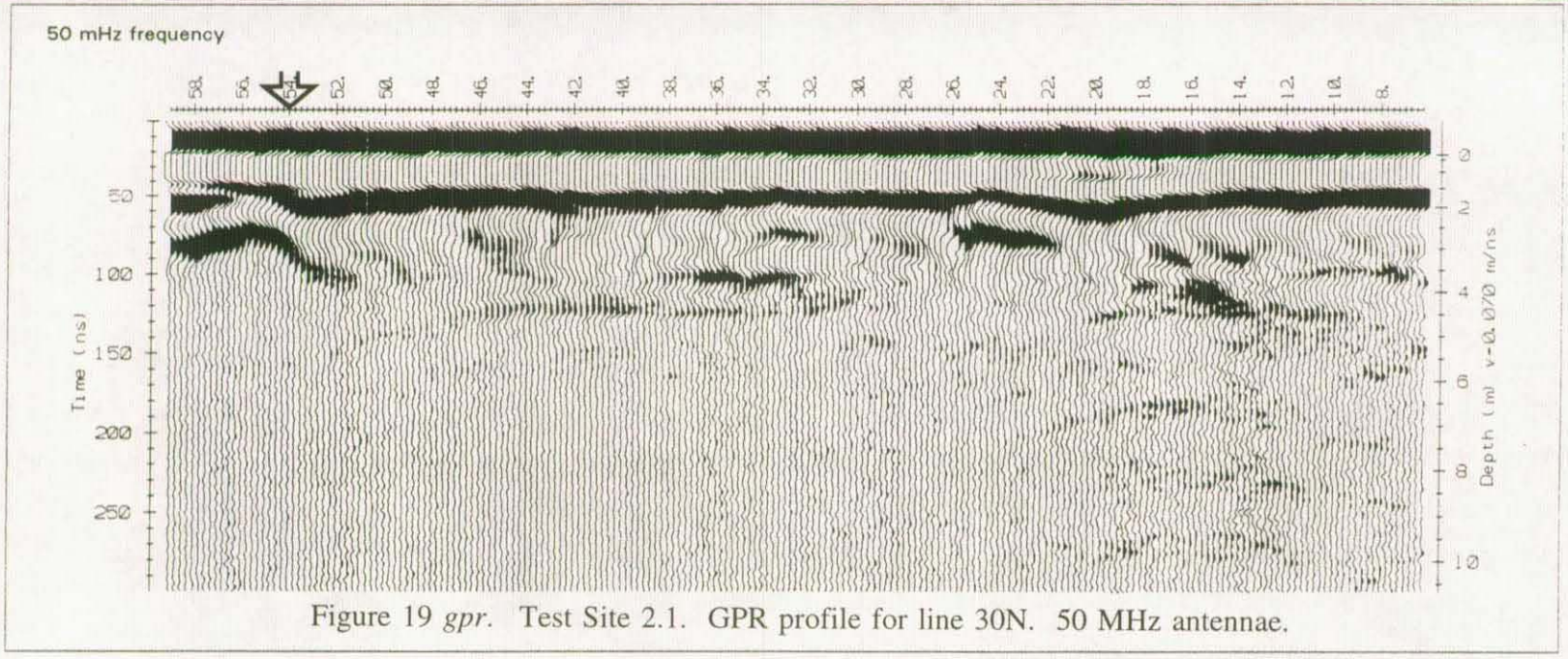

Figure 19 *gpr*. Test Site 2.1. GPR profile for line 30N. 50 MHz antennae.

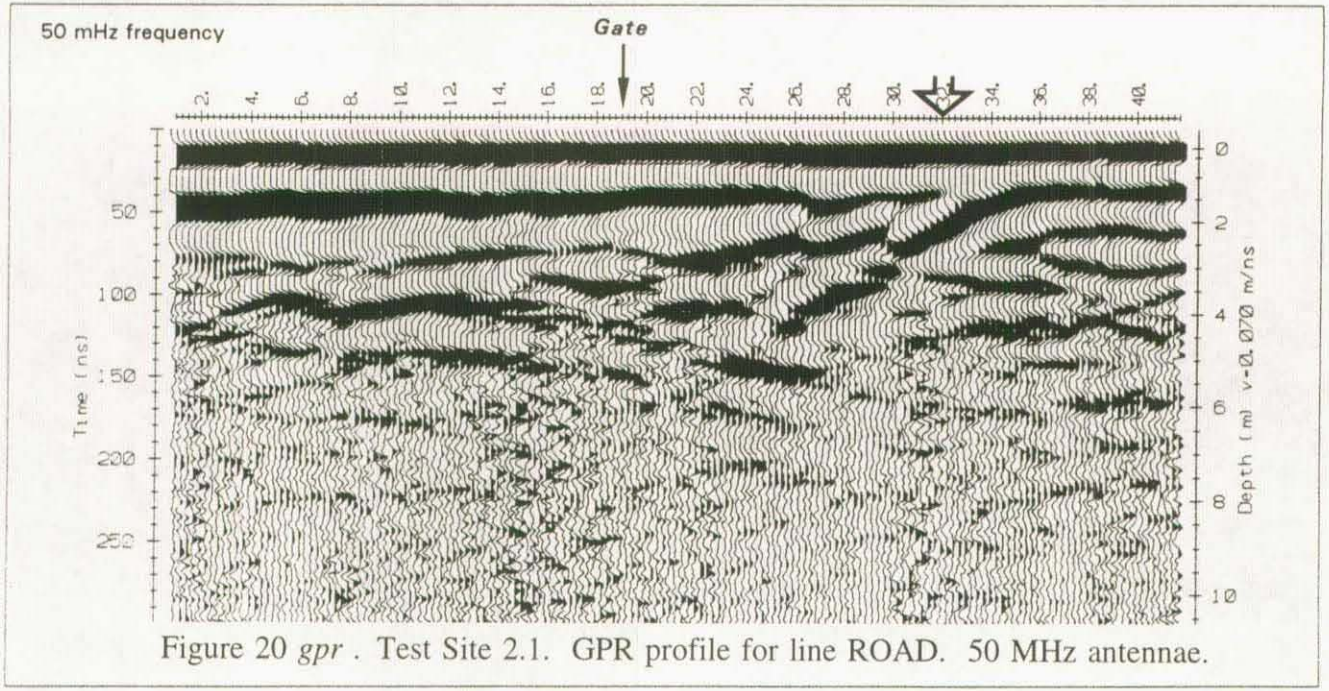

Figure 20 *gpr* . Test Site 2.1. GPR profile for line ROAD. 50 MHz antennae.

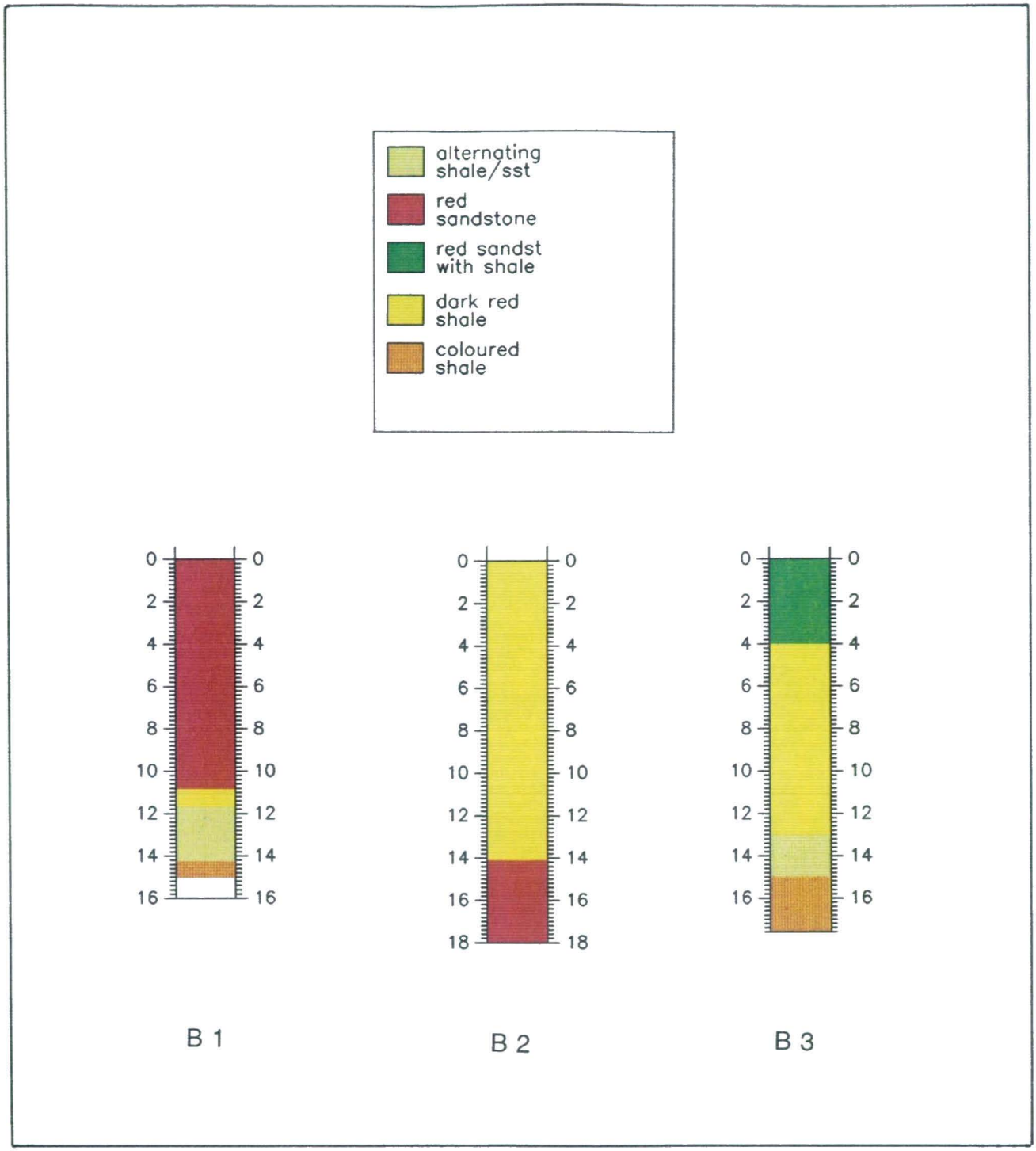

Figure 18. Test Site 2.1. Geological section: boreholes B1, B2, B3.

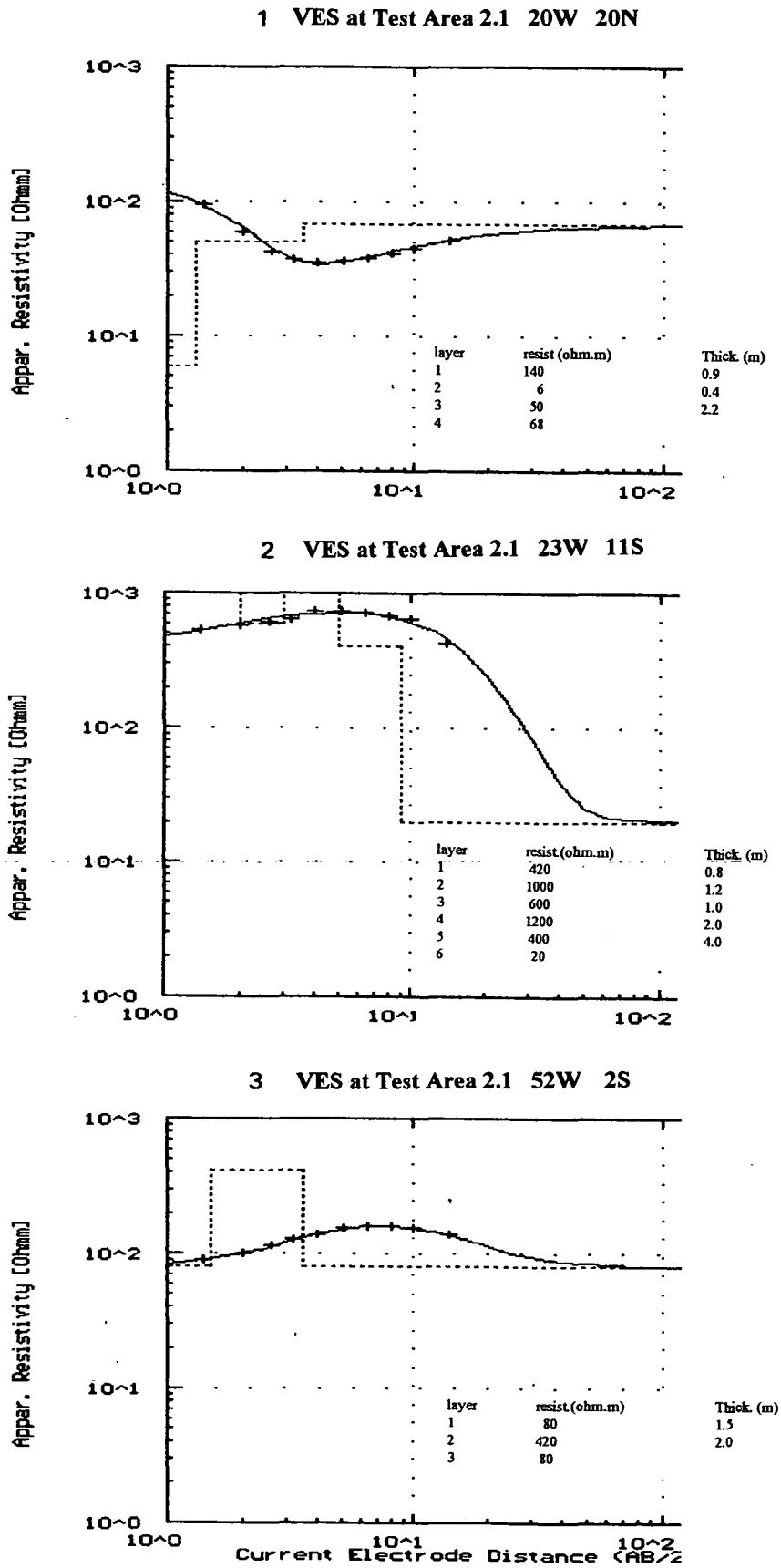

Figure 6 *res.* Test Site 2.1. Interpretation of VES 1, 2, and 3.

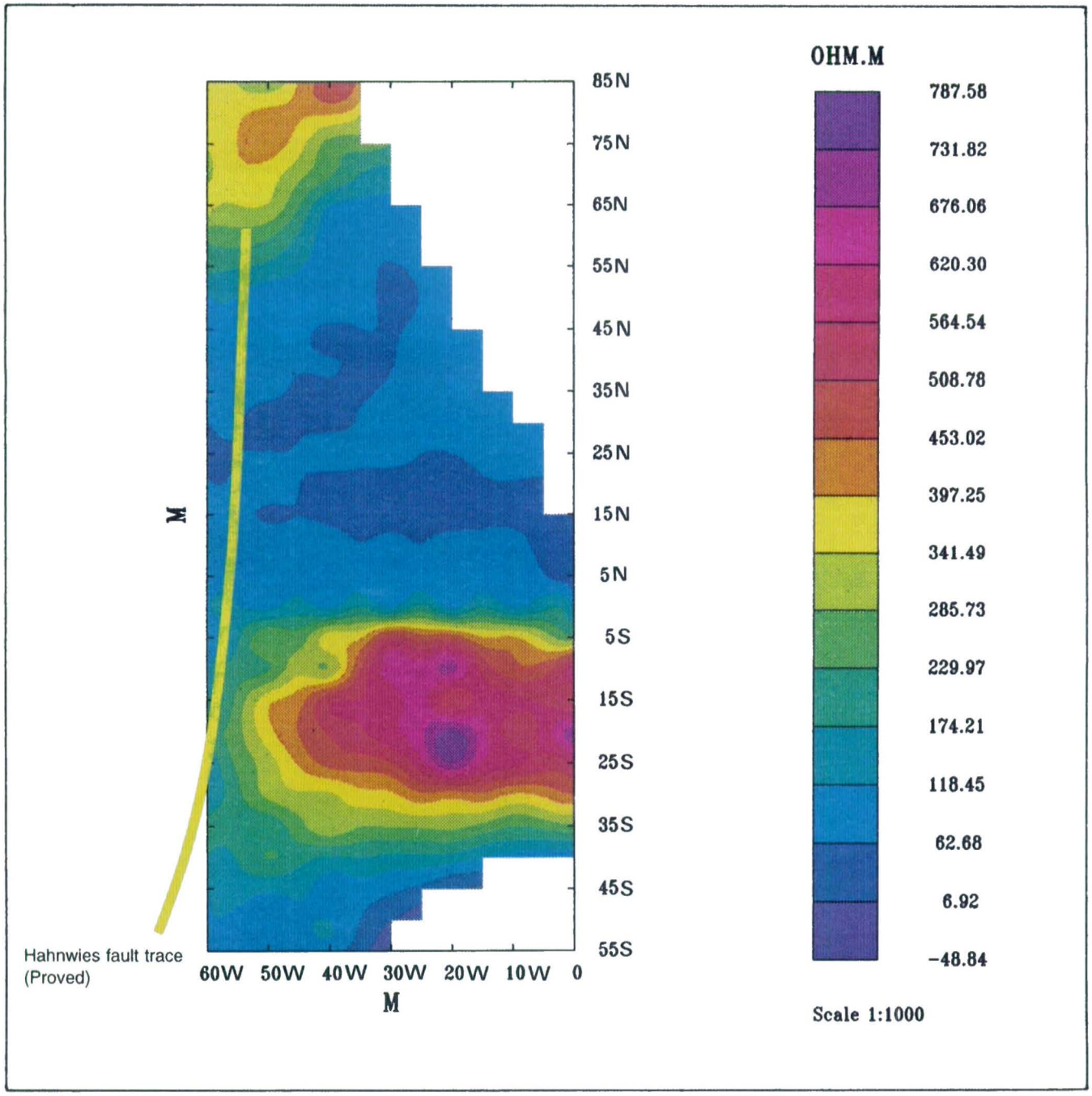

Figure 7 *res.* Test Site 2.1. Schlumberger array resistivity contours.

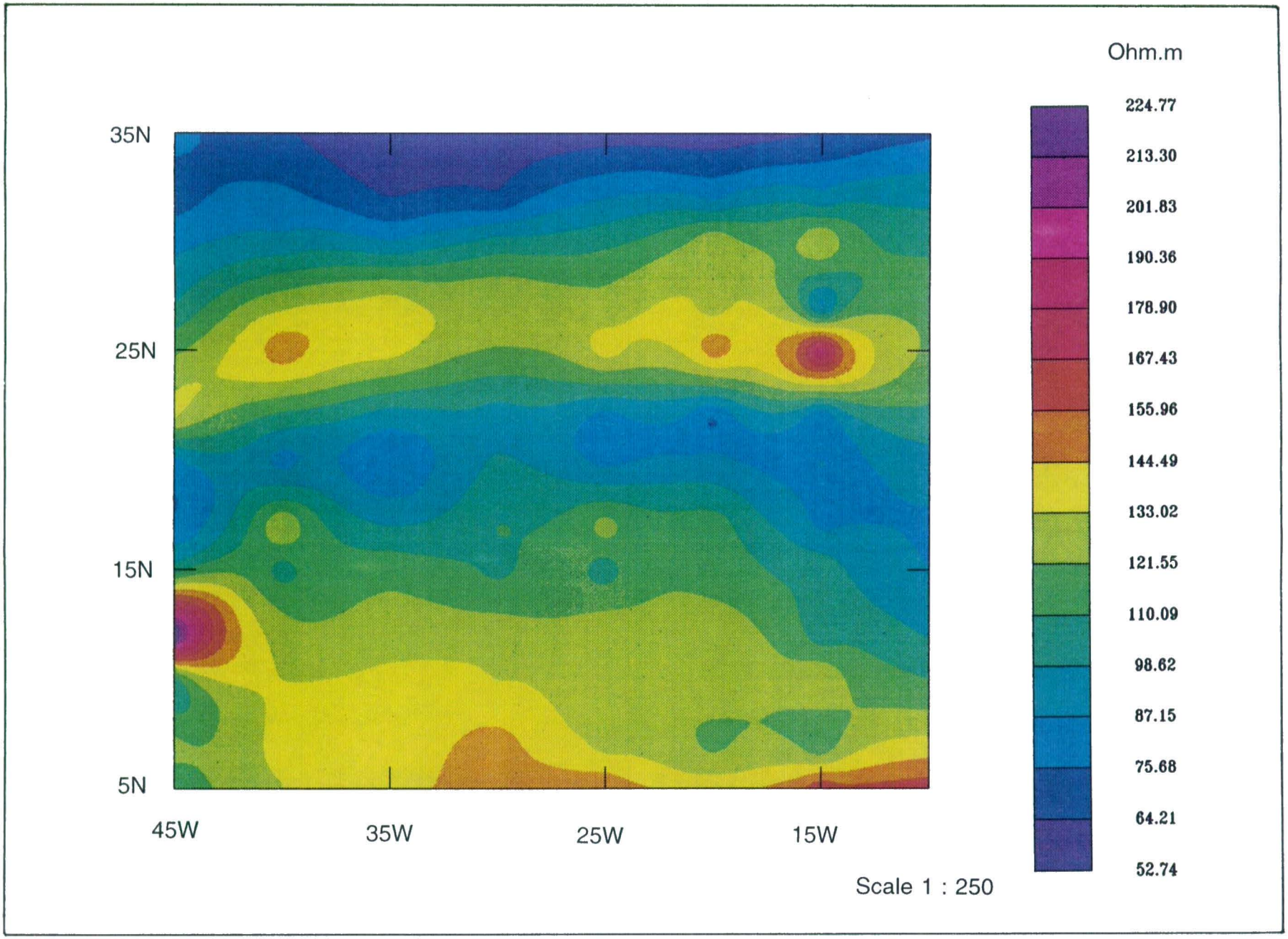

Figure 8 *res.* Test Site 2.1. Gradient array resistivity contours.

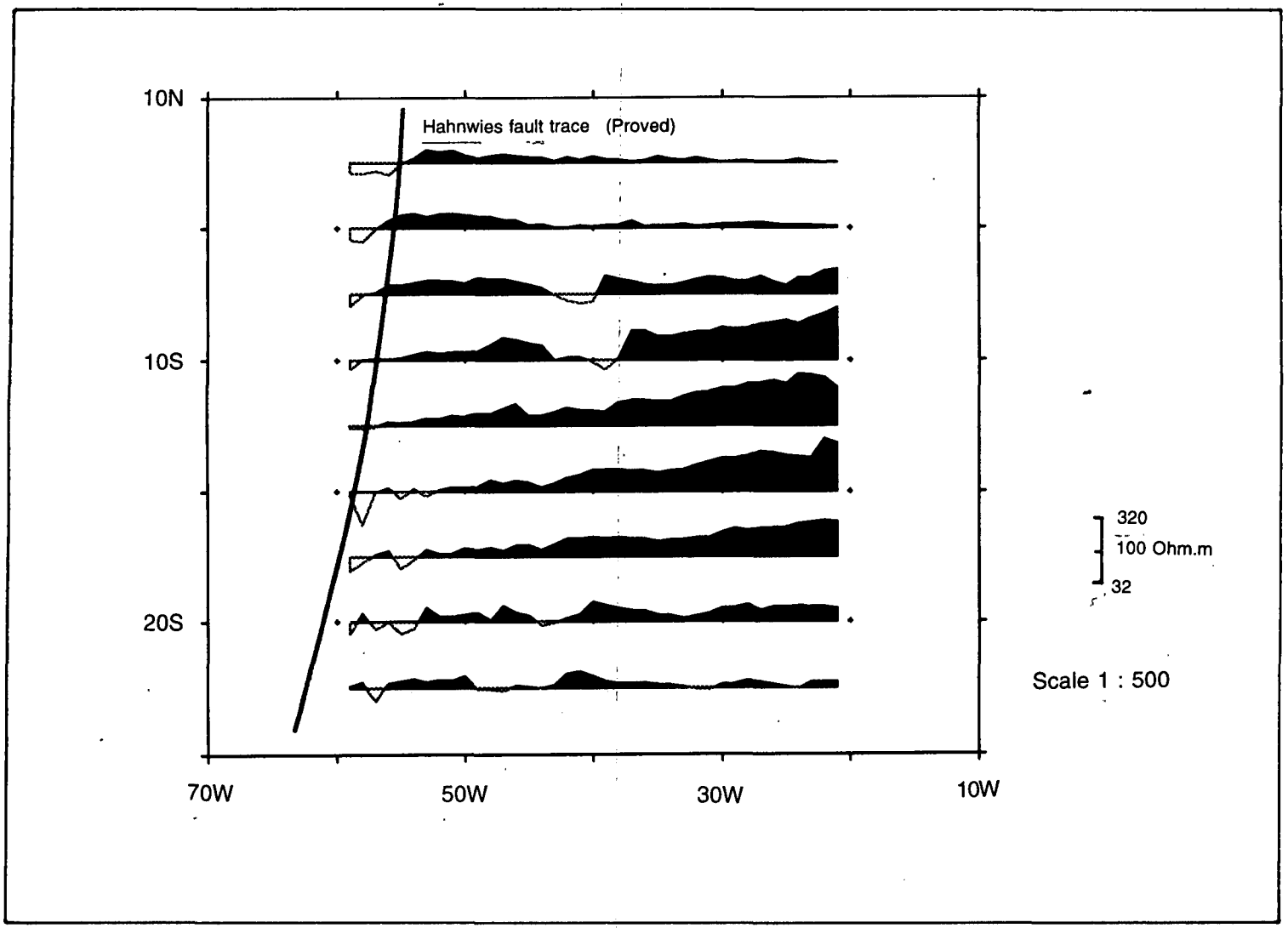

Figure 9 *res.* Test Site 2.1. Gradient array resistivity profiles (logarithmic scale).

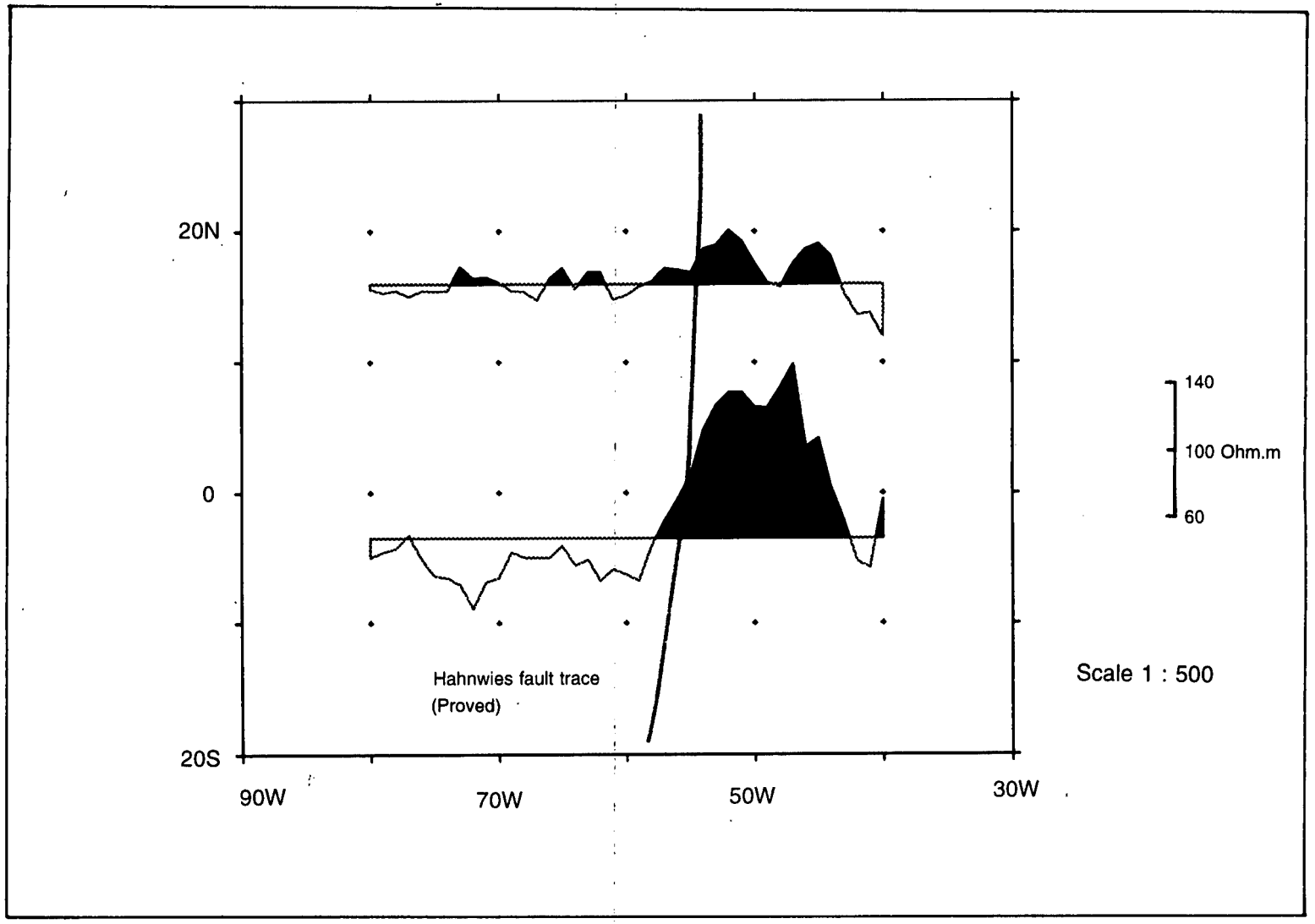

Figure 10 *res.* Test Site 2.1. Gradient array detail over proven fault trace.

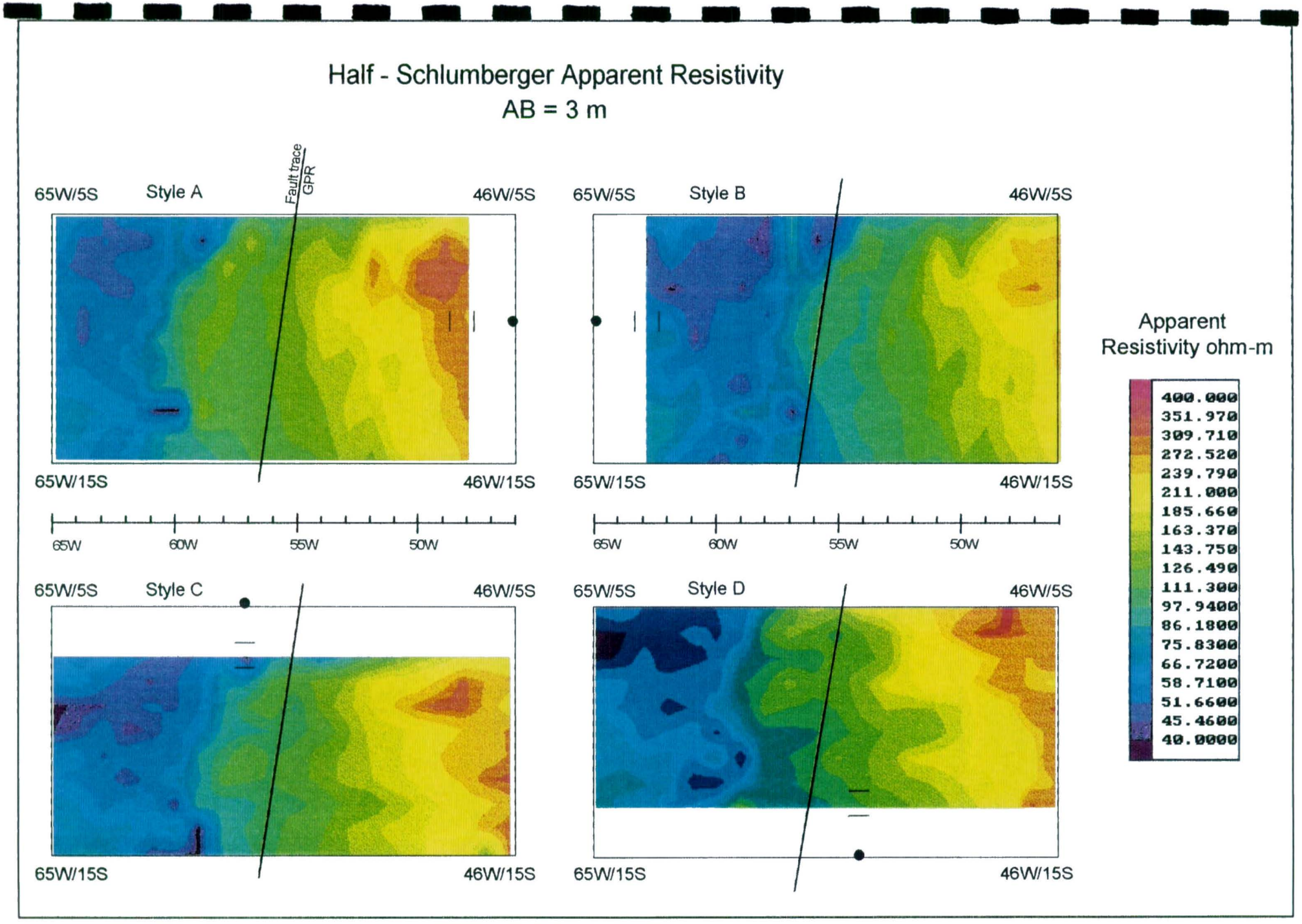

Figure 3 *rsc*. Test Site 2.1. Half Schlumberger apparent resistivity maps for AB=3m.

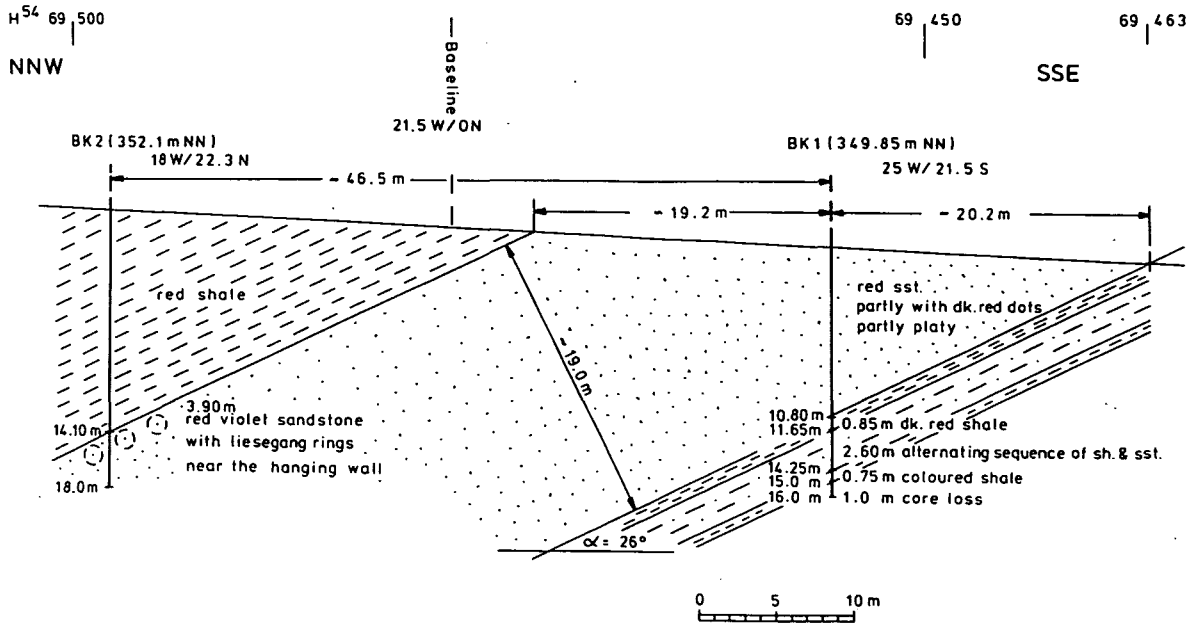

Geological section between core drill holes BK 1 and BK 2 (1992)
Test Area 2.1 Lummerschied-Kutzhof
Lower Heusweiler Layers about 425 m above Seam Lummerschied (970)

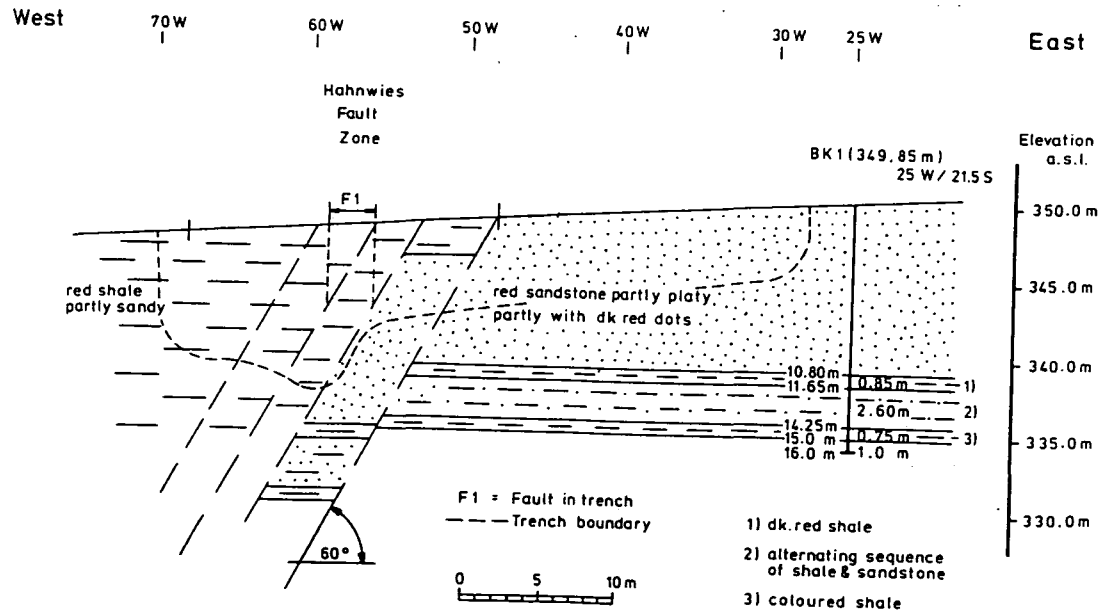

Longitudonal section // traverse line 20 S along drill hole BK 1 and trench T 1
in Test trea 2.1

Figure 1 *rsc.* Test Site 2.1. Geological sections constrained by boreholes B1 and B2 and Trench T1.

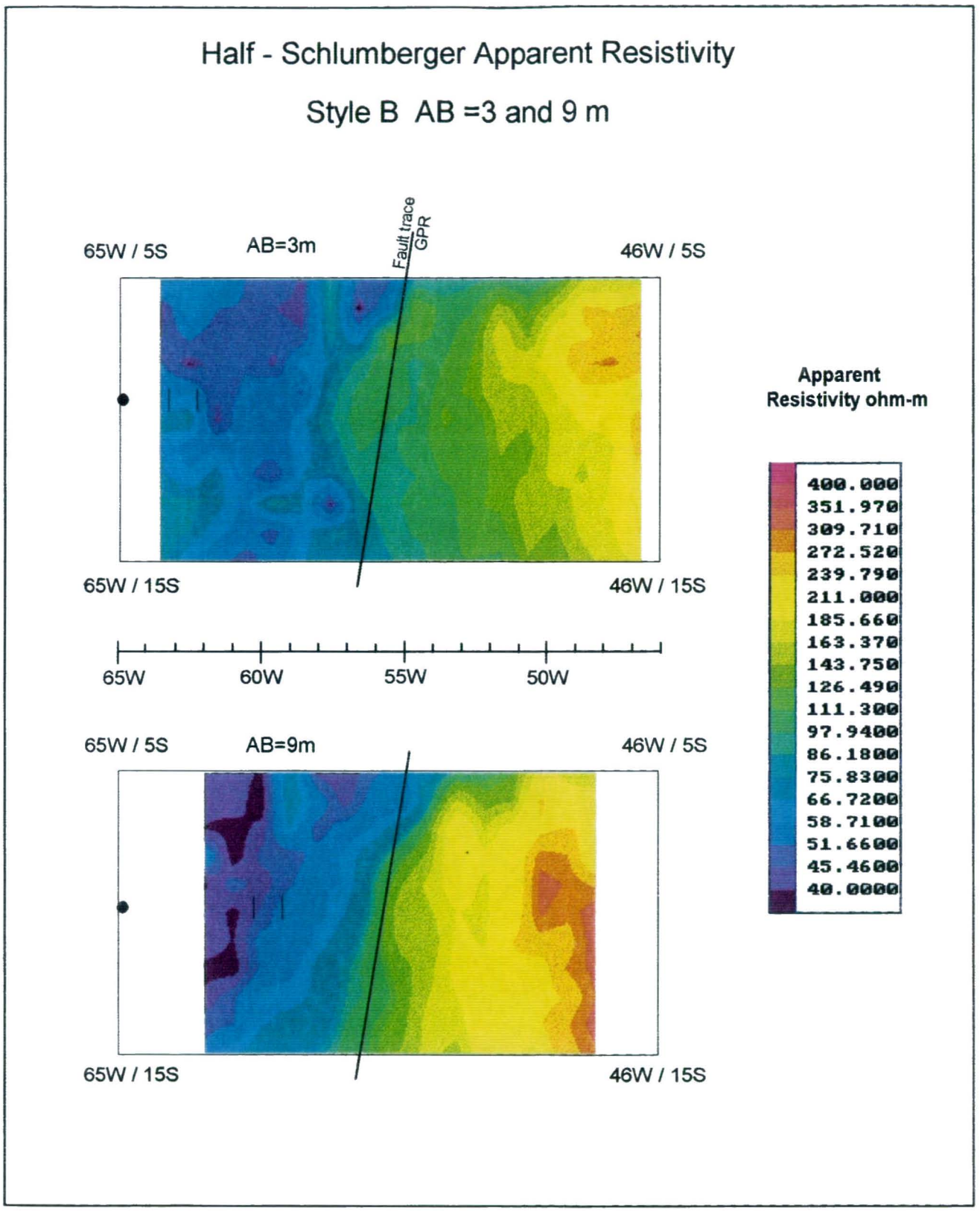

Figure 4 *rsc*. Test Site 2.1. Variable response from different depths of investigation (proportional to AB).

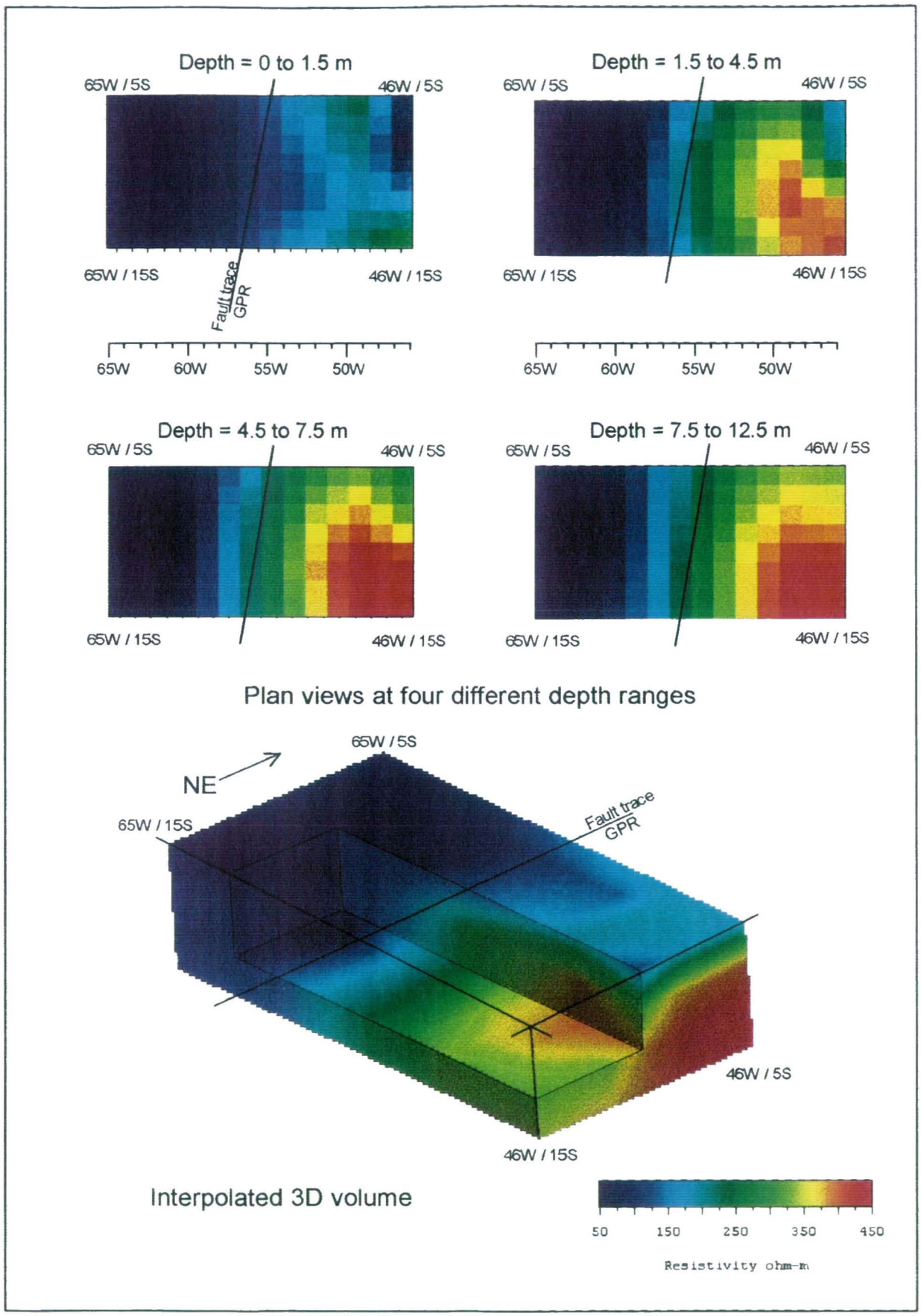

Figure 5 *rsc*. Test Site 2.1. Smooth inversion of resistivity data illustrating the 3D nature of the geological structure.

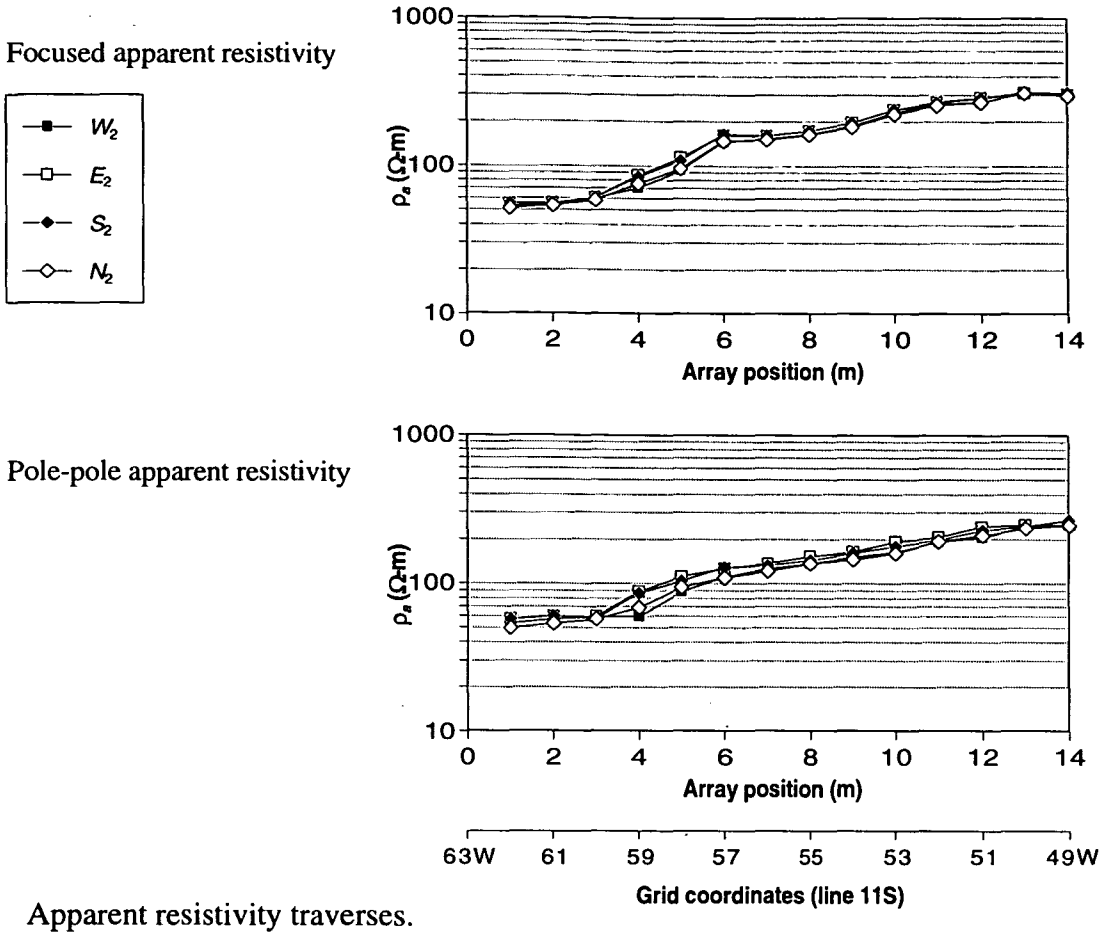

Figure 20 *rsc.* Apparent resistivity traverses.

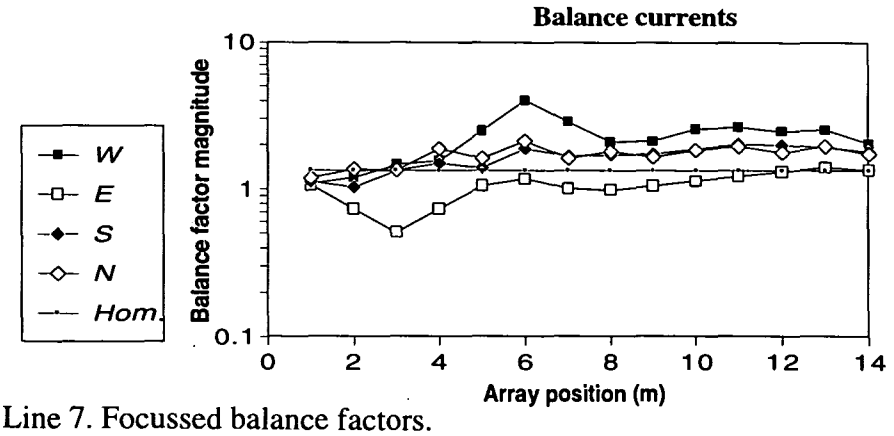

Figure 21 *rsc.* Test Site 2.1. Line 7. Focussed balance factors.

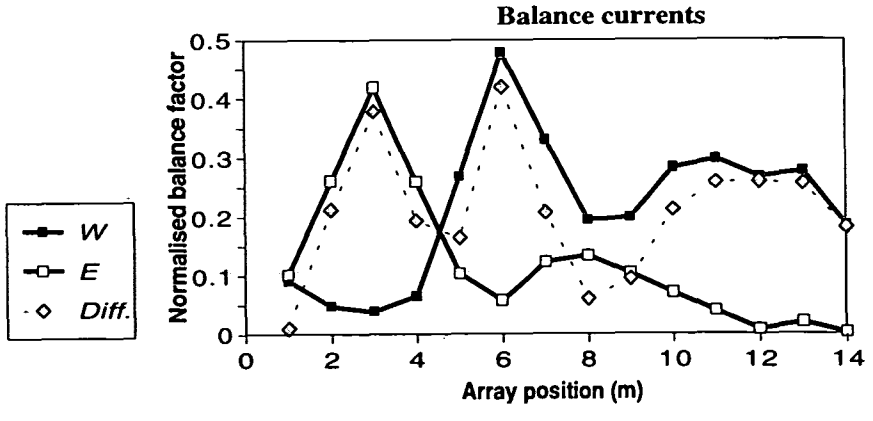

Figure 22 *rsc.* Test Site 2.1. Line 7. Normalised W-E balance factors.

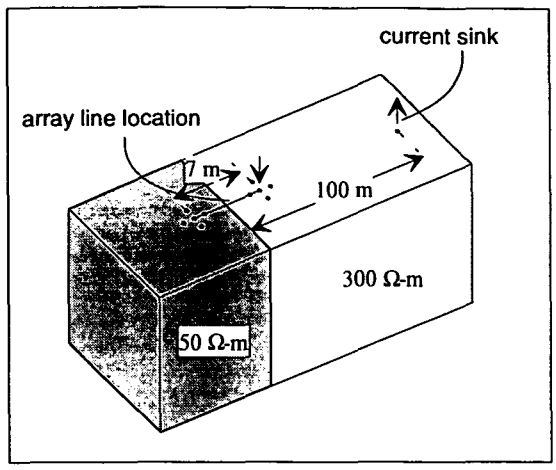

Figure 23 *rsc*. Idealised model of a vertical face.

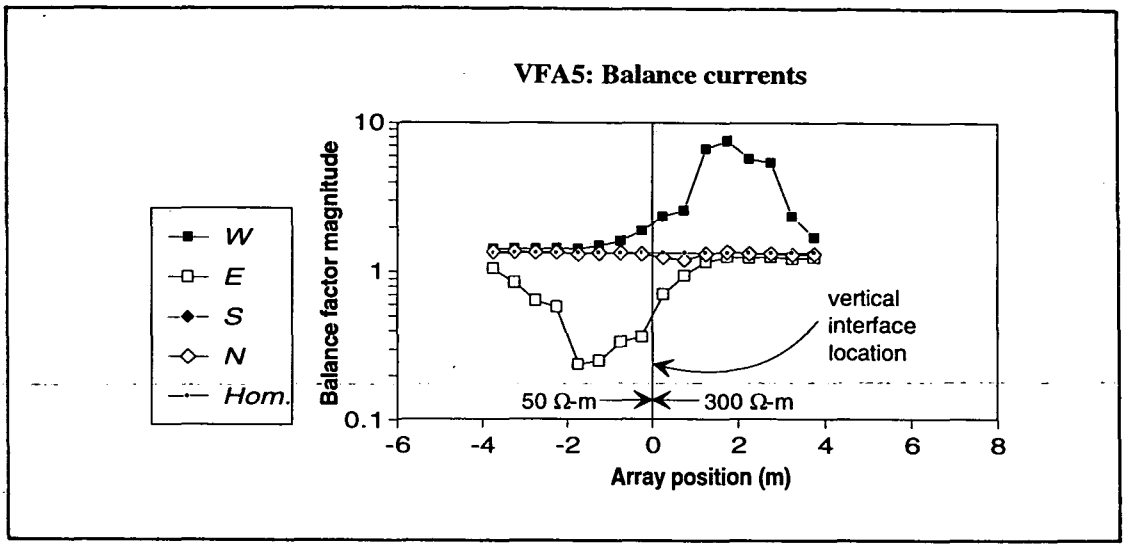

Figure 24 *rsc*. Vertical interface model results, Focussed balance factors.

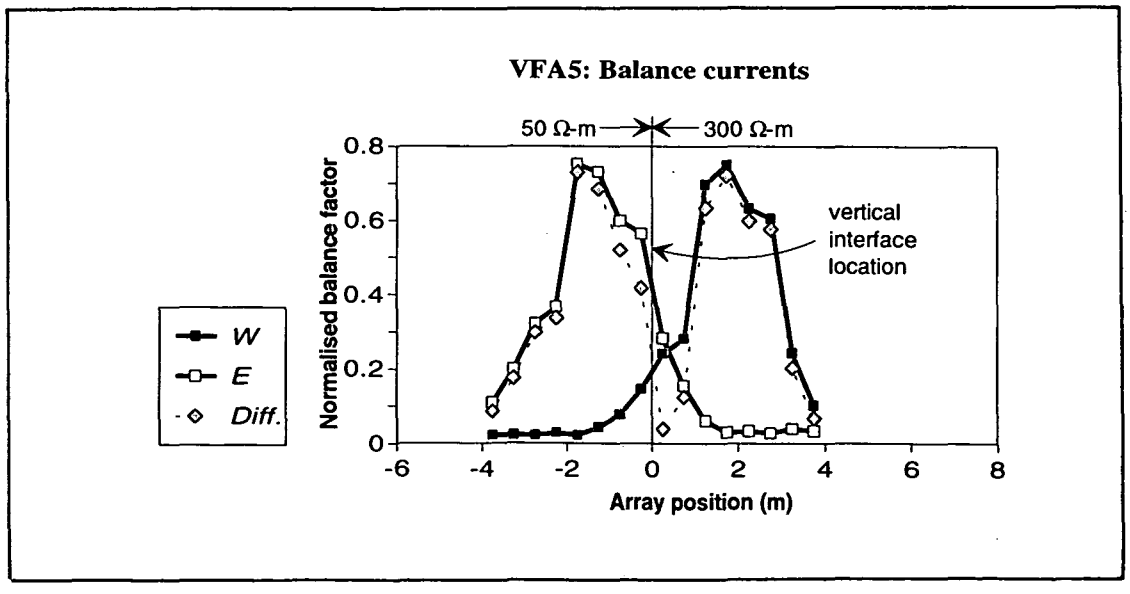

Figure 25 *rsc*. Vertical interface model results, Normalised W-E balance factors.

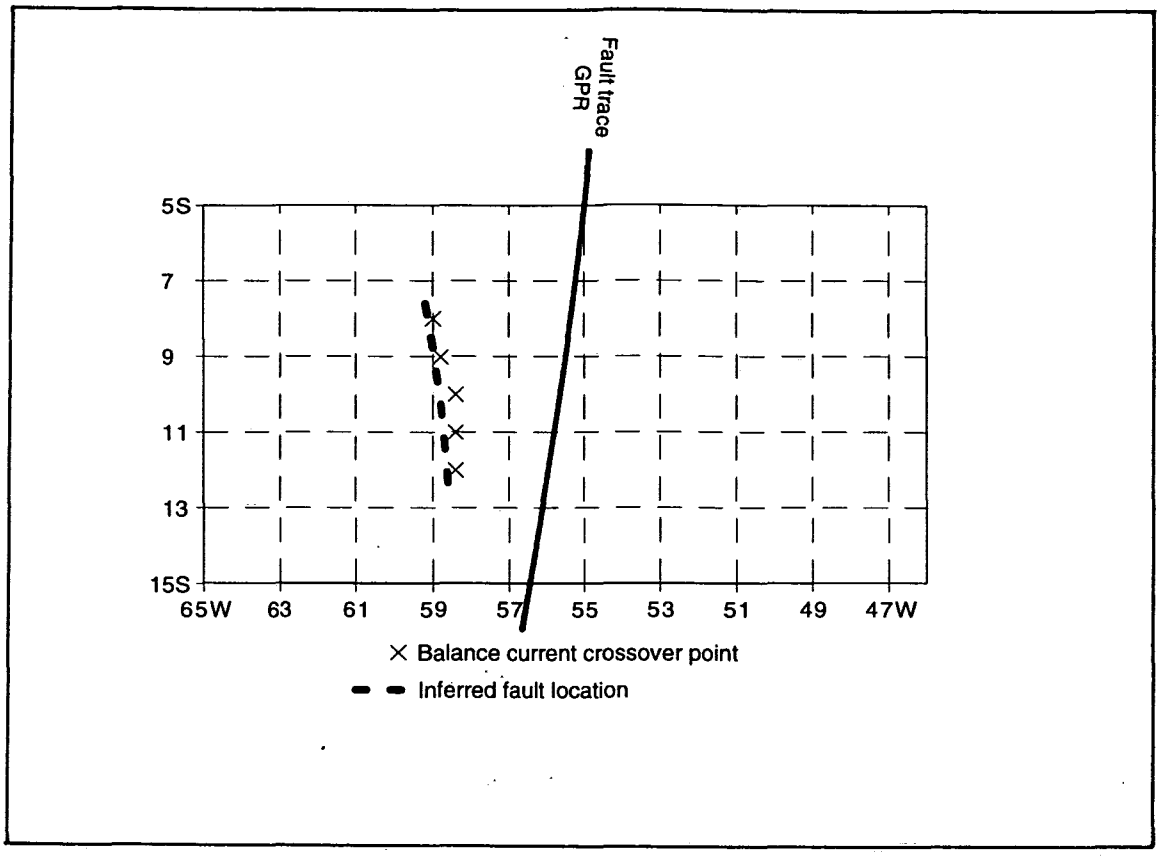

Figure 26 *rsc*. Test Site 2.1. Inferred surface location of fault trace.

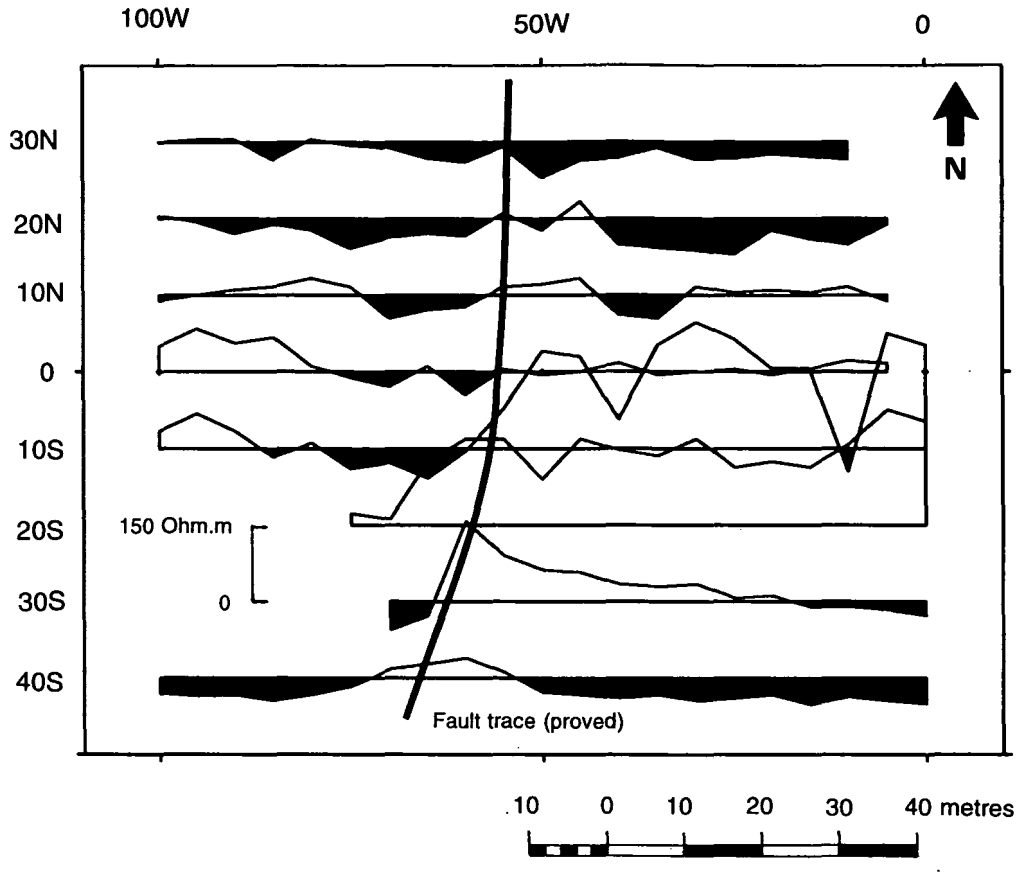

A. Arithmetic scale. Scale datum 100 Ohm.m

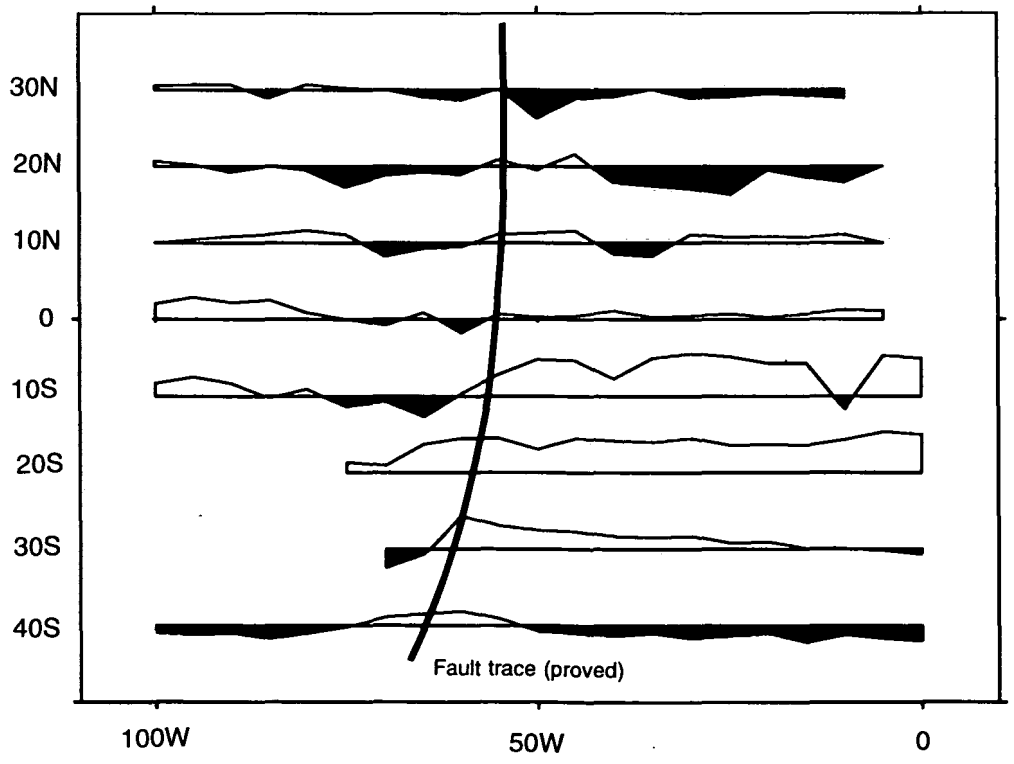

B. Logarithm scale. Scale datum 90 Ohm.m

Figure 20 *vlf.* Test Site 2.1. VLF R-field (Interuran data) profiles and proved fault trace.

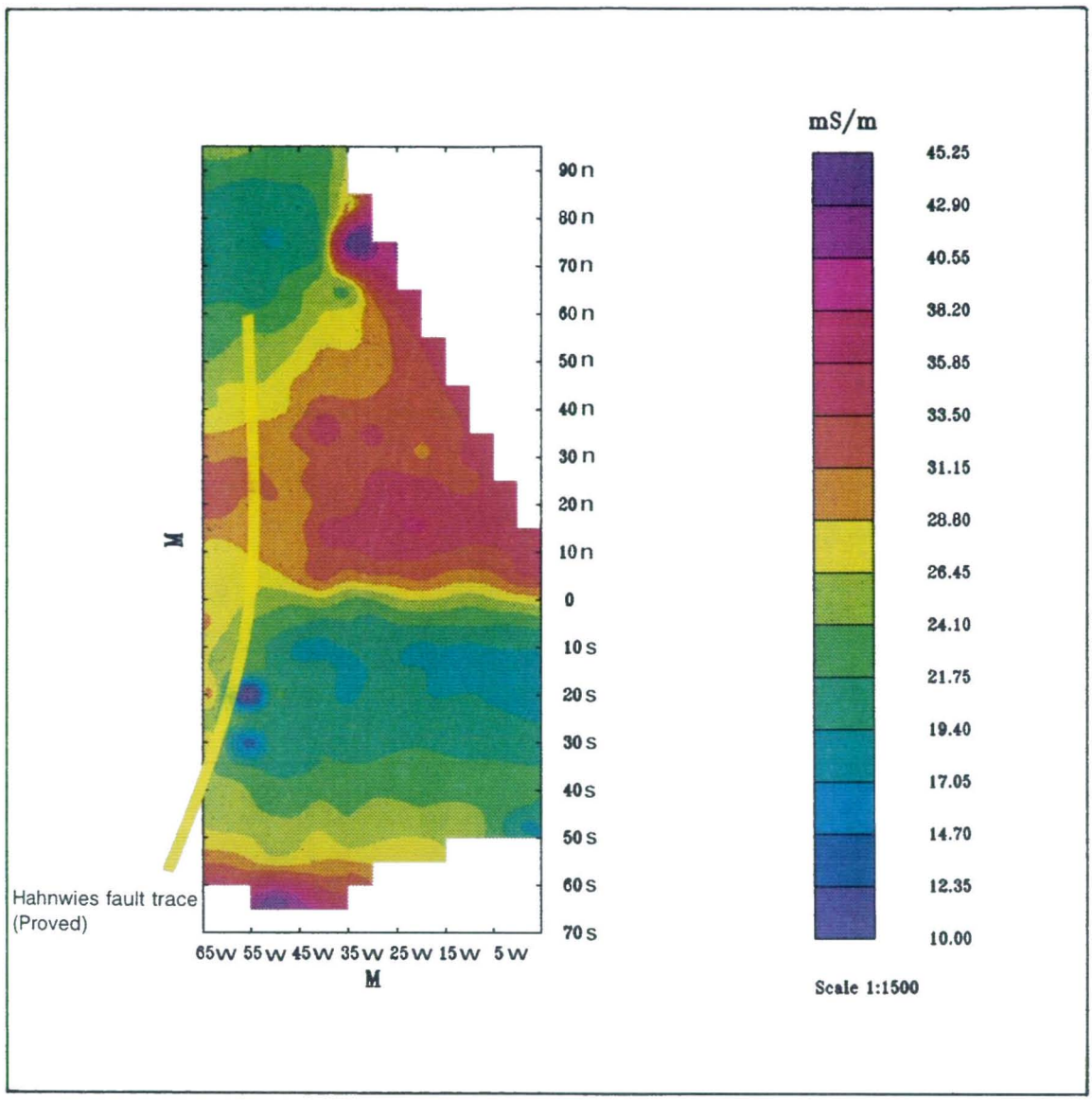

Figure 8 *em*. Test Site 2.1. Apparent conductivity contours (EM31 horizontal dipole).

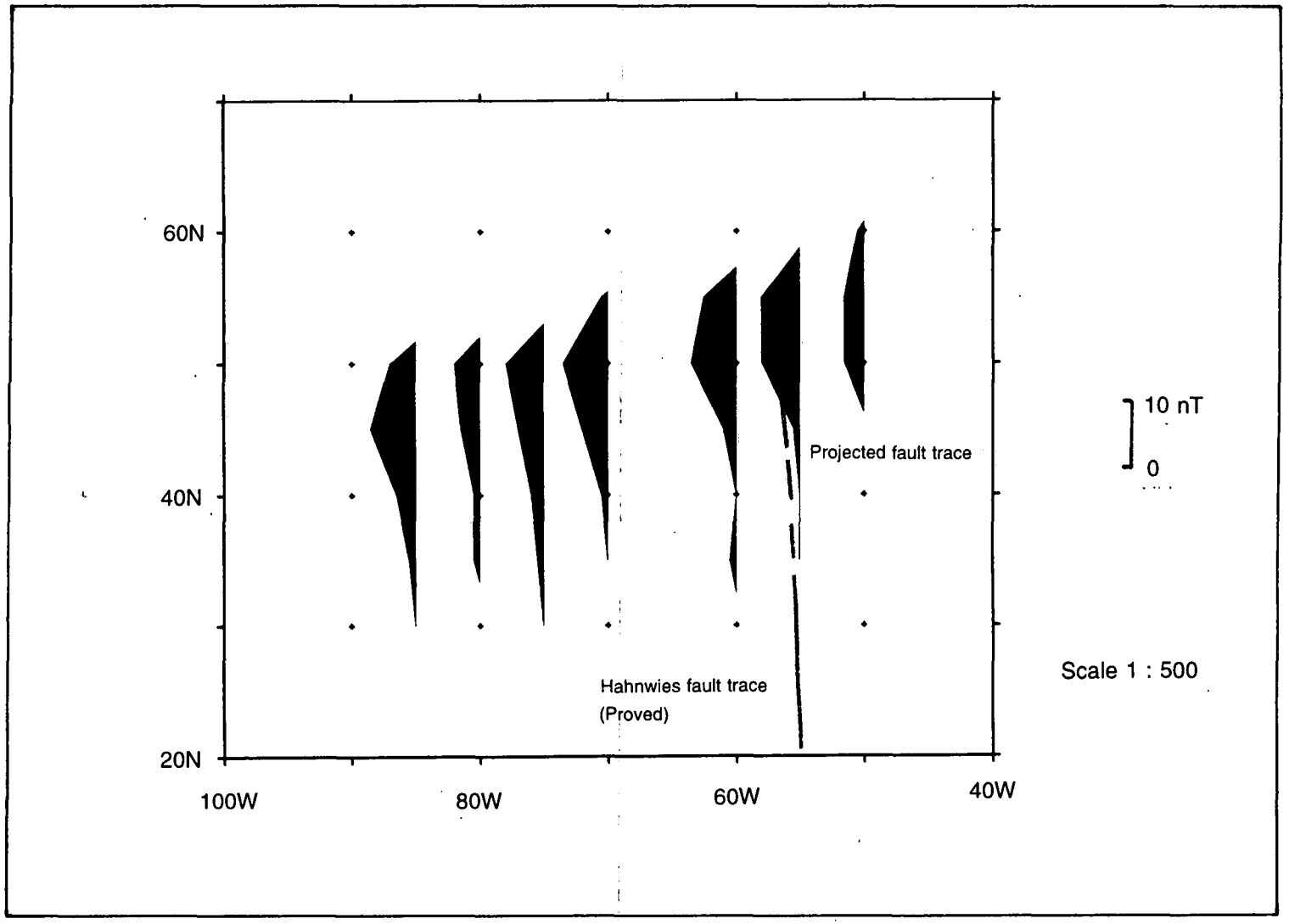

Figure 1 *mag*. Test Site 2.1. Total field magnetic profiles.

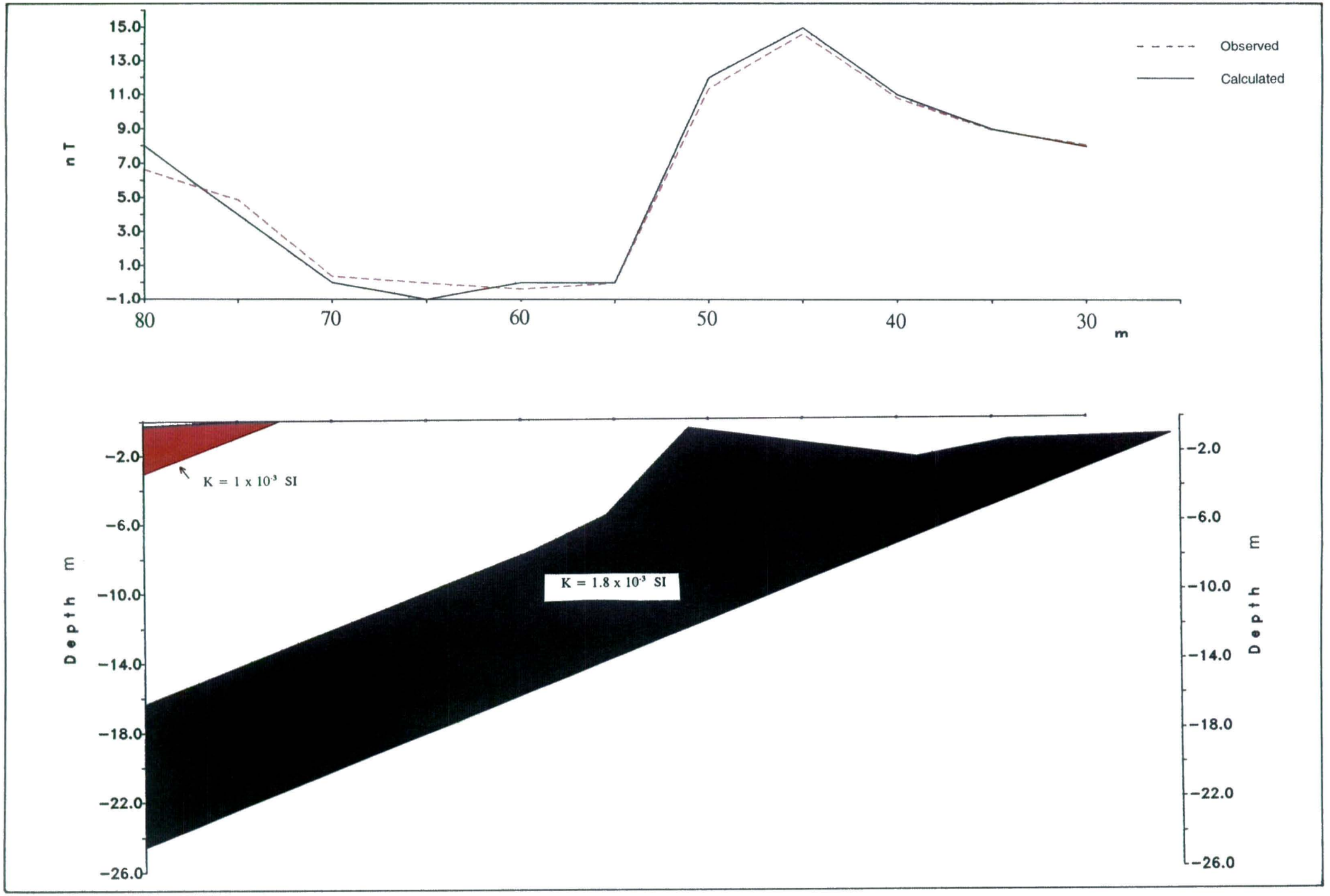

Figure 2 *mag*. Test Site 2.1. Magnetic model line 85W.

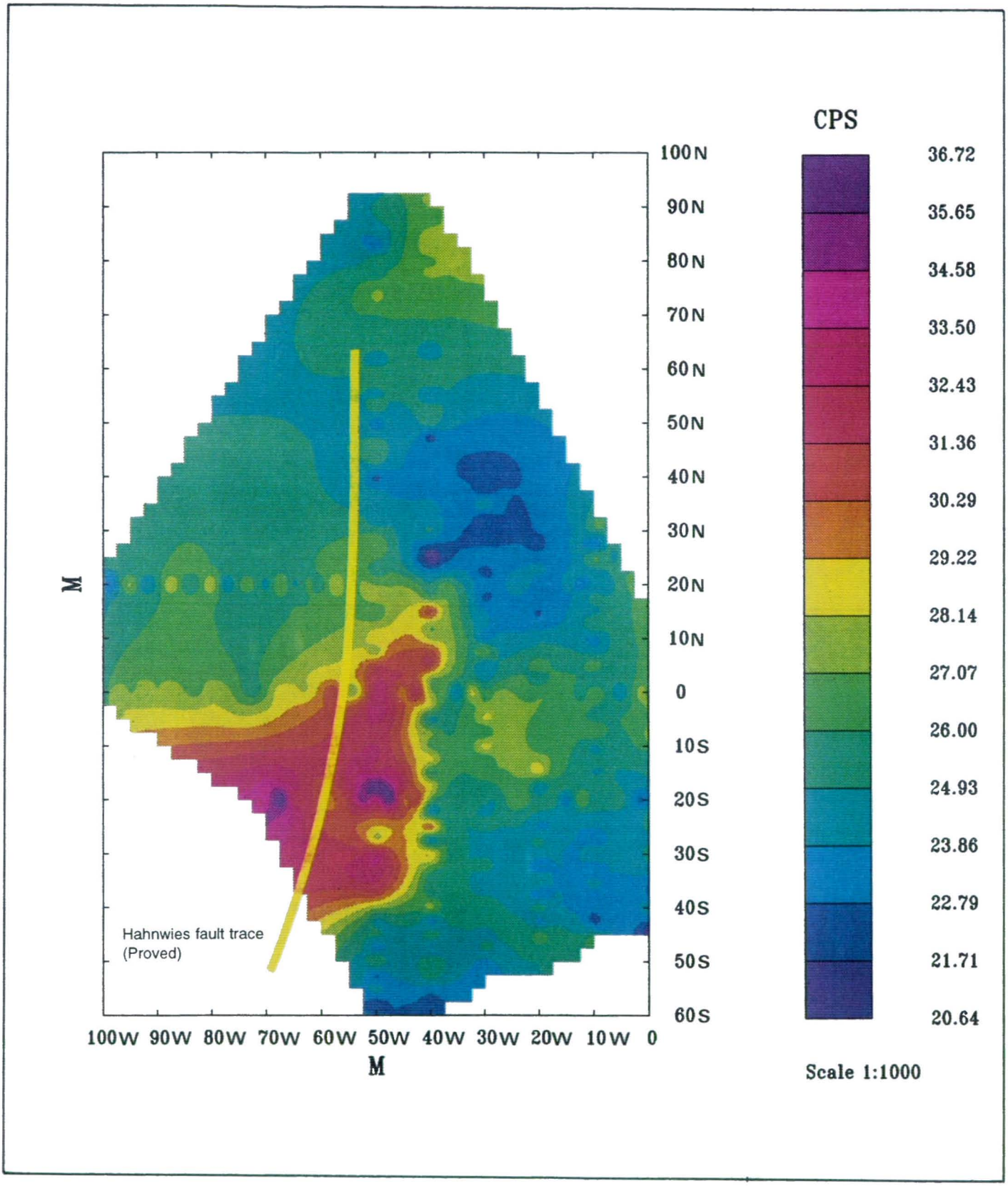

Figure 3 *gam.* Test Site 2.1. Natural gamma surface mapping.

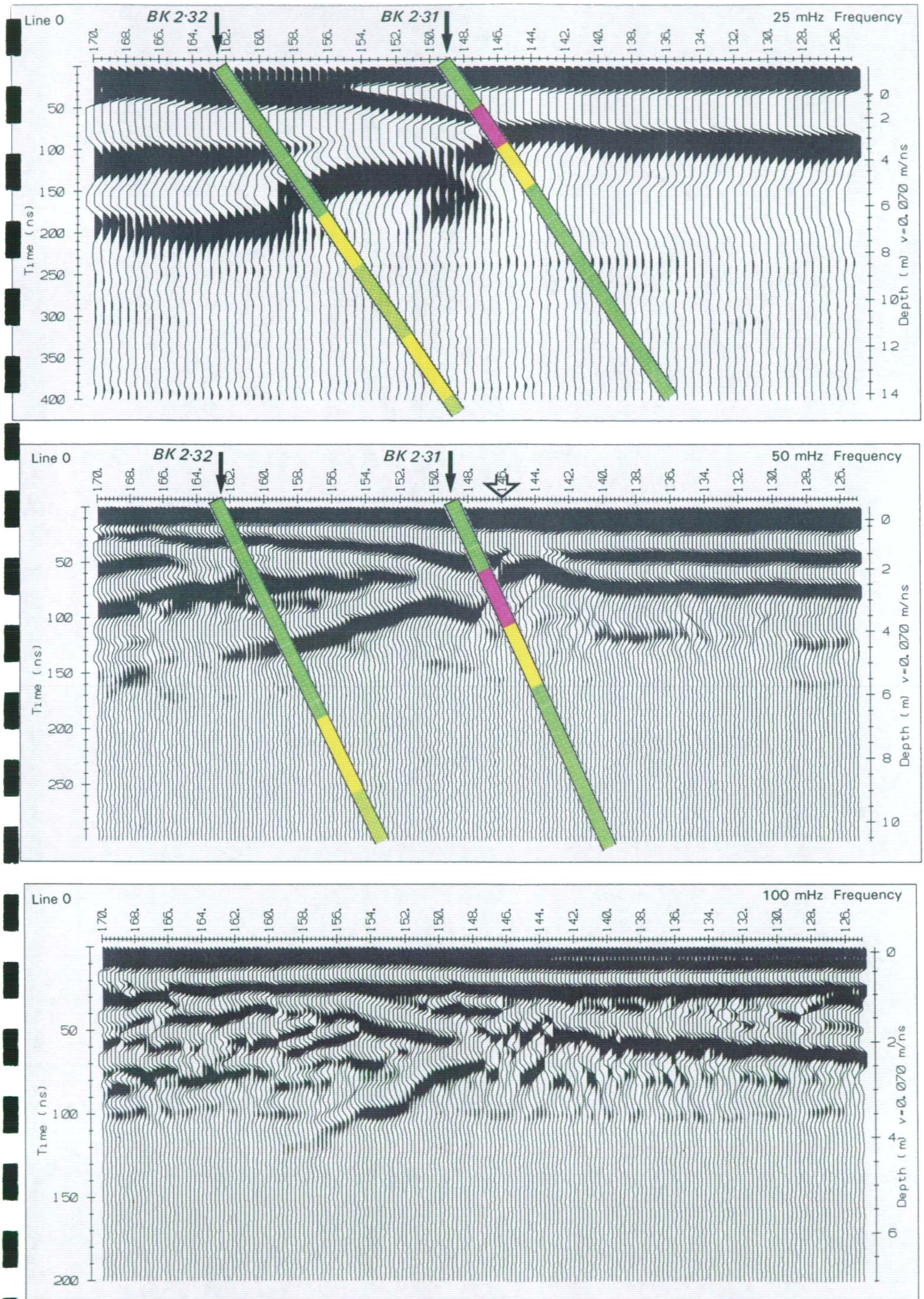

Figure 21 *gpr*. Test Site 2.3. GPR profile for line 0. Comparison of 25, 50, and 100 MHz antennae frequencies.

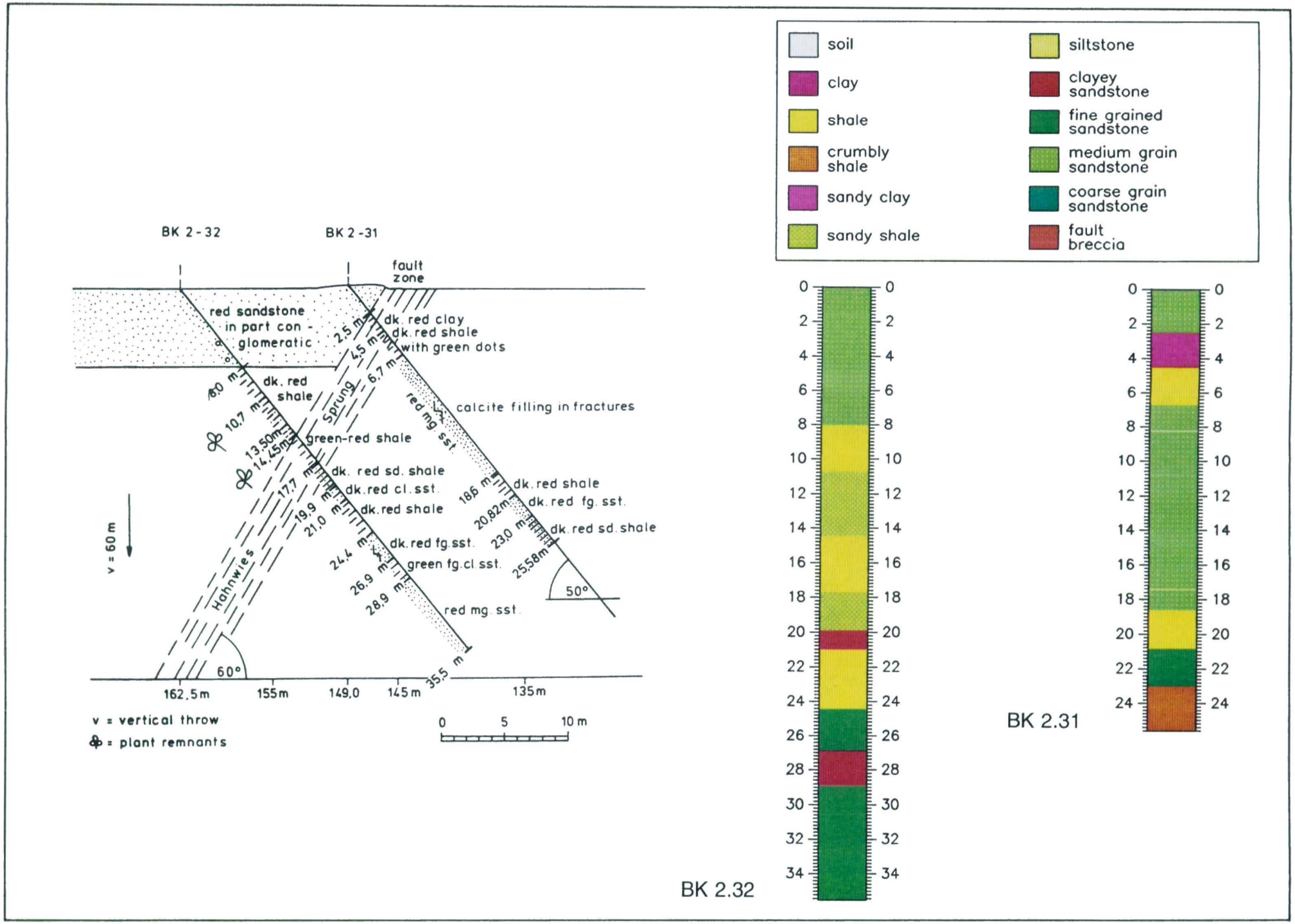

Figure 20. Test Site 2.3. Geological section: boreholes BK2.31 and BK2.32.

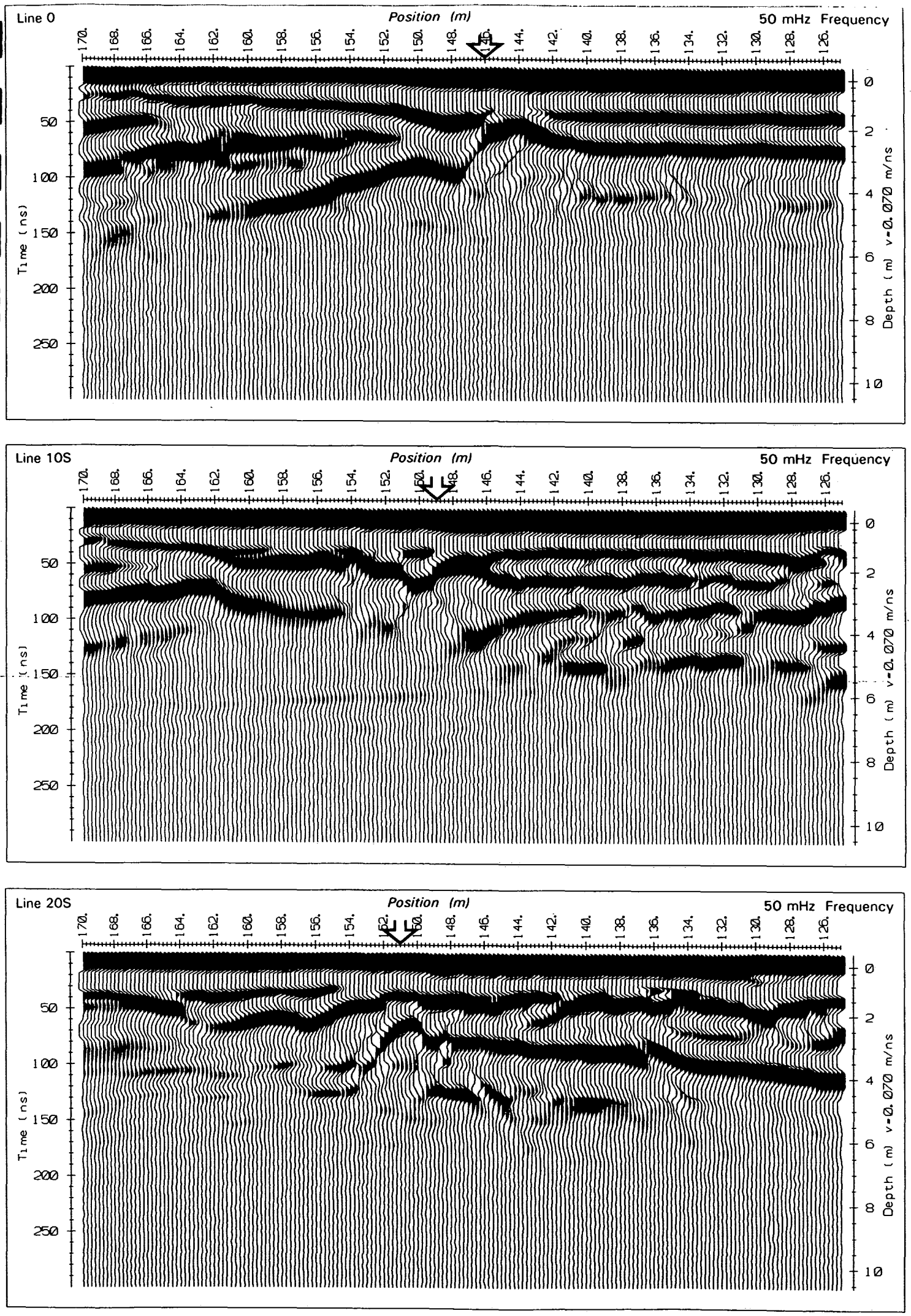

Figure 22 *gpr*. Test Site 2.3. GPR profiles for lines 0, 10S, and 20S. 50 MHZ antennae.

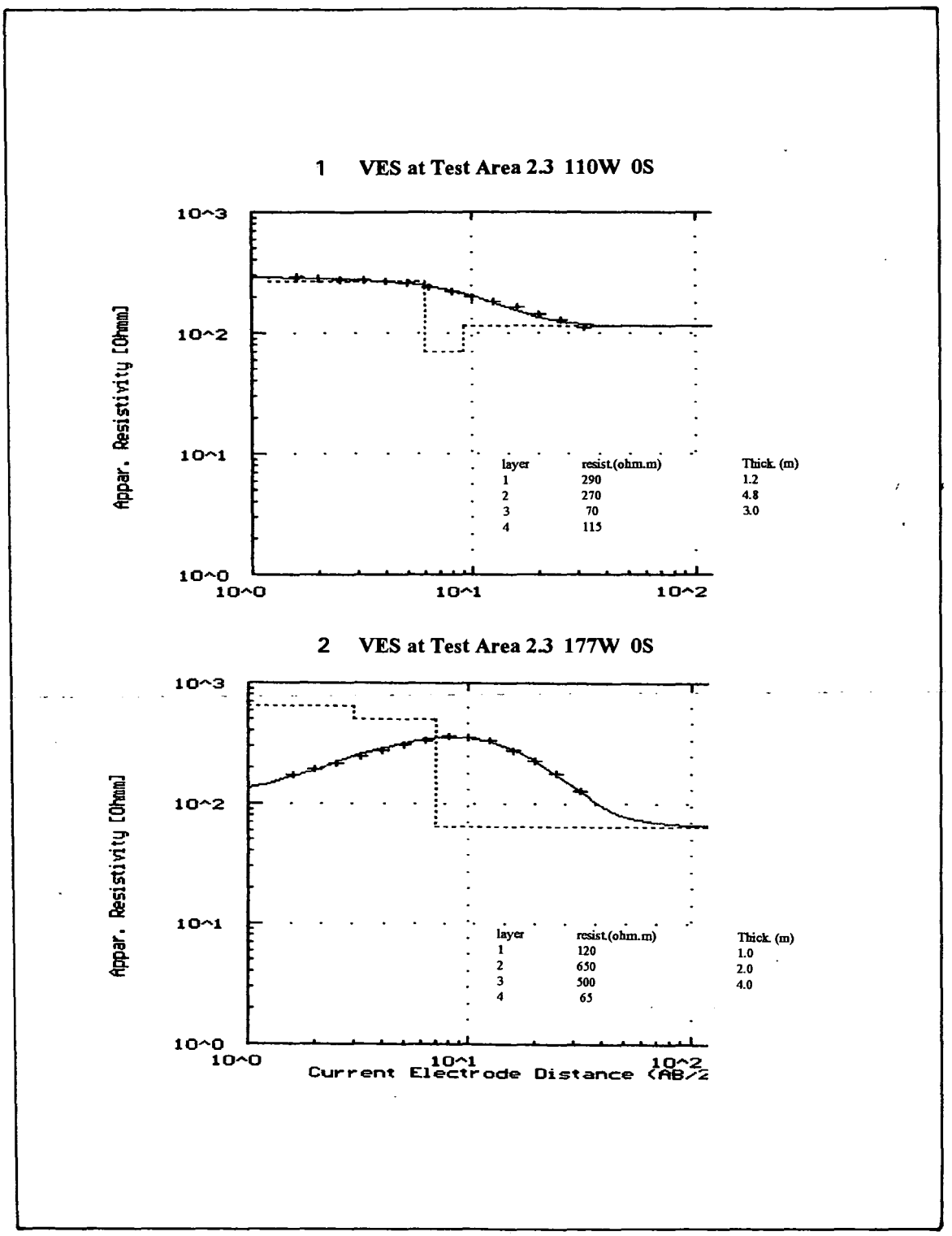

Figure 11 *res.* Test Site 2.3. Interpretation of VES 1, and 2.

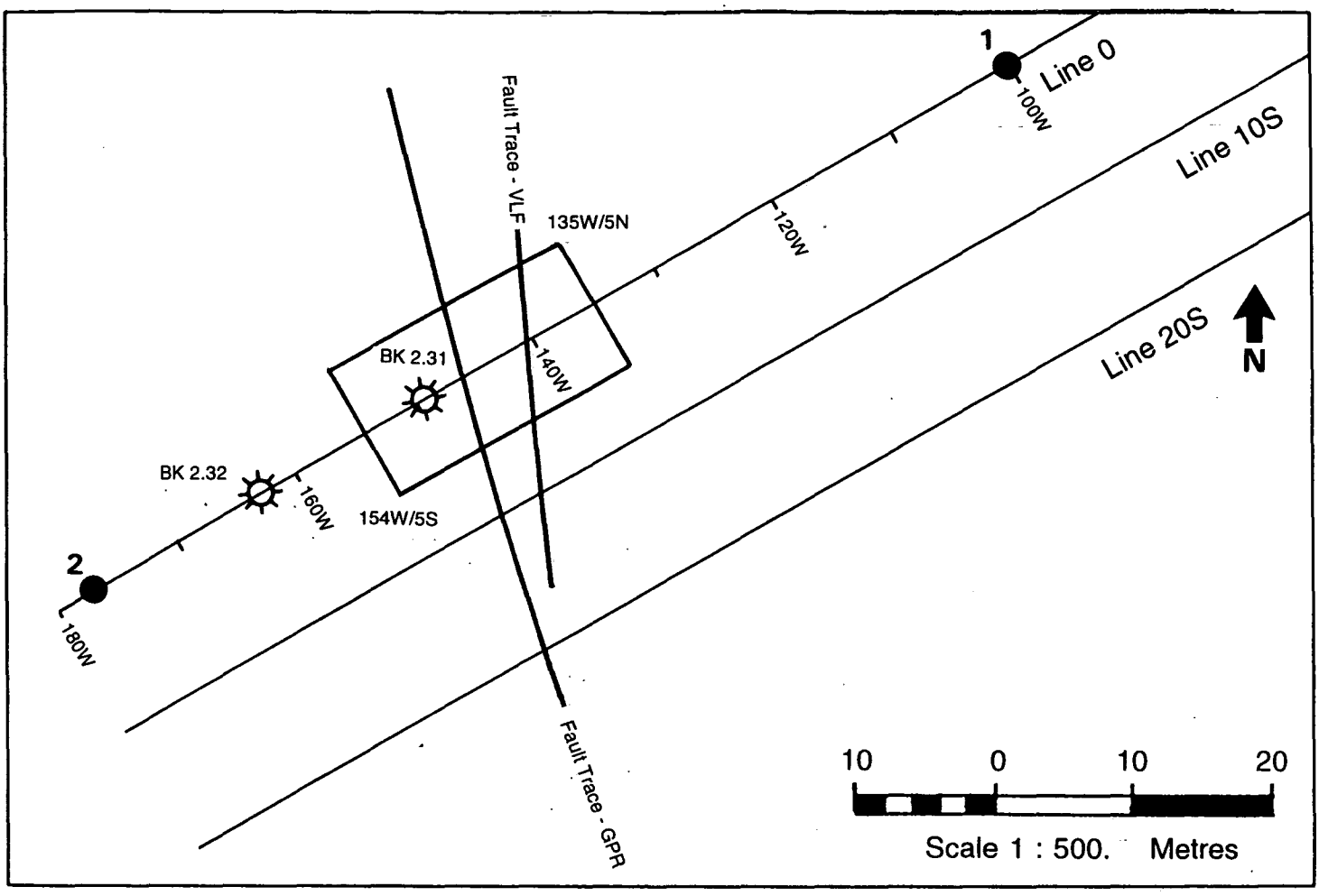

Figure 32 *rsc*. Test Site 2.3. Plan (partial) of site showing location of RESCAN grid.

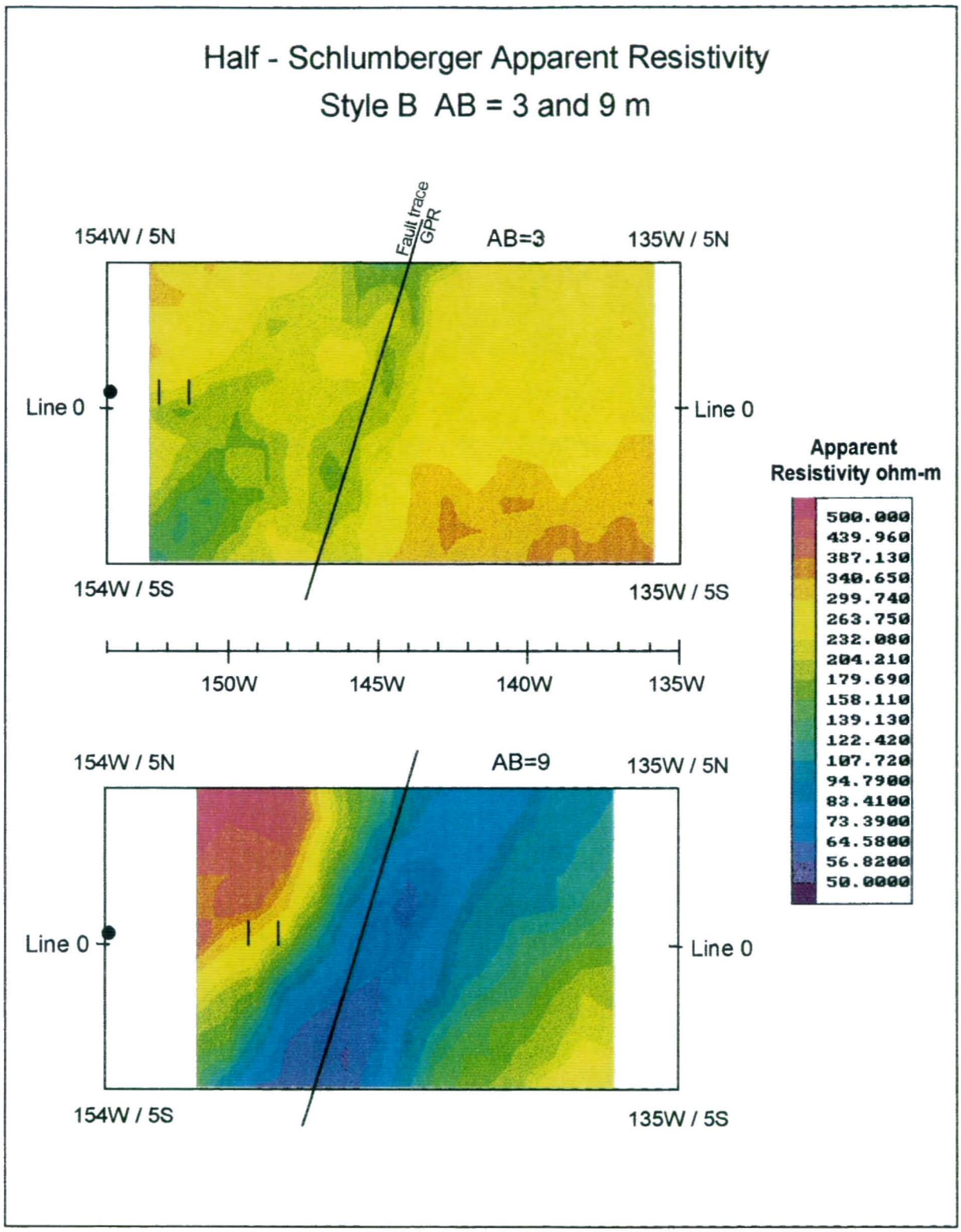

Figure 6 *rsc*. Test Site 2.3. Apparent resistivity maps for two depths of investigation.

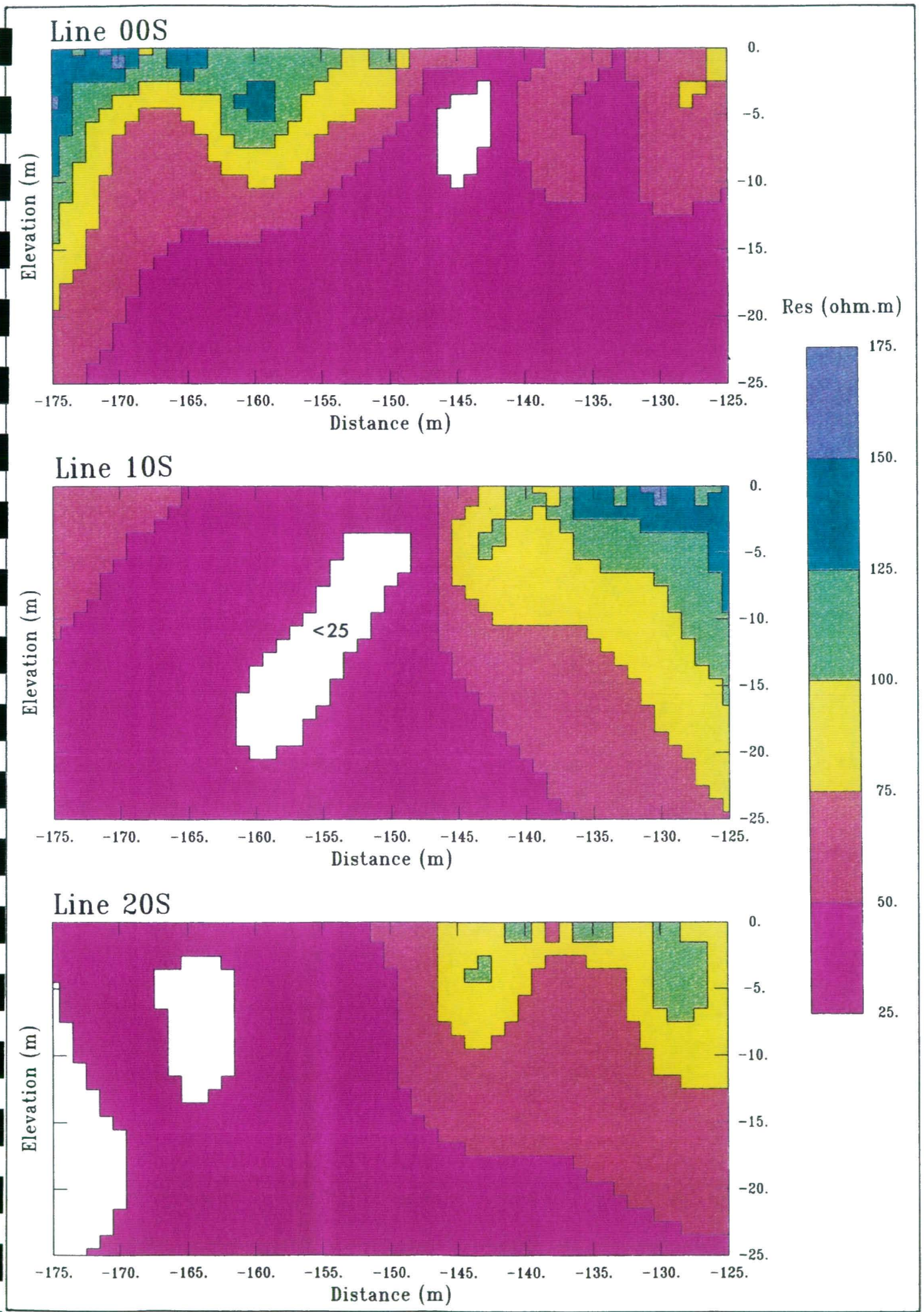

Figure 21 *vlf.* Test Site 2.3. Modelled resistivity cross sections for lines 0, 10S, and 20S.

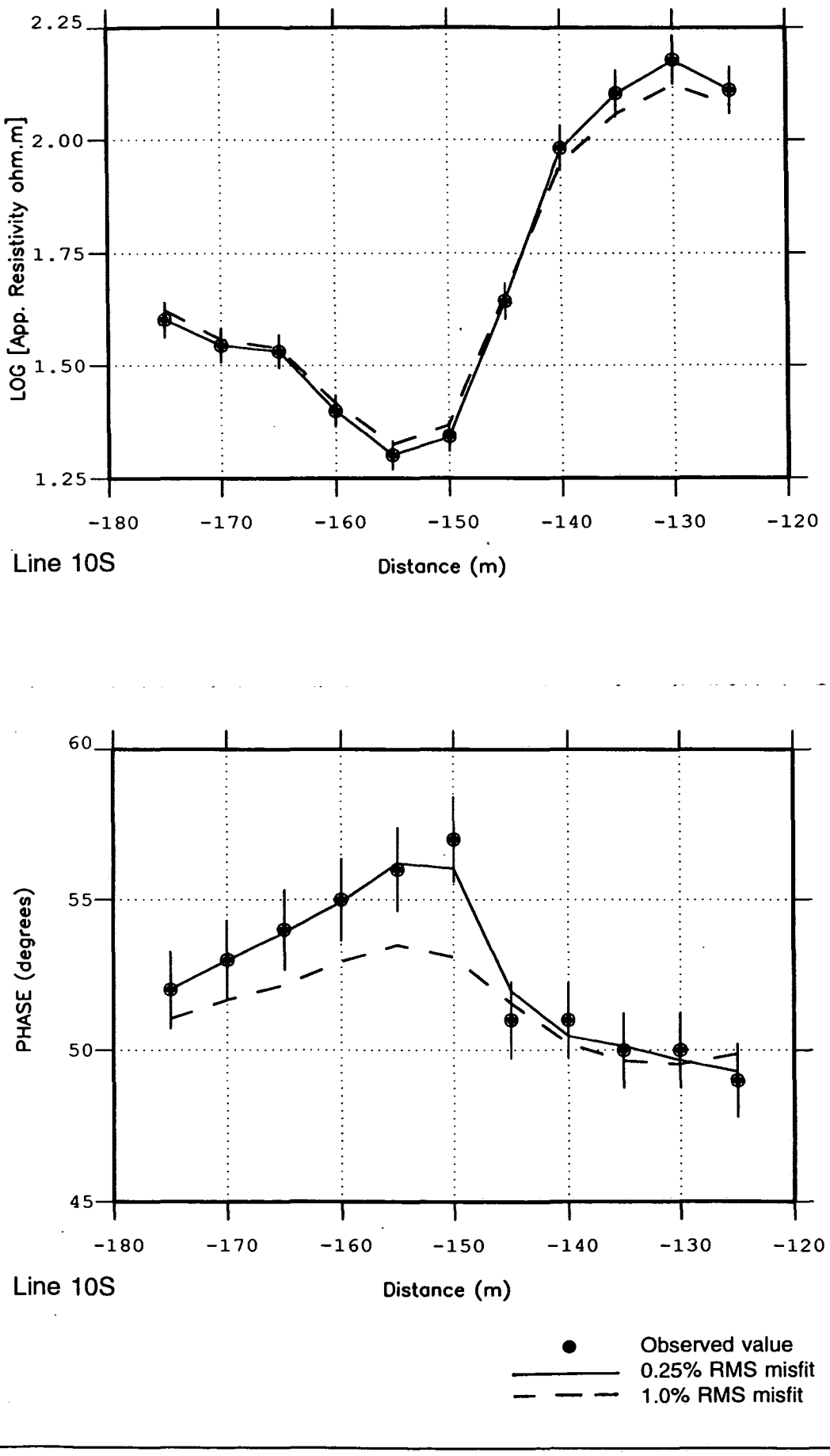

Figure 22 *vlf.* Test Site 2.3. Occam inversion: levels of fit of models to observed data.

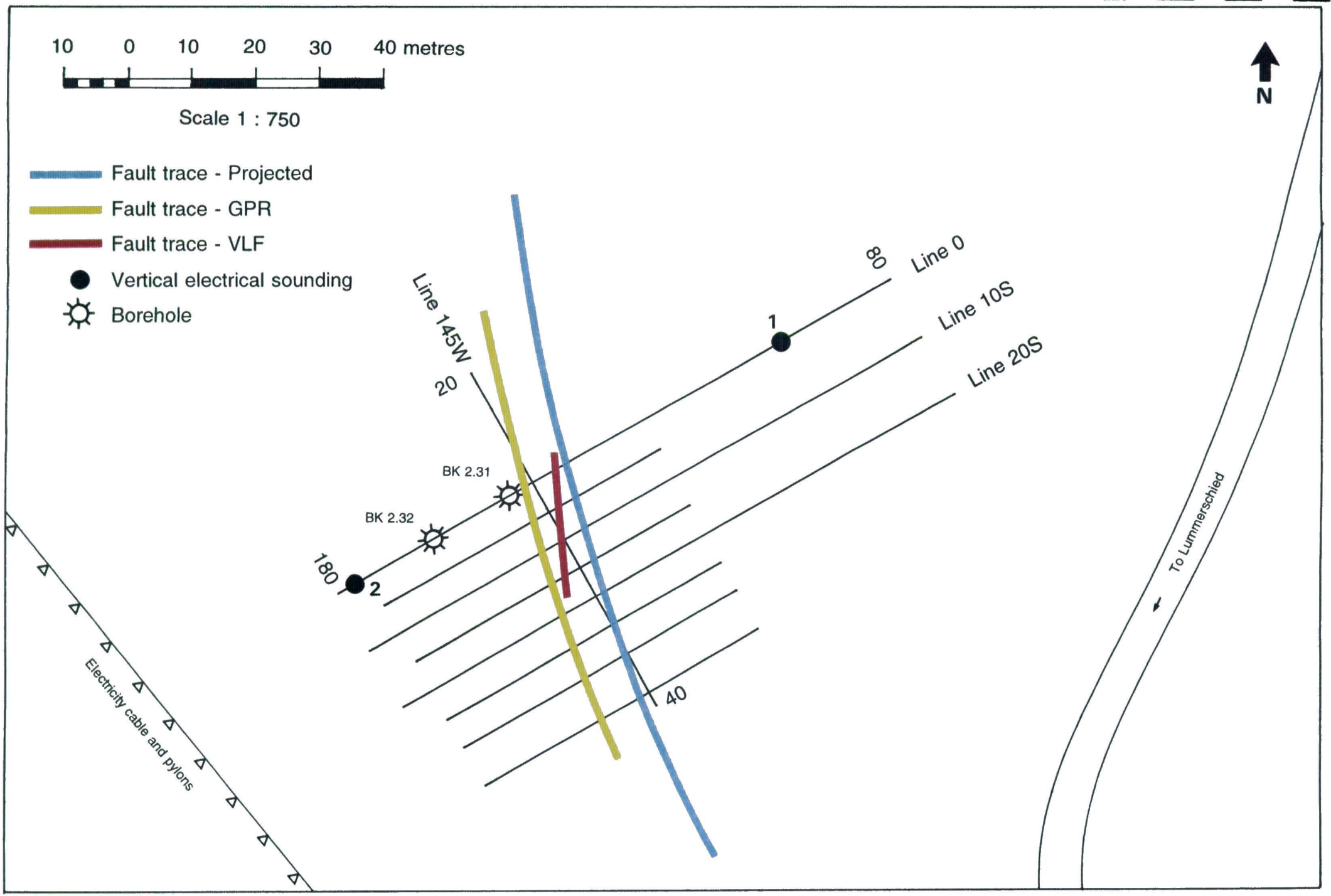

Figure 19. Test Site 2.3. Geophysical grid, borehole locations, and interpretation.

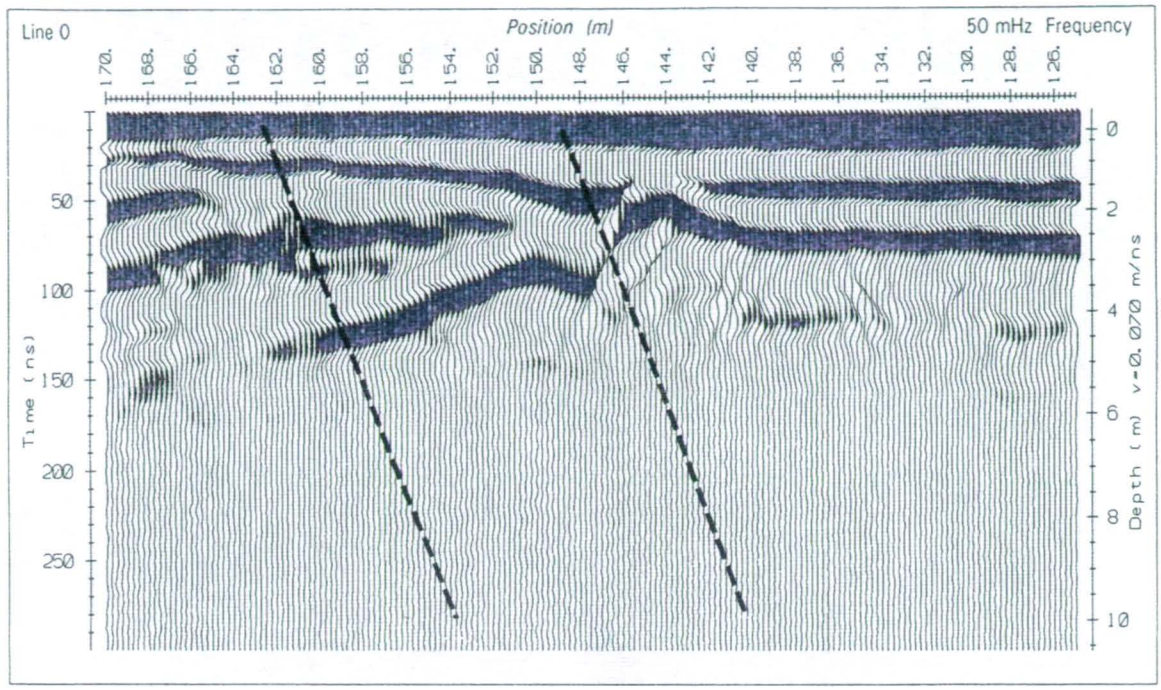

Ground Probing Radar (50MHz)
dx = 0.25m, V.E. x 2.3

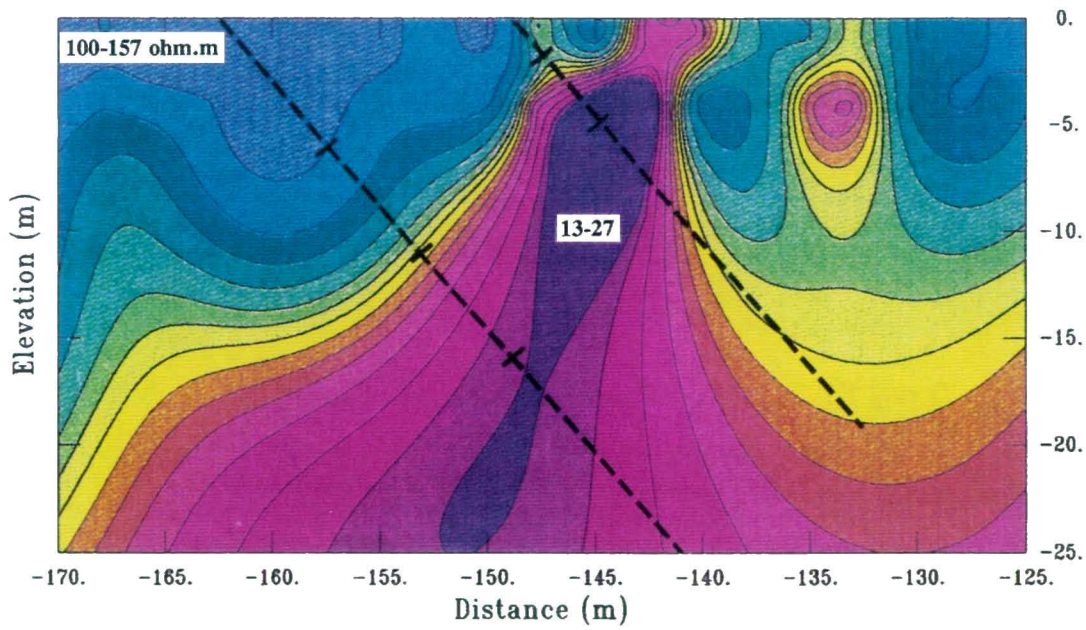

VLF (16kHz) Resistivity Model (Equal Area Colour)
dx = 5m, True Scale

Figure 23 *vlf*. Test Site 2.3. Coincident GPR and VLF resistivity cross sections for line 10S.

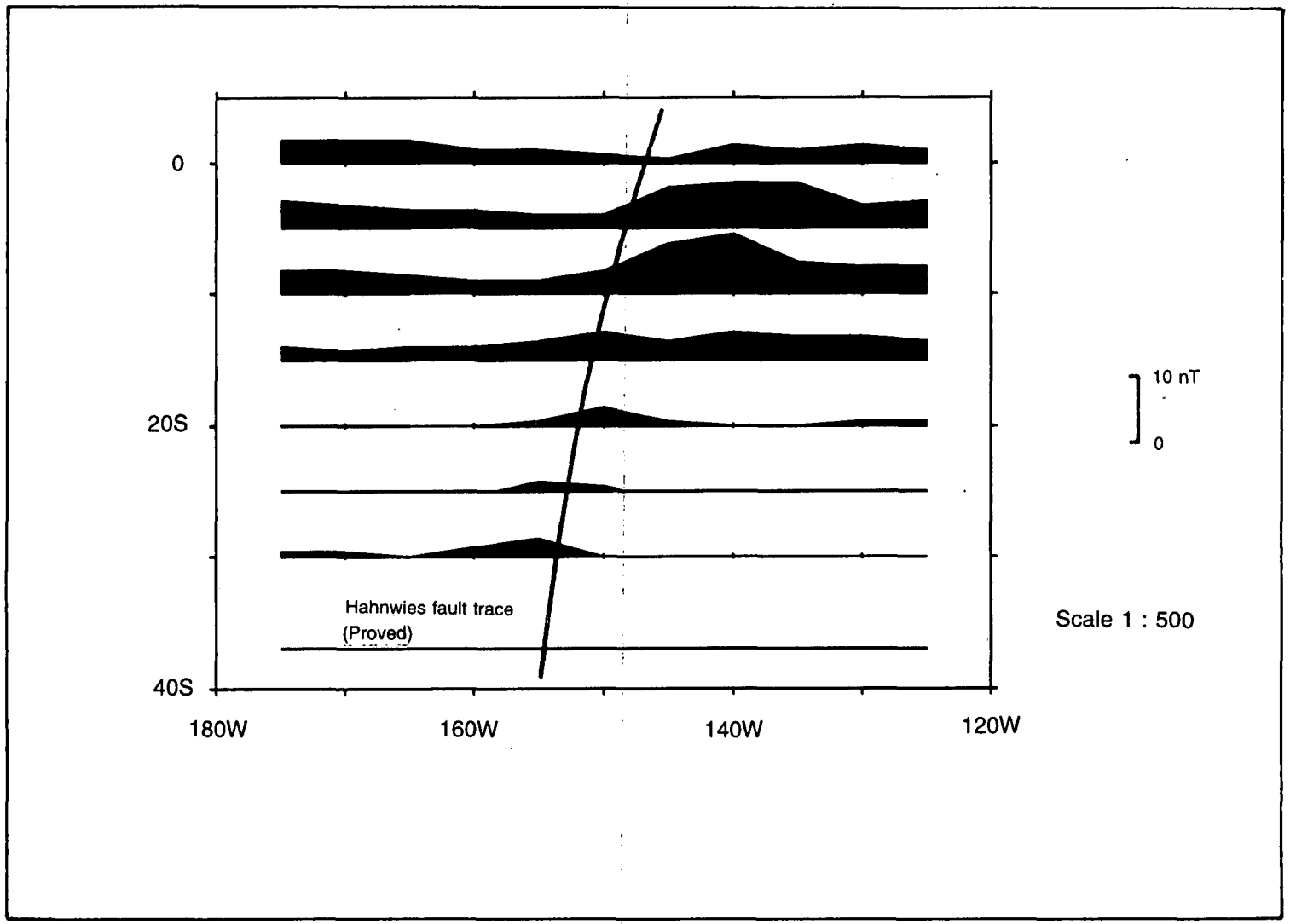

Figure 3 *mag*. Test Site 2.3. Total field magnetic profiles.

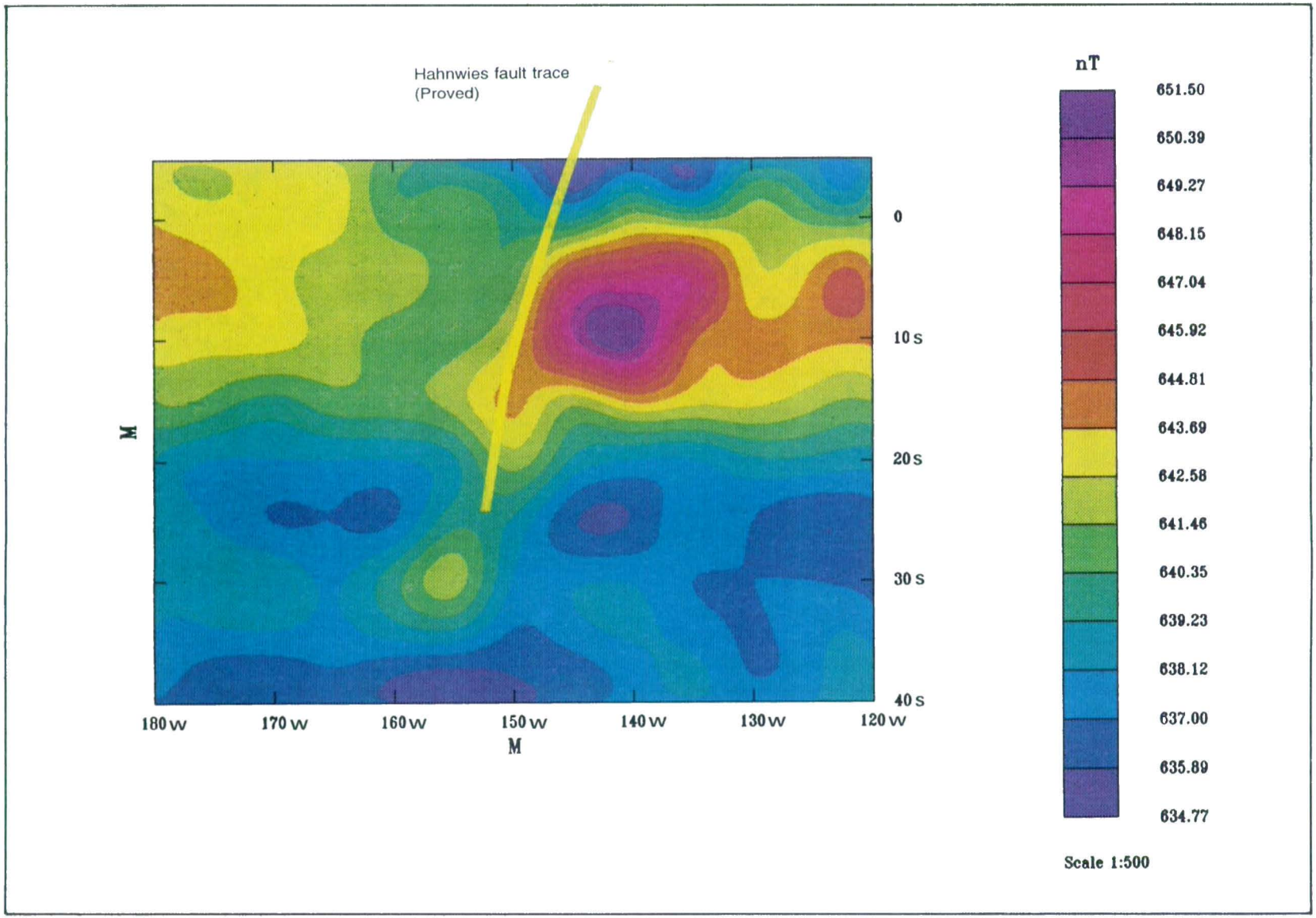

Figure 4 *mag*. Test Site 2.3. Total field magnetic contours.

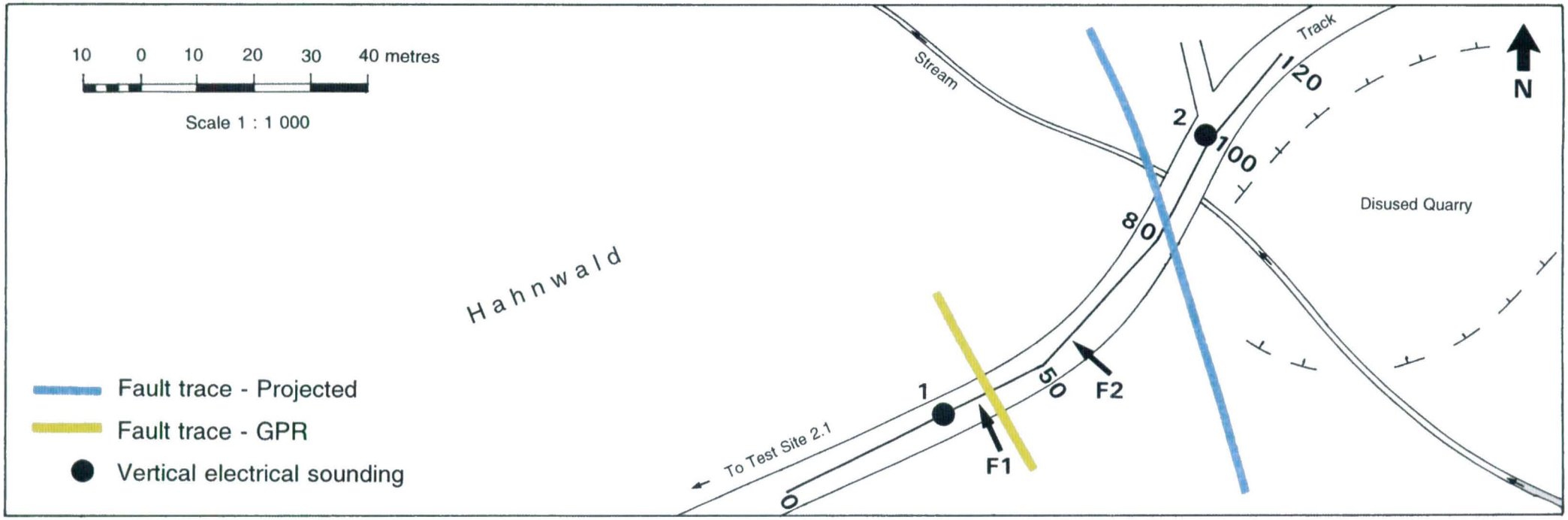

Figure 21. Test Site Hahnwald. Hahnwald traverse and interpretation.

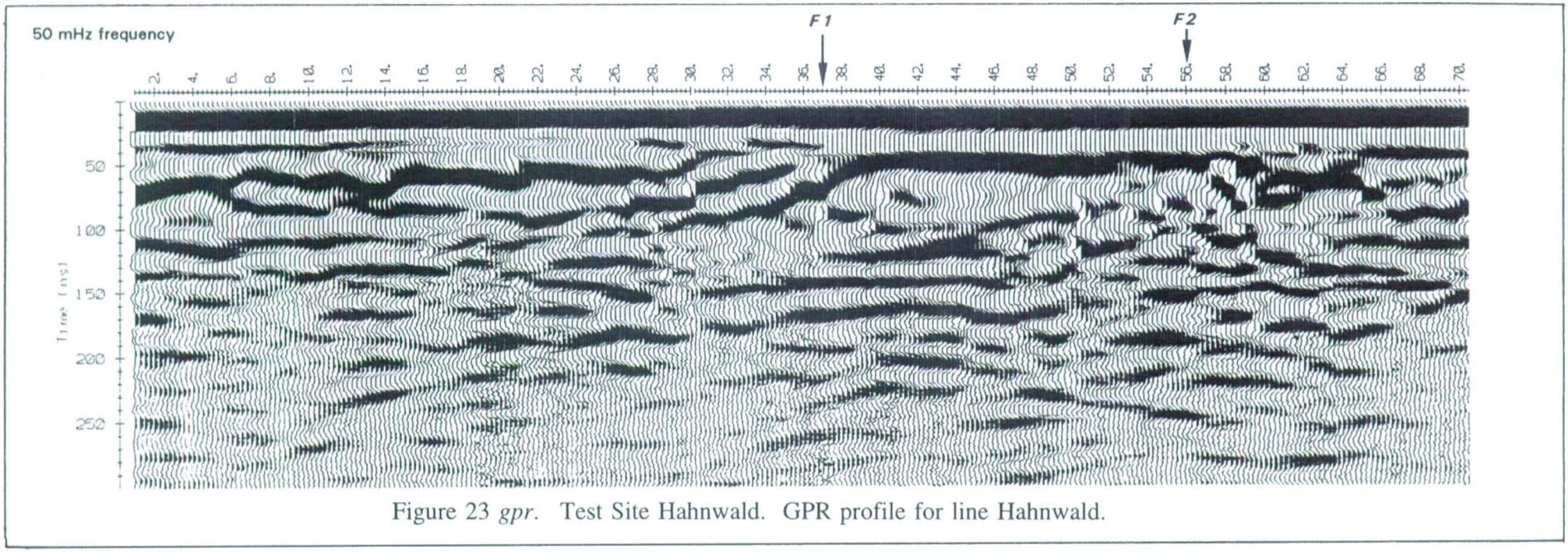

Figure 23 *gpr*. Test Site Hahnwald. GPR profile for line Hahnwald.

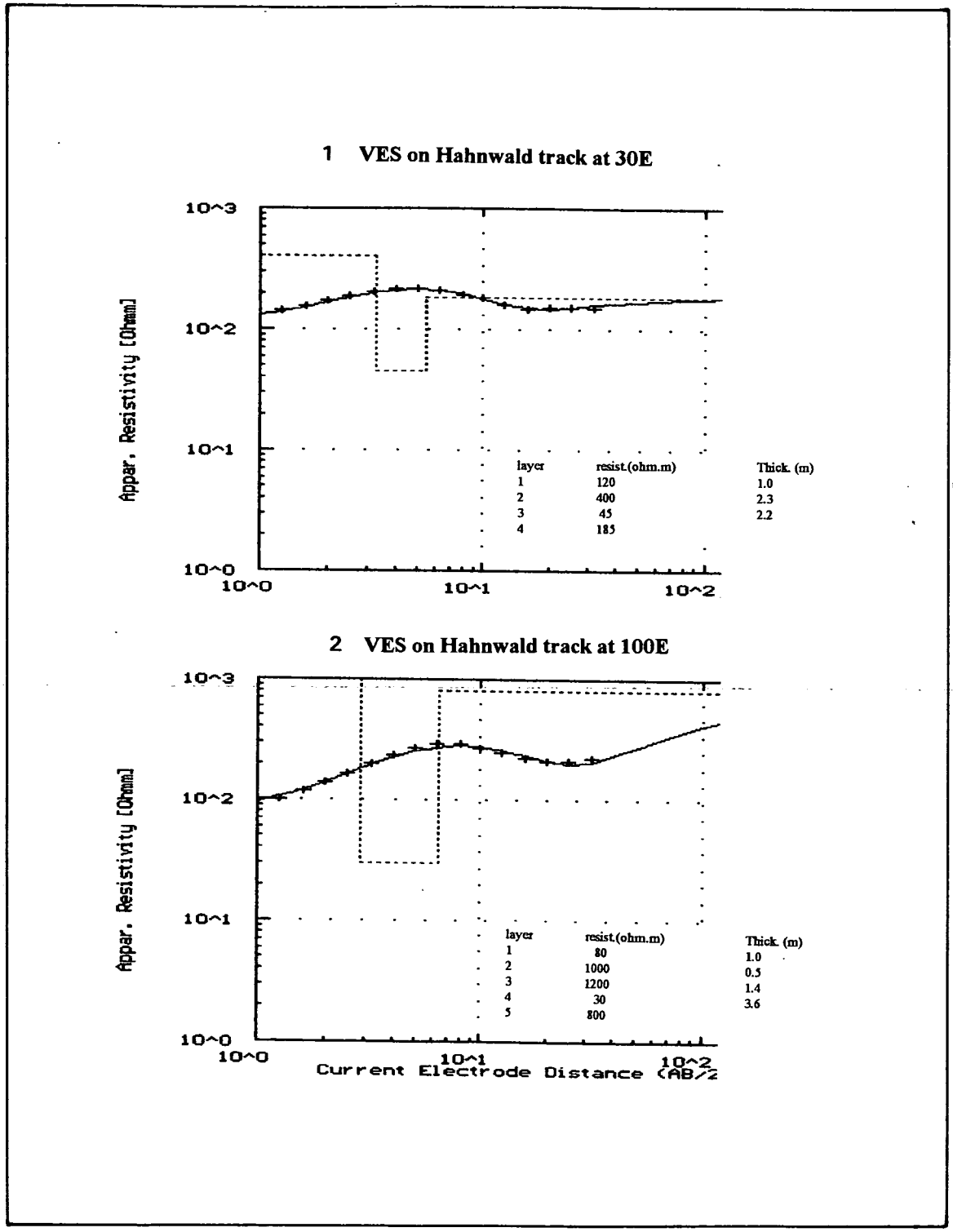

Figure 12 *res.* Hahnwald track. Interpretation of VES 1, and 2.

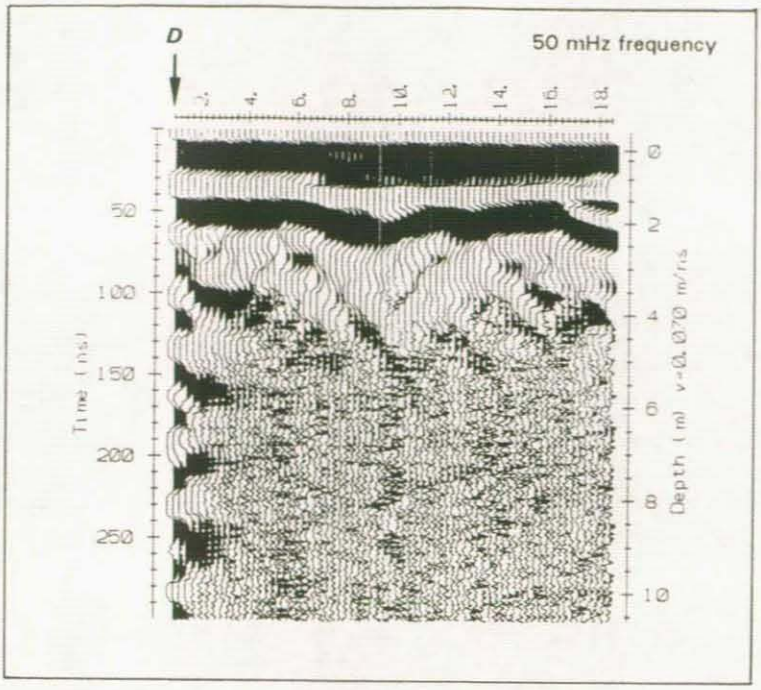

Figure 24 *gpr*. Test Site 2.5. GPR profile for line Fence.

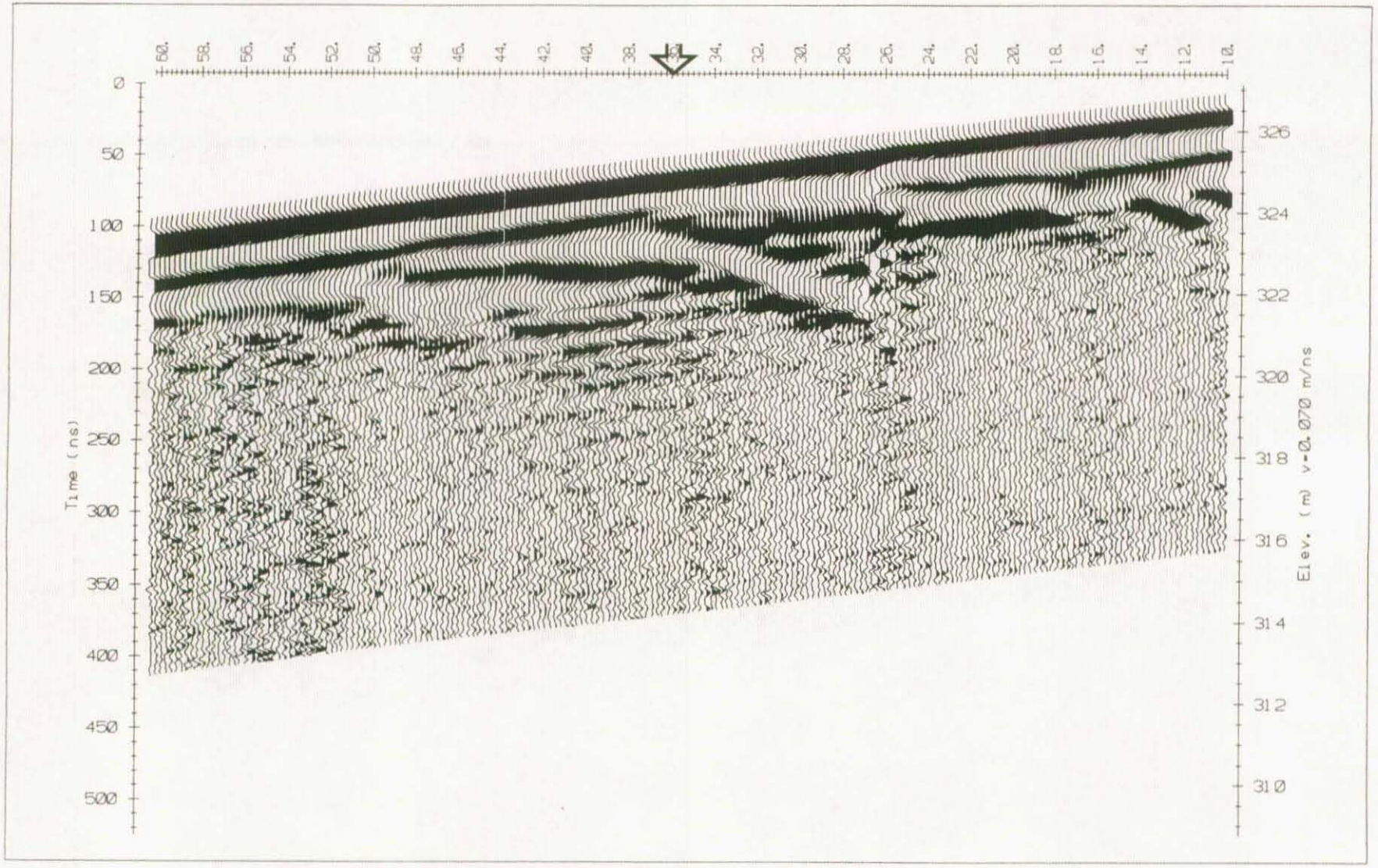

Figure 25 *gpr*. Test Site 3.1. GPR profile for line 80W. 50 MHz antennae.

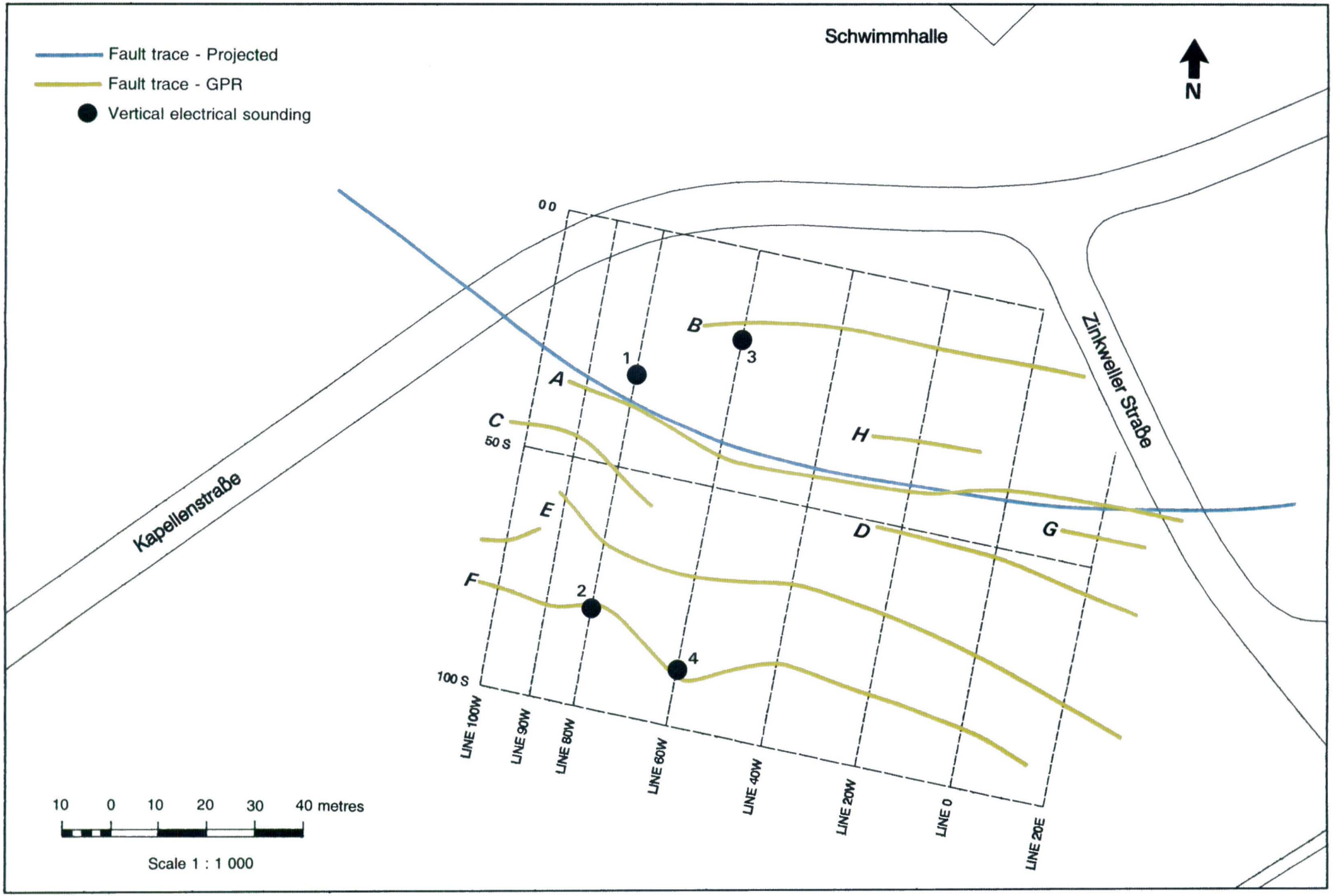

Figure 22. Test Site 3.1. Geophysical grid and interpretation.

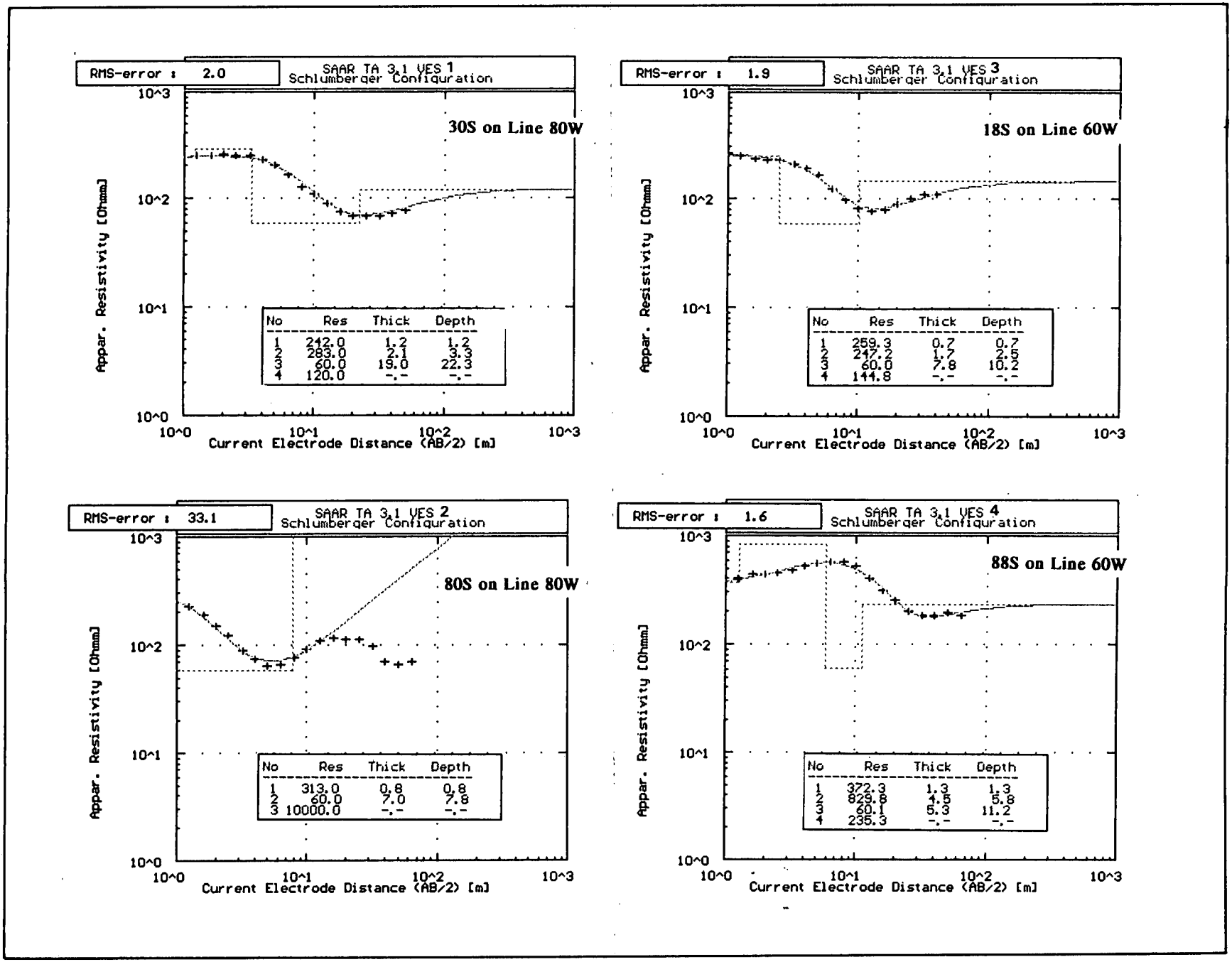

Figure 14 *res.* Test Site 3.1. Interpretation of VES 1, 2, 3, and 4.

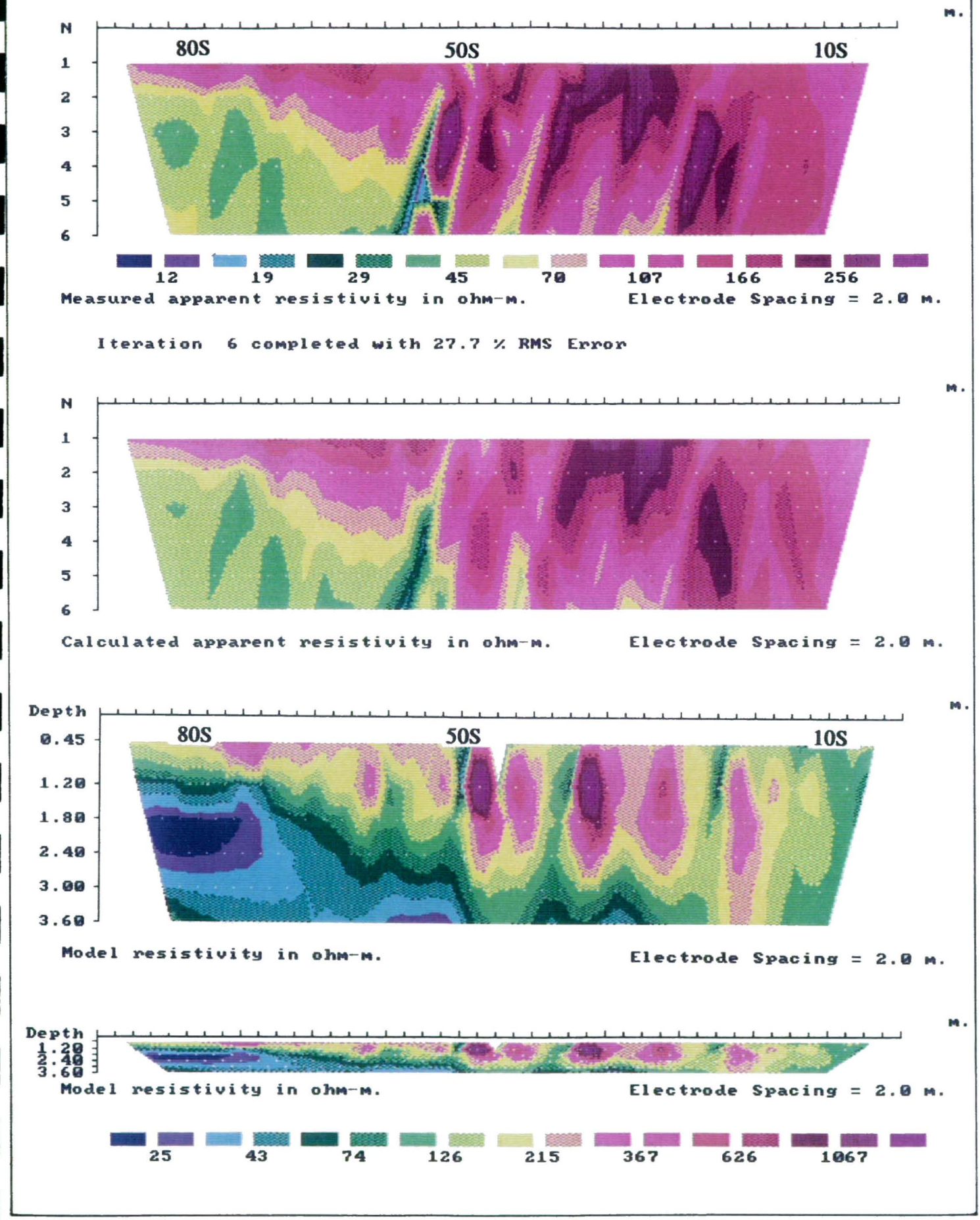

Figure 13 *res.* Test Site 3.1. Line 80W. Dipole-dipole resistivity data.

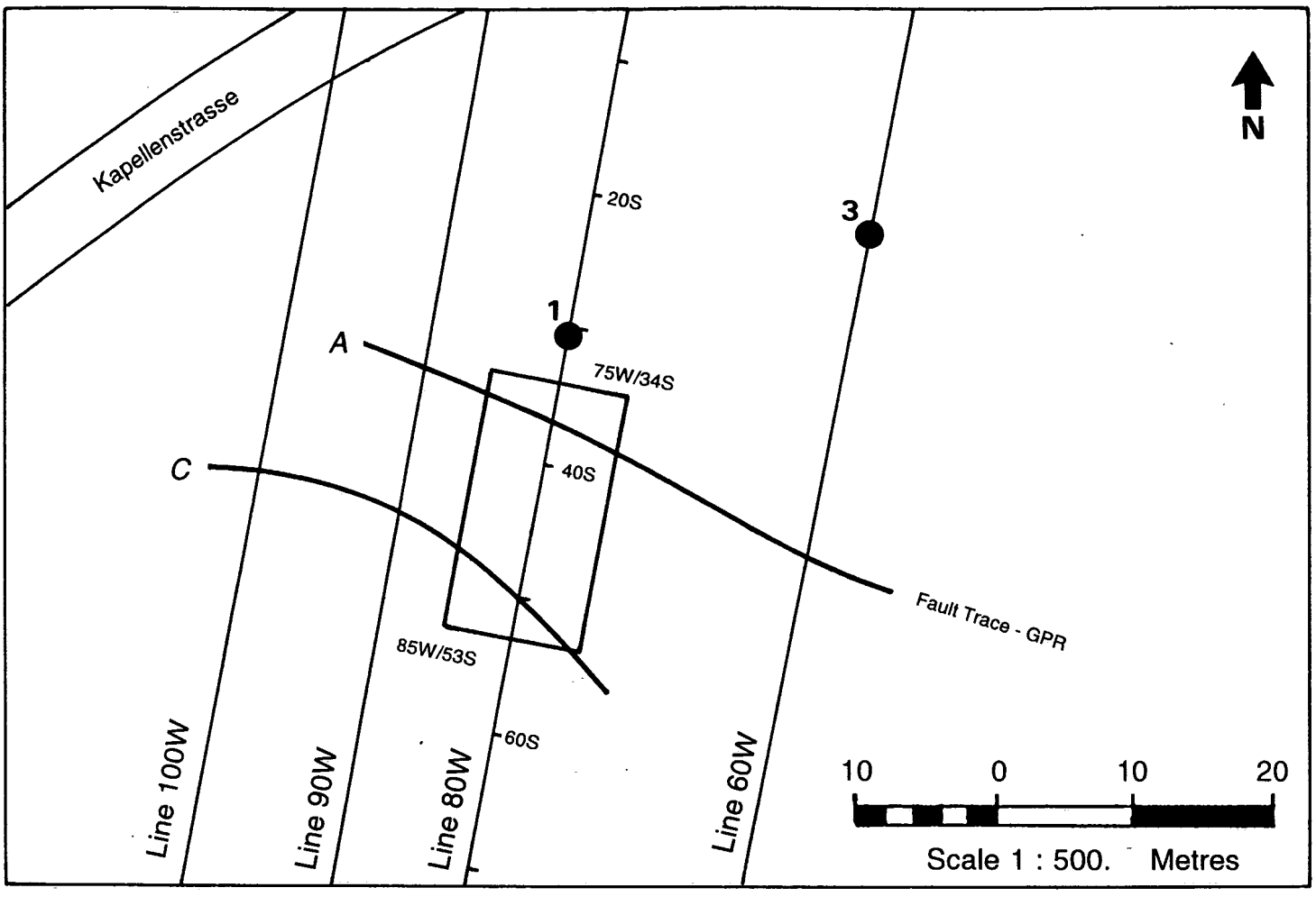

Figure 11 *rsc*. Test Site 3.1. Plan (partial) of site showing location of RESCAN survey grid.

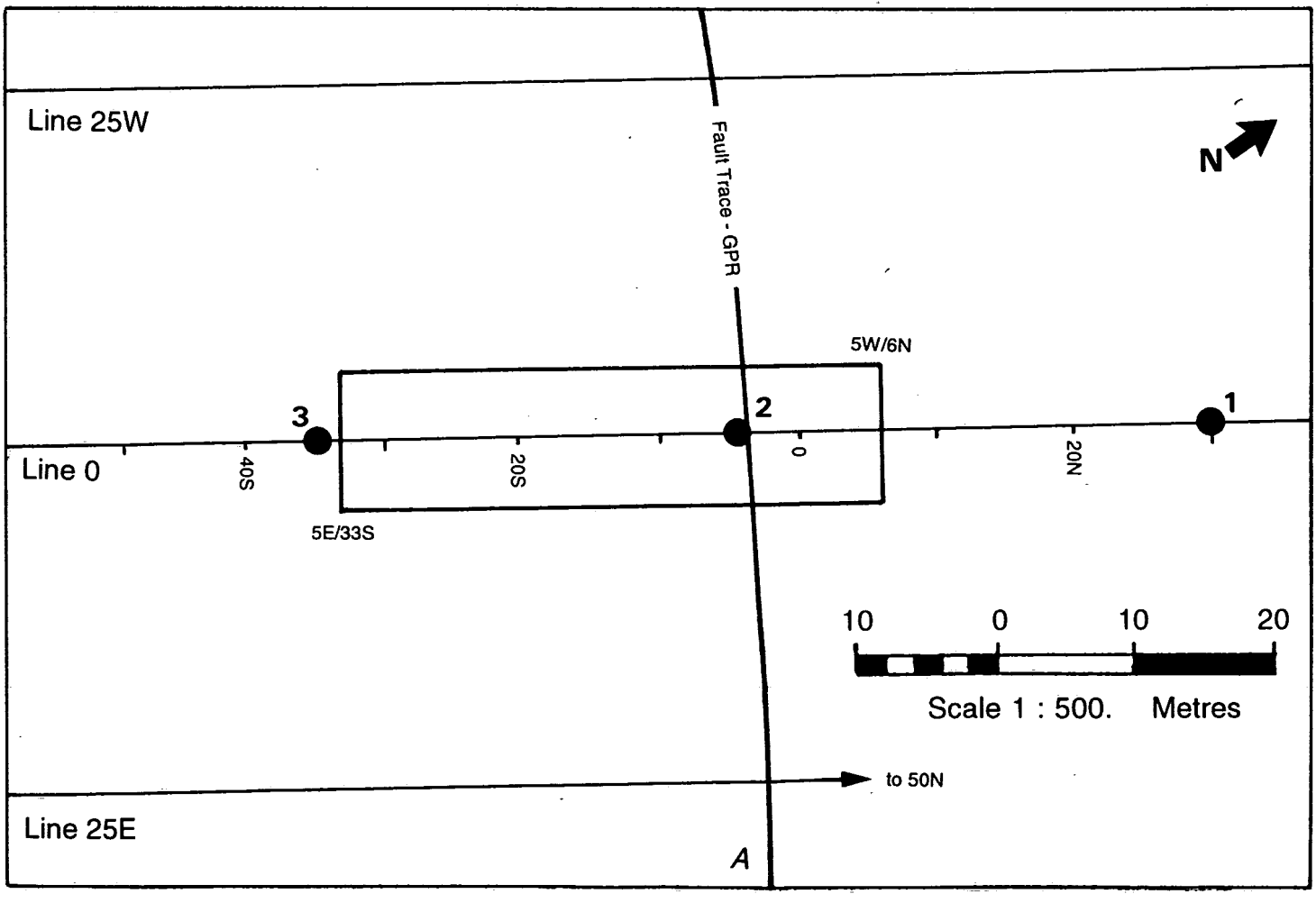

Figure 13 *rsc*. Test Site 3.2. Plan (partial) of site showing location of RESCAN survey grid.

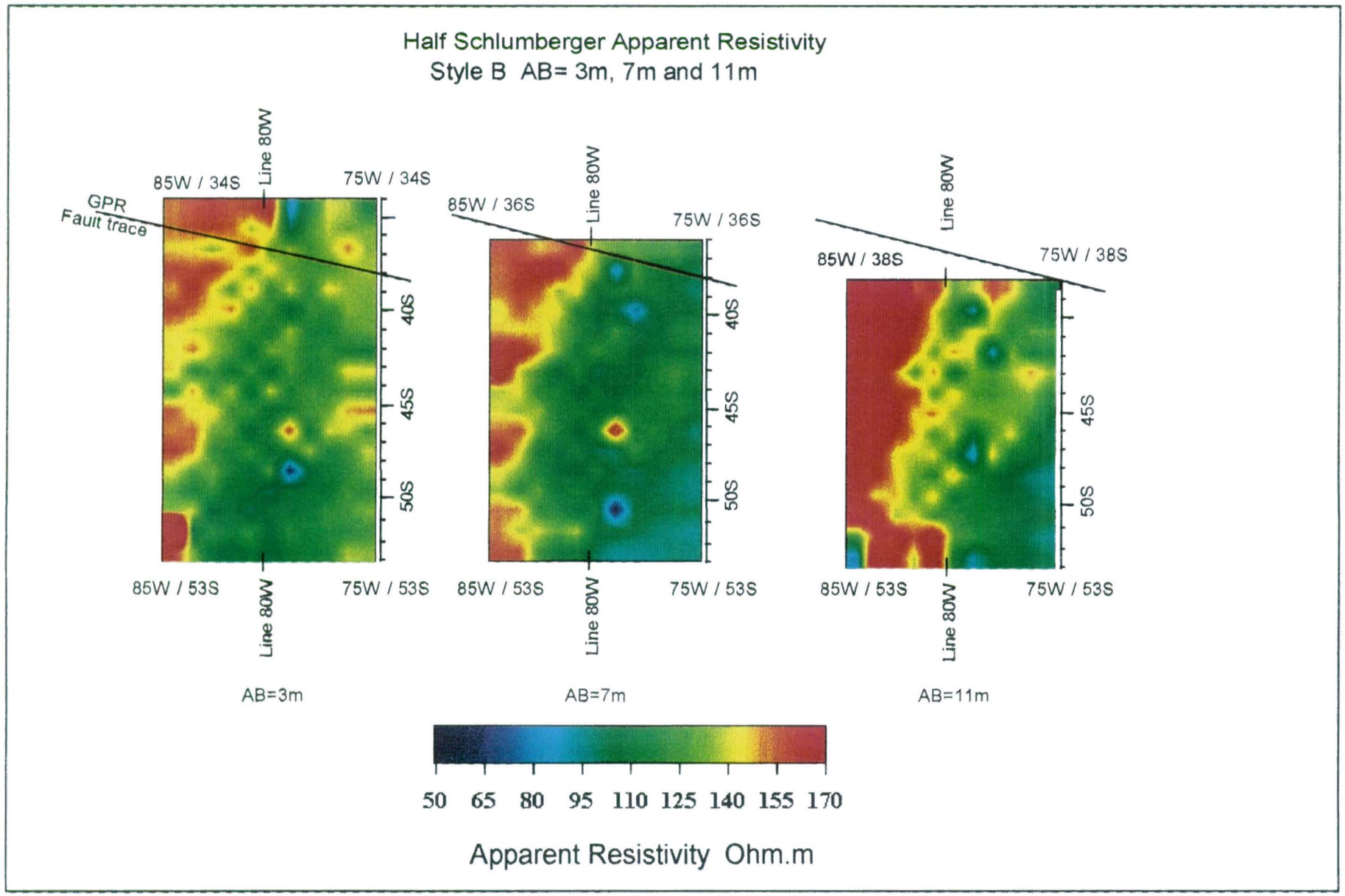

Figure 12 *rsc*. Test Site 3.1. Apparent resistivity data, showing projected position of the fault.

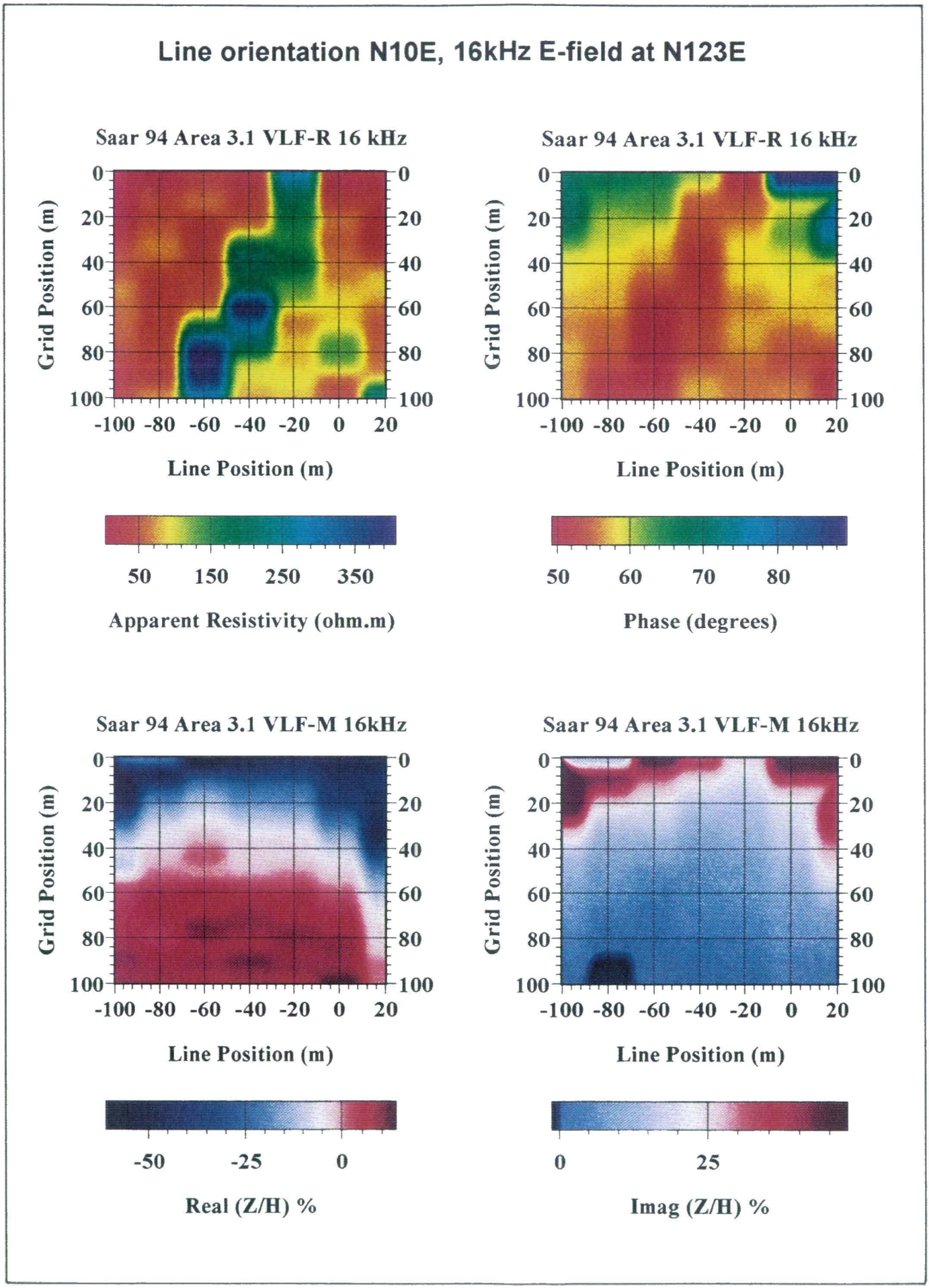

Figure 24 *vlf*. Test Site 3.1. VLF-R and VLF-Z field data for 16 kHz transmitter.

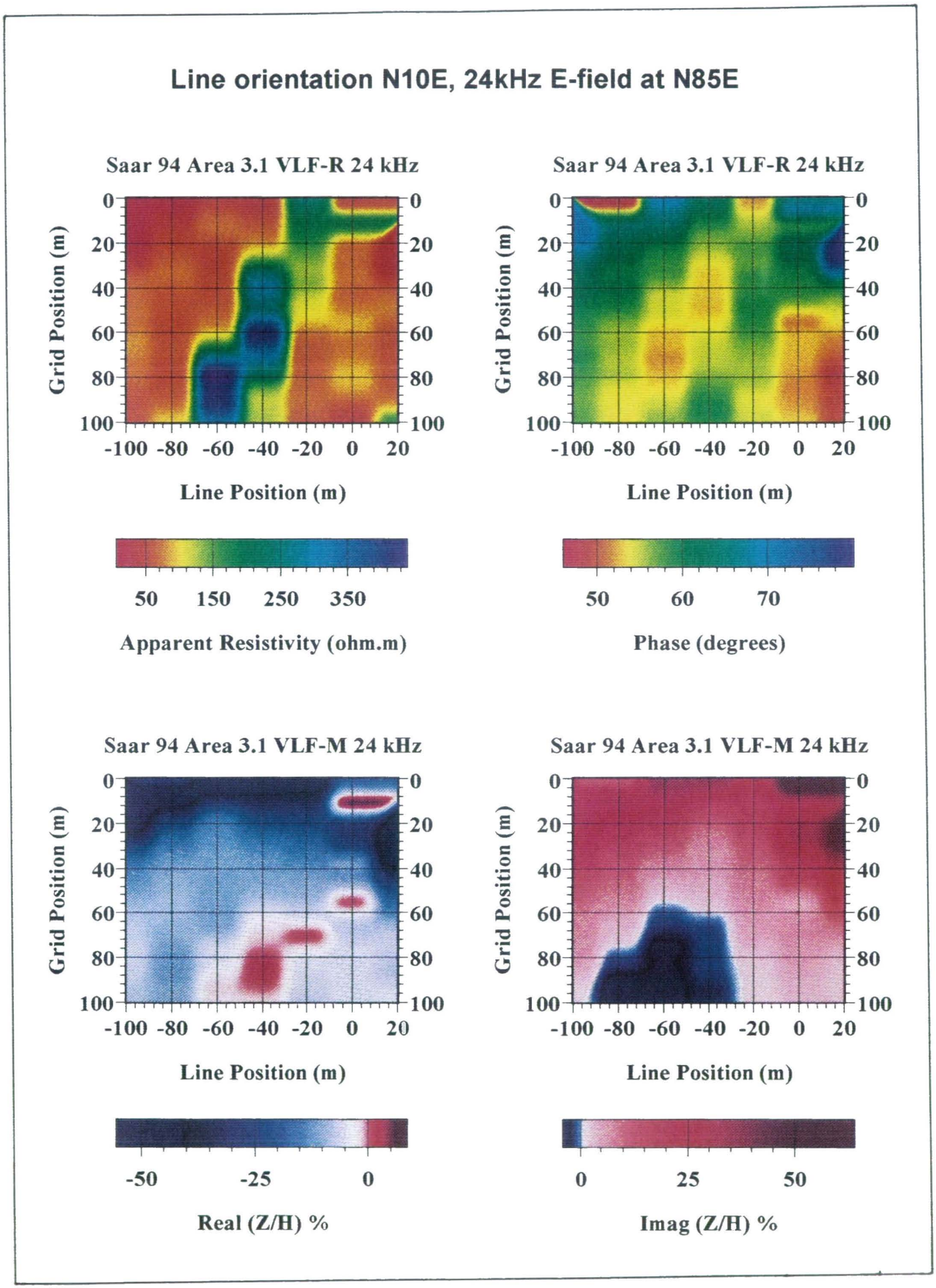

Figure 25 *vlf*. Test Site 3.1. VLF-R and VLF-Z field data for 24 kHz transmitter.

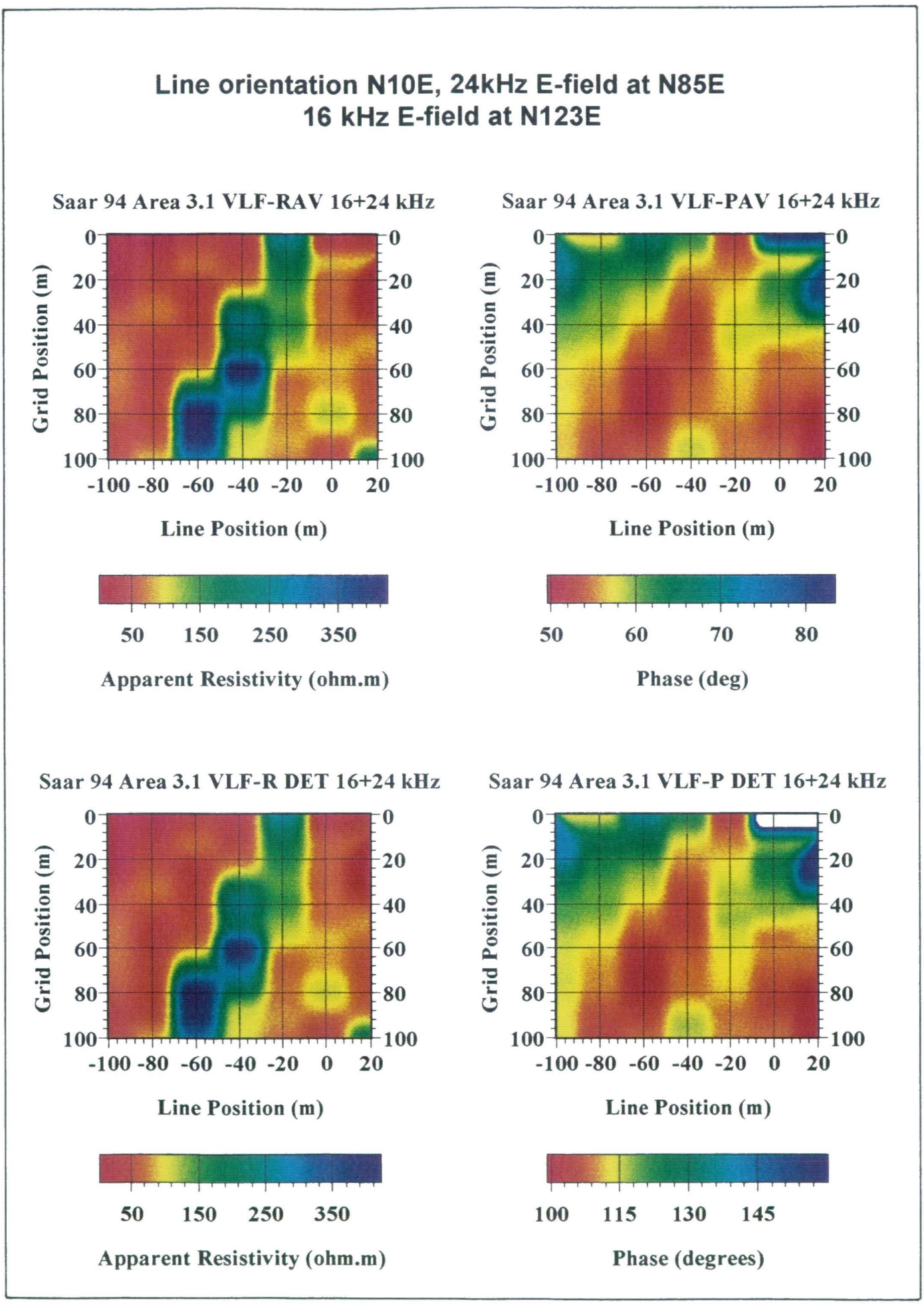

Figure 26 *vlf*. Test Site 3.1. Invariant mapping: 16 kHz and 24 kHz transmitters.

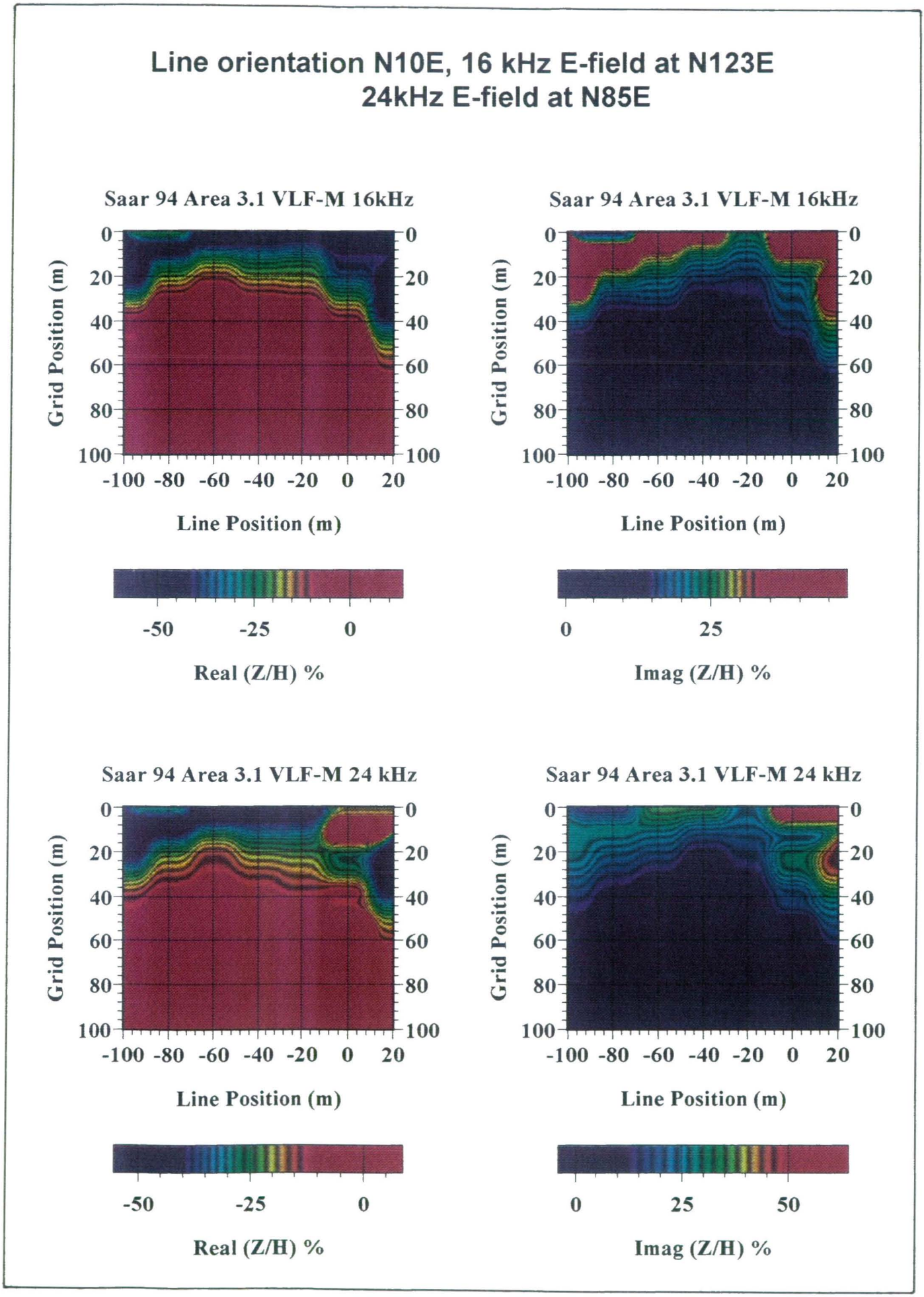

Figure 27 *vlf.* Test Site 3.1. VLF-Z field data using banded contour scale.

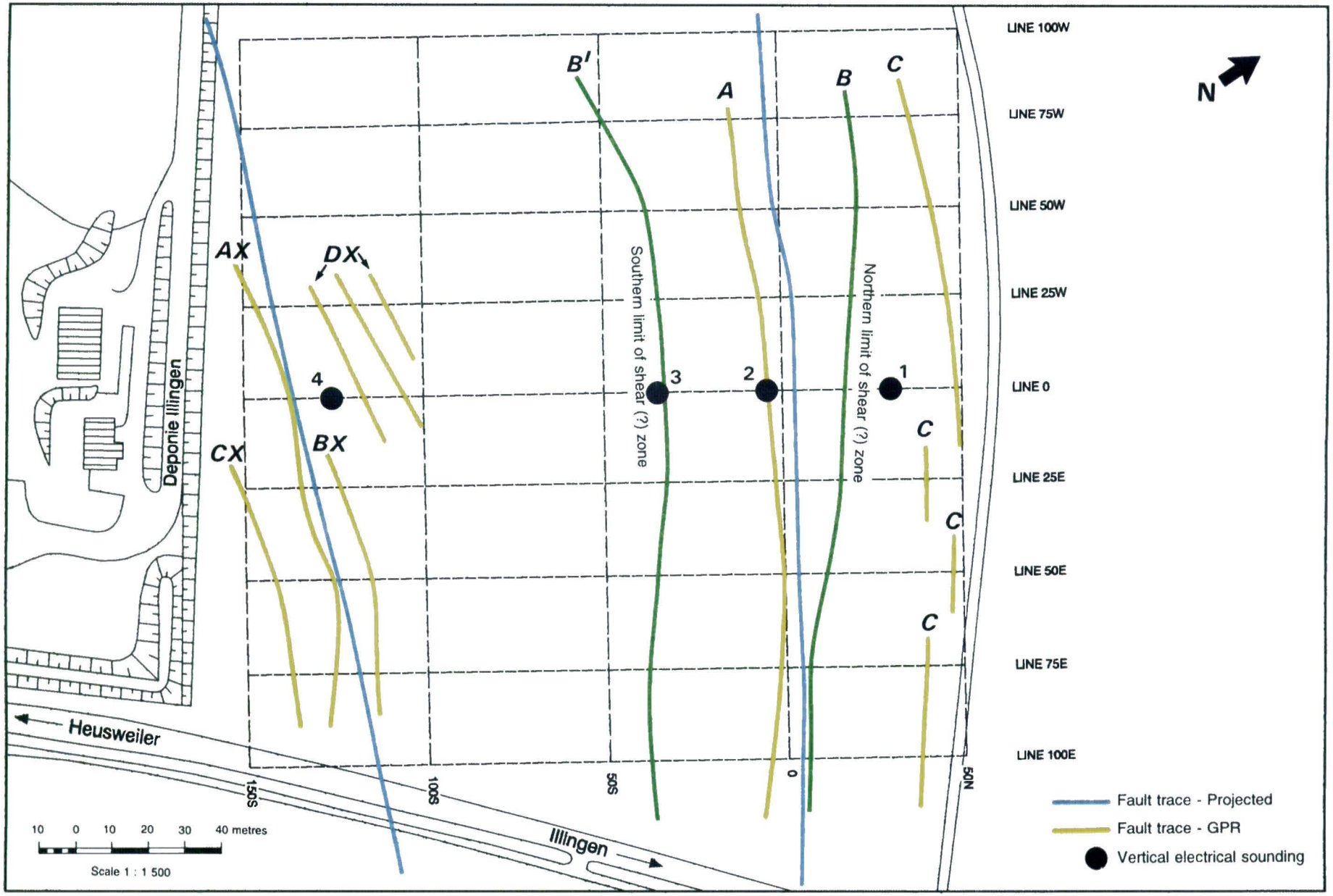

Figure 23. Test Sites 3.2 and 3.2 (Ext). Geophysical grid and interpretation.

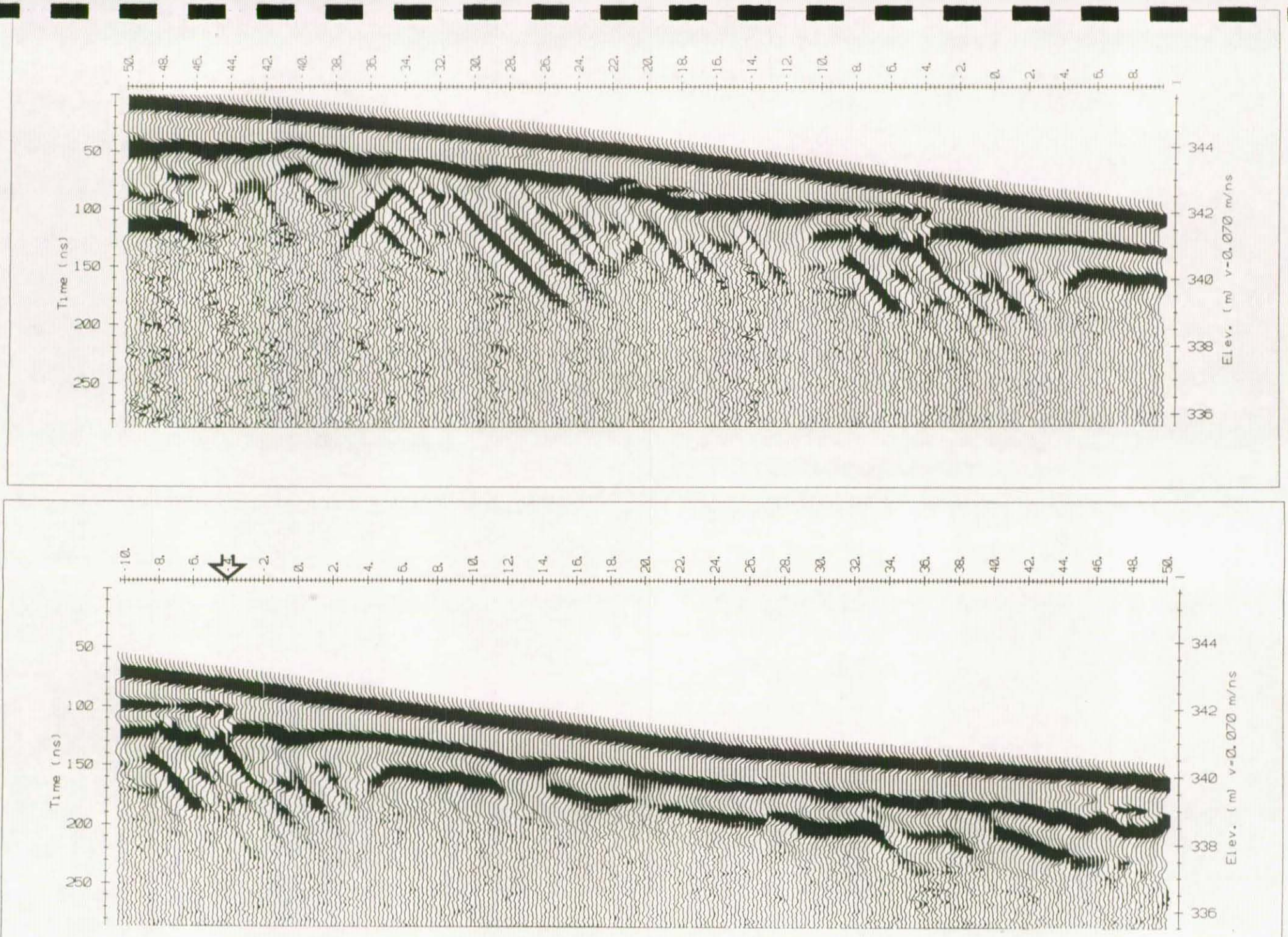

Figure 26 *gpr*. Test Site 3.2. GPR profile for line 100E. 50 MHz antennae.

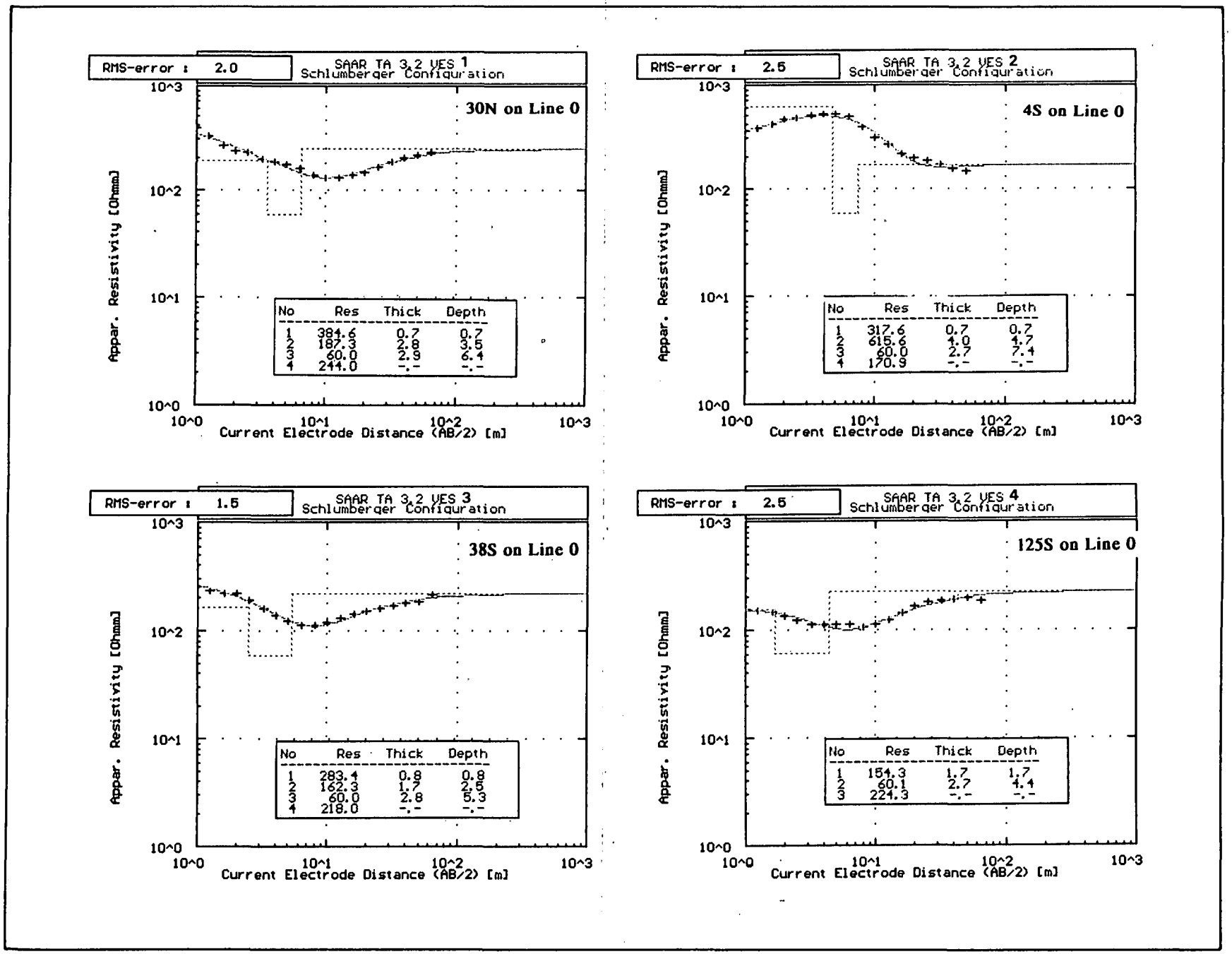

Figure 16 *res.* Test Site 3.2. Interpretation of VES 1, 2, 3, and 4.

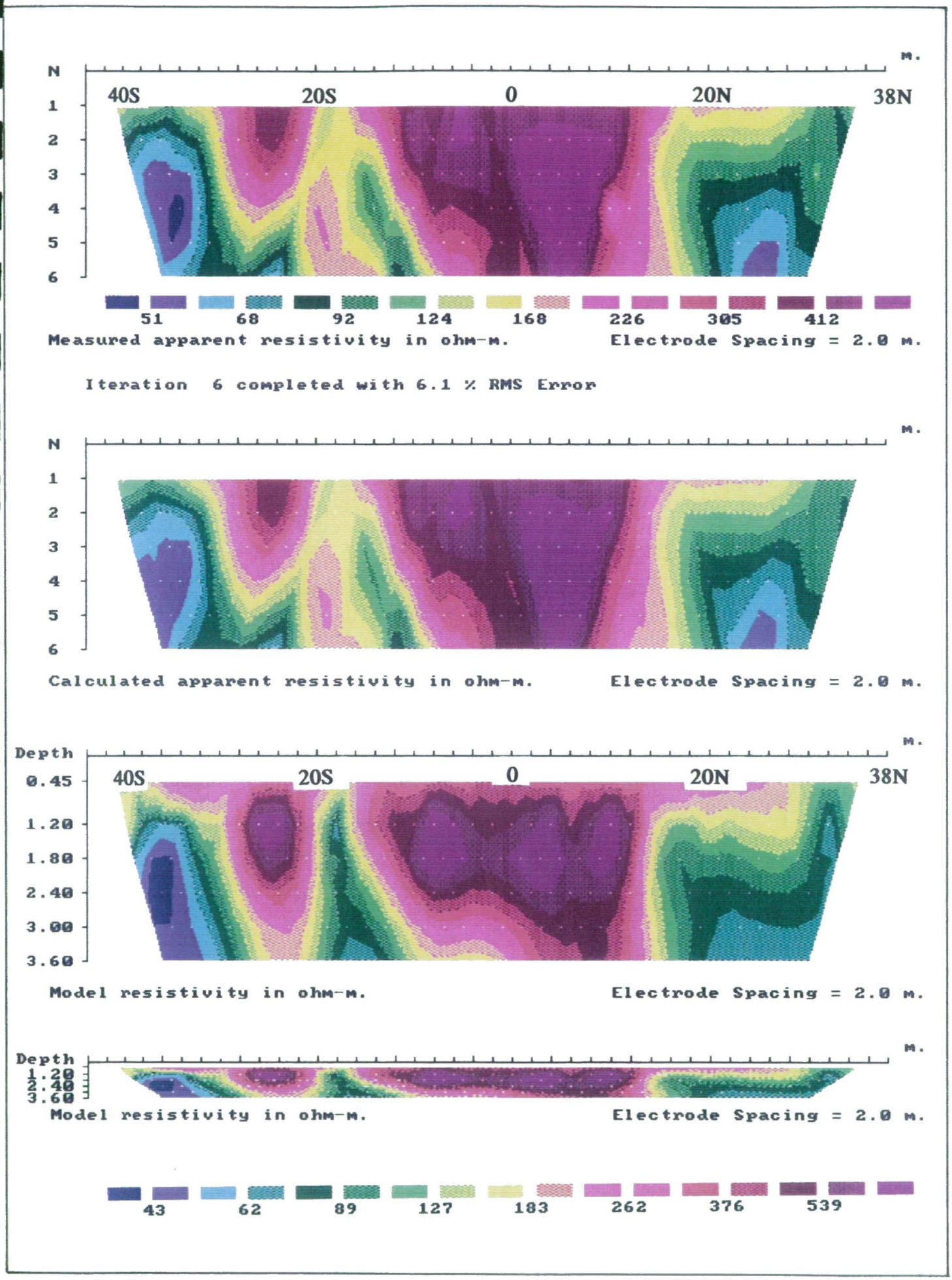

Figure 15 *res.* Test Site 3.2. Line 0. Dipole-dipole resistivity data.

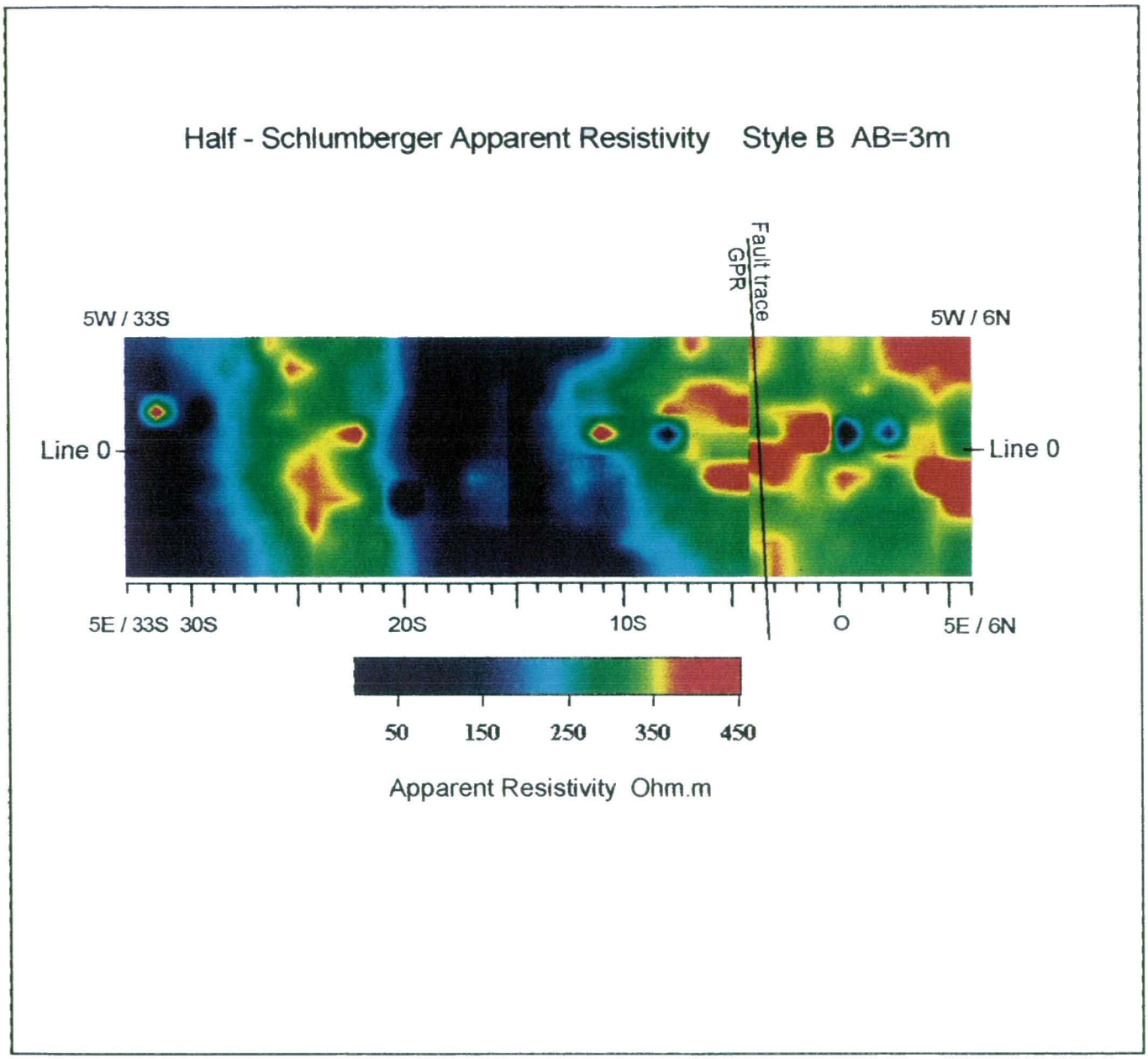

Figure 14 *rsc*. Test Site 3.2. RESCAN apparent resistivity maps for three overlapping sections.

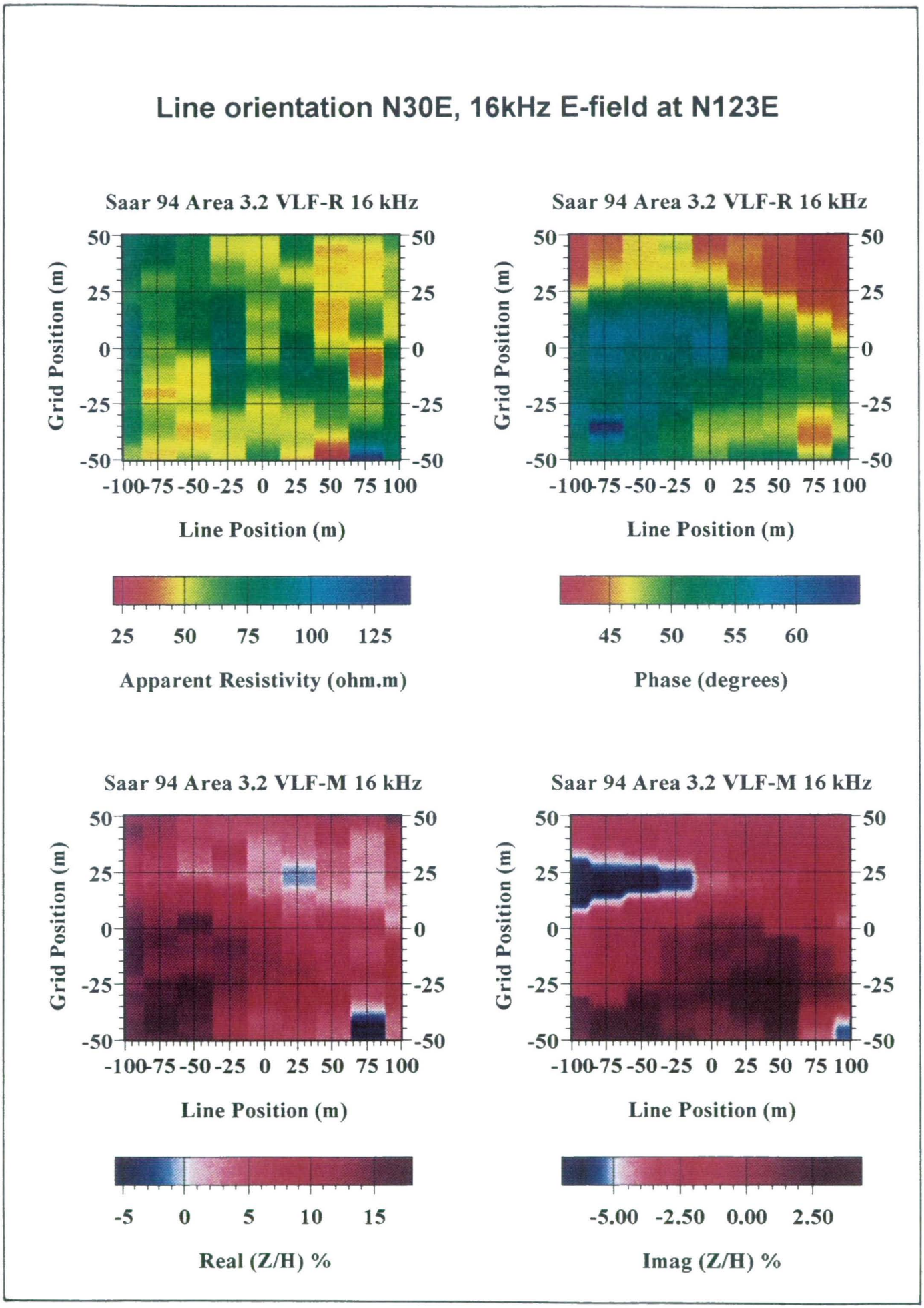

Figure 28 *vlf*. Test Site 3.2. VLF-R and VLF-Z field data for 16 kHz transmitter.

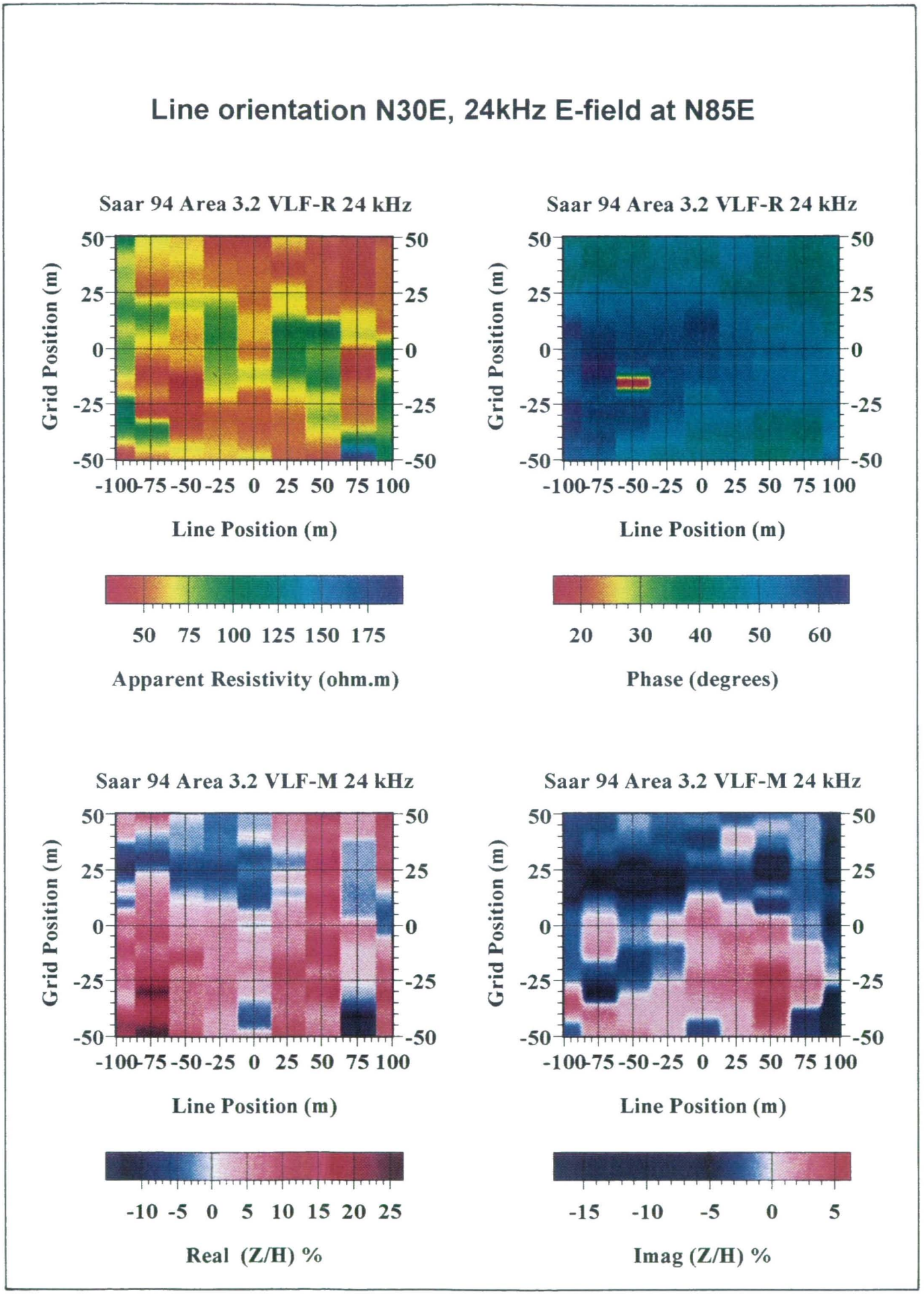

Figure 29 *vlf*. Test Site 3.2. VLF-R and VLF-Z field data for 24 kHz transmitter.

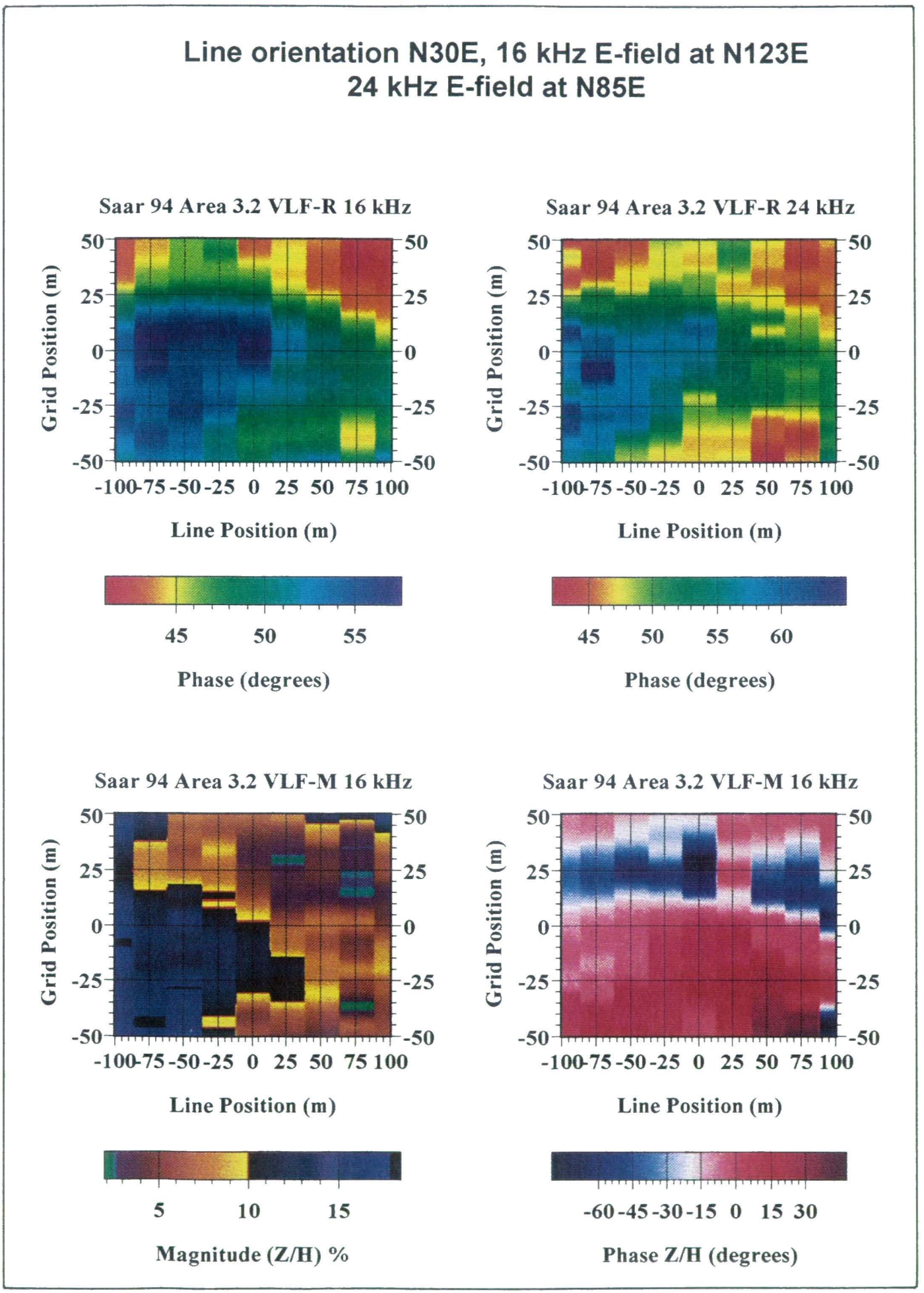

Figure 30 *vlf*. Test Site 3.2. VLF-R (phase) for 16 and 24 kHz transmitters and VLF-Z (converted magnitude and phase) for 16 kHz transmitter.

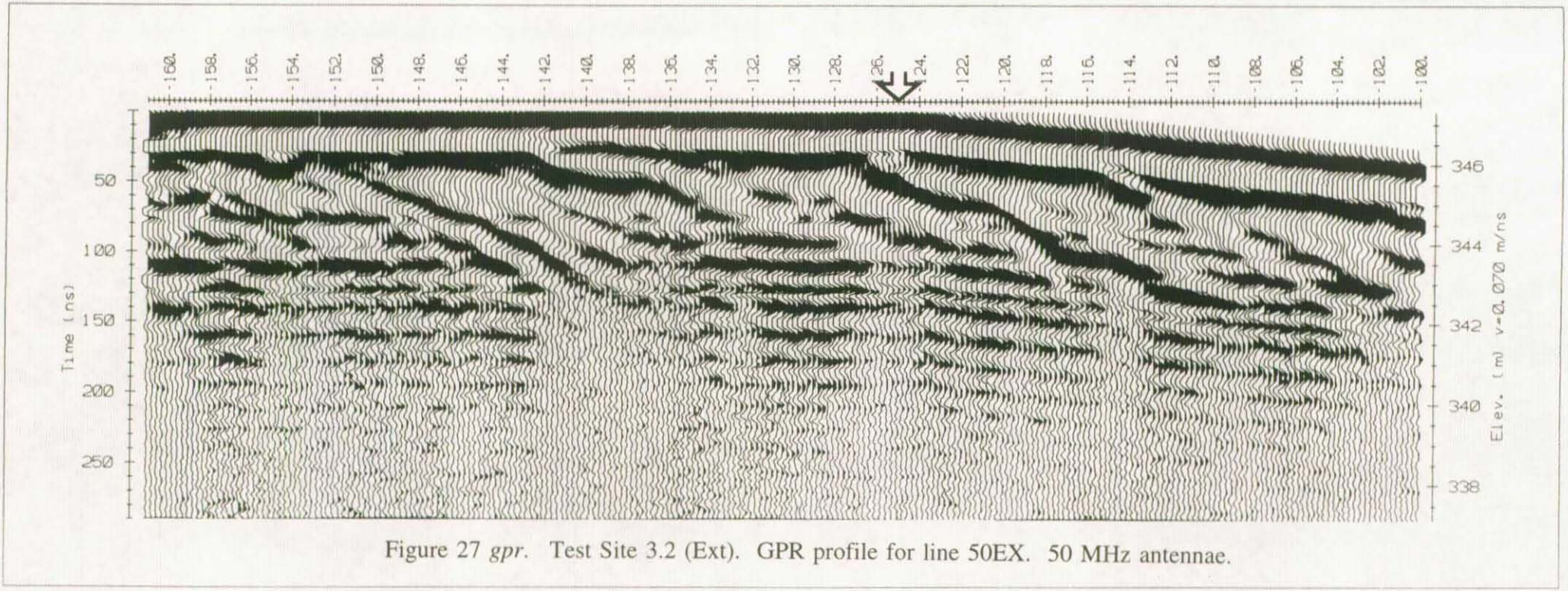

Figure 27 *gpr*. Test Site 3.2 (Ext). GPR profile for line 50EX. 50 MHz antennae.

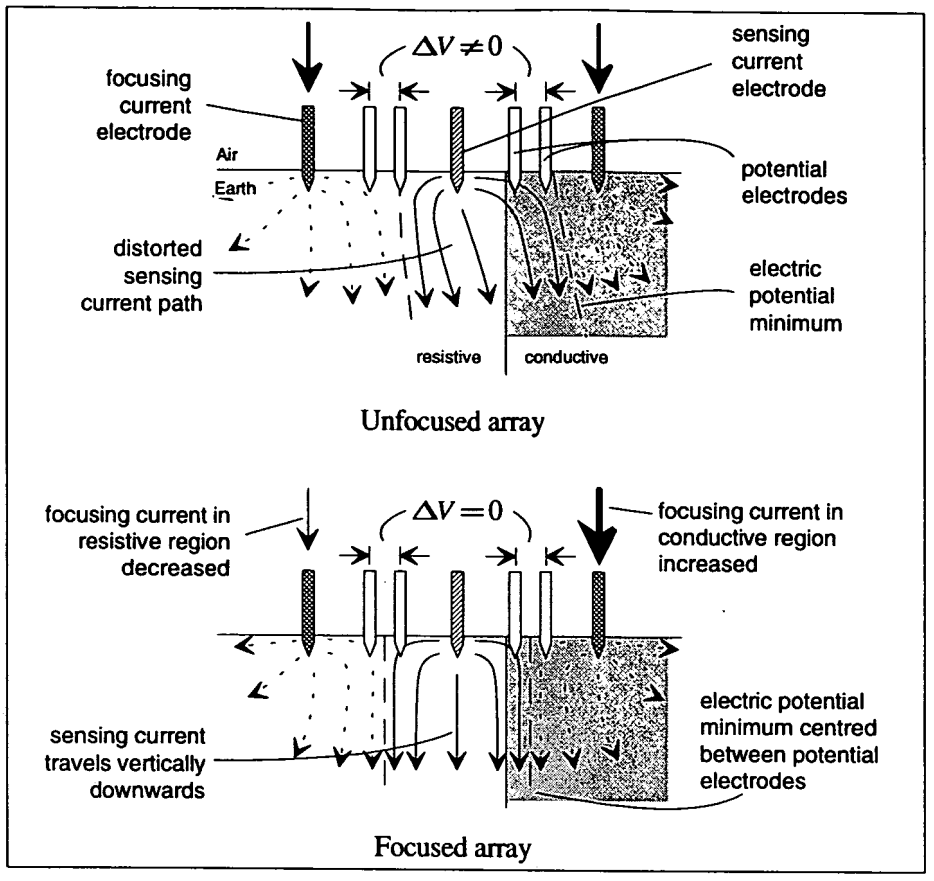

Figure 15 *rsc*. Focussed currents over a conductive/resistive boundary (schematic).

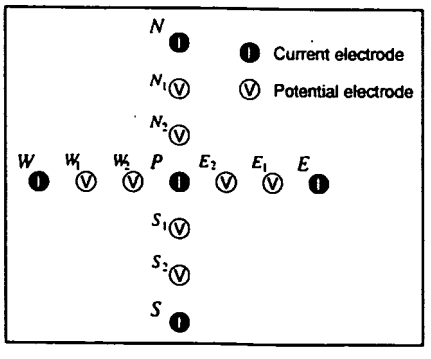

Figure 16 *rsc*. Electrode configuration (schematic) for a 'double laterolog' focussed array proposed by Jackson (1981).

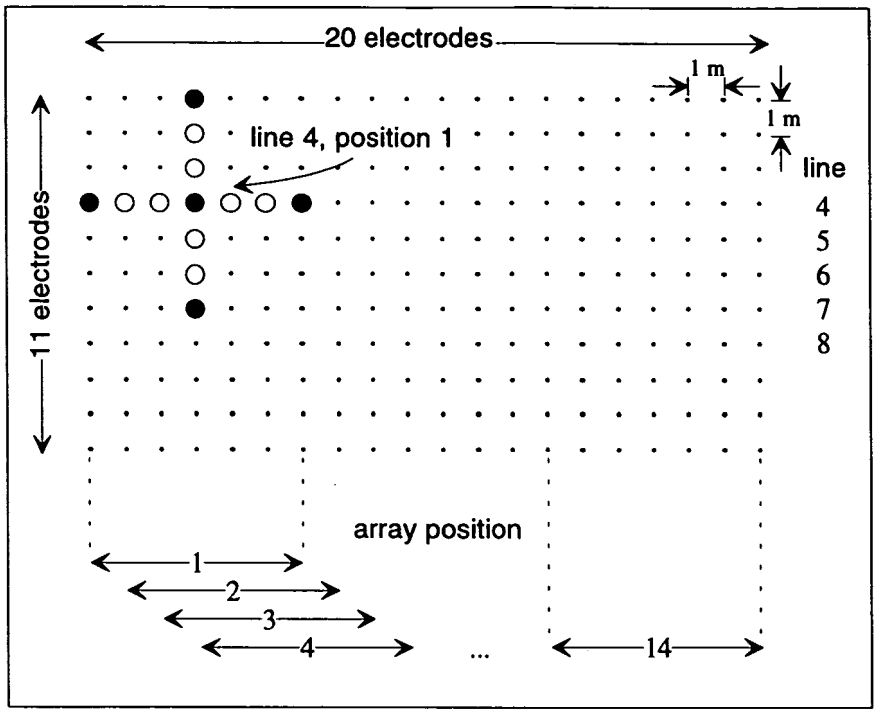

Figure 17 *rsc*. RESCAN electrode grid and focussed array positions.

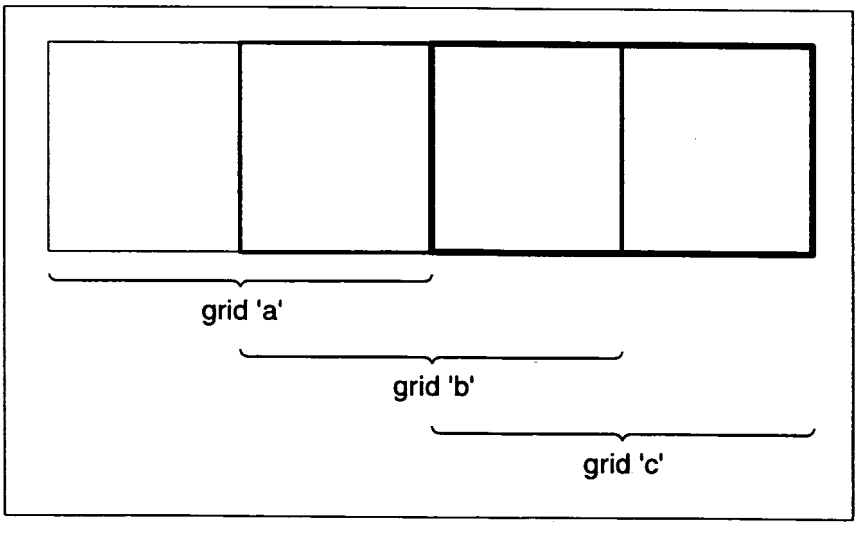

Figure 18 *rsc*. Adjacent grids.

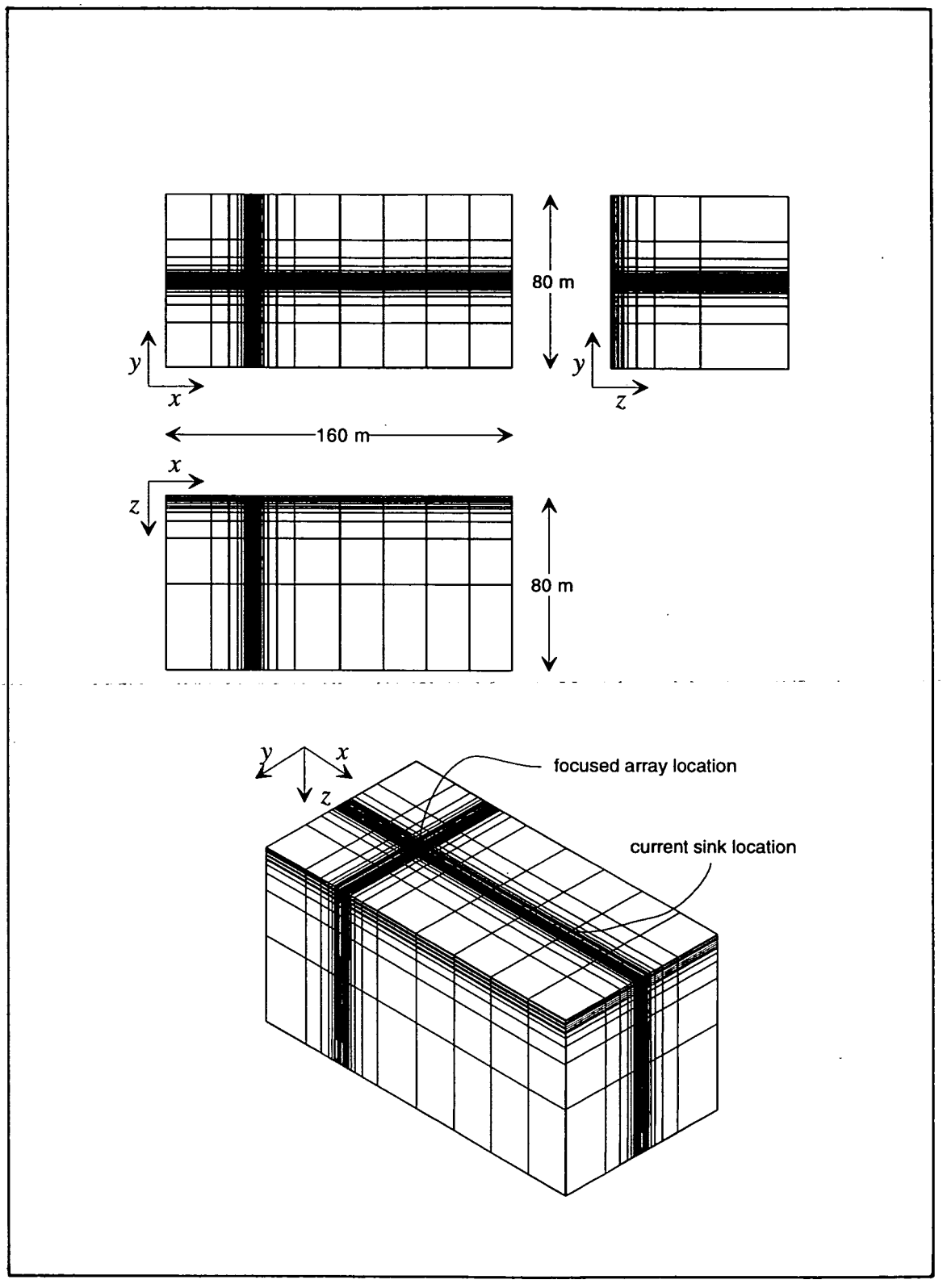

Figure 19 *rsc.* Model grid used in simulations of the focussed array.